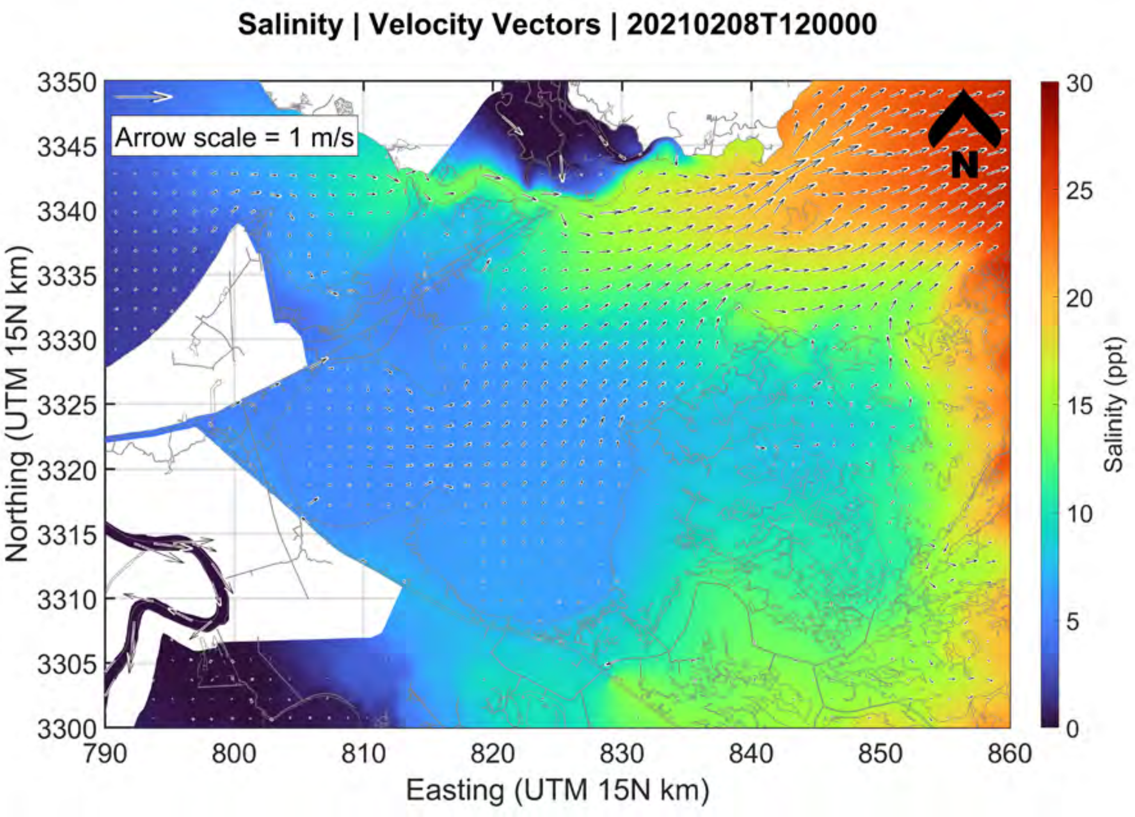

DEVELOPMENT OF A HYDRODYNAMIC MODEL FOR LAKE PONTCHARTRAIN AND LAKE BORGNE TO INFORM GULF STURGEON HABITAT CHARACTERIZATION

FRANCESCA MESSINA, MARTIJN BREGMAN, SHAN ZOU,
IOANNIS Y. GEORGIOU, SOUPY DALYANDER, MIKE MINER

Produced for and funded by Coastal Protection and Restoration Authority under Task Order 81

THE WATER
INSTITUTE

November 2023

ABOUT THE WATER INSTITUTE

SUGGESTED CITATION

Messina F., Bregman, M., Zou S., Georgiou I.Y., Dalyander S., Miner M., (2023). Development of a Hydrodynamic Model for Lake Pontchartrain and Lake Borgne to Inform Gulf Sturgeon Habitat Characterization. The Water Institute. Prepared for and/or funded by the Coastal Protection and Restoration Authority. Baton Rouge, LA.

PREFACE

This report was developed by The Water Institute (the Institute) for the Coastal Protection and Restoration Authority under Task Order 81: Lake Borgne Gulf Sturgeon Monitoring and Habitat Characterization.

The report summarizes the development of a hydrodynamic model for Lake Pontchartrain, Lake Borgne, and surrounding areas to inform the development of a sturgeon habitat characterization. The hindcast simulations of this model were shared with Louisiana State University and the U.S. Fish and Wildlife Service who used them to quantify coastal estuarine environmental parameters that are important to provide suitable habitat for Gulf sturgeon.

ACKNOWLEDGEMENTS

This analysis, report, and all related items of information were prepared by the authors through Task Order 81 (Lake Borgne Gulf Sturgeon Monitoring and Habitat Characterization) with the Louisiana Coastal Protection and Restoration Authority, who were awarded under Award No. LA-2020-031 from the Louisiana Trustee Implementation Group (LATIG) to implement the Lake Borgne marsh creation project. The data, statements, findings, conclusions, and recommendations are those of the authors and do not necessarily reflect any determinations, views, or policies of the LATIG Council.

Jessica Converse and Jim Pahl at CPRA provided technical guidance throughout the project and editing suggestions that improved this report.

The authors thank our collaborators at the U.S. Fish and Wildlife Service (Glenn Constant, Ashley Baer, Logan Leblanc) and Louisiana State University (Michael Dance, Cassie Glaspie, Jenna Brogdon) for the collection of important field data and for sharing their expertise on Gulf sturgeon with the modeling team to produce an interdisciplinary product. Editing suggestions that improved this report were also provided by Glenn Constant.

Geologists, geomorphologists, scientists, and engineers from the Institute and CPRA contributed to this work and to the development of this report and are acknowledged with thanks.

This report was reviewed, edited, and formatted by Charley Cameron of the Institute.

EXECUTIVE SUMMARY

This report describes the development, calibration, and validation of a depth-averaged Delft3D-FM hydrodynamic model for the Pontchartrain Basin in coastal Louisiana. Specifically, the model extent included Lake Maurepas, Lake Pontchartrain, Lake St. Catherine, Lake Borgne, the lower Pearl River Valley, Mississippi Sound, Breton Basin, a portion of the lower Mississippi River and the modern delta were included in the model. These areas are part of the habitat of the Gulf sturgeon species. In conjunction with existing telemetry data, the results from this hydrodynamic model were used to develop a programmatic approach to Gulf sturgeon habitat evaluation. As such, the model spatial resolution varied resolving critical areas of transit for adult species to and from spawning grounds, and areas where juvenile species are likely to be found; to accurately resolve these corridors the mesh included mixing quadrilateral and triangular mesh elements.

The initial landscape and bathymetry in the model were informed by using United States Geological Survey (USGS) Digital Elevation Model (DEM) datasets. Similarly, USGS gauging stations and derived rating curves were used to impose the tributary boundary conditions to the model including the Mississippi River. For years in which the Bonnet Carré spillway was open, observed flows were used to represent freshwater inflow into Lake Pontchartrain, and when the Bonnet Carré was closed, but stage in the Mississippi River was high, leakage flows were established using previous observations and analysis (McCorquodale et al., 2009). Meteorological and atmospheric forcing was accomplished through use of the National Centers for Environmental Prediction (NCEP) North American Mesoscale (NAM) spatially variable datasets.

The model was calibrated for water level, salinity, and temperature using National Oceanic and Atmospheric Administration (NOAA), USGS and Coastwide Reference Monitoring System (CRMS) data from the year 2016. Stations from the same networks as well as conductivity, temperature, and depth (CTD) casts collected by USFWS in 2020–2021 were used to validate the model. The model captures the water level variation and fluctuation (tidal and non-tidal), the salinity seasonal variation and the temperature trends very well and shows excellent agreement with the CTD cast data.

The CTD data collected mostly showed a lack of stratification in the areas sampled. Knowing that intermittent stratification is possible in deep water under specific conditions, a proxy for low dissolved oxygen (DO) condition was developed using results from a previous three-dimensional FVCOM model and other empirical datasets. The approach developed allows the estimation of the likelihood of low DO conditions using the depth averaged results from the Delft3D-FM model developed under this study.

A turbidity proxy was also developed by using the Soulsby method to calculate the combined wave-current bottom shear stress as a function of bottom orbital velocity amplitude, wave period, angle between wave and current, depth-average flow velocity magnitude, water depth and bed roughness length.

Water level, water depth, salinity, water temperature, wind speed, and water velocity timeseries at 94 stations where the sturgeon receivers were deployed and mapped output for six different years (from 2016 to 2022) were shared with Louisiana State University (LSU) and U.S. Fish and Wildlife Service (USFWS) for the development of the habitat suitability maps for Gulf sturgeon.

TABLE OF CONTENTS

LIST OF FIGURES

LIST OF TABLES

LIST OF ACRONYMS

Acronym	Term
ADCP	Acoustic Doppler Current Profiler
BACI	Before-After-Control-Impact
CPRA	Coastal Protection and Restoration Authority
CRMS	Coastwide Reference Monitoring System
CTD	Conductivity, temperature, and depth
Delft3D-FM	Delft3D Flexible Mesh Modeling Suite
DEM	Digital Elevation Model
DO	Dissolved Oxygen
ESA	Endangered Species Act
FVCOM	Finite-Volume Community Ocean Model
HyCOM GOFS	Hybrid Coordinate Ocean Model Global Ocean Forecasting System 3.1
HOP	Head of Passes
ICWW	Intracoastal Waterway
LDWF	Louisiana Department of Wildlife and Fisheries
LMRMP	Lowermost Mississippi River Management Program
LSU	Louisiana State University
MRGO	Mississippi River Gulf Outlet
MVN	New Orleans District
NAM	North American Mesoscale
NCEP	National Centers for Environmental Prediction
NGOM	Northern Gulf of Mexico
NMFS	National Marine Fisheries Service
NOAA	National Oceanic and Atmospheric Administration
RMSE	Root Mean Square Error
3D	Three-Dimensional
2D	Two-Dimensional
USACE	U.S. Army Corps of Engineers
USFWS	U.S. Fish and Wildlife Service
USGS	U.S. Geological Survey
WSE	Water Surface Elevation

UNIT TABLE

Abbreviation	Term
°C	Degrees Celsius
cm	Centimeter
cms	Cubit meter per second
km	Kilometers
Hz	Hertz
m	Meters
m^2	Square Meters
mg/L	Milligrams per liter
mm/yr	Millimeters per year
ppt	Parts per thousand
s	Second

1.0 INTRODUCTION

Gulf sturgeon (*Acipenser oxyinchus desotioi*) are a sub-species of Atlantic sturgeon (*A. o.* oxyrinchus) with a range in the northern Gulf of Mexico that includes Lake Pontchartrain and the Pearl River system to the west and extends east to the Suwannee River in Florida (Sulak et al., 2016). The National Marine Fisheries Service (NMFS)[1] has designed several areas of the region as critical habitat for Gulf sturgeon (Figure 1), a designation that is used to denote areas that require special protection under the Endangered Species Act (NOAA Fisheries, 2022b). There are multiple restoration projects in various stages of planning and implementation within Louisiana coastal areas (marsh, estuarine, etc.,) that overlap with this region. Due to the limited current understanding of the spatial and seasonal variability of Gulf sturgeon habitat within the broad spatial area of their critical habitat, many of these restoration projects are, or potentially will be, required to have an informal consultation with the U.S. Fish and Wildlife Service (USFWS) and NMFS as a first step under Section 7 of the ESA (USFWS, 1973). This often-lengthy process can result in the need for expensive data collection (e.g., telemetry data, water quality, benthic invertebrate characterization) to support evaluation of whether or not a given project may adversely affect Gulf sturgeon. Such consultations are required to evaluate if a project will impact Gulf sturgeon habitat, which would then potentially require mitigation. Even if the amount of impacted habitat is inconsequential for a single project, USFWS and NMFS may have concerns that the additive effect of impacts from multiple projects may start to influence behavior and occurrence of this sub-species. Finally, the full spatial range of designated critical habitat is currently classified as being of equal value to Gulf sturgeon, which provides no guidance as to where sediment borrow projects should be sited to have the least impact on this sub-species.

There is an opportunity to develop a programmatic approach to habitat evaluation for Gulf sturgeon in the northern Gulf of Mexico by using telemetry data that track the movement of the sub-species. A programmatic approach to habitat delineation and monitoring can reduce the need for data collection and analysis by individual restoration projects where there is a need to assess Gulf sturgeon impacts and address requirements for consultation under the ESA. One of the foundations needed to establish a programmatic approach to Gulf sturgeon habitat evaluation is a more detailed understanding of the spatial and temporal distribution of Gulf sturgeon within their critical habitat designation in the northern Gulf, including identification of the key environmental factors that drive that distribution. Although there is some understanding of what factors likely influence sturgeon distribution, including salinity, temperature, and substrate type, no models exist that quantify the relative influence of these factors, or which can be used to project that distribution in space and time.

---

[1] NMFS is also referred to as “NOAA [National Oceanic and Atmospheric Administration] Fisheries.

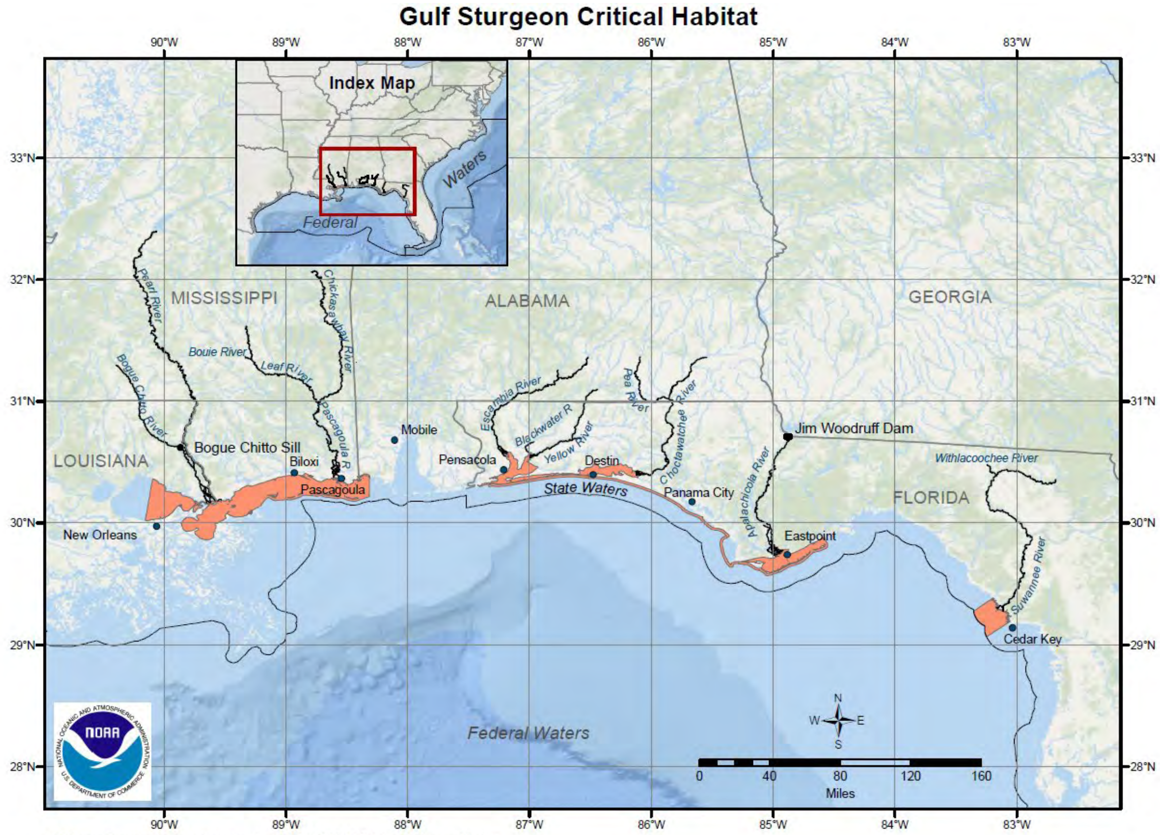

Esri Ocean Basemap Sources: Esri, Garmin, GEBCO, NOAA NGDC, and other contributors

Figure 1. Gulf sturgeon critical habitat (orange polygons) map. From NOAA Fisheries (2022).

To address this need, the Lake Borgne Gulf Sturgeon Monitoring and Habitat Characterization project was developed as a collaborative effort of the Water Institute of the Gulf (the Institute), USFWS, and Louisiana State University (LSU) to monitor Gulf sturgeon movement in Lake Borgne and Lake Pontchartrain; couple those observations with hindcast simulations from hydrodynamic modeling and substrate data; and characterize Gulf sturgeon habitat preference. The ongoing project (as of November 2023) is supported by the Louisiana Trustee Implementation Group (LA TIG) with the Department of the Interior (DOI) as the lead Federal Trustee. The Louisiana Coastal Protection and Restoration Authority (CPRA) oversee Work by the Institute and LSU, with DOI and CPRA jointly reporting to the LA TIG. The project began in August 2020 and is scheduled for completion in July 2024.

This report focuses on the Deltares Delft3D Flexible Mesh Modeling Suite (Delft3D FM) hydrodynamic model (“Hydrodynamic Model” herein) that was developed to project coastal and estuarine parameters that are important in providing suitable habitat for Gulf sturgeon. These model results will be combined with observational data in a future phase of the project to develop a model which correlates Gulf sturgeon occupancy with environmental conditions.

Delft3D-FM is a two-dimensional (2D), depth-averaged numerical model that simulates environmental parameters including salinity, temperature, water depth, and flow. Output from this model was also used to explore a simple methodology for the development of a proxy for dissolved oxygen (DO), which was identified to be of potential relevance to Gulf sturgeon occupancy. In addition, a numerical wave model was developed over a portion of the domain that included Lake Pontchartrain, Lake Borgne, and the western Mississippi Sound. The Wave Model was developed and coupled to the flow model to better estimate the bottom shear stress, which serves as a proxy for near-bed turbulence that may contribute to sturgeon habitat suitability. Section 2.0 of this report describes the development of the Hydrodynamic and Wave models, the main features of these models, and the calibration/validation process used. Section 3.0 describes the exploratory methodology to develop a DO proxy to estimate the likelihood of low DO conditions. Section 4.0 describes the output of the hindcast simulations and associated uncertainties, as well as the calculation of the turbidity proxy.

1.1 AREA OF INTEREST

The area of interest for this project includes designated critical habitat for Gulf sturgeon in Lake Pontchartrain, Lake St. Catherine, Lake Borgne, and the Pearl River and its mouth (Figure 2).

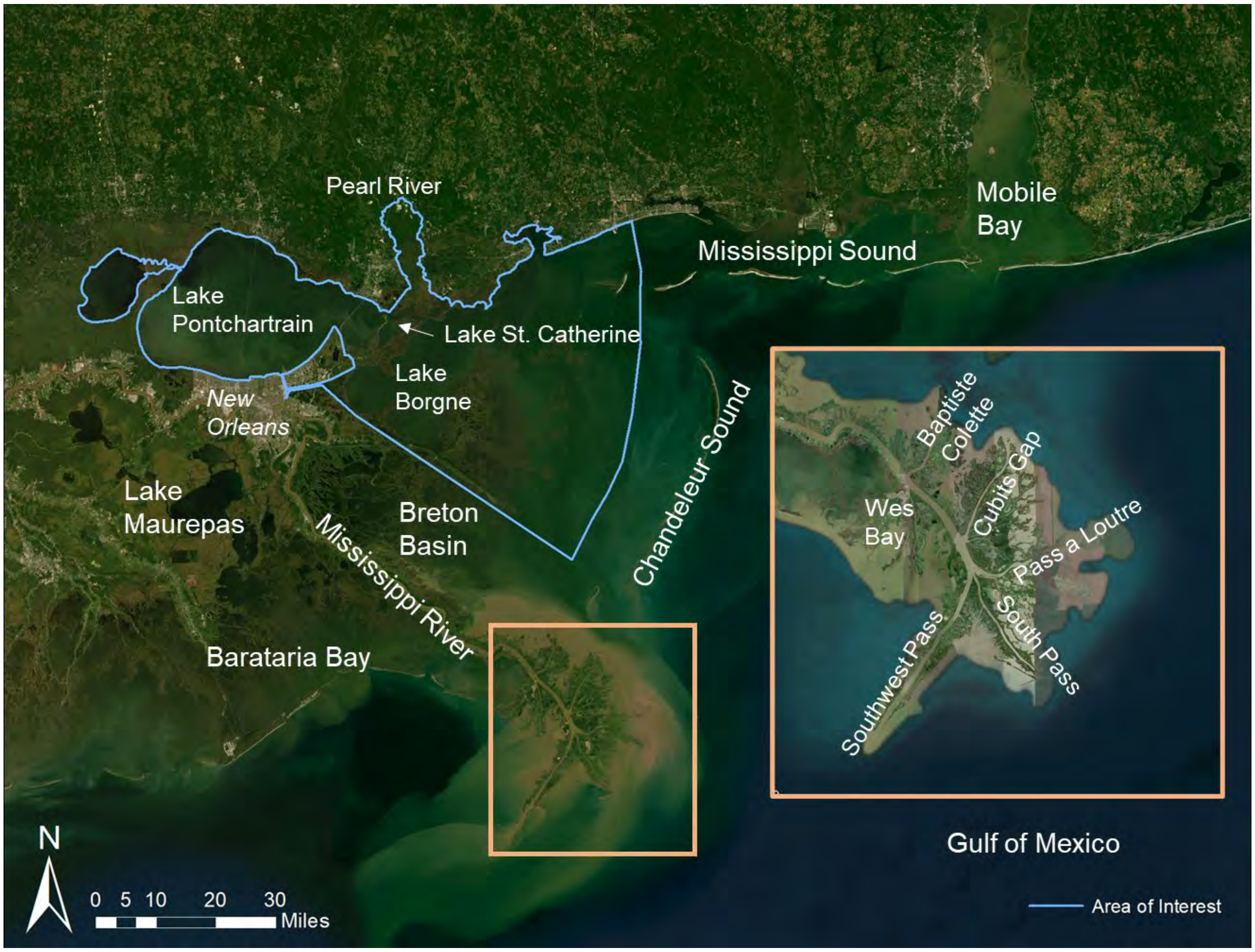

Figure 2. Geographic study area. Blue polygon highlights the specific area of interest.

2.0 HYDRODYNAMIC MODELLING

The model used in this project was developed using Delft3D FM (Deltares, 2019), which consists of multiple tools to model the flow of water in coastal settings (D-Flow FM), waves (D-Waves, which is based on the SWAN model), water quality, and sediment transport and morphology (D-Morphology). These models have been widely used for both practical project applications as well as for research applications within the scientific and academic communities (Booij et al., 1999; Holthuijsen et al., 1994; Ris et al., 1999). For this project, D-Flow FM and D-Waves were used to simulate hydrodynamics including waves, water temperature, and salinity. This report focuses on the D-Flow FM model (Hydrodynamic Model) that was developed to simulate water motion, salinity, and temperature and exchange key information with the D-Waves model (Wave Model) that was coupled with D-Flow FM.

2.1 MODEL DOMAIN

The Hydrodynamic Model was developed to represent water motion, salinity, and temperature in the area of interest and in the surrounding areas. The Hydrodynamic Model includes Lake Maurepas, Pontchartrain, Lake St. Catherine, Lake Borgne, the lower Pearl River valley, Mississippi Sound, Breton Basin, and a portion of the lower Mississippi River and its delta. To the west of the Mississippi River, the model resolves the Barataria Bight and Barataria Basin, and to the east, the Biloxi Sound, Mobile Bay, and the proximal northern Gulf of Mexico shelf (Figure 3). A flexible mesh grid was developed using triangular and quadrilateral elements (Figure 3; Figure 4). The grid resolution varies between 50–100 m (0.03–0.06 miles) in channels and passes (e.g., near the Rigolets, Pearl River, and Pass Manchac; Figure 4), and between 200 m to 5 km (0.12 and 3.1 miles) in open water areas (e.g., Lake Pontchartrain, Lake Borgne, the Mississippi Sound, and the Gulf of Mexico; Figure 4).

A second, coarser grid was developed for the Wave Model that was coupled with the Hydrodynamic Model. The Wave Model resolution was selected following testing and optimization that started with a larger domain (see 2.5.7), to ensure that the selected resolution did not influence wave model predictions. The Wave Model grid has a spatially varying resolution ranging between 200 m (0.12 miles) near the Rigolets and 2 km (1.24 miles) in open water areas (Figure 5). The Wave Model exchanged information with the Hydrodynamic Model every 3 hours, with results from the two models interpolated between the flow and wave domains.

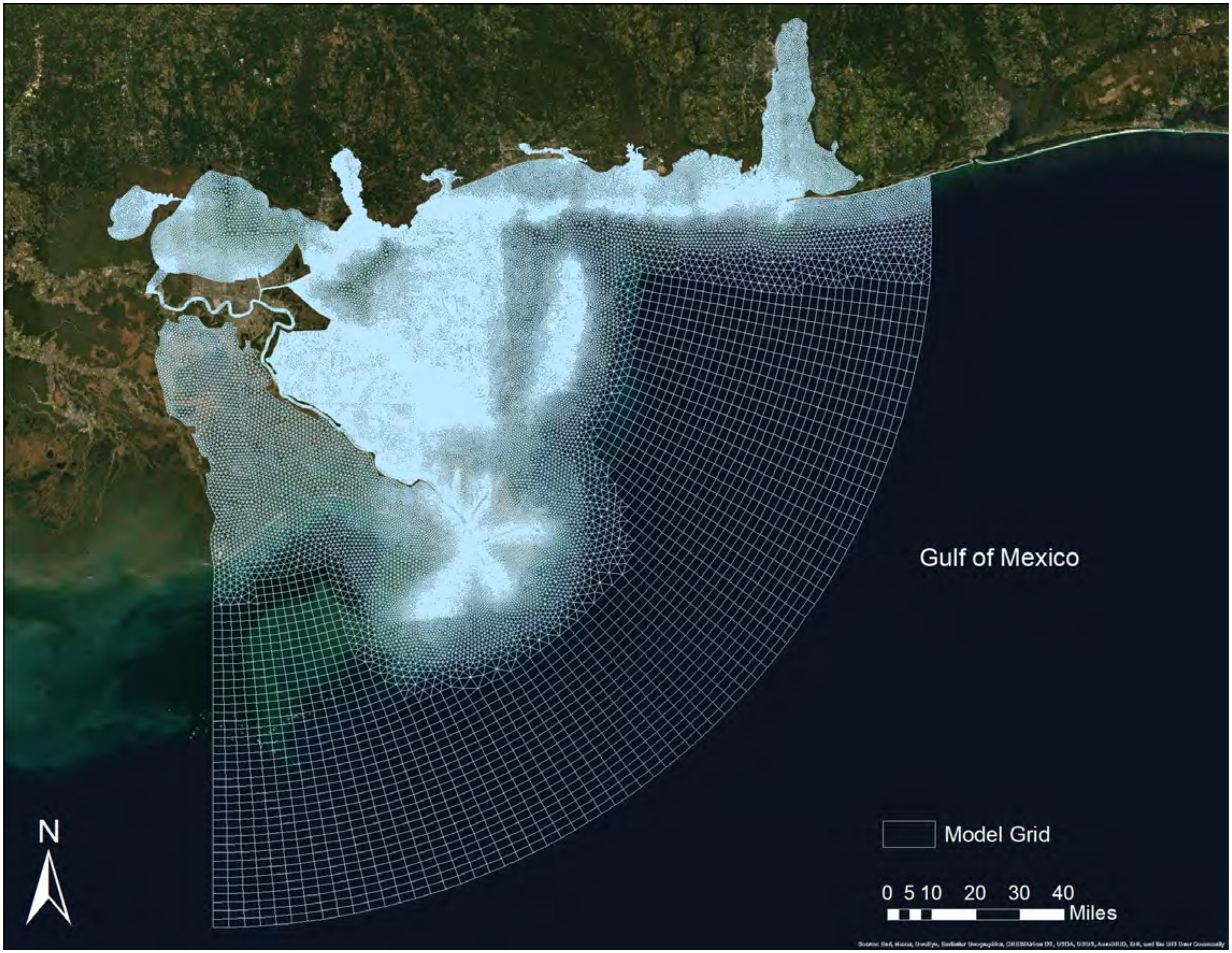

Figure 3. Overview of the Hydrodynamic Model domain grid.

Figure 4. Details of the Deflt3D-FM unstructured grid.

Figure 5. Wave grid used in Delft3D FM D-Waves (SWAN).

2.2 TOPOGRAPHY AND BATHYMETRY

An accurate representation of the topography and bathymetry of the study area is important to be able to numerically reproduce the hydrodynamics of the modeled environment and the exchange of fresh water and saltwater masses throughout the estuary. The implementation of topography and bathymetry in a numerical model depends on the model grid resolution and on the resolution of the original topography/bathymetry dataset. The Hydrodynamic Model used a comprehensive Digital Elevation Model (DEM) developed by the United States Geological Survey (USGS) to support the Lowermost Mississippi River Management Program (LMRMP), referred to as Northern Gulf of Mexico (NGOM) version 2, supplemented by additional datasets including a recent USGS survey of the Chandeleur Islands (USGS, 2018) .

After interpolating the DEM onto the model grid, the following additional edits and adjustments were implemented (Figure 6):

1. The 2017 Coastal Master Plan DEM (Couvillion, 2017) was used to address bathymetric discrepancies in Breton and Chandeleur sounds found in the draft NGOM 2 DEM. These changes were required because there were discrepancies in the underlying data which was composed of several data sources collected at different times. Smoothing at the edges of the datasets was required to obtain a realistic surface for the model grid.
2. The correct elevation was re-assigned to the Mississippi River East Bank (along the Bohemia to Baptiste Collette region) because the interpolation algorithms resulted in erroneous elevations on the model grid compared to observations.
3. The Mardi Gras Pass and Fort St. Philip channel size were manually edited after interpolation to ensure channel continuity and proper conveyance as in the original DEM.
4. Bathymetry throughout the modern Mississippi River Delta distributaries was adjusted post-interpolation to reflect the original DEM and to ensure accurate hydrological connection and thus enable accurate flow distribution.

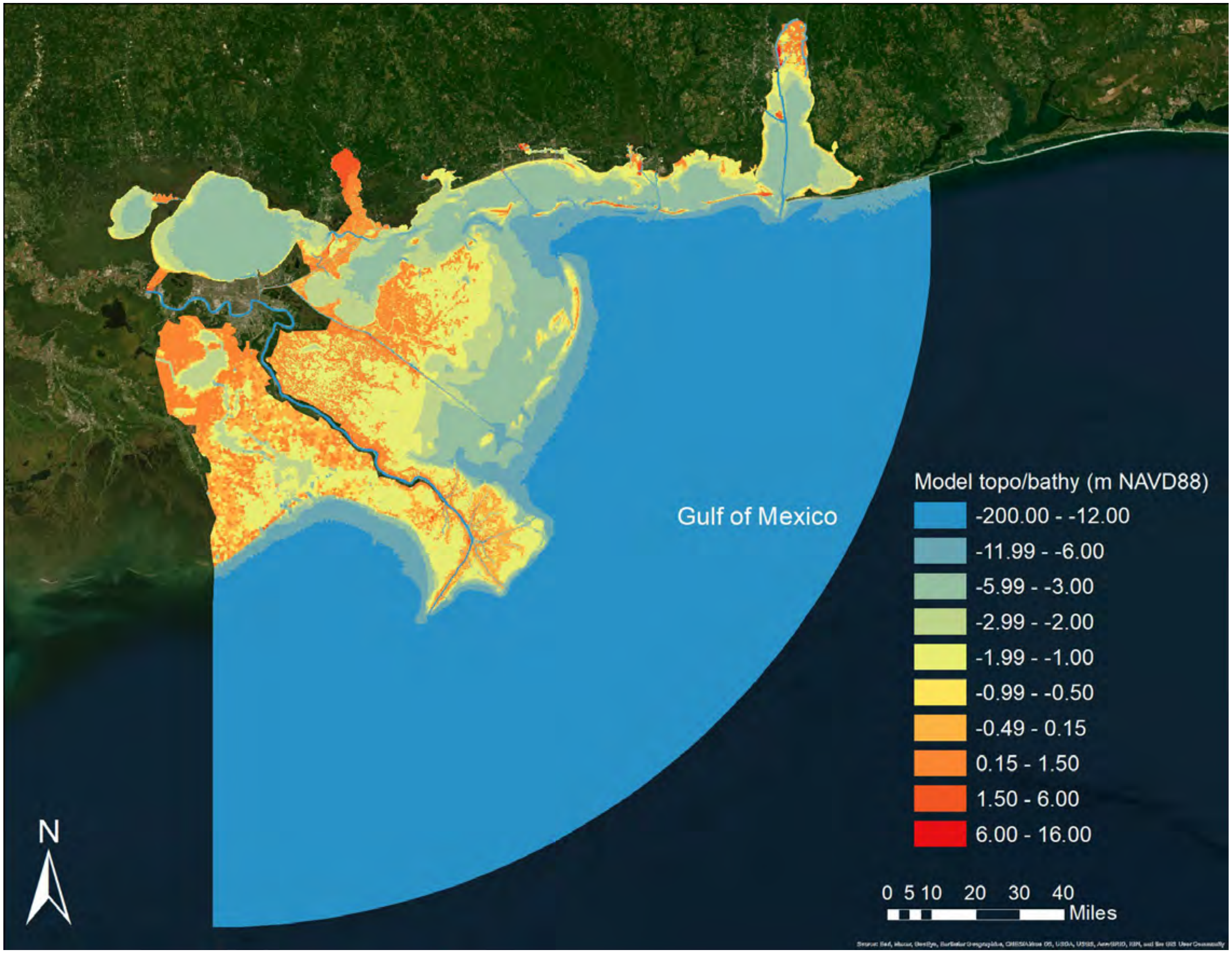

Figure 6. Model topography and bathymetry reported in meters NAVD88 reflected onto the model grid following interpolation from the DEM.

2.3 BOUNDARY CONDITIONS

2.3.1 Riverine Inputs

Riverine inflows were included in the Hydrodynamic Model to correctly characterize all existing freshwater inputs into the model domain (see Figure 3). Table 1 lists all the riverine inflow included in the Hydrodynamic Model and their corresponding source of discharge data. For the majority of river and diversion inflows, USGS data were used; however, for the Bonnet Carré Spillway, Mardi Gras Pass, and the Pearl River, additional calculations or rating curves were implemented (see Table 1 for details).

For all riverine inputs, salinity was set equal to zero to represent the salinity of freshwater, and temperature was set using data from the corresponding USGS station used for flow. If temperature data were not available, data from the nearest river or from the Mississippi River was used.

Figure 7. Riverine and diversion inflows included in the Hydrodynamic Model and implemented as boundary conditions.

Table 1. List of all the riverine inflows included in the Hydrodynamic Model and the source of corresponding flow data. 2016 timeseries were used for model calibration and 2016–2022 timeseries were used for the production run simulations.

Inflow	Discharge data
Mississippi River	USGS station 07374000 Mississippi River at Baton Rouge, LA.
Bonnet Carré Spillway	Flow data were retrieved from U.S. Army Corps of Engineers (USACE)website[2, 3]. In addition to USACE dataset, the spillway leakage was also calculated and implemented in the model. The calculations are based on the formula provided in McCorquodale et al. (2009).
Mardi Gras Pass	Calculated as a rating curve using the Mississippi River discharge (Bregman et al., 2020). Rating curve was developed using data from Georgiou et al. (2019).
Caernarvon Freshwater Diversion	USGS 295124089542100 Caernarvon Outfall Channel at Caernarvon, LA.
Davis Pond Freshwater Diversion	USGS station 295501090190400 Davis Pond Freshwater Diversion near Boutte, LA
Amite	USGS station 07378500 Amite River near Denham Springs, LA.
Tickfaw	USGS station 07376000 Tickfaw River at Holden, LA; Tickfaw and Natalbany were summed and implemented as one inflow.
Natalbany	USGS station 07376500 Natalbany River at Baptist, LA Tickfaw and Natalbany were summed and implemented as one inflow.
Tangipahoa	USGS station 07375500 Tangipahoa River at Robert, LA.
Tchefuncte	USGS station 07375000 Tchefuncte River near Folsom, LA.
Pearl West	Flow data at USGS station 02492000 Bogue Chitto River near Bush, LA and USGS stations 02489500 Pearl River near Bogalusa, LA were used. Specifically, at high discharges 50% of the sum of these two flows was assigned to Pearl West; at low discharges 95% of the sum of these two flows was assigned to Pearl West. Discharge values were interpolated in between. This distribution was based on dataset reported on a USGS report[4].
Pearl East	Flow data at USGS station 02492000 Bogue Chitto River near Bush, LA and USGS stations 02489500 Pearl River near Bogalusa, LA were used. Specifically, at high discharges 50% of the sum of these two flows was assigned to Pearl East; at low discharges 5% of the sum of these two flows was assigned to Pearl East. Discharge values were interpolated in between. This distribution was based on dataset reported on a USGS report[4].
Wolf	USGS station 02481510 Wolf River Nr Landon, MS.
Biloxi	USGS station 02481000 Biloxi River at Wortham, MS.
Pascagoula	USGS station 02479310 Pascagoula River at Graham Ferry, MS.
Mobile	USGS station 02470629 Mobile River at River Mile 31.0 at Bucks, AL.
Tensaw	USGS station 02471019 Tensaw River Nr Mount Vernon, AL.

---

[2] https://www.mvn.usace.army.mil/Missions/Mississippi-River-Flood-Control/Bonnet-Carre-Spillway-Overview/Spillway-Operation-Information/

[3] https://www.mvn.usace.army.mil/Missions/Mississippi-River-Flood-Control/Bonnet-Carre-Spillway-Overview/Historic-Operation-of-Bonnet-Carre/

[4] pubs.usgs.gov/wri/1982/4119/report.pdf

2.3.2 Offshore

The open domain boundary in the Gulf of Mexico, extending from 130 km south of Port Fourchon, LA (see green circle in Figure 8) and near Orange Beach, AL (see orange circle in Figure 8) is forced by tidal conditions derived from the TOPEX/Poseidon Global database (Egbert & Erofeeva, 2002). Spatial variability in tidal conditions is accounted for by dividing the open boundary into six sections, each with a length of approximately 60–80 km on the southern boundary (bounded with seven equidistant points—see circles Figure 8). A Neumann boundary condition was applied on the west boundary (Deltares, 2019). A total of 8 astronomic tidal constituents (M2, S2, N2, K2, K1, O1, P1, Q1; described in Table 2) were extracted for each support point, of which K1, O1, P1, and Q1 form the majority of the tidal amplitude. Interpolation between the support points is handled by the Hydrodynamic Model to calculate the astronomic constituents for each grid cell along the open boundary. Additionally, the offshore mean sea level was included to account for the effects of fluctuations in oceanic and atmospheric conditions on mean sea levels. This is time-varying to account for variability resulting from regular and irregular fluctuations in oceanic and atmospheric conditions. The variation of monthly mean sea levels was obtained from NOAA's Grand Isle tide gauge records (gauge number 8761724) and superimposed at the open boundary water level after interpolation to a weekly interval (Figure 9).

Table 2. Main astronomic tidal constituents and their significance

Tidal Constituent Name	Description
M2	Principal lunar semidiurnal constituent
S2	Principal solar semidiurnal constituent
N2	Lunar elliptic semidiurnal constituent
K2	Lunar/Solar declination semidiurnal constituent
K1	Lunar/Solar declinational diurnal constituent
O1	Lunar declinational diurnal constituent
P1	Principal solar diurnal constituent
Q1	Larger lunar elliptic

Salinity and temperature imposed at the offshore open boundary of the Hydrodynamic Model used monthly average salinity and temperature derived from the Hybrid Coordinate Ocean Model Global Ocean Forecasting System 3.1 (HyCOM GOFS; National Ocean Partnership Program, n.d.). HyCOM GOFS also provided offshore current speed and direction. The HyCOM model employs the Navy Coupled Ocean Data Assimilation (NCOCA) system which corrects the model prediction every 24 hours using a combination of satellite altimetry (for water levels), satellite and in-situ surface temperature sensors, and in-situ vertical profiles of temperature and salinity from in-situ surface floats and moored buoys (Chassignet et al., 2003, 2007).

As the Wave Model only covers Lake Pontchartrain, Lake Borgne, and the westernmost portion of the Mississippi Sound, all of which are—as systems—largely sheltered from incoming offshore wave energy (Figure 5), only locally generated wind waves were considered, as these are sufficient to resolve wave dynamics.

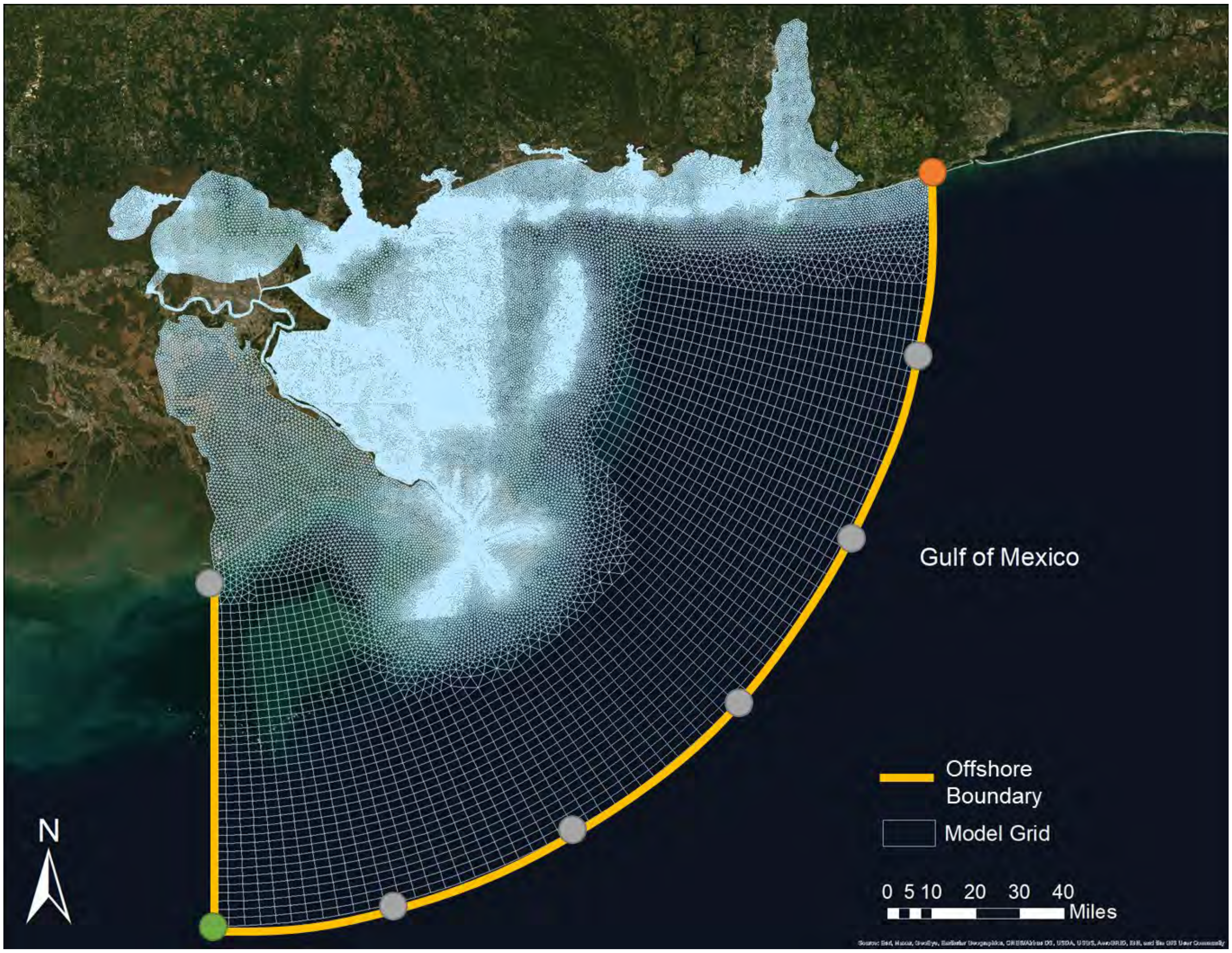

Figure 8. Location of the offshore boundary conditions in the Deflt3d-FM model. The circles show the locations where the offshore water level, salinity and temperature boundaries were defined. The green circle is 130 km south of Port Fourchon, LA. The orange circle is Orange Beach, AL.

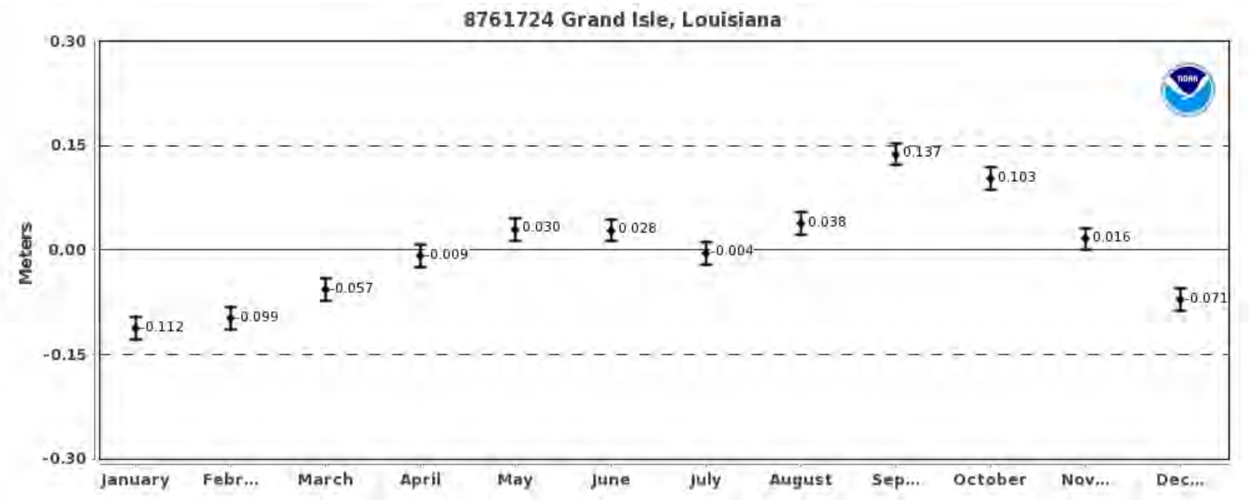

Figure 9. Monthly mean sea levels at Grand Isle (points) and the monthly upper and lower 95% (bars; NOAA, n.d.). Note the annual variation in mean sea level varies by approximately 0.25 m during the year. Figure taken from https://tidesandcurrents.noaa.gov/sltrends/sltrends_station.shtml?plot=seasonal&id=8761724Metereological Forces.

Several meteorological forces are required in the Hydrodynamic Model to capture hydrodynamics, salinity, and temperature.

The National Centers for Environmental Prediction (NCEP) North American Mesoscale (NAM) Analysis wind and atmospheric pressure data, provided at a 12-km grid with a 6-hour temporal resolution, were used for the wind input files.

Relative humidity, air temperature, cloud coverage, and precipitation were obtained from NOAA's NCEP/NCAR (National Center for Atmospheric Research) Water Management Institute's World Water and Climate Data Atlas (International Water Management Institute, n.d.), and subtracted from the precipitation rate to obtain the excess rainfall boundary condition (Meselhe et al., 2015). Solar radiation was computed by D-Flow FM's composite heat flux model based on the latitude and longitude of the Hydrodynamic Model grid (Deltares, 2019; Gill, 1982; Lane, 1989).

The Wave Model uses the same wind input as the Hydrodynamic Model, but directly from the Hydrodynamic Model during the coupling step, where information is passed from the Hydrodynamic Model to the Wave Model, since the Hydrodynamic Model starts the simulation first.

2.4 INITIAL CONDITIONS

Initial conditions are required to initialize the model. Initial conditions files for the final simulations were created from restart files based on the final calibration runs to ensure that the initial conditions for all hydrodynamic parameters were spatially variable, they better resembled realistic environmental conditions, and the system had dynamic equilibrium. All final simulations included an additional month of simulation time to ensure that dynamic equilibrium was reached prior to the period of interest and that there were no residual influences from the initial conditions.

2.5 CALIBRATION

Water level, salinity, and water temperature observations from USACE, USGS, NOAA, and Coastwide Reference Monitoring System (CRMS) stations were used for model calibration. Model results at specific locations were compared with observations at the same physical locations. Model parameters (e.g., roughness, diffusivity, wind drag coefficients, etc.) were adjusted, as described in the following chapters 2.5.3, 2.5.4, and 2.5.5, until a reasonable model skill was achieved in comparison to observational data (Wilcock, 2001; Willmott et al., 2012).

The Hydrodynamic Model calibration focused on Lake Borgne and Lake Pontchartrain. The water level and flow distribution in the Mississippi River was also calibrated against observations due to the influence of the Mississippi River on the surrounding areas during spring floods. The year 2016 was selected and used for calibration of the Hydrodynamic Model, as there were sufficient available data for this year.

Meselhe et al (2017) provides criteria and benchmarks to evaluate the model performance. The desired and acceptable targets for both water level (in the river and in the basin) and for salinity are provided. The desired target represents a “good” match between the model predictions and the field observations, whereas the acceptable target represents a “moderate” match. As clarified by Meselhe et al (2017) these ranges are not intended to be rigid metrics to assess performance; rather, they should be viewed as guidelines. These targets are included in this report in Table 3, Table 4, and Table 5.

2.5.1 Statistics

Model results and observational data were compared, and statistics were calculated to assess the Hydrodynamic Model performance in predicting a specific parameter. Three main statistics were calculated: bias, correlation coefficient, and Root Mean Square Error (RMSE). These are reported for selected stations for all three calibrated variables: water level, salinity, and temperature.

2.5.1.1 Bias

Model bias is a statistic used to evaluate a model’s tendency to over- or underestimate a specific variable. When possible, steps to improve the bias during the model calibration can be pursued. If this is not possible, it is important to quantify the bias value so that it can be considered when analyzing the results and, if necessary, the model results be bias-corrected. The bias was calculated using daily-averaged values as follows:

$$\boldsymbol{Bias} = \overline{(O - \boldsymbol{P})} \qquad \text{Eq.1}$$

where:

P = daily averaged time series of the model predicted values

O = daily averaged time series of the observed values

The daily differences between model and observations were averaged over the entire year to calculate the final bias. Bias value has a sign: positive means that the model is underestimating, negative means that the model is overestimating. Bias has the same unit as the variable it refers to.

The percent bias can also be calculated as follow (Meselhe et al., 2017; Moriasi et al., 2007):

$$\%\boldsymbol{Bias} = \frac{\overline{(\boldsymbol{O} - \boldsymbol{P})}}{\bar{\boldsymbol{O}}} \cdot \mathbf{100} \qquad \text{Eq.2}$$

The percent bias is included in the target presented by Meselhe et al (2017) and included in this report.

2.5.1.2 Root Mean Square Error

RMSE is estimated as the square root of the average of the squared residuals, calculated as differences between the model results and the observed data. RMSE is calculated as follows:

$$\boldsymbol{RMSE} = \sqrt{\frac{\sum_{i=1}^{n} (\boldsymbol{P}_i - \boldsymbol{O}_i)^2}{\boldsymbol{n}}} \qquad \text{Eq.3}$$

where:

P = daily averaged time series of the model predicted values

O = daily averaged time series of the observed values

n = number of observations

The smaller the RMSE, the closer model projections are to observed data. RMSE is always positive, and it has the unit of the variable it refers to.

The percent RMSE can also be calculated as follow (Meselhe et al., 2017):

$$\%\boldsymbol{RMSE} = \boldsymbol{RMSE} \cdot \frac{\boldsymbol{n}}{\sum_{i=1}^{n} \boldsymbol{O}_i} \cdot \mathbf{100} \qquad \text{Eq.4}$$

The percent RMSE is included in the target presented by Meselhe et al (2017) and included in this report.

2.5.1.3 Correlation Coefficient

The correlation coefficient, *r*, is a measure of the strength of a linear relationship between the model results and the observed data. It is calculated as follows:

$$\boldsymbol{r} = \frac{\sum_{i=1}^{n} (\boldsymbol{P}_i - \bar{\boldsymbol{P}})(\boldsymbol{O}_i - \bar{\boldsymbol{O}})}{\sqrt{\sum_{i=1}^{n} (\boldsymbol{P}_i - \bar{\boldsymbol{P}})^2} \sqrt{\sum_{i=1}^{n} (\boldsymbol{O}_i - \bar{\boldsymbol{O}})^2}} \qquad \text{Eq.5}$$

where:

P = daily averaged time series of the model predicted values

$\bar{P}$ = mean of model predicted values

O = daily averaged time series of the observed values

$\bar{O}$ = mean of observed values

n = number of observations

The correlation coefficient ranges from -1.0 to +1.0, where -1 means that the model results are perfectly inversely correlated to the observation; +1 means that the model results are perfectly correlated to the observation and 0 means that they are not correlated at all. The correlation coefficient does not have units.

2.5.2 Water Level in the Mississippi River

One of the first steps in calibrating the Hydrodynamic Model was to ensure that the water level in the Mississippi River was correctly represented in the model, as the water level influences flow distribution through the modern delta distributaries as well as overbank flow along the river's East Bank. USACE stations located in the river were used to compare Hydrodynamic Model results with observational data (Figure 10). Figure 11 shows the Hydrodynamic Model results compared to the USACE observations and Table 2 shows summary statistics from the comparison with model and observations. All stations met the desired targets (Meselhe et al., 2017), including the Alliance and New Orleans stations, even though the model skill at these two locations is lower compared to observations than other stations downriver. While the Mississippi River is not part of the area of interest (see Figure 2), it was included in the model to route freshwater to the lower reaches of the river where natural crevasses and distributary channels exist connecting the river to the receiving basin and obtaining reasonable agreement with observations. The model shows good agreement below West Point a La Hache, therefore, the lower model performance at Alliance and New Orlans does not influence the model performance at key locations proximal to areas of interest.

Figure 10. Locations of the USACE stations in the Mississippi River and of NOAA, CRMS and USGS stations in the basins where the Hydrodynamic Model was compared with observations.

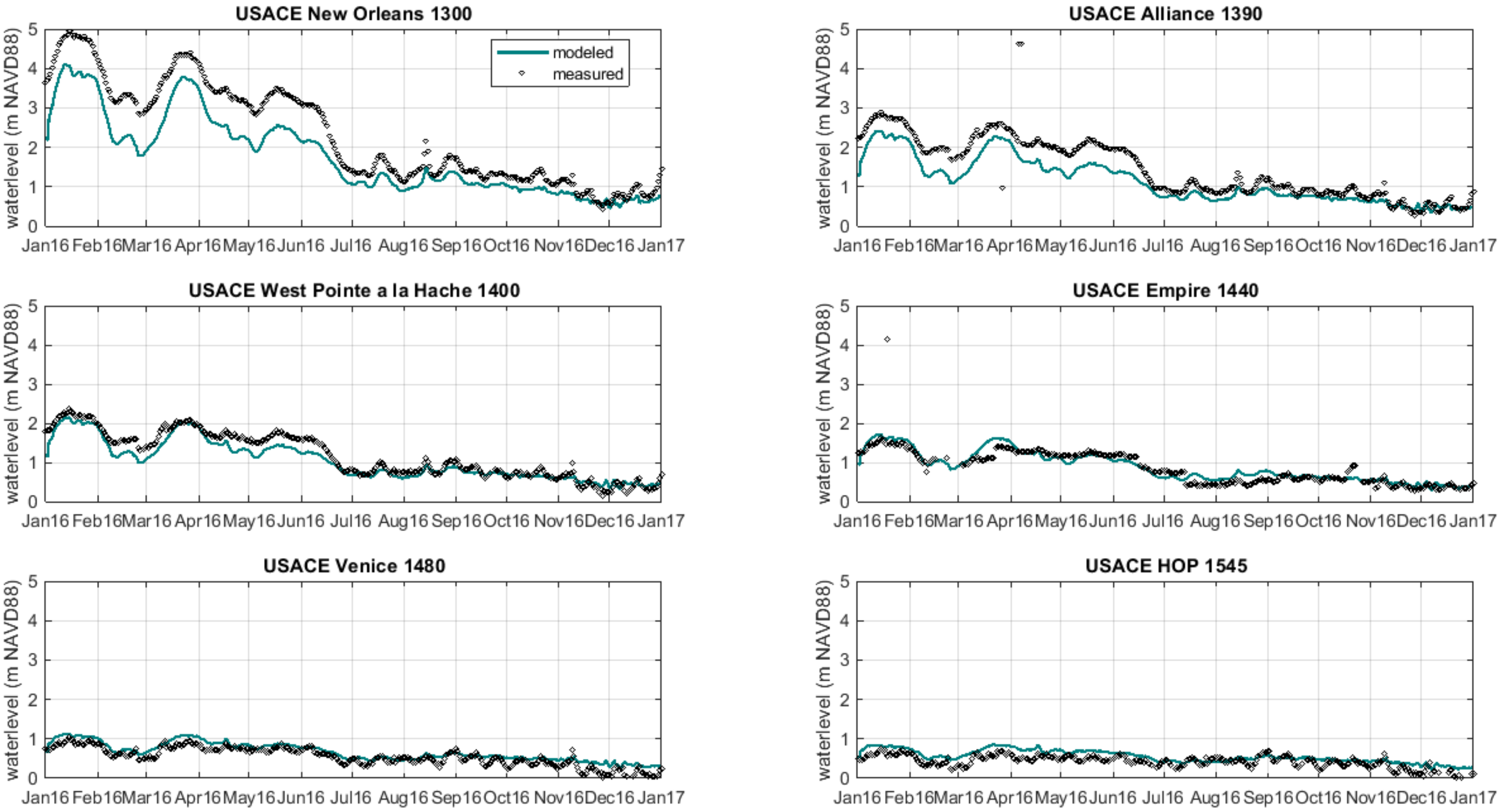

Figure 11. Water level in the Mississippi River at six different USACE stations. Comparison between Hydrodynamic Model projections (green line) and observations (black dots).

Table 3. Water level statistics from the model calibration evaluating model skill by comparing daily averaged model results to observations for the USACE stations located in the Mississippi River. Desired targets are met for %BIAS and %RMSE. Acceptable target is met for r.

USACE Station	BIAS (m)	BIAS %	RMSE (m)	RMSE %	*r*	Number of datapoints
New Orleans	-0.56	-2	0.65	3	0.98	363
Alliance	-0.32	-1	0.44	2	0.94	364
West Pointe à la Hache	-0.13	-1	0.20	1	0.97	362
Empire	0.04	0	0.20	1	0.88	345
Venice	0.12	1	0.15	1	0.92	364
Head of Passes (HOP)	0.13	1	0.17	1	0.78	346
Meselhe et al. (2017) Criteria						
Target Desired		< 10% for all stations		< 15% for all stations	> 0.9 for all stations	
Target Acceptable		< 10% for 80% of stations		< 15% for 80% of stations	> 0.9 for 80% of stations	
Model Skill		All stations are < 10%		All stations are < 15%	83% of the stations are > 0.9	

2.5.3 Flow Distribution

As part of the Mississippi River calibration, the flow distribution in the modern delta distributaries and the East Bank overbank flow was calibrated, as the freshwater exiting the Mississippi River influences the hydrodynamics and salinity of the Breton Basin and Chandeleur Sound. Two different datasets were used for this calibration. The first dataset was based on a long record of synoptic acoustic doppler current profiler (ADCP) surveys at Baptiste Colette, Grand Pass and Tiger Pass, West Bay, Cubits Gap, Pass a Loutre, South Pass, and Southwest Pass conducted by USACE New Orleans District (MVN; see Figure 2). The second dataset was based on Allison et al. (2012) which provides flows distribution along the lower reach of the Mississippi River and specifically at Baptiste Colette, Grand Pass and Tiger Pass, West Bay, Cubits Gap, Pass a Loutre, South Pass, and Southwest Pass.

Figure 12 shows the mean annual discharge from the Hydrodynamic Model results compared with the mean annual observed discharge reported as a percentage of the flow through the Mississippi River at Venice. The second dataset, from Allison et al. (2012), was used for the remaining reaches: Belle Chasse, Bohemia Spillway, Ostrica, and Fort St. Philip. Figure 13 shows mean annual discharge predicted by the Hydrodynamic Model compared to the flow predicted by Allison et al. (2012) reported as a percentage of the flow through the Mississippi River just downstream of Bonnet Carré. Allison et al. (2012) also provides flows for Baptiste Colette, Grand Pass, and Tiger Pass, West Bay, Cubits Gap, Pass a Loutre, South Pass, and Southwest Pass, which were included in Figure 13. The relationships from the Synoptic ADCP surveys by USACE MVN were prioritized and used to calibrate the Hydrodynamic Model because they are based on more recent flow observations and longer records.

Incremental adjustments to the Hydrodynamic Model roughness were carried out until the comparison between model results and target values (Figure 12; Figure 13) were achieved. To prevent unrealistic selections of roughness, if targets were not met by adjusting friction alone, minor adjustments to the bathymetry followed to tune conveyance and flow distribution, as described in 2.2. The final Manning roughness values were realistic and ranged between 0.025 and 0.015, in the Mississippi River.

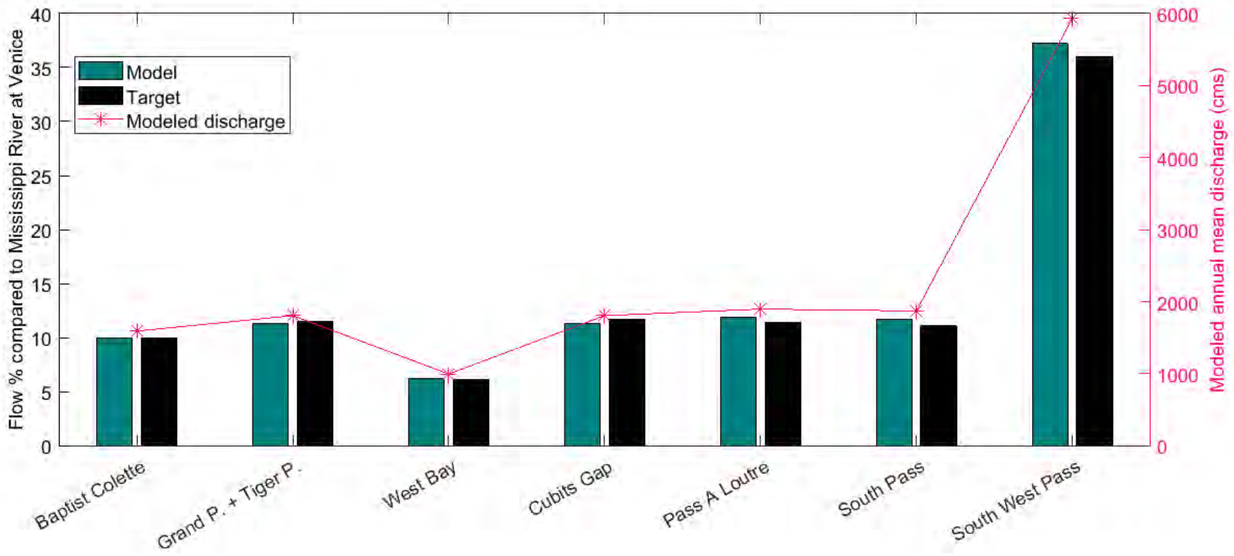

Figure 12. Flow distribution calibration results at Baptiste Colette, Grand Pass and Tiger Pass, West Bay, Cubits Gap, Pass a Loutre, South Pass, and Southwest Pass.

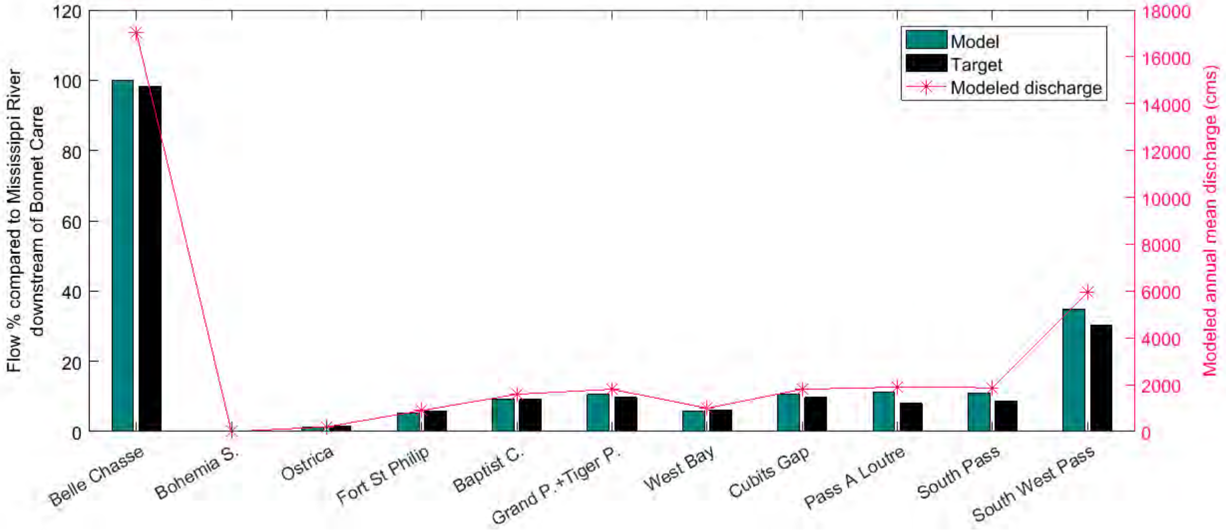

Figure 13. Flow distribution calibration results at Belle Chasse, Bohemia Spillway, Ostrica, Fort St. Philip, Baptiste Colette, Grand Pass and Tiger Pass, West Bay, Cubits Gap, Pass a Loutre, South Pass, and Southwest Pass.

2.5.4 Water Level in the Basin

After calibrating water levels and flow distribution in the Mississippi River and delta, the calibration process focused on water level in the basins using available water level stations. Eight USGS stations, fifteen CRMS stations and six NOAA stations were used to calibrate water level in the basins (Figure 10). Comparisons between model results and observations for all these stations are presented in Appendix A. A subset of six USGS stations were selected and included in the main report (Figure 14), including statistics for all stations (Table 3). The main parameters that were adjusted during water level calibration were the Manning's roughness and the drag coefficient. The initial Manning's friction coefficients were derived from Coastal Change Analysis Program data which is used for 2023 Coastal Master Plan (Baustian et al., 2020). After calibration for water levels was completed, the final Manning's roughness varied between 0.025 and 0.015 in the Mississippi and Pearl rivers, 0.013 to 0.018 in the open water, 0.05 at emergent herbaceous wetlands, and 0.015 at woody wetlands. The drag coefficient was set equal to 0.00125 for zero wind speed, equal to 0.0025 for wind speed of 6 m/s or above, and linearly varied between these values when the wind speed is between zero and 6 m/s (Deltares, 2014; Smith & Banke, 1975).

Results (Figure 14) show a good agreement between modeled water level and observations. The model captures seasonal water level fluctuations and peaks. A consistent vertical discrepancy can be observed at the USGS station Mississippi Sound at East Ship Island Light 301527088521500. The gauge datum correction for this station was unknown and therefore the observation could not be converted to NAVD88. Nevertheless, modeled water level at this location reproduces the seasonal variation and fluctuations seen in the observations. All stations met the desired targets (Meselhe et al., 2017; Table 3).

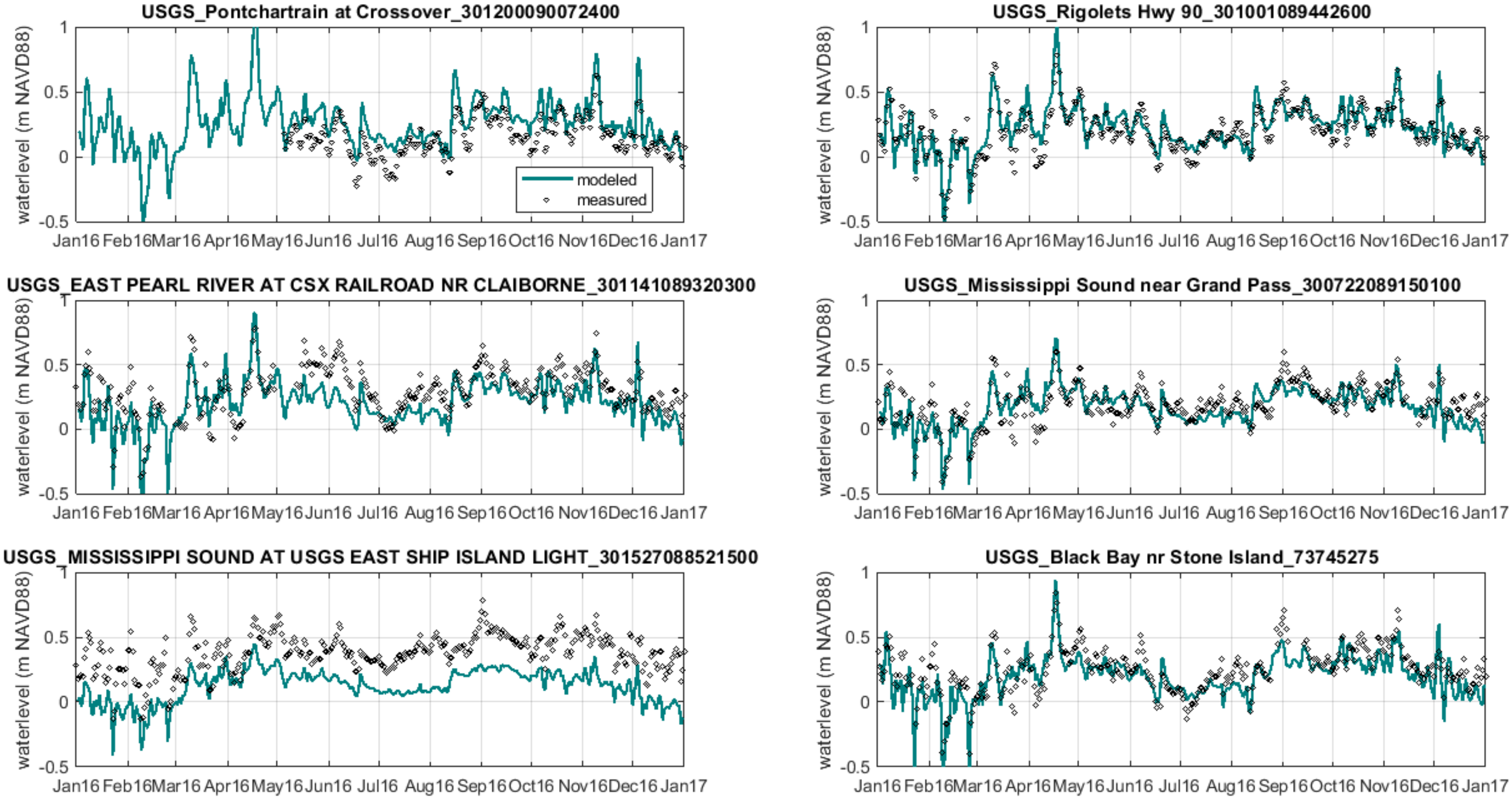

Figure 14. Simulated daily averaged water levels by the Hydrodynamic Model (green line) compared to observations at six USGS stations (black dots). Observations at USGS station Mississippi Sound at East Ship Island Light 301527088521500 were not converted to NAVD88 because of lack of gauge datum information.

Table 4. Model skill statistics using daily averaged water level comparing model output and observations for all CRMS, USGS and NOAA stations located in the basins. % BIAS and %RSME are calculated based on water depth. Accepted target met for %BIAS, %RMSE and r.

Station Name	**BIAS (m)**	**BIAS %**	**RMSE (m)**	**RMSE %**	***r***	**Number of datapoints**
CRMS0002	0.02	2	0.09	8	0.85	363
CRMS0003	-0.01	-1	0.1	11	0.83	281
CRMS0006	-0.05	-4	0.13	9	0.82	365
CRMS0030	0.01	0	0.1	4	0.89	365
CRMS0108	0.01	1	0.11	10	0.81	365
CRMS1024	0.05	4	0.12	10	0.77	365
CRMS1069	-0.04	-4	0.11	12	0.78	365
CRMS3626	0.04	5	0.1	13	0.88	313
CRMS3667	-0.02	-1	0.12	6	0.77	359
CRMS3784	0.07	11	0.12	19	0.8	362
CRMS4094	-0.01	0	0.09	4	0.91	354
CRMS4551	-0.01	-1	0.1	10	0.86	365
CRMS4572	0.00	0	0.09	14	0.84	365
CRMS4596	-0.04	-3	0.1	7	0.82	220
CRMS6299	-0.01	-1	0.1	16	0.85	352
USGS Pontchartrain at Crossover 301200090072400	0.11	2	0.14	3	0.85	241
USGS Rigolets Hwy 90 301001089442600	0.02	0	0.1	1	0.85	365
USGS East Pearl River at Csx Railroad Nr Claiborne 301141089320300	-0.09	-1	0.15	2	0.79	341
USGS Mississippi Sound near Grand Pass 300722089150100	-0.03	-1	0.1	3	0.78	358
USGS Black Bay nr Stone Island 73745275	-0.05	-3	0.12	7	0.81	353
USGS Crooked B NW of L Cuatro Caballo near Delacroix 073745257	-0.08	-5	0.13	9	0.81	365
USGS Barataria Pass at Grand Isle 73802516	-0.01	0	0.12	3	0.56	347
USGS Biloxi Bay at Point Cadet Harbor at Biloxi 302318088512600	-0.04	-2	0.11	4	0.8	365
NOAA Bay Waveland Yacht Club	-0.01	-1	0.1	6	0.84	361
NOAA New Canal Station	0.06	2	0.11	3	0.88	365

Station Name	BIAS (m)	BIAS %	RMSE (m)	RMSE %	*r*	Number of datapoints
NOAA Coast Guard Sector Mobile	-0.12	-8	0.15	11	0.77	365
NOAA Dauphin Island	-0.09	-3	0.13	5	0.62	365
NOAA Shell Beach	0.03	2	0.1	7	0.86	365
NOAA Pascagoula NOAA Lab	-0.05	-2	0.11	4	0.71	365
Meselhe et al. (2017) Criteria						
Target Desired		< 10% for all stations		< 15% for all stations	> 0.9 for all stations	
Target Acceptable		< 10% for 80% of the stations		< 15% for 80% of the stations	> 0.8 for 80% of the stations	
Model Skill		97% of stations are < 10%		93% of stations are < 15%	90% of stations are > 0.8	

2.5.5 Salinity

Once the water levels were calibrated to ensure the hydrology was well reproduced, the salinity calibration was then conducted. The main parameter that was adjusted in this phase was the horizontal eddy diffusion coefficient. The value of the horizontal eddy diffusivity depends on the flow and the grid size used in the simulation. For high-resolution models where many of the details of the flow are resolved by the grid (e.g., grid sizes in the order of tens of meters), the value typically ranges between 1 and 10 m^2/s. For areas with a coarse grid (e.g., tidal areas with grid sizes of hundreds of meters or more), this coefficient typically ranges from 10 to 100 m^2/s (Deltares, 2014). Further adjustments are made during the calibration process. The final calibrated horizontal eddy diffusion coefficient for this application ranges between 10–30 m^2/s in areas that are inland, marsh, or nearshore (e.g., Barataria Basin, Breton Basin, Lake Pontchartrain, Pearl River Valley and all the rivers in Mississippi Sound, and the Mississippi River Delta). Locally higher values were assigned for the Mississippi River and tidal passes such as the Rigolets and Chef Menteur Pass, and values of 100 m^2/s and higher were used in the offshore parts of the model domain to allow for saltwater to diffuse back into the estuaries following spring tributary flows.

Nine USGS stations and fifteen CRMS stations were used to calibrate salinity (Figure 10). Comparison between model results and observation for all these stations is presented in Appendix B. A subset of six USGS stations were selected and included in Figure 15. Table 4 shows statistics for all stations. Model skill statistics are acceptable according to Meselhe & Rodrigue’s (2013) criteria.

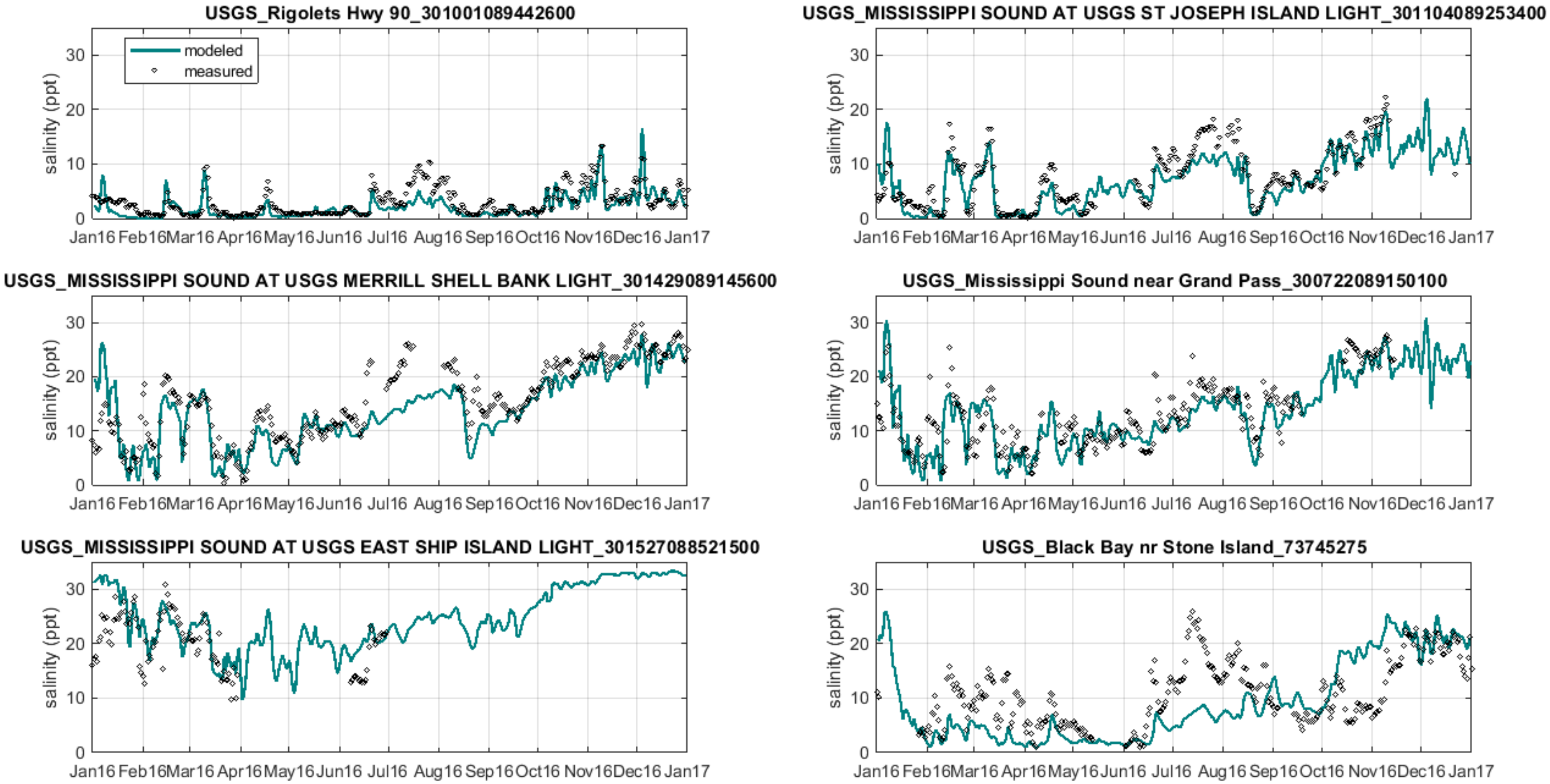

Figure 15.Simulated daily averaged salinity by the Hydrodynamic Model (green line) compared to observations at six USGS stations (black dots).

Table 5. Model skill statistics using daily averaged salinity comparing model output and observations at all CRMS and USGS stations located in the basins. Acceptable targets for %BIAS and r are met, not for %RMSE.

Station Name	**BIAS (ppt)**	**BIAS %**	**RMSE (ppt)**	**RMSE %**	***r***	**Number of datapoints**
CRMS0002	-1.13	-47	1.54	64	0.66	363
CRMS0003	-0.81	-5	3.66	24	0.86	365
CRMS0006	-0.68	-47	1.20	84	0.03	365
CRMS0030	-0.27	-57	0.44	94	0.14	365
CRMS0108	-1.44	-14	4.61	46	0.71	365
CRMS1024	-0.35	-3	5.33	43	0.55	365
CRMS1069	-0.49	-3	4.49	29	0.84	365
CRMS3626	-1.05	-50	1.40	67	0.60	313
CRMS3667	-0.70	-39	1.36	77	0.31	359
CRMS3784	-1.04	-27	2.40	63	0.59	362
CRMS4094	-0.01	-6	0.24	111	-0.05	354
CRMS4551	1.45	35	3.31	79	0.53	365
CRMS4572	-2.62	-42	3.42	55	0.71	365
CRMS4596	-1.97	-24	3.30	40	0.78	220
CRMS6299	-0.72	-72	0.88	87	-0.46	327
USGS Rigolets Hwy 90 301001089442600	-0.94	-31	1.87	61	0.78	363
USGS Mississippi Sound at USGS St Joseph Island Light 301104089253400	-1.28	-17	2.95	38	0.87	285
USGS Mississippi Sound at USGS Merrill Shell Bank Light 301429089145600	-1.81	-12	4.14	27	0.85	339
USGS Mississippi Sound near Grand Pass 300722089150100	-1.11	-9	3.84	30	0.82	285
USGS Mississippi Sound at USGS East Ship Island Light 301527088521500	2.49	12	5.16	25	0.58	112
USGS Black Bay nr Stone Island 73745275	-1.75	-16	6.69	61	0.55	312
USGS Crooked B NW of L Cuatro Caballo near Delacroix 073745257	0.37	11	2.13	61	0.77	347
USGS Barataria Pass at Grand Isle 73802516	2.52	13	4.56	24	0.68	295
USGS Biloxi Bay at Point Cadet Harbor at Biloxi 302318088512600	-2.28	-16	4.05	29	0.88	365
(Meselhe & Rodrigue, 2013) Criteria						
Target Desired		< 20% for all stations		< 20% for all stations	> 0.7 for all stations	
Target Acceptable		< 20% for 50% of the stations		< 40% for 50% of the stations	> 0.5 for 50% of the stations	
Model Skill		54% of stations are < 20%		37% of stations are < 40%	79% of stations are > 0.5	

2.5.6 Temperature

Temperature calibration did not require further adjustments. Nine USGS stations and fifteen CRMS stations were used to calibrate temperature (Figure 10). Comparison between model results and observation for all these stations is presented in Appendix C. A subset of six USGS stations were selected and included in the report (Figure 16) as well as statistics for all stations (Table 6).

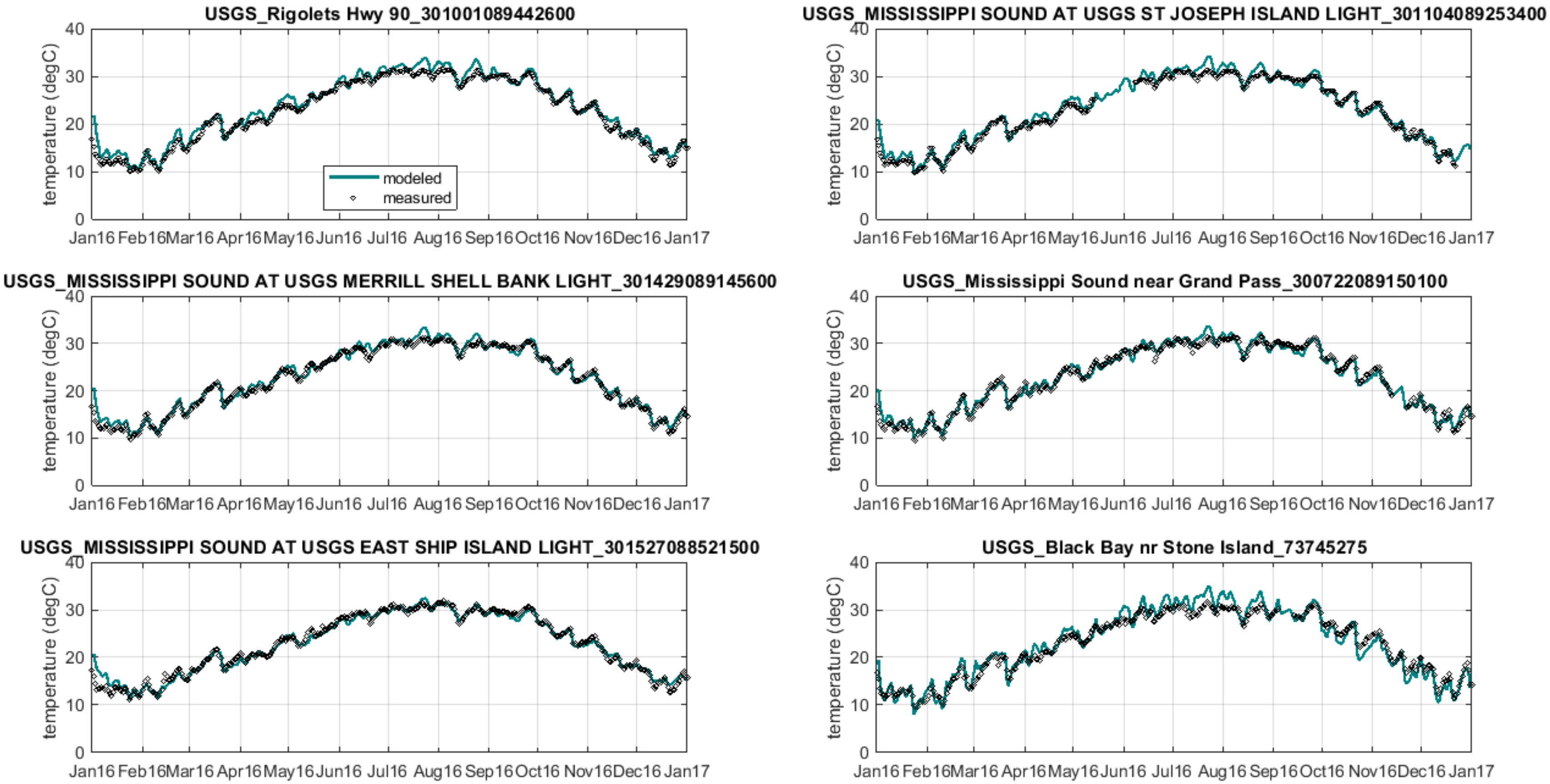

Figure 16.Simulated daily averaged temperature by the Hydrodynamic Model (green line) compared to observations at six USGS stations (black dots).

Table 6. Model skill statistics using daily averaged temperature comparing model output and observations at all CMS and USGS stations located in the basins.

Station Name	BIAS (C)	BIAS %	RMSE (C)	RMSE %	*r*	Number of datapoints
CRMS0002	0.96	4	1.82	8	0.97	363
CRMS0003	-0.51	-2	1.21	5	0.99	365
CRMS0006	0.88	4	2.36	10	0.95	365
CRMS0030	1.10	5	2.06	9	0.97	365
CRMS0108	0.00	0	1.32	6	0.98	365
CRMS1024	-0.31	-1	1.48	6	0.98	365
CRMS1069	-0.23	-1	1.35	6	0.98	365
CRMS3626	0.80	4	1.59	7	0.98	313
CRMS3667	0.67	3	2.40	11	0.94	359
CRMS3784	0.52	2	1.97	9	0.96	362
CRMS4094	1.31	6	1.96	9	0.98	354
CRMS4551	0.08	0	1.25	5	0.98	365
CRMS4572	0.16	1	1.48	6	0.98	365
CRMS4596	0.25	1	1.26	6	0.99	220
CRMS6299	0.71	3	2.74	12	0.95	331
USGS Rigolets Hwy 90 301001089442600	0.80	4	1.23	5	0.99	363
USGS Mississippi Sound at USGS St Joseph Island Light 301104089253400	0.51	2	1.06	5	0.99	332
USGS Mississippi Sound at USGS Merrill Shell Bank Light 301429089145600	0.36	2	0.92	4	0.99	365
USGS Mississippi Sound near Grand Pass 300722089150100	0.13	1	0.89	4	0.99	357
USGS Mississippi Sound at USGS East Ship Island Light 301527088521500	-0.04	0	0.90	4	0.99	365
USGS Black Bay nr Stone Island 73745275	0.28	1	1.54	7	0.98	355
USGS Crooked B NW of L Cuatro Caballo near Delacroix 073745257	0.10	0	1.38	6	0.98	365
USGS Barataria Pass at Grand Isle 73802516	-0.87	-4	1.48	6	0.98	347
USGS Biloxi Bay at Point Cadet Harbor at Biloxi 302318088512600	0.21	1	1.09	5	0.99	365
USGS East Pearl River at Csx Railroad Nr Claiborne 301141089320300	0.75	3	1.45	6	0.98	357

2.5.7 Wave Model

The Wave Model was not calibrated for Lake Pontchartrain or Lake Borgne due to the lack of wave observations, with the exception of limited recent observations located near the southern shores of Lake Pontchartrain. Since these observations were very close (less than 500 m) to the shoreline and in very shallow water, they could not be used for calibrating the wave model. To ensure high Wave Model skill, calibration used deployments collected by USGS at the Chandeleur Islands during the summer and fall of 2010 (Sherwood, 2010). First, a larger Wave Model domain extending offshore of the Chandeleur Islands (Figure 17) was used to cover the deployment area. The measured and modeled wave data were compared at three deployment sites (Figure 17): CI-1 (Figure 18), a deep-water deployment (~31 m) located east of the Chandeleur Islands, CI-2 (Figure 19), a shallow water deployment (~15 m) situated to the north of the islands, and CI-6 (Figure 20), a shallow water deployment (~5 m) located to the west (i.e., at the inland side of the Chandeleur Islands).

The results (Figure 18 through Figure 20; panels A) demonstrate a good agreement between modeled and measured wave heights, particularly for cold front passages that typically occur from mid-September onward, which is the period of interest for this study due to migration patterns of Gulf Sturgeon. However, during the summer months (i.e., July, August, and the first part of September), the model underestimates wave heights, likely due to typical summer thunderstorms that can occur at spatial and temporal scales smaller than those of the meteorological forcing (12-km; 6-hour) of the North American Model (NAM) wind data used to drive the model. The model consistently predicts lower wave periods compared to observations (Panels B of Figure 18 through Figure 20) at the offshore sites (CI-1 and CI-2) despite resolving a range of frequencies (0.03 and 1 Hz) corresponding to a range of wave periods (33 and 1 second). The higher wave periods in the observations could be due to wave swell originating from offshore areas in the Gulf of Mexico outside the model domain and, thus, why the model underestimates periods. Furthermore, the measured wave periods also depend on processing methodology (including cutoff frequency, sampling frequency, etc.), not detailed in the data reports by (Dickhudt et al., 2010). The site located to the west of the Chandeleur Islands in the back barrier lagoon (CI-6) shows a better agreement between measured and modeled wave periods. A reasonable agreement exists between the modeled and measured wave directions during periods with larger waves (Panels C of Figure 18 through Figure 20). More significant differences between modeled and measured wave directions are found for periods with significant wave heights of less than 0.3 m.

To ensure the Wave Model Grid was computationally efficient, the extended wave model domain (Figure 17) was truncated for use in this study (Figure 5) since inland water bodies (e.g., Lake Pontchartrain, Lake Borgne) experience predominantly locally generated waves. To verify the accuracy of the final truncated Wave Model Grid used within this study (Figure 5), waves between the two model domains were compared at five locations throughout Lake Pontchartrain and Lake Borgne (Figure 17). The wave comparison showed that both wave domains produce very similar wave heights at these locations, confirming the presence of primarily locally generated waves and suggesting that the truncated Wave Model Grid is sufficiently accurate (Figure 21).

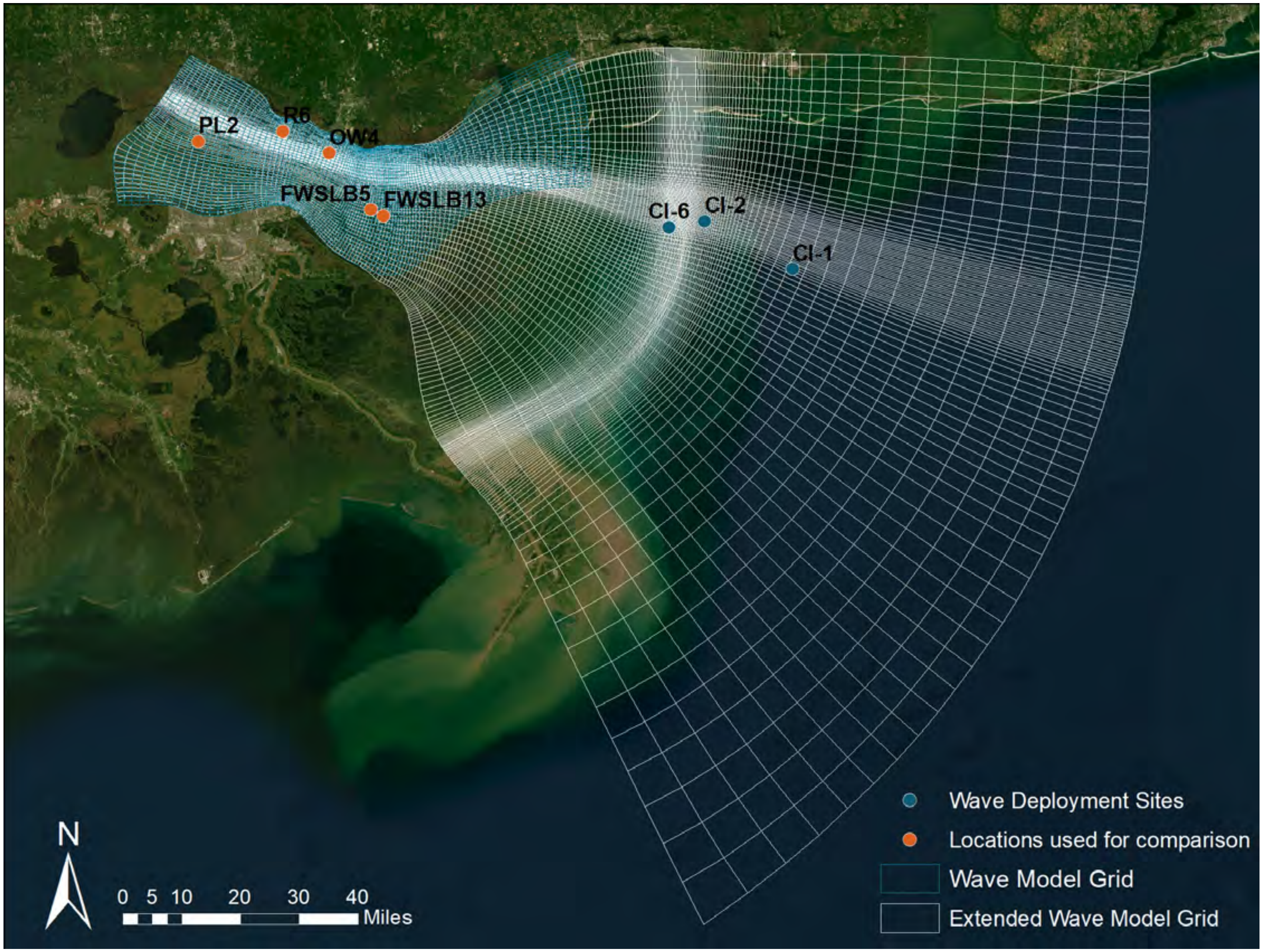

Figure 17. Wave grid used in Delft3D FM D-Waves (in light blue), extended wave model grid in Delft3D FM D-Waves (in white), deployment site where wave observations were collected by USGS between July and November 2010 (Dickhudt et al., 2010), locations used for comparison between the two models (in orange).

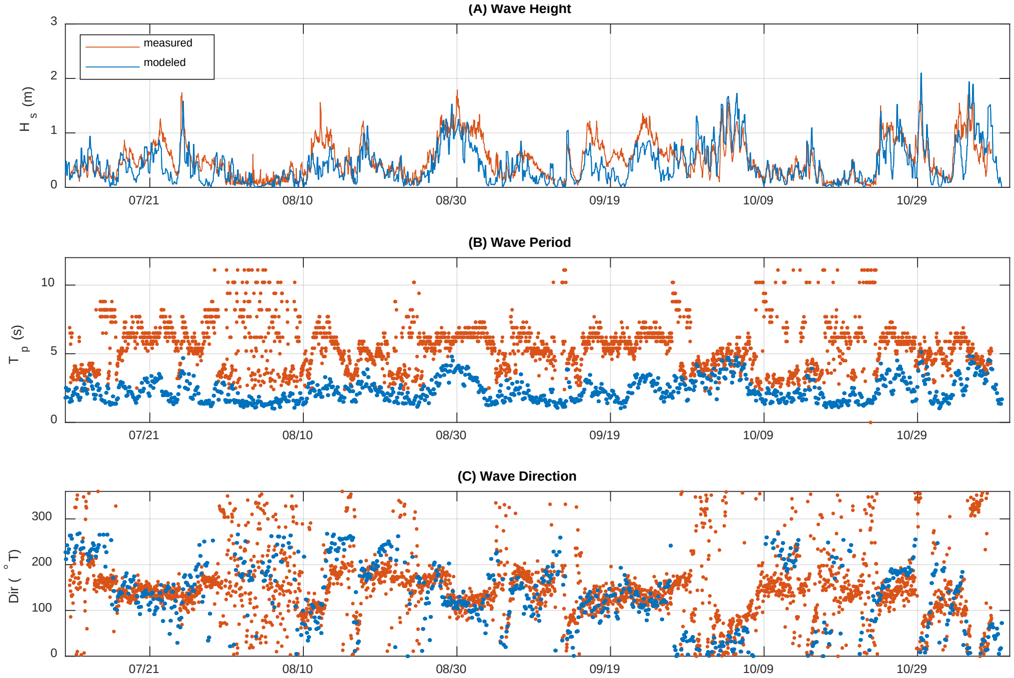

Figure 18. Comparison between measured (orange) and modeled (blue) significant wave heights (A), peak periods (B), and wave directions (C), at USGS deployment site CI-1 (Sherwood, 2010), a deep-water deployment (~31 m) located east of the Chandeleur Islands (Figure 17). The wave direction is shown as the angle in degrees measured clockwise from true north, representing the direction from which the waves are approaching.

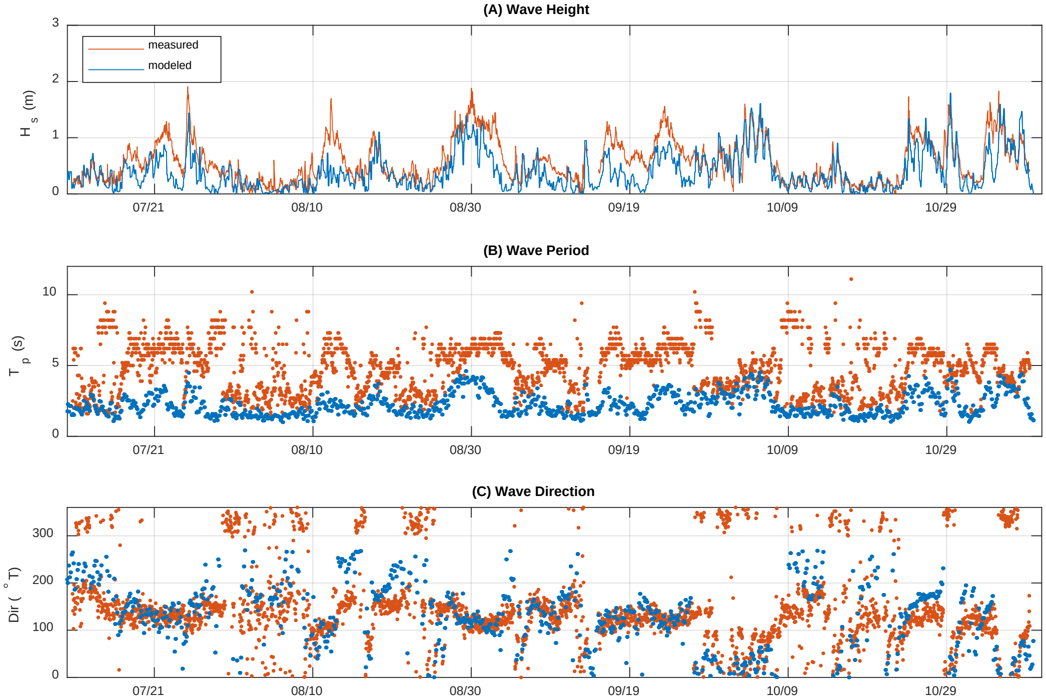

Figure 19. Comparison between measured (orange) and modeled (blue) significant wave heights (A), peak periods (B), and wave directions (C), at USGS deployment site CI-2 (Sherwood, 2010), a shallow water deployment (~15 m) situated to the north of the Chandeleur Islands (Figure 17). The wave direction is shown as the angle in degrees measured clockwise from true north, representing the direction from which the waves are approaching.

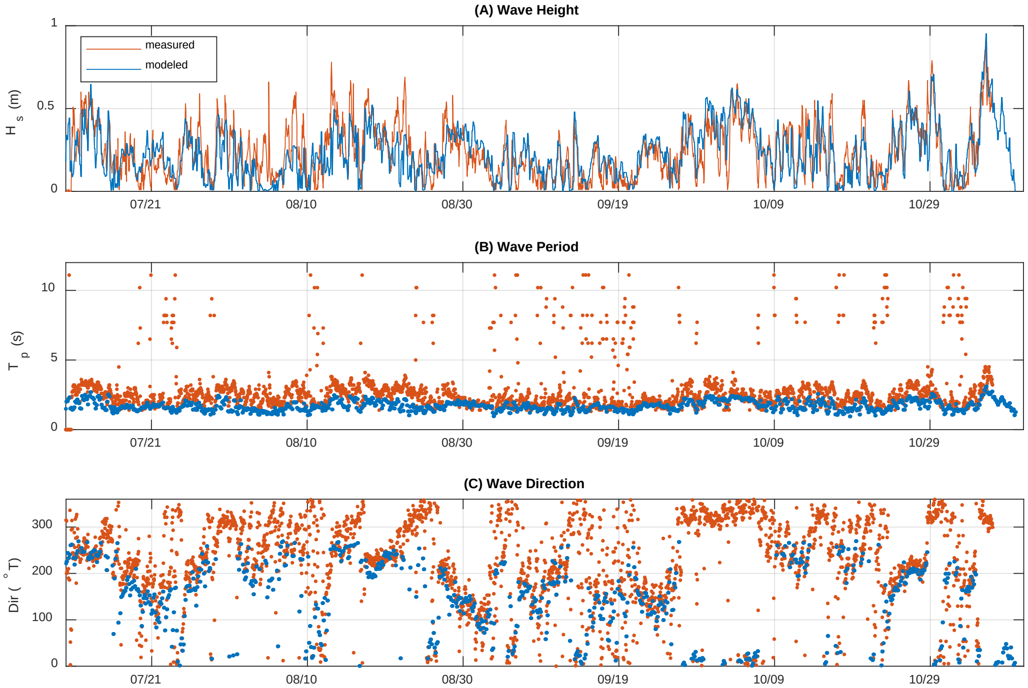

Figure 20. Comparison between measured (orange) and modeled (blue) significant wave heights (A), peak periods (B), and wave directions (C), at USGS deployment site CI-6 (Sherwood, 2010), a shallow water deployment (~5 m) located to the west, i.e., at the inland side, of the Chandeleur Islands (Figure 17). The wave direction is shown as the angle in degrees measured clockwise from true north, representing the direction from which the waves are approaching.

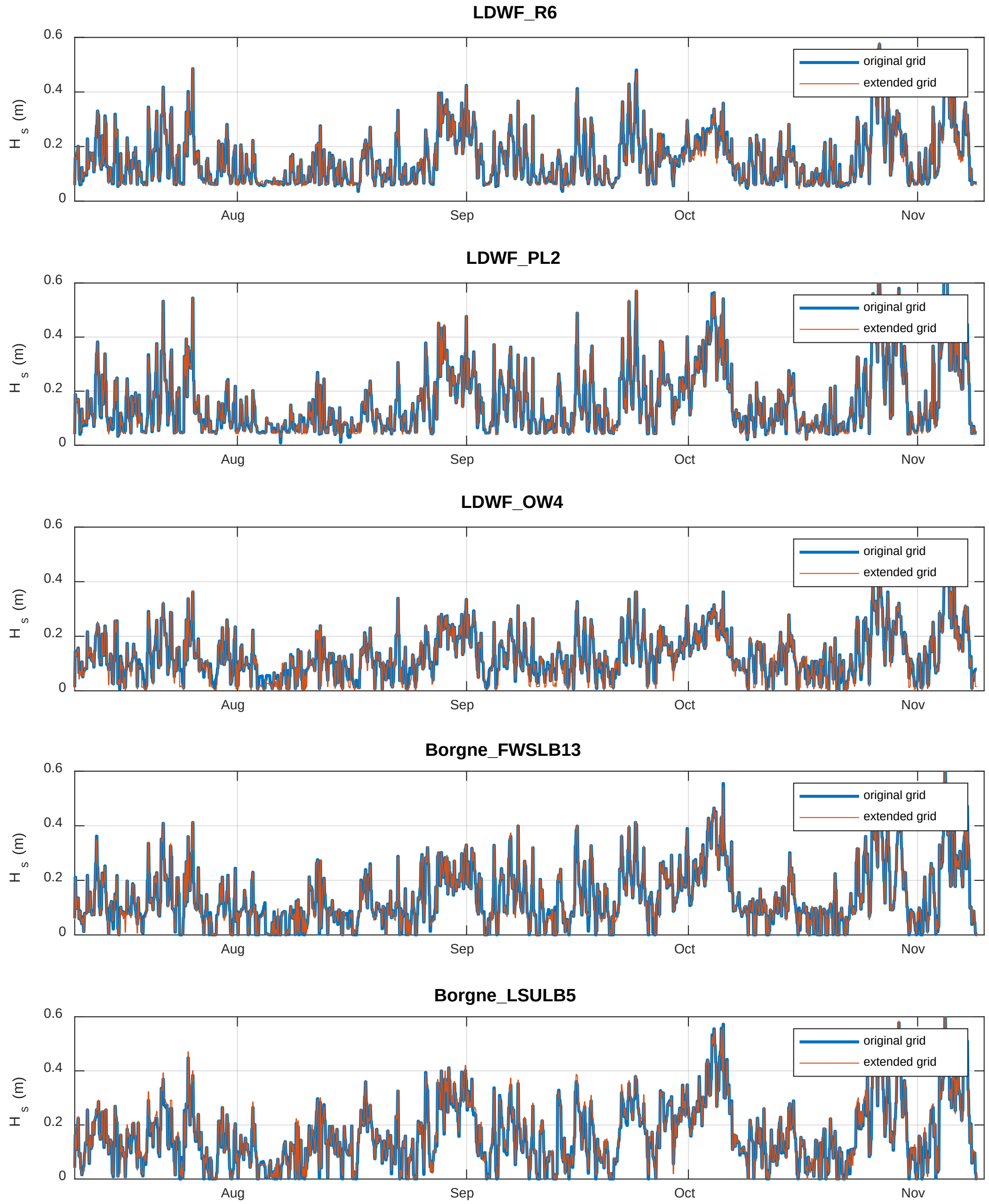

Figure 21. Comparison of wave heights between the truncated Wave Model grid and the extended grid (Figure 17), indicating similar wave heights at five locations across Lake Pontchartrain and Lake Borgne. These five sites are a subset of the Louisiana Department of Wildlife and Fisheries (LDWF) sites where model outputs were provided (Figure 41). Site LDWF_R6 is located in the northeastern part of Lake Pontchartrain, LDWF_PL2 in the center of Lake Pontchartrain, LDWF_OW4 in the far eastern part of Lake Pontchartrain, Borgne_FWSLB13 in the center of Lake Borgne, and Borgne_LSULB5 in the far east of Lake Borgne.

3.0 DISSOLVED OXYGEN PROXY

Temperature, salinity, and DO are environmental factors that influence most physiological and many ecological responses in estuarine species. In addition, DO is necessary for sustaining aquatic life, with tolerances to oxygen concentrations varying among species and life stages (Niklitschek & Secor, 2009). Since DO measurements were collected along with fish telemetry data to test if DO was a key parameter driving fish migration behavior, developing a methodology to have similar output from the model was needed. Since developing a full water quality model was beyond the scope of this study, an exploratory methodology to develop a DO proxy was employed instead to test the likelihood of DO contributing to the Habitat Suitability Indexes. This methodology leveraged historical observations on salinity stratification and DO observations in Lake Pontchartrain (Georgiou, 2002), and previously developed three-dimensional salinity models (Schindler, 2010).

DO concentration typically depends on water temperature, DO saturation, and stratification conditions in the water column (i.e., how well the water column is mixed). The stratification intensity hinders mixing between the upper and low part of the water column, and over time DO in the lower part of the water column is depleted leading to hypoxic, or anoxic conditions (USEPA, 2015). Low DO conditions typically occur during the summer when the temperature is above 20–25°C, DO saturation is low and well below 8 mg/L, and highly-stratified conditions exist (USEPA, 2015). One way to quantify stratification intensity is by evaluating the salinity difference between the top and the bottom layers of the water column (Georgiou, 2002).

The Hydrodynamic Model developed for this project (see Section 2.0) was a 2D depth-averaged model; depth-averaged models do not provide representations of vertical variation in salinity, and thus cannot predict stratification throughout the water column. For this reason, a methodology was developed to estimate the likelihood of low DO occurrence using the available results from the 2D Delft3D-FM Hydrodynamic Model presented in this report. (i.e., water level, water velocity, tidal and subtidal water level variation). The methodology leveraged the results from an existing three-dimensional (3D) Finite Volume Community Ocean Model (FVCOM) model which covered the same area of interest and existing simulations for a period during which stratification was present (Schindler, 2010).

The methodology developed is summarized below:

1. Use the 3D FVCOM model results to identify stratification and de-stratification conditions.
2. Identify, within the FVCOM model domain, the areas that have the potential to develop stratification and the corresponding environmental drivers.
3. Develop correlations between hydrodynamic variables and salinity stratifications using the results of the FVCOM model. These correlations could vary spatially based on the results of step 2.
4. Apply this correlation to the Hydrodynamic Model results to estimate salinity stratification conditions for the timeframe of interest.

5. Use the estimated salinity stratification and projected temperature to estimate the level of DO for the timeframe of interest.

These five steps are described in detail in the following sections of this report.

3.1 FVCOM MODEL RESULT ANALYSIS

Model results from a previous study which used a 3D FVCOM model were used to develop the DO proxy methodology. Details about this model can be found in Schindler (2010).

Some samples of the model output from the 3D FVCOM model are presented in Figure 17. Panel A shows salinity in the top layer of the water column, panel B shows the salinity at the bottom layer of the water column and panel C shows the difference between the two, which is an indication of stratification. The outputs are presented for neap tide conditions, during which the stratification of the water column typically occurs.

3.1.1 Stratification Areas and Selected Timeseries

Salt fluxes enter Lake Borgne mainly from the east via the Intracoastal Waterway (ICWW) and Cat Island Pass, which connect Lake Borgne with Chandeleur Sound. Additional salt fluxes also arrive through Bayou La Loutré via the Mississippi River Gulf Outlet (MRGO, Figure 18).

By analyzing the results in Figure 17, seven areas within the study domain can be identified as influenced by stratification: Cat Island Offshore, Cat Island, Pearl River, Lake Borgne, MRGO, the Inlets (e.g., Rigolets) and portions of Lake Pontchartrain. Timeseries results were extracted from the 3D FVCOM model outputs at seven selected locations (Figure 18), identified to obtain a trend between salinity stratification and other physical variables predicted by the model. Figure 18 shows the location map of stations used for the timeseries data.

Figure 19 to Figure 21 show timeseries of salinity stratification (difference between top and bottom layers in the water column) and water surface elevation (WSE) at the seven selected locations. Each location exhibits a different trend and relationship between stratification and tide level. The trends are influenced by environmental conditions, regional bathymetry, flushing or mixing characteristics, and proximity to a fluvial or coastal ocean.

Lake Pontchartrain (Figure 19) shows punctuated moderate stratification during sub-tidal or tidal/subtidal interaction. The Rigolets tidal pass (Figure 20) shows a nearly continuous weak stratification, likely due to the water depth in this area, tidal straining in a well-mixed tidal channel (Li et al., 2008), and proximity to a freshwater source (i.e., the Pearl River). The ICWW towards Mississippi Sound near Cat Island (Figure 21) shows similar punctuated moderate salinity stratification. The Cat Island Channel (Figure 22) shows punctuated moderate stratification and occasional strong stratification (during sub-tidal transitions, tidal/subtidal interaction, and during neap tides).

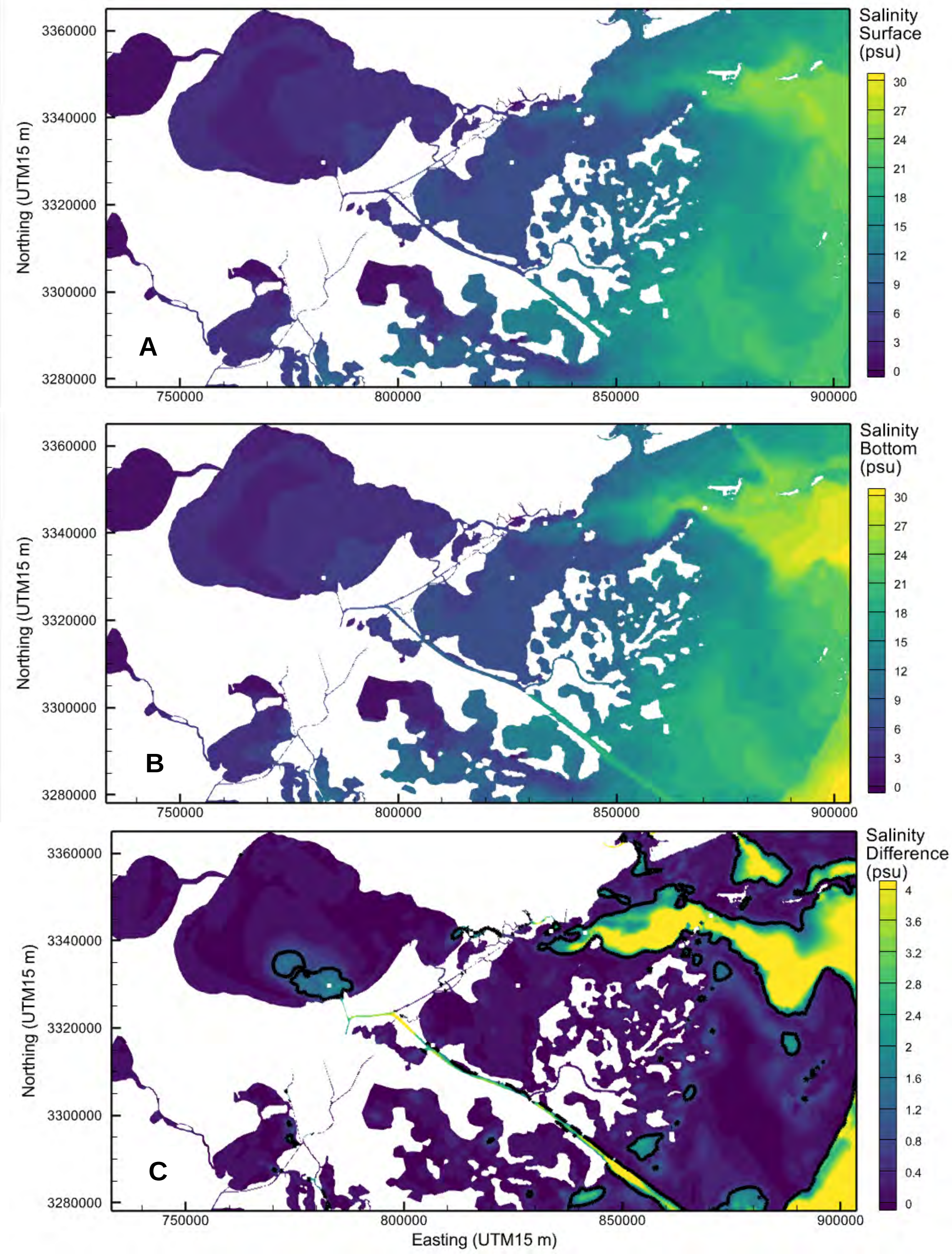

Figure 22. Model results from the 3D FVCOM model : A) salinity at the top layer, B) salinity at the bottom layer, C) difference between the two.

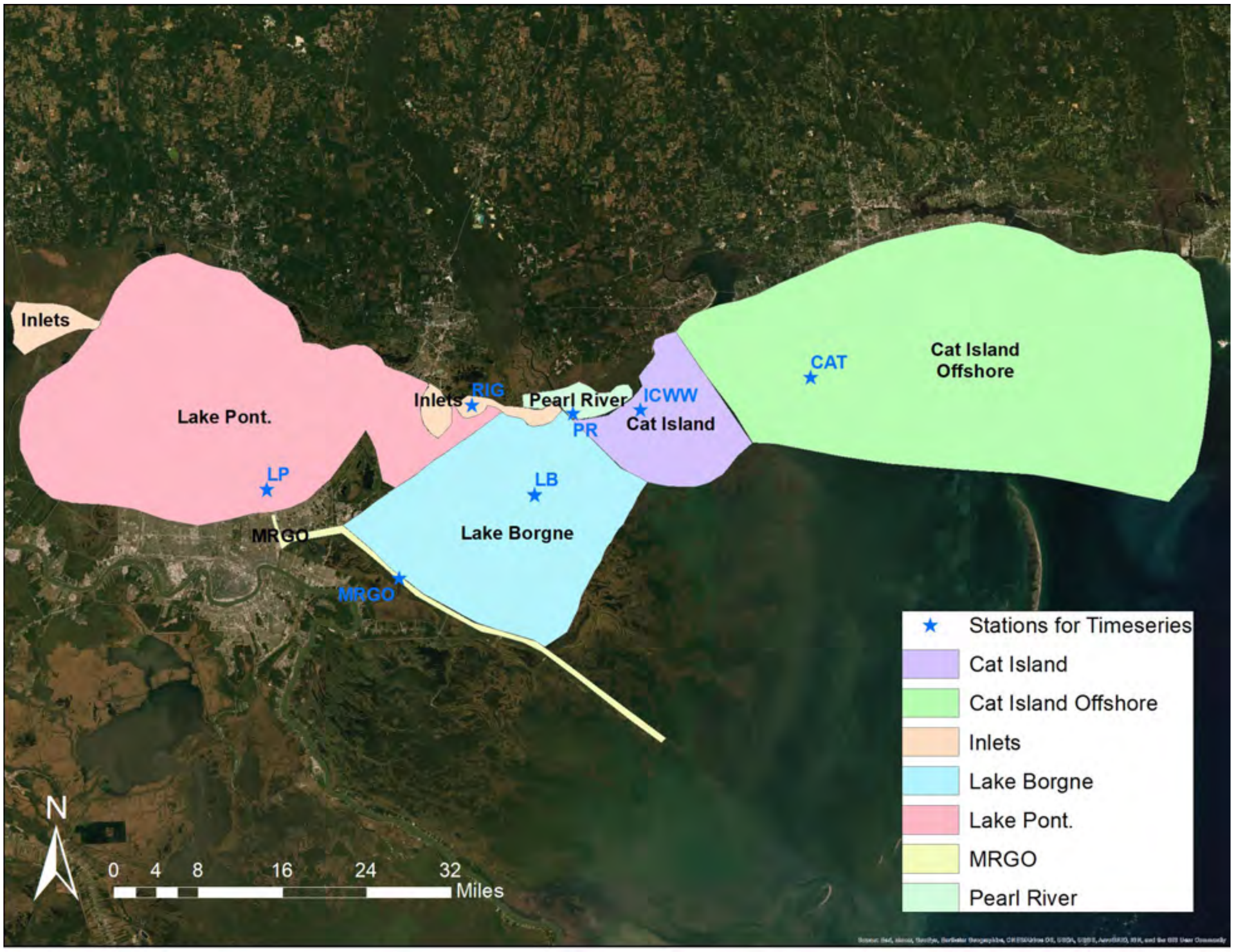

Figure 23. Location of the seven points (stars) used to extract FVCOM model results and develop correlations between salinity stratification and other variables, and location of the polygons used to identify areas with different stratification patterns and to develop correlations between salinity stratification and other variables.

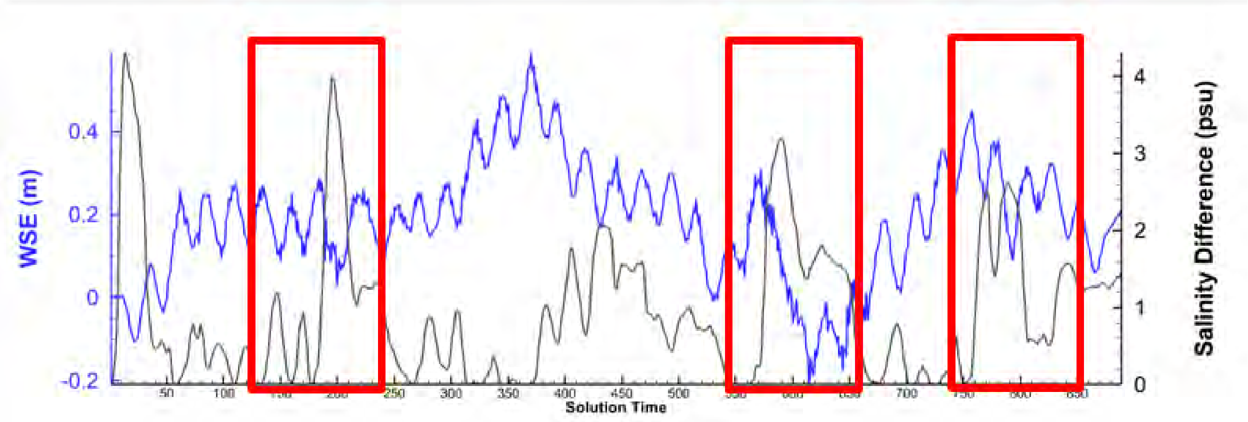

Figure 24. Salinity difference and water surface elevation at LP station (see Figure 18) in Lake Pontchartrain.

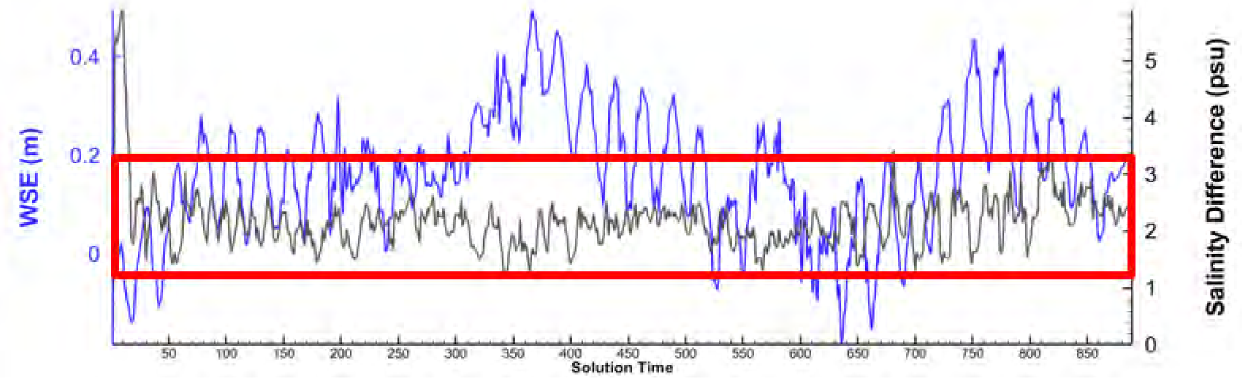

Figure 25. Salinity difference and water surface elevation at RIG station (see Figure 18) in the Inlet polygons (Rigolets).

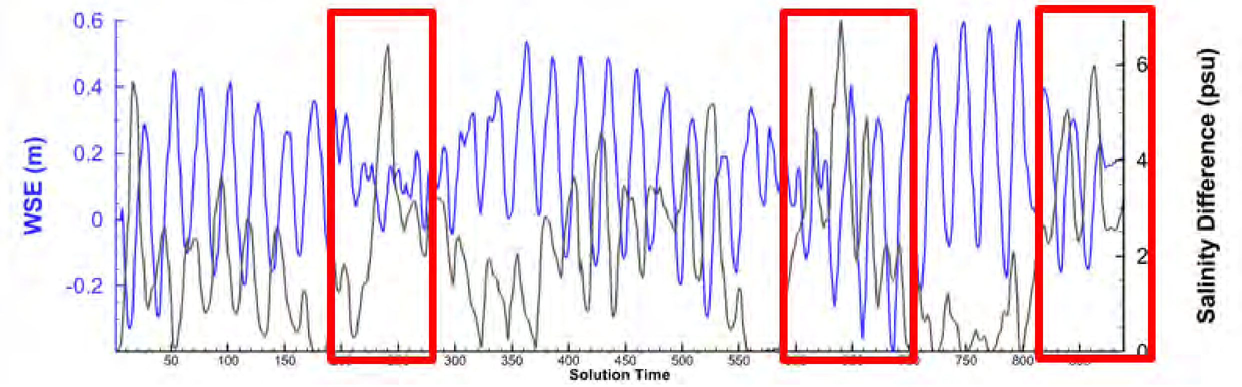

Figure 26. Salinity difference and water surface elevation at ICWW (see Figure 18) in the Cat Island polygon.

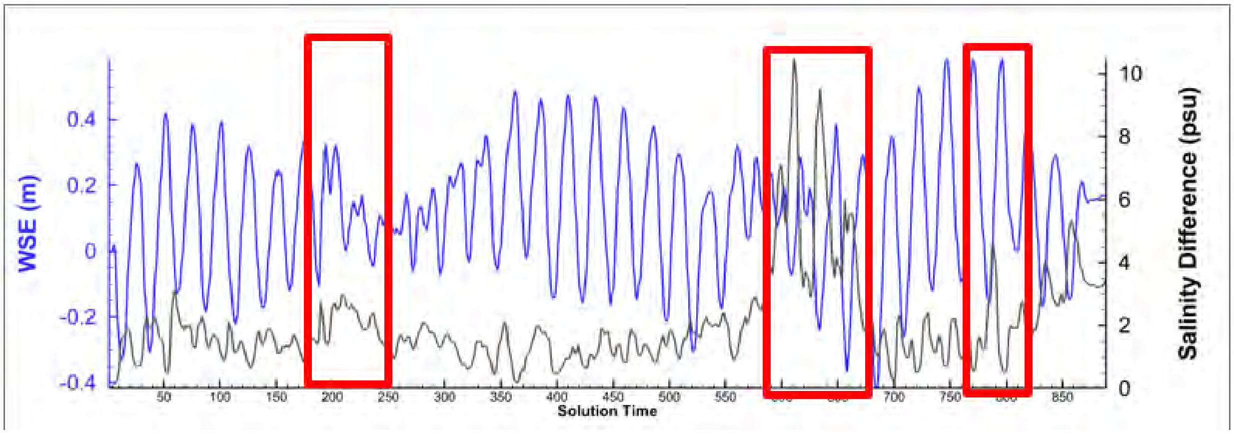

Figure 27. Salinity difference and water surface elevation at (see Figure 18) in the Cat Island Offshore polygon.

3.2 SALINITY STRATIFICATION CORRELATION PATTERNS

The analysis of the 3D FVCOM model results was used to establish a correlation that was in turn used to estimate salinity stratification using results from the 2D model.

The correlation analysis included three main parameters: background salinity difference value (e.g., daily mean value), salinity variation (i.e., oscillation of salinity difference due to the diurnal tide), and the location of the peaks of salinity difference, which are caused by the interaction of tidal and subtidal transitions. Figure 19 to Figure 22 shows that salinity difference depends strongly on the tidal signal. Specifically, salinity difference can be correlated to both tide level and tidal current velocity, both of which exhibit strong correlations. Tide level was selected for this correlation analysis because it is a scalar value rather than a vector, as current velocity is driven by the tides.

Depending on the station, different correlation patterns can be observed between tide level and salinity differences. These patterns were used as the base for the correlation analysis and for the proxy prediction methodology.

The first pattern to observe is the correlation between tide range and salinity differences. This correlation is strong in some locations, but weak in others (Figure 23). The variations of salinity difference have similar periods to the diurnal tide signal. The salinity difference peaks are significant and are related to the rapid decrease of low tide troughs due to freshwater input from lake or riverine sources. On the contrary, there are salinity differences smaller in magnitude that are correlated with the increase of high tide peaks, causing offshore water to push the freshwater back in the lake or riverine systems.

After analyzing all seven stations and their patterns, the following formula was developed to correlate tide levels with salinity differences:

$$S = k\left(m + \frac{r}{2}E(t)\right) + b \qquad \text{Eq.6}$$

where:

- S is the predicted salinity difference.
- k is the multiplier for significant salinity difference peaks due to neap tides during which the linear regression is not applicable.
- m is the data regression of mean salinity difference. This is a function of the tidal range (TR): $a_1TR + b_1$, where a_1 and b_1 are the results of the data regression and they depend on the stations. See Table 6 for their values.
- r is the data regression of salinity difference variation. This is a function of the tidal range (TR): $a_2TR + b_2$, where a_2 and b_2 are the results of the data regression and they depend on the stations. See Table 6 for their values.
- E is the position of the instantaneous tide range relative to the maximum and minimum values. E varies between -1, at high tide, and 1, at low tide.
- b is the mean value adjustment for tide envelop trends.

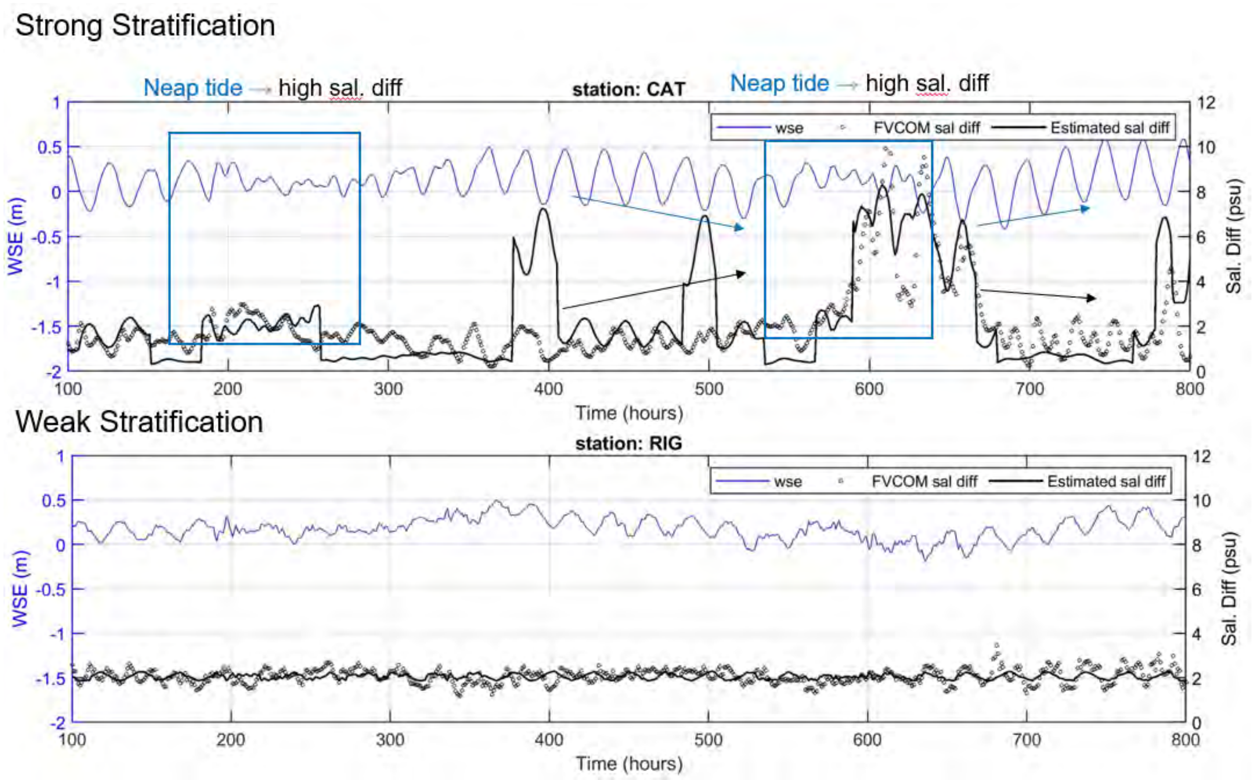

Figure 28. Example of correlation patterns for a strong (top; salinity difference up to 8-10 ppt) and a weak (bottom; salinity difference below 4 ppt) stratification case. "FVCOM sal diff" is the salinity difference predicted by the FVCOM model, "estimated sal diff" is the salinity difference estimated with Eq. 4, "wse" is the WSE predicted by the FVCOM model.

Table 7. Summary of the data regression parameters for each area

Station / Area	k	m		r	
		a_1	b_1	a_2	b_2
CAT / Cat Island Offshore	3.0	-1.30	2.61	0.73	0.73
ICWW/ Cat Island	2.0	-1.05	2.42	-0.37	2.04
LB / Lake Borgne	1.0	-0.06	0.06	-0.06	0.14
LP / Lake Pontchartrain	3.0	-0.48	0.99	-0.47	0.88
MRGO/MRGO	1.0	-0.48	3.26	-0.02	0.26
PR / Pearl River	2.0	-1.36	2.00	0.03	1.51
RIG / Inlets (Rigolets)	1.0	0.10	2.05	0.27	0.35

The correlation formula considers both statistics (i.e., results of the regression) and physics (i.e., tide signal elevation, range and derivative of high tide and low tide). However, this estimation methodology should be considered a qualitative assessment, instead of a quantitative calculation.

Figure 24 to Figure 30 presented the results for all seven stations used to represent the seven sub-areas. Each figure presents:

- The regression of the 24-hour average salinity difference as function of tidal range (a1 and b1), in the top left of every figure.
- The regression of the salinity difference range as a function of tidal range (a2 and b2), in the top right of every figure.
- FVCOM model WSE (in blue) and salinity difference (in green) results with the salinity difference predicted (in dashed green) by this correlation method (bottom graph of every figure).

The correlation formula (Eq. 4) can predict the salinity difference reasonably well for both minimums and peaks. Several false peaks can be observed for certain stations (see Figure 24 and Figure 29). However, salinity difference peaks can be considered conservative when estimating DO concentration. For this reason, and because the goal was to have formulations valid for the entire areas identified in Figure 23 , no specific corrections were implemented for these stations.

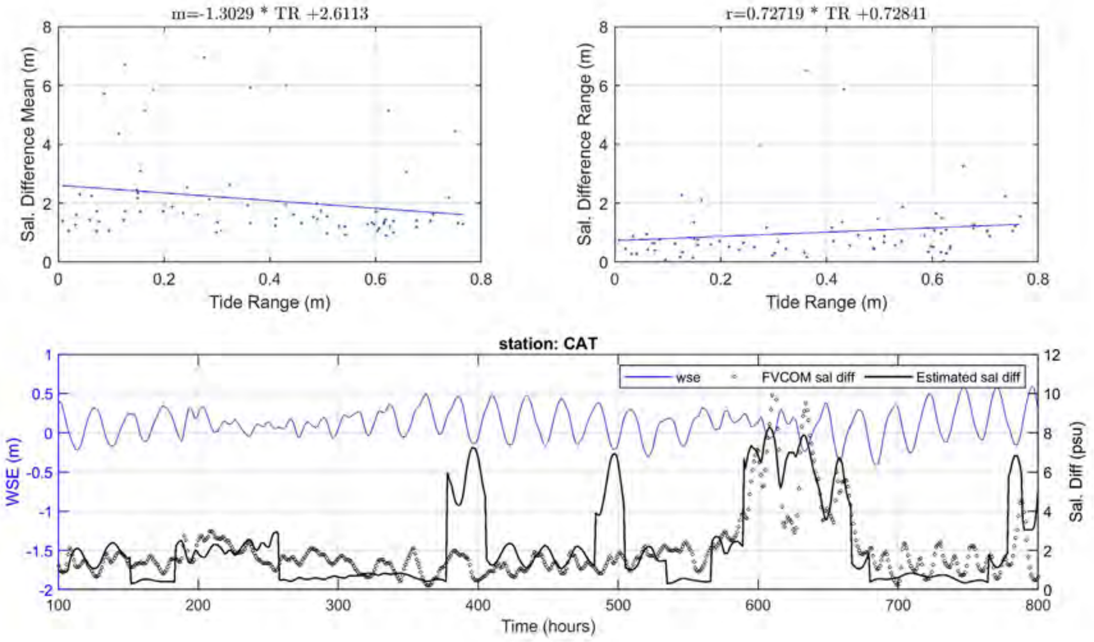

Figure 29. Salinity difference regression for CAT station in the Cat Island Offshore area. "FVCOM sal diff" is the salinity difference predicted by the FVCOM model, "estimated sal diff" is the salinity difference estimated with Eq. 4, "wse" is the WSE predicted by the FVCOM model.

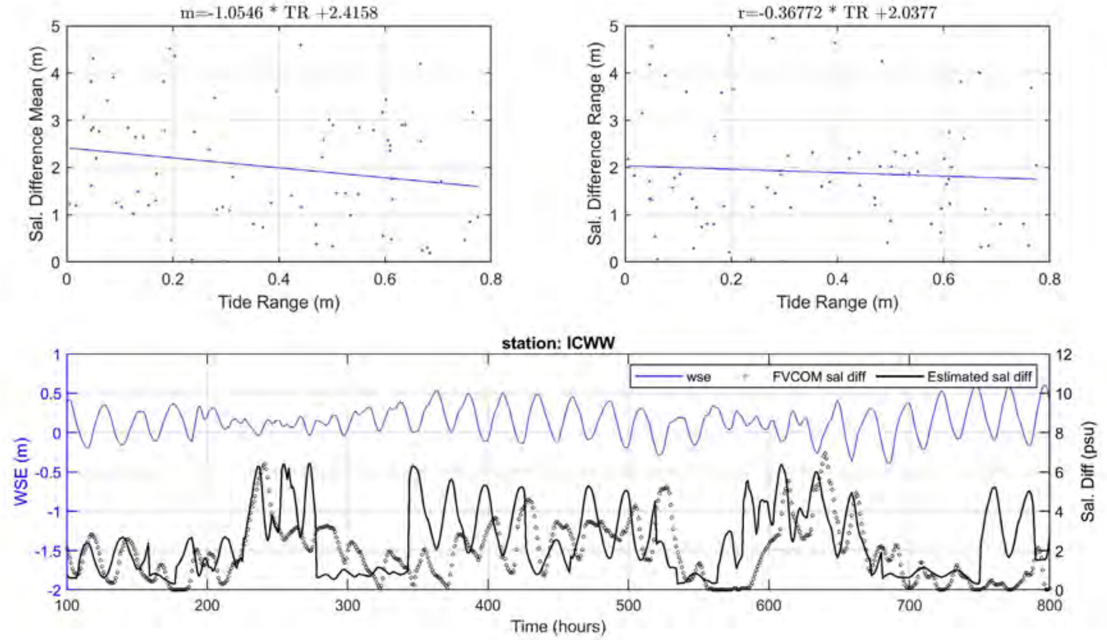

Figure 30. Salinity difference regression for ICWW station in Cat Island area. "FVCOM sal diff" is the salinity difference predicted by the FVCOM model, "estimated sal diff" is the salinity difference estimated with Eq. 4, "wse" is the WSE predicted by the FVCOM model.

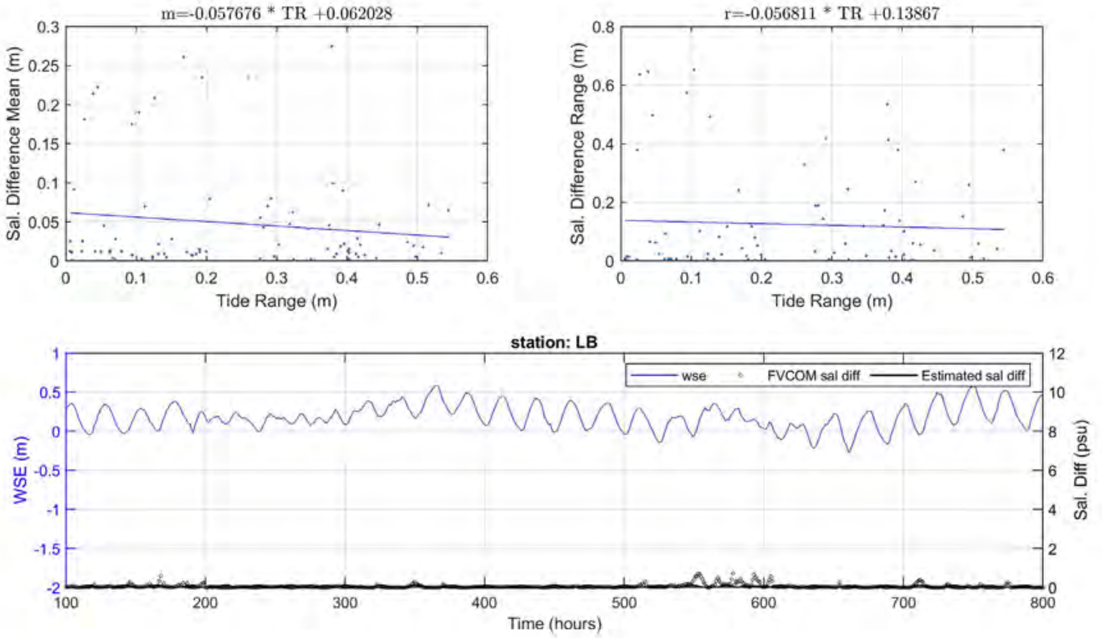

Figure 31. Salinity difference regression for LB station in Lake Borgne. "FVCOM sal diff" is the salinity difference predicted by the FVCOM model, "estimated sal diff" is the salinity difference estimated with Eq. 4, "wse" is the WSE predicted by the FVCOM model.

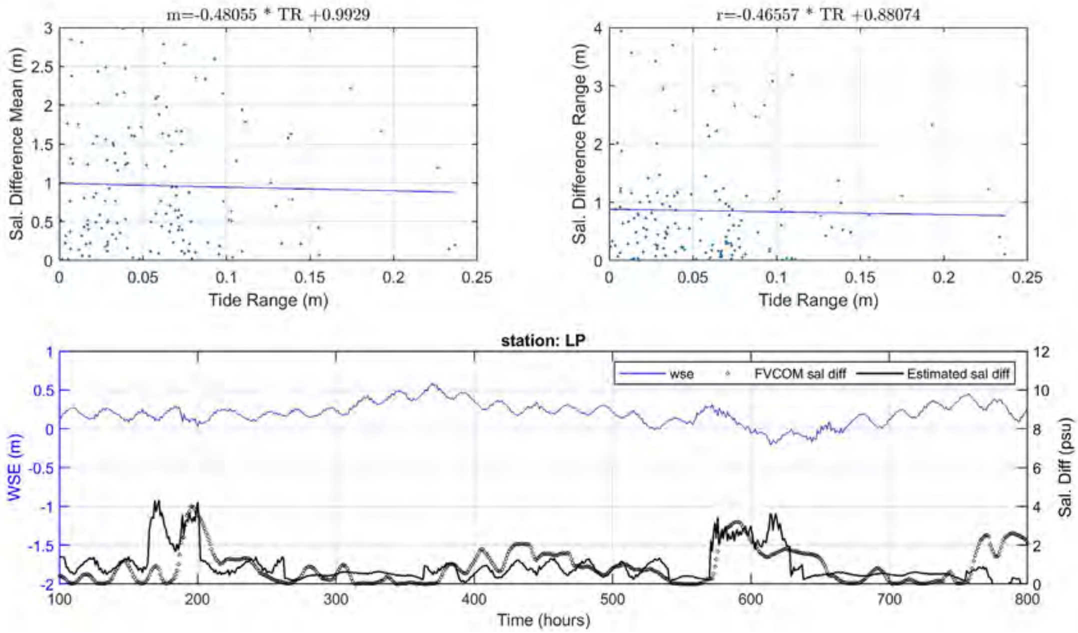

Figure 32. Salinity difference regression for LP station in Lake Pontchartrain. "FVCOM sal diff" is the salinity difference predicted by the FVCOM model, "estimated sal diff" is the salinity difference estimated with Eq. 4, "wse" is the WSE predicted by the FVCOM model.

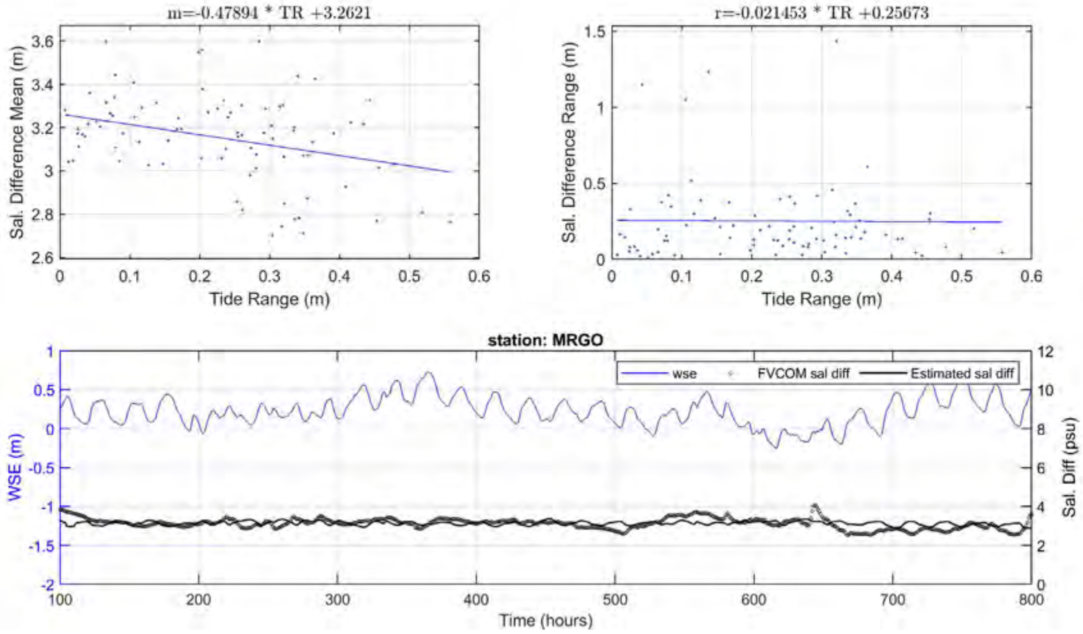

Figure 33. Salinity difference regression for MRGO station in the MRGO. "FVCOM sal diff" is the salinity difference predicted by the FVCOM model, "estimated sal diff" is the salinity difference estimated with Eq. 4, "wse" is the WSE predicted by the FVCOM model.

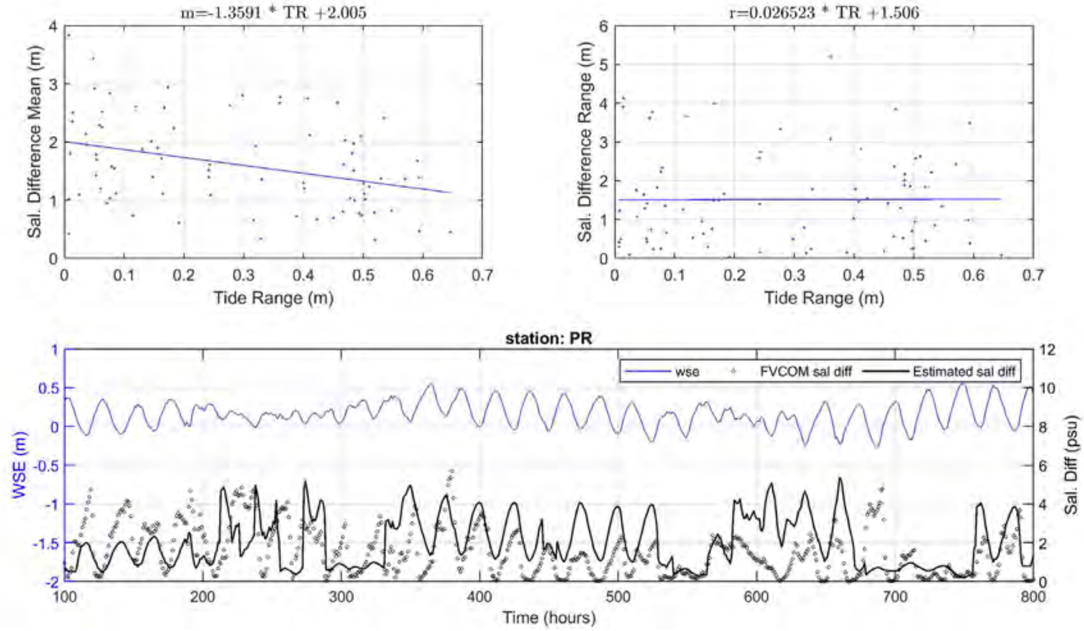

Figure 34. Salinity difference regression for PR station in the Pearl River area. "FVCOM sal diff" is the salinity difference predicted by the FVCOM model, "estimated sal diff" is the salinity difference estimated with Eq. 4, "wse" is the WSE predicted by the FVCOM model.

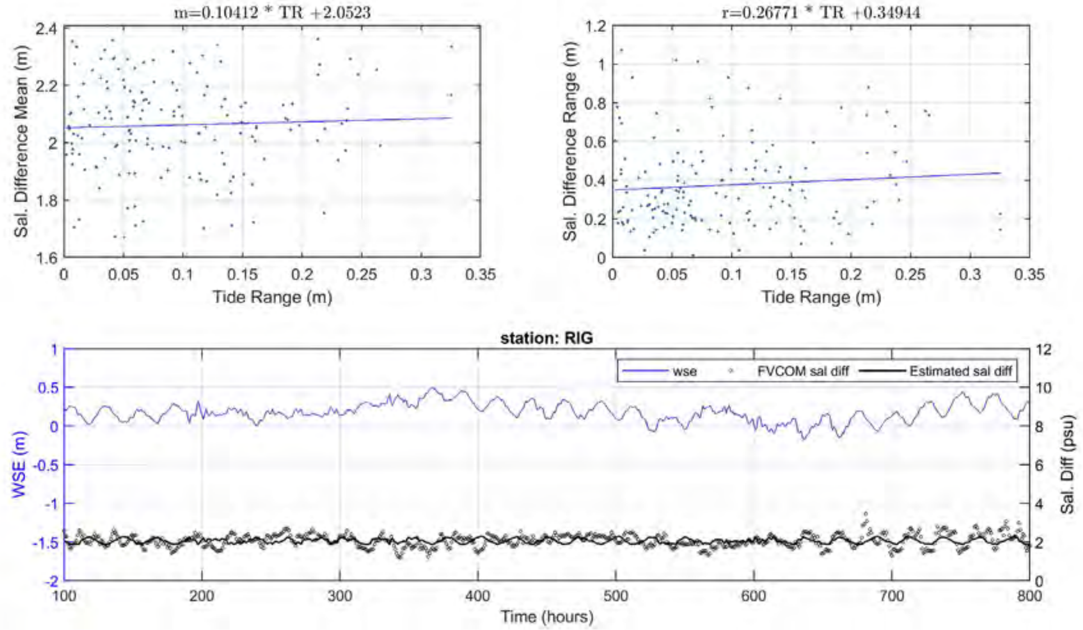

Figure 35. Salinity difference regression for RIG station in the Rigolets area. "FVCOM sal diff" is the salinity difference predicted by the FVCOM model, "estimated sal diff" is the salinity difference estimated with Eq. 4, "wse" is the WSE predicted by the FVCOM model.

3.3 DISSOLVED OXYGEN PROXY

The previous section describes the development of a formulation to estimate salinity difference as a function of the tidal range. In this section, the estimated salinity stratification is used to calculate the likelihood of low DO, which also depends on other variables, such as water temperature and DO saturation.

3.3.1 DO Saturation Calculation

First, DO saturation was calculated using the Thomann and Mueller (1987) formulation:

$$\ln\left(c_{sf}\right) = -139.34411 + \frac{1.575701 \cdot 10^{5}}{T} - \frac{6.642308 \cdot 10^{7}}{T^{2}} + \frac{1.243800 \cdot 10^{10}}{T^{3}} - \frac{8.621949 \cdot 10^{11}}{T^{4}} \qquad \text{Eq.7}$$

$$\ln(c_{ss}) = \ln\left(c_{sf}\right) - S\left(1.7674 \cdot 10^{-2} - \frac{1.0754 \cdot 10^{1}}{T} + \frac{2.1407 \cdot 10^{3}}{T^{2}}\right) \qquad \text{Eq.8}$$

where:

- c_{sf} is the freshwater DO saturation concentration in mg/L at 1 atmosphere
- c_{ss} is the saline water DO saturation concentration in mg/L at 1 atmosphere
- *ln* is the natural logarithm
- T is the absolute temperature (in Kelvin)
- S is the salinity (average across the water column) in ppt

The DO saturation required to calculate DO concentration is c_{ss}, which can be calculated using all the Hydrodynamic Model results.

3.3.2 Likelihood of Low DO Calculation

The equations described and presented in the previous sections enable estimation, using the Hydrodynamic Model results, of the following parameters:

1. Salinity stratification (using tide level predictions),
2. DO saturation (using 2D depth average salinity and temperature prediction). and
3. Temperature (direct output of the Delft3D-FM model).

The combination of these three variables controls the DO concentration. This methodology should be considered a qualitative assessment instead of a quantitative calculation; for this reason, the three parameters above were used to estimate the likelihood of low DO concentration, rather than a precise calculation of DO concentration.

A set of observations collected in Lake Pontchartrain in 1999 and 2000 by Georgiou (2002) were used to set the rules for the final DO proxy (Georgiou, 2002; Haralampides, 2000). An example of this dataset is provided in Figure 36; additional timeseries can be found in Figure 3.3 to 3.14 in Georgiou (2002) The field data show that low DO occurs when oxygen demand in the lower part of the water column is larger than oxygen supply via re-aeration of the upper water column. This often occurs when stratification is "stable" (i.e., not enough mixing) and persists for extended periods, typically in the order of days. In addition, oxygen supply through re-aeration is reduced at higher water temperatures, and when DO saturation is lower (i.e., ~6–7 mg/L), typical of summer conditions, versus the 10–11 mg/L typical of the winter conditions. By using these observations, the rules described in Table 7 were defined and applied to the Hydrodynamic Model results.

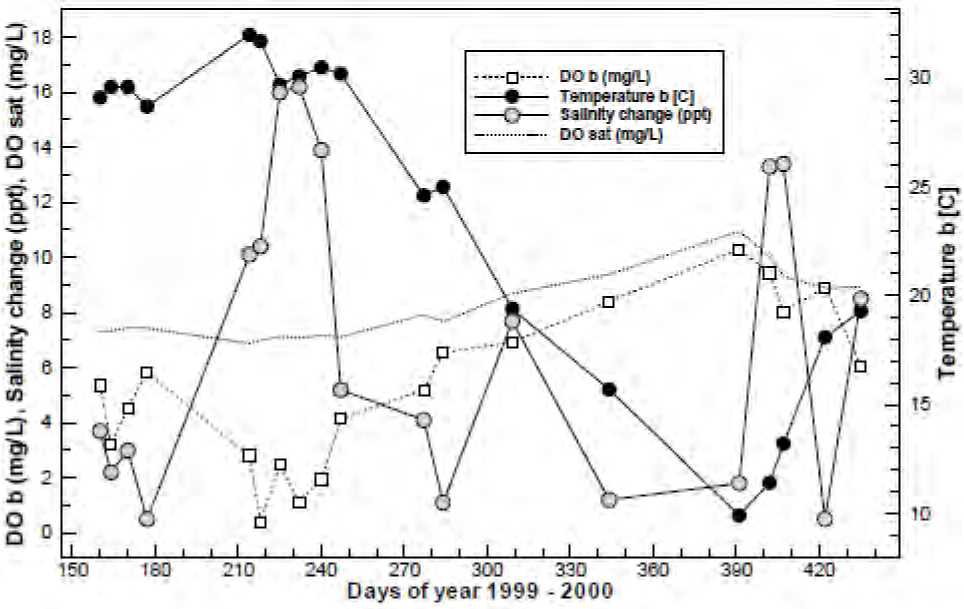

Figure 36. DO concentration, DO saturation, temperature and salinity change timeseries for a station in Lake Pontchartrain. This is Figure 3.7 from (Georgiou, 2002).

Table 8. Rules for the calculation of the Likelihood of Low DO selected using observations in Lake Pontchartain during stratification and destratification episodes (Georgiou, 2002).

DO saturation (mg/L)	Water Temperature (°C)	Salinity Difference (ppt)	Likelihood of Low DO	Persistancy of stratification
DO saturation > 8 mg/L	T > 25 °C	<1	Very Low	
		1–3	Very Low	
		3–5	Very Low	
		>5	Very Low	
	20°C < T < 25 °C	<1	Very Low	
		1–3	Low	
		3–5	Intermediate	
		>5	Intermediate	
	T < 20 °C	<1	Very Low	
		1–3	Low	
		3–5	Low	
		>5	Low	
DO saturation < 8 mg/L	T > 25 °C	<1	Very Low	
		1–3	Low	
		3–5	Intermediate	If this conditions persists for more than 6 days, the likelihood becames High
		>5	High	
	20°C < T < 25 °C	<1	Very Low	
		1–3	Low	
		–	Intermediate	If this conditions persists for more than 6 days, the likelihood becames High
		>5	High	
	T < 20 °C	<1	Very Low	
		1–3	Very Low	
		3–5	Very Low	
		>5	Very Low	

4.0 VALIDATION WITH CTD CASTS

Multiple conductivity, temperature, and depth (CTD) casts collected by USFWS were used to validate the Hydrodynamic Model. A CTD is a marine-grade suite of instruments and sensors attached together via a pumped system, which is used by oceanographers to detect how conductivity, DO content, turbidity, and temperature change vertically throughout the water column. Conductivity is then used to calculate salinity and water density. These profiles were used to evaluate the ability of the Hydrodynamic Model to predict salinity, temperature, and likelihood of low DO.

NOAA, USGS, and CRMS stations were prioritized for model calibration because they provide continuous and instantaneous datasets which are key to calibrating the model and making sure the model captures the seasonal variations and fluctuations over time (see Section 5.2). The CTD casts collected as part of this project represented a unique opportunity to validate the Hydrodynamic Model especially in areas where continuous monitoring stations do not exist, namely in southern Lake Borgne.

The CTD casts were collected at the locations shown in Figure 37.

Figure 37. Locations of CTD measurements collected by USFWS and used to validate the Hydrodynamic Model.

The top of Figure 38 shows the comparison between salinity predicted by the Hydrodynamic Model (depth averaged – blue line) and the CTD profiles (depth averaged – circles) at the RIGOLETS2 station located in the Rigolets tidal pass. The bottom graphs of Figure 38 shows the salinity vertical profiles collected at the same location (RIGOLETS2). The salinity validation plots for all the other stations shown in Figure 37 are included in Appendix D.

The top of Figure 39 shows the comparison between temperature predicted by the Hydrodynamic Model (depth averaged – blue line) and the CTD profiles (depth averaged – circles) at the RIGOLETS2 station located in the Rigolets tidal pass. The bottom graphs of Figure 39 shows the temperature vertical profiles collected at the same location (RIGOLETS2). The temperature validation plots for all the other stations shown in Figure 37 are included in Appendix E.

The top of Figure 40 shows the comparison between DO saturation estimated with Eq. 8 (blue line) and the DO saturation and concentration (circles and triangles, respectively) measured by the CTD casts at RIGOLETS2, in the Rigolets tidal pass. The background color shows the likelihood of low DO predicted using the rules in Table 8 applied to the Hydrodynamic Model salinity and temperature results. The bottom graphs of Figure 40 shows the DO concentration profiles collected at the same location (RIGOLETS2). The likelihood of low DO validation plots for all the other stations shown in Figure 37 are included in Appendix F.

The CTD casts collected largely showed a lack of stratification in the areas and time periods sampled. However, intermittent stratification is possible, either in areas of deeper water not sampled or during conditions that did not coincide with the sampling for servicing the telemetry equipment, and as such additional methodologies were exploited to inform the DO proxy development. These included using other empirical datasets (Georgiou, 2002)., and previous three-dimensional modeling results (Schindler, 2010), as explained in Section 3.0.

Figure 38. Top graph: simulated daily averaged salinity by the Hydrodynamic Model (blue line) compared to depth averaged CTD casts at RIGOLETS2. Bottom graph: vertical salinity CTD profiles collected at RIGOLETS2. The colors of the CTD vertical profiles in the bottom graph match the color of the depth averaged CTD observation in the top graph.

Figure 39. Top graph: simulated daily averaged temperature by the Hydrodynamic Model (blue line) compared to depth averaged CTD casts at RIGOLETS2. Bottom graph: vertical temperature CTD profiles collected at RIGOLETS2. The colors of the CTD vertical profiles in the bottom graph match the color of the depth averaged CTD observation in the top graph.

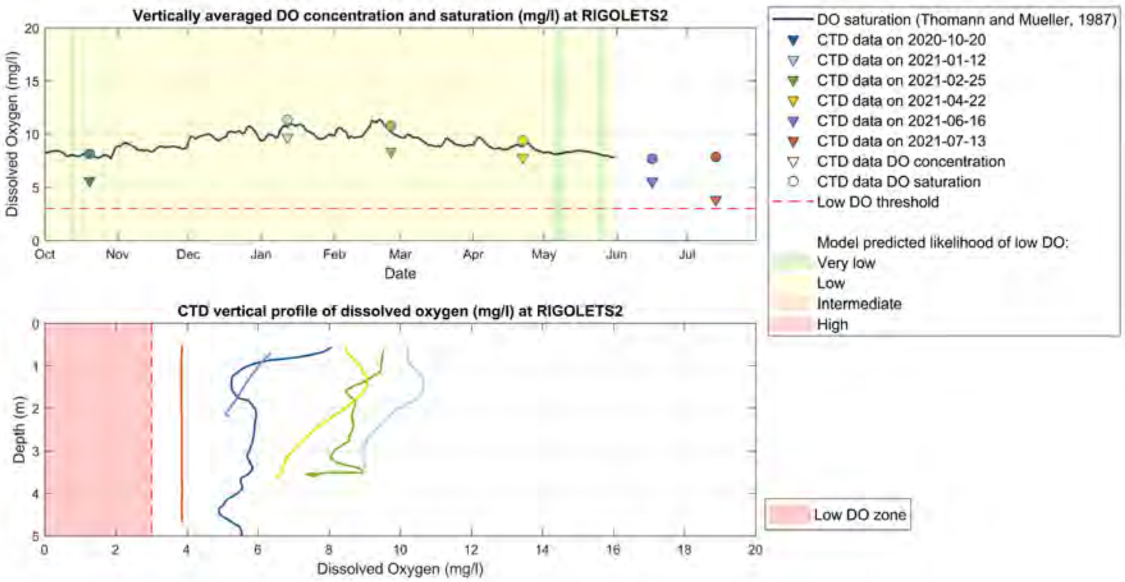

Figure 40. Top graph: DO saturation estimated with Eq.8 (blue line), depth averaged DO saturation (circles) and concentration (triangles) measured by the CTD casts at CHEF1. Background color shows the likelihood of low DO predicted using the Hydrodynamic Model results and the rules in Table 8. Bottom graph: vertical DO concentration CTD profiles collected at CHEF1. The colors of the CTD vertical profiles in the bottom graph match the color of the depth averaged CTD observation in the top graph. The zone of low DO is highlighted in red.

5.0 SIMULATIONS PERFORMED AND OUTPUT GENERATED

The Hydrodynamic Model developed as part of this study was used to hindcast the hydrodynamics, salinity, and temperature of the area of interest for six time periods:

1. October 2016 to May 2017
2. October 2017 to May 2018
3. October 2018 to May 2019
4. October 2019 to May 2020
5. October 2020 to May 2021
6. October 2021 to May 2022

The following variables were provided as time series to LSU for the development of the Habitat Suitability Maps methodology: water level, water depth, salinity, water temperature, wind speed, and water velocity (x and y direction, magnitude, and direction). The time series included: daily average, daily maximum, daily minimum, and daily standard deviation, all calculated from the hourly Hydrodynamic Model output. The time series were generated for all 94 stations where the sturgeon receivers were deployed (see Figure 37). Time series were provided as .csv files, one per station, with samples of these files provided in Figure 38 and Figure 43.

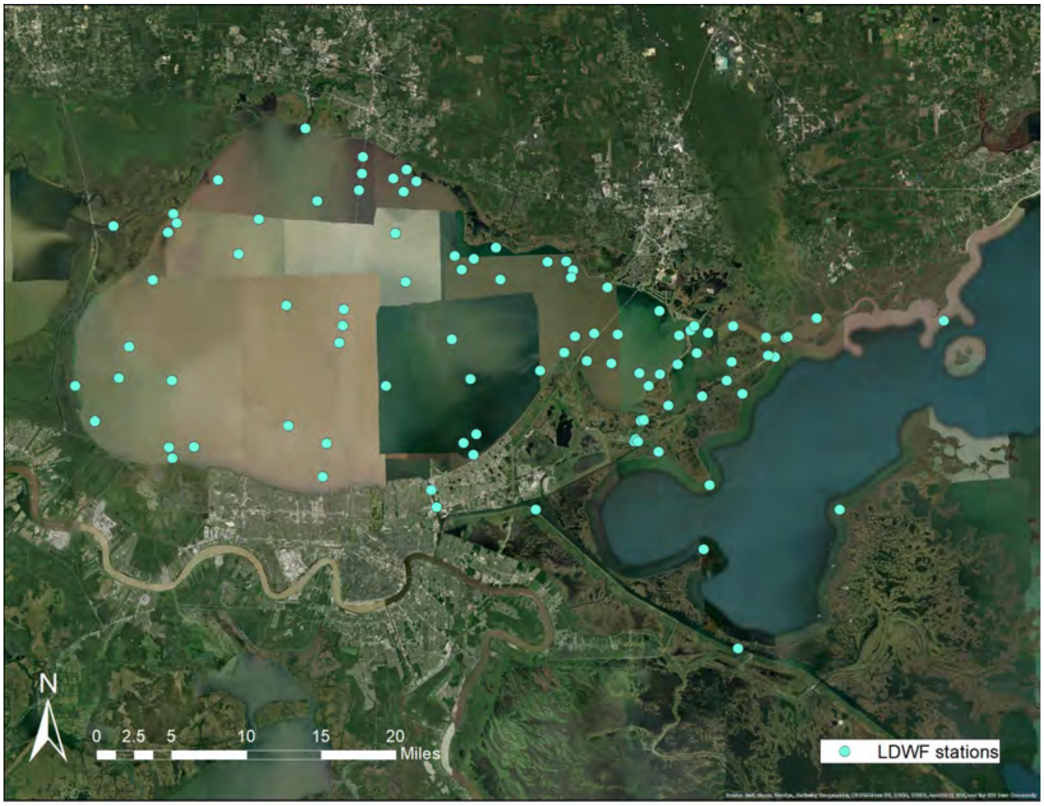

Figure 41. Stations in Lake Pontchartrain, Lake St. Catherine, and Lake Borne used to deliver the Hydrodynamic Model results.

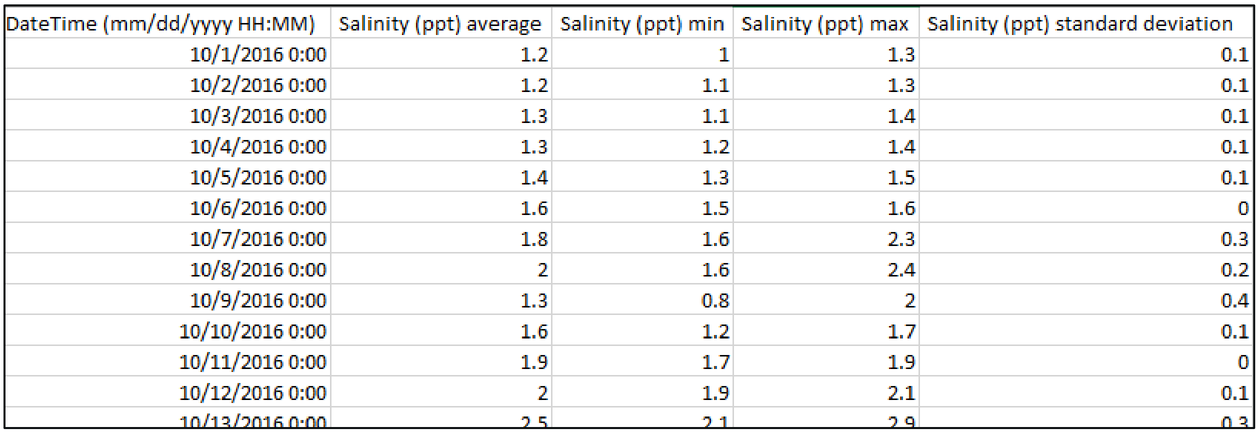

DateTime (mm/dd/yyyy HH:MM)	Salinity (ppt) average	Salinity (ppt) min	Salinity (ppt) max	Salinity (ppt) standard deviation
10/1/2016 0:00	1.2	1	1.3	0.1
10/2/2016 0:00	1.2	1.1	1.3	0.1
10/3/2016 0:00	1.3	1.1	1.4	0.1
10/4/2016 0:00	1.3	1.2	1.4	0.1
10/5/2016 0:00	1.4	1.3	1.5	0.1
10/6/2016 0:00	1.6	1.5	1.6	0
10/7/2016 0:00	1.8	1.6	2.3	0.3
10/8/2016 0:00	2	1.6	2.4	0.2
10/9/2016 0:00	1.3	0.8	2	0.4
10/10/2016 0:00	1.6	1.2	1.7	0.1
10/11/2016 0:00	1.9	1.7	1.9	0
10/12/2016 0:00	2	1.9	2.1	0.1
10/13/2016 0:00	2.5	2.1	2.9	0.3

Figure 42. Example of the csv file generated for salinity at station CF2.

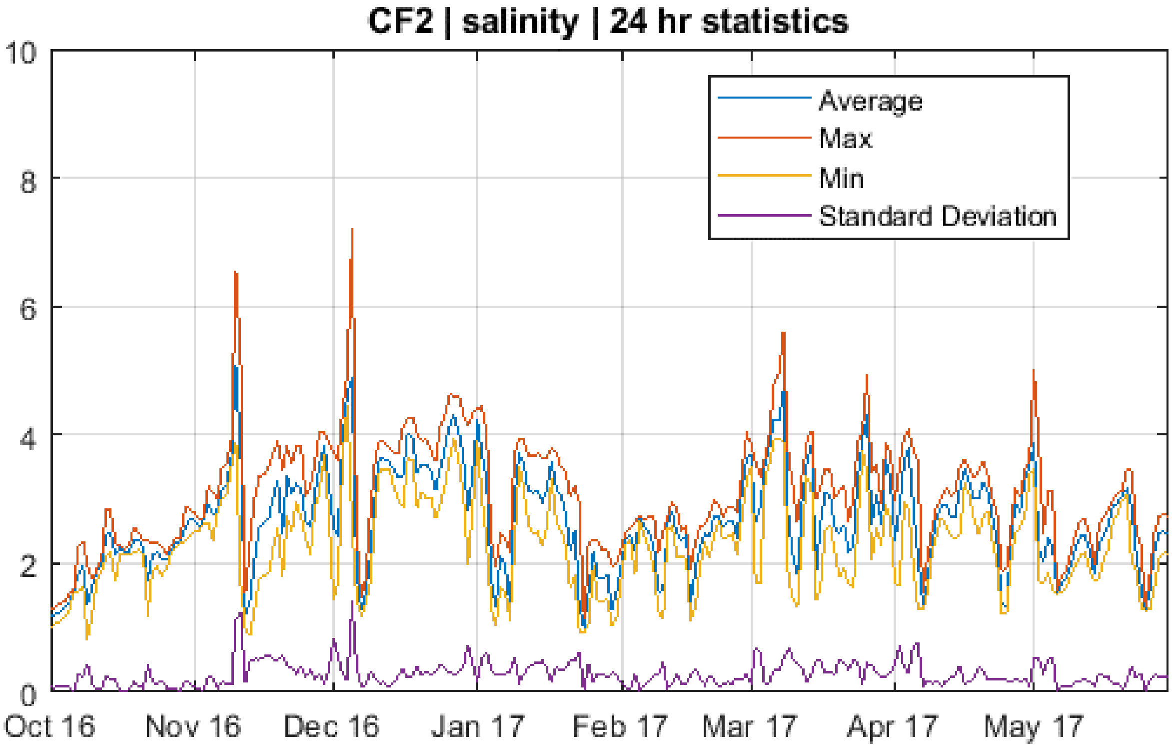

Figure 43. Example of salinity daily statistics (average in blue, maximum in orange, minimum in yellow and standard deviation in purple) at station CF2. These results were provided as csv files

5.1 TURBIDITY PROXY: BOTTOM SHEAR STRESS

One important parameter to consider when assessing Gulf sturgeon habitat is turbidity. The Hydrodynamic Model did not include sediment transport, and for this reason, the Wave Model was developed to calculate bottom shear stress as a proxy to estimate turbidity.

The Soulsby (1997) method was used to calculate the combined wave-current bottom shear stress as a function of bottom orbital velocity amplitude, wave period, angle between wave and current, depth-average flow velocity magnitude, water depth and bed roughness length. The methodology used was the GM79 method (Soulsby, 1997). The wave-current bottom shear stress was calculated for all 94 stations where the Sturgeon receivers were deployed: daily average, maximum, minimum, and standard deviation were provided. At 18 stations there were potentially inaccurate bottom shear stress values. The overall trends (i.e., day-to-day variability) were still accurate, but the absolute values were likely overestimated or underestimated. This is due to the limited resolution of the Wave Model grid in the areas where these stations were located, typically sites within 1–2 km of the bank of a lake or channel. These stations were flagged when the bottom shear stress-estimated values were delivered.

REFERENCES

Allison, M. A., Demas, C. R., Ebersole, B. A., Kleiss, B. A., Little, C. D., Meselhe, E. A., Powell, N. J., Pratt, T. C., & Vosburg, B. M. (2012). A water and sediment budget for the lower Mississippi–Atchafalaya River in flood years 2008–2010: Implications for sediment discharge to the oceans and coastal restoration in Louisiana. *Journal of Hydrology*, *432–433*, 84–97. https://doi.org/10.1016/j.jhydrol.2012.02.020

Baustian, M. M., Reed, D. J., Visser, J. M., Duke-Sylvester, S., Snedden, G., Wang, H., DeMarco, K., Foster-Martinez, M., Sharp, L. A., McGinnis, T., & Jarrell, E. (2020). *2023 Coastal master plan: Model improvement plan, ICM-Wetlands, vegetation, and soil. Version I.* (2023 Coastal Master Plan, p. 165). Coastal Protection and Restoration Authority.

Booij, N., Ris, R. C., & Holthuijsen, L. H. (1999). A third-generation wave model for coastal regions: 1. Model description and validation. *Journal of Geophysical Research: Oceans*, *104*(C4), 7649–7666. https://doi.org/10.1029/98JC02622

Bregman, M., Messina, F., Jung, H., Yuill, B. T., Baustian, M. M., & Georgiou, I. Y. (2020). *Basin Wide model Version 4: Basin Wide model for Mid-Breton Sediment Diversion modeling* (p. 137 + Appendices) [Task Order 51.3. Final Report]. The Water Institute of the Gulf. Funded by the Coastal Protection and Restoration Authority.

Chassignet, E. P., Hurlburt, H. E., Smedstad, O. M., Halliwell, G. R., Hogan, P. J., Wallcraft, A. J., Baraille, R., & Bleck, R. (2007). The HYCOM (HYbrid Coordinate Ocean Model) data assimilative system. *Journal of Marine Systems*, *65*(1), 60–83. https://doi.org/10.1016/j.jmarsys.2005.09.016

Chassignet, E. P., Smith, L. T., Halliwell, G. R., & Bleck, R. (2003). North Atlantic Simulations with the Hybrid Coordinate Ocean Model (HYCOM): Impact of the Vertical Coordinate Choice, Reference Pressure, and Thermobaricity. *Journal of Physical Oceanography*, *33*(12), 2504–2526. https://doi.org/10.1175/1520-0485(2003)033<2504:NASWTH>2.0.CO;2

Couvillion, B. R. (2017). *2017 Coastal Master Plan: Attachment C3-27: Landscape data* (Louisiana's Comprehensive Master Plan for a Sustainable Coast, pp. 1–84) [Version Final]. Coastal Protection and Restoration Authority. http://coastal.la.gov/our-plan/2017-coastal-master-plan/

Deltares. (2014). *Delft3D-FLOW: Simulation of multidimensional hydrodynamic flows and transport phenomena, including sediments* (User Manual Version 3.15.32158). Deltares. http://oss.deltares.nl/documents/183920/eeb97903-151a-49bf-a13a-54b616da47a9

Deltares. (2019). *D-Flow Flexible Mesh Suite: User Manual* (p. 412) [Version 1.5.0]. Deltares.

Dickhudt, P. K., Sherwood, C. R., Montgomery, E. T., & Martini, M. A. (2010). *Oceanographic Measurements—Chandeleur Islands, Louisiana, after Deepwater Horizon oil spill*. https://stellwagen.er.usgs.gov/GOMEX_CI.html

Egbert, G. D., & Erofeeva, S. Y. (2002). Efficient inverse modeling of barotropic ocean tides. *American Meteorological Society*, *19*, 183–204.

Georgiou, I. (2002). *Three-dimensional hydrodynamic modeling of saltwater intrusion and circulation in Lake Pontchartrain* [PhD Dissertation]. University of New Orleans.

Georgiou, I., Yocum, T., & Brown, M. (2019). *Measurements of lateral flow from the Mississippi River at Mardi Gras Pass and flow distribution within the Bohemia Spillway using synoptic ADCP* (p. 29). Coastal and Environmental Hydrodynamics Laboratory, Pontchartrain Institute for Environmental Sciences, University of New Orleans.

Gill, A. E. (1982). *Atmosphere—Ocean Dynamics* (Vol. 30, pp. 1–662). Elsevier. https://doi.org/10.1016/S0074-6142(08)X6002-4

Haralampides, K. (2000). *A study of the hydrodynamics and salinity regimes of the Lake Pontchartrain system*. University of New Orleans.

Holthuijsen, L. H., Booij, N., & Ris, R. C. (1994). *A Spectral Wave Model for the Coastal Zone*. 630–641. https://cedb.asce.org/CEDBsearch/record.jsp?dockey=0087343

International Water Management Institute. (n.d.). *World Water and Climate Atlas*. Retrieved April 13, 2022, from https://cmr.earthdata.nasa.gov/search/concepts/C1214173181-SCIOPS

Lane, A. M. (1989). *The heat balance of the North Sea*. https://www.semanticscholar.org/paper/The-heat-balance-of-the-North-Sea-Lane/e5a369c561e60a2d0578acd0f85d1845e7efadd3

Li, C., Chen, C., Guadagnoli, D., & Georgiou, I. Y. (2008). Geometry-induced residual eddies in estuaries with curved channels: Observations and modeling studies. *Journal of Geophysical Research, 113*(C1), C01005. https://doi.org/10.1029/2006JC004031

McCorquodale, J. A., Roblin, R. J., Georgiou, I. Y., & Haralampides, K. A. (2009). Salinity, Nutrient, and Sediment Dynamics in the Pontchartrain Estuary. *Journal of Coastal Research*, *10054*, 71–87. https://doi.org/10.2112/SI54-000.1

Meselhe, E. A., Baustian, M. M., & Allison, M. A. (2015). *Basin wide model development for the Louisiana Coastal Area Mississippi River hydrodynamic and delta management study* (Task Order 27, p. 253 + app.). The Water Institute of the Gulf. Prepared for and funded by the Coastal Protection and Restoration Authority.

Meselhe, E. A., Costanza, K., Jung, H., Ainsworth, C., Simpson, E., Chagaris, D., Addis, D., Rodrigue, M. D., & Smits, J. (2017). *Models Performance Assessment Metrics for the LCA Mississippi River Hydrodynamic and Delta Management Study (TO5)* (p. 48). The Water Institute of the Gulf. Funded by the Coastal Protection and Restoration Authority under Task Order 05.

Meselhe, E. A., & Rodrigue, M. D. (2013). *Models performance assessment metrics and uncertainty analysis* (Louisiana Coastal Area Program Mississippi River Hydrodynamics and Delta Management Study, p. 27). Louisiana Coastal Area Program.

Moriasi, D. N., Arnold, J. G., Van Liew, M. W., Bingner, R. L., Harmel, R. D., & Veith, T. L. (2007). Model evaluation guidelines for systematic quantification of accuracy in watershed simulations. *Trans. ASABE*, *50*(3), 885–900.

National Ocean Partnership Program. (n.d.). *National Ocean Partnership Program*. National Ocean Partnership Program - U.S. Global Ocean Data Assimilation Experiment. “Hybrid Coordinate Ocean Model Global Ocean Forecasting System.” Https://Www.Hycom.Org/Dataserver/Gofs-3pt1/Analysis. Retrieved January 15, 2020, from https://www.hycom.org/dataserver/gofs-3pt1/analysis

Niklitschek, E. J., & Secor, D. H. (2009). Dissolved oxygen, temperature and salinity effects on the ecophysiology and survival of juvenile Atlantic sturgeon in estuarine waters: II. Model development and testing. *Journal of Experimental Marine Biology and Ecology*, *381*, S161–S172. https://doi.org/10.1016/j.jembe.2009.07.019

NOAA. (n.d.). *Sea Level Trends—NOAA Tides & Currents*. Retrieved April 13, 2022, from https://tidesandcurrents.noaa.gov/sltrends/sltrends_station.shtml?id=8761724

NOAA Fisheries. (2022a). *Gulf Sturgeon Critical Habitat Map and GIS Data*. https://www.fisheries.noaa.gov/resource/map/gulf-sturgeon-critical-habitat-map-and-gis-data

NOAA Fisheries. (2022b, November 10). *Critical Habitat | NOAA Fisheries* (National). NOAA. https://www.fisheries.noaa.gov/national/endangered-species-conservation/critical-habitat

Ris, R. C., Holthuijsen, L. H., & Booij, N. (1999). A third-generation wave model for coastal regions: 2. Verification. *Journal of Geophysical Research: Oceans*, *104*(C4), 7667–7681. https://doi.org/10.1029/1998JC900123

Schindler, J. (2010). *Estuarine Dynamics as a Function of Barrier Island Transgression and Wetland Loss: Understanding the Transport and Exchange Processes* [University of New Orleans]. https://scholarworks.uno.edu/td/1260/

Sherwood, C. R. (2010). *DRAFT - Measurements of Waves, Storm Surge, and Currents off the Chandeleur Islands*.

Smith, S. D., & Banke, E. G. (1975). Variation of the sea surface drag coefficient with wind speed. *Quarterly Journal of the Royal Meteorological Society*, *101*(429), 665–673. https://doi.org/10.1002/qj.49710142920

Soulsby, R. (1997). *Dynamics of marine sands: A manual for practical applications*. Thomas Telford.

Sulak, K. J., Parauka, F., Slack, W. T., Ruth, R. T., Randall, M. T., Luke, K., Mettee, M. F., & Price, M. E. (2016). Status of scientific knowledge, recovery progress, and future research directions for the Gulf Sturgeon, *Acipenser oxyrinchus desotoi* Vladykov, 1955. *Journal of Applied Ichthyology*, *32*(S1), 87–161. https://doi.org/10.1111/jai.13245

Thomann, R. V., & Mueller, J. A. (1987). *Principles of Surface Water Quality Modeling and Control*. Harper & Row.

USEPA. (2015, November 4). *Dissolved Oxygen* [Data and Tools]. https://www.epa.gov/caddis-vol2/dissolved-oxygen

USFWS. (1973). *Endangered Species Act of 1973, As Amended through the 108th Congress* (p. 44). U.S. Fish and Wildlife Service.

USGS. (2018). *Coastal National Elevation Database (CoNED) Applications Project*. https://www.usgs.gov/special-topics/coastal-national-elevation-database-applications-project

Wilcock, P. R. (2001). Toward a practical method for estimating sediment-transport rates in gravel-bed rivers. *Earth Surface Processes and Landforms*, *26*(13), 1395–1408. https://doi.org/10.1002/esp.301

Willmott, C. J., Robeson, S. M., & Matsuura, K. (2012). A refined index of model performance. *International Journal of Climatology*, *32*(13), 2088–2094. https://doi.org/10.1002/joc.2419

APPENDICES

APPENDIX A. WATER LEVEL CALIBRATION

Figure A-1 through Figure A-29 show the comparison between daily averaged water level predicted by the Hydrodynamic Model and observations at all CRMS, USGS, and NOAA stations used for calibration. The location of all stations is displayed in Figure 10. The USGS stations for which figures are not provided either did not have water level observations available or the gauge datum correction was not available on the public website.

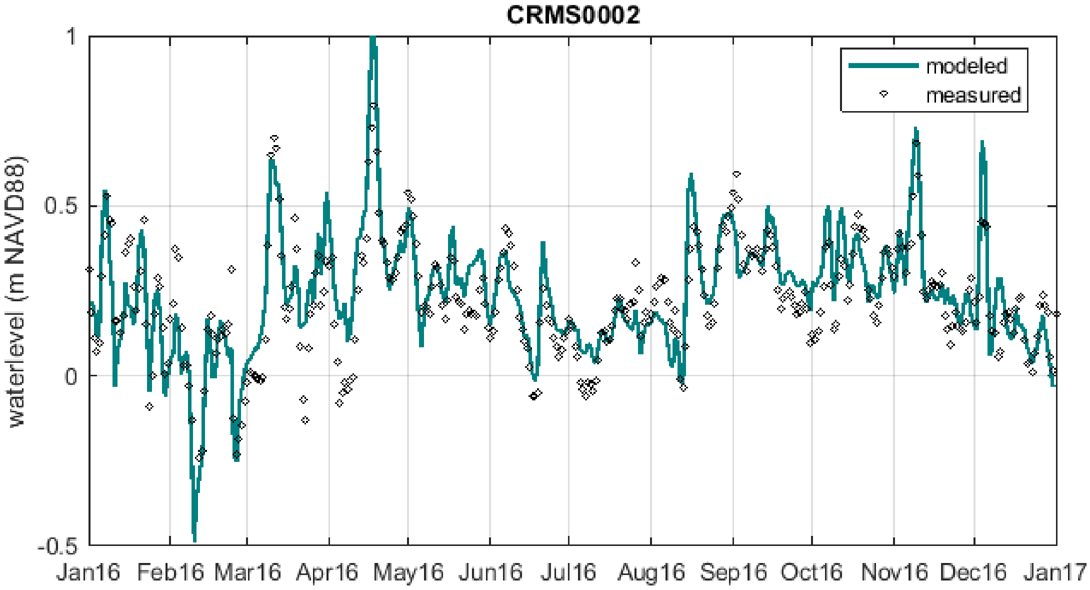

Figure A-1. Simulated daily averaged water levels by the Hydrodynamic Model (green line) compared to observations at CRMS0002 (black dots). The station location is displayed in Figure 10.

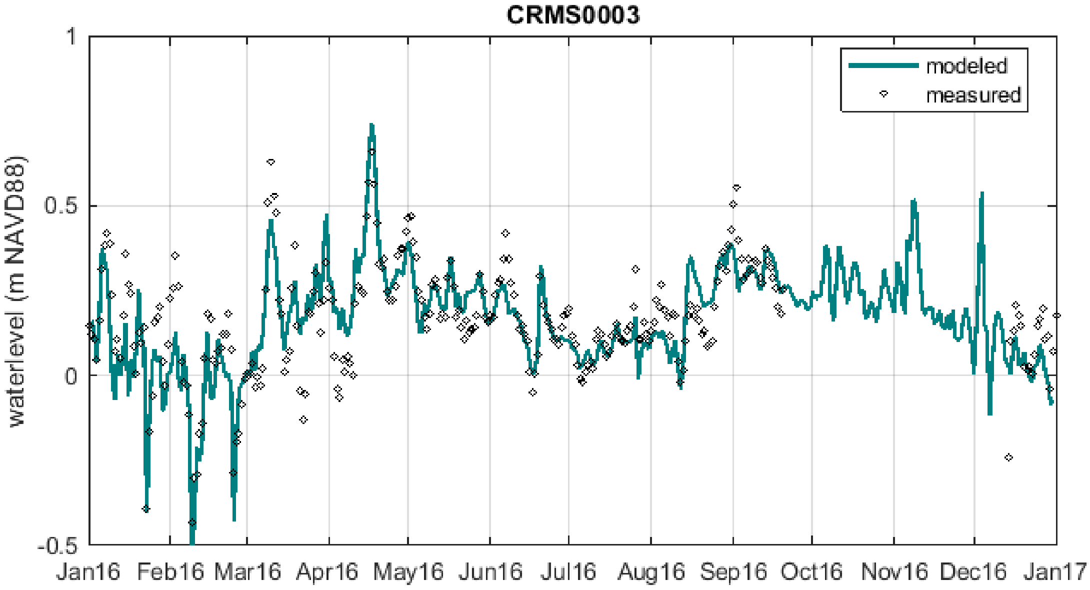

Figure A-2. Simulated daily averaged water levels by the Hydrodynamic Model (green line) compared to observations at CRMS0003 (black dots). The station location is displayed in Figure 10.

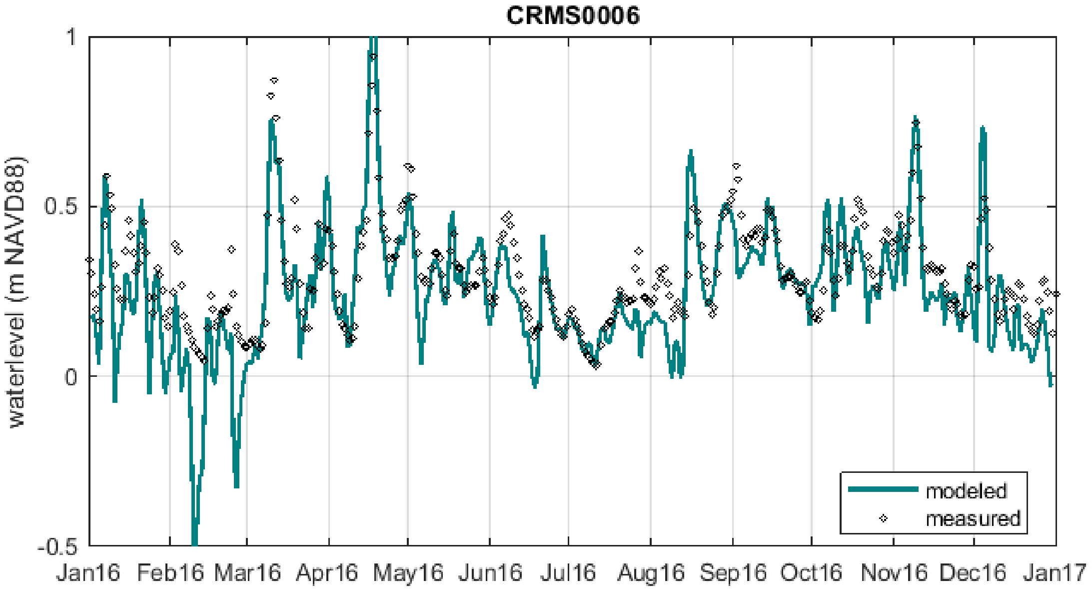

Figure A-3. Simulated daily averaged water levels by the Hydrodynamic Model (green line) compared to observations at CRMS0006 (black dots). The station location is displayed in Figure 10.

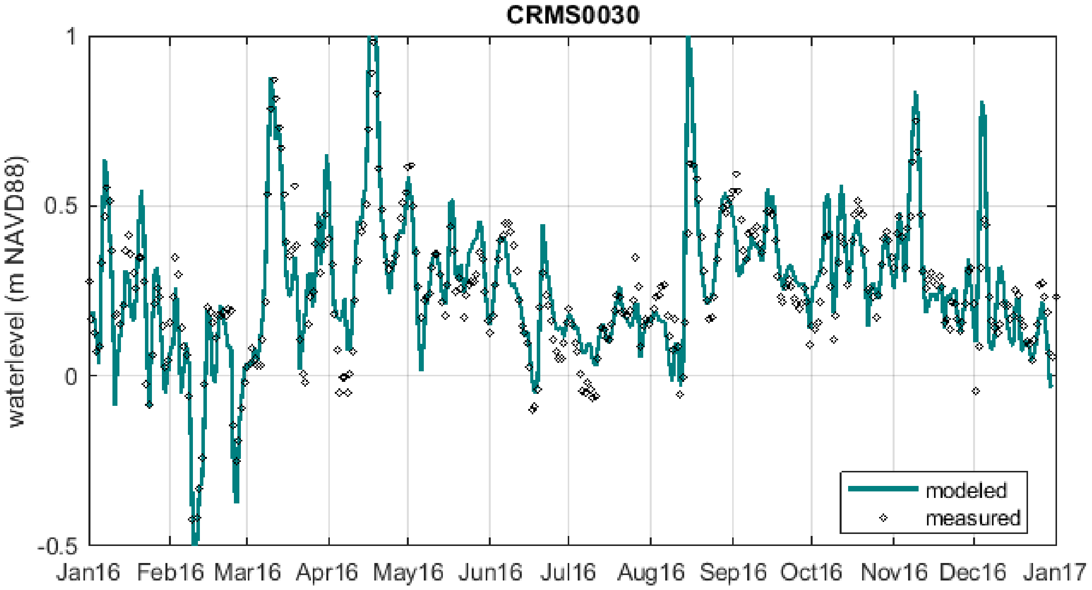

Figure A-4. Simulated daily averaged water levels by the Hydrodynamic Model (green line) compared to observations at CRMS0030 (black dots). The station location is displayed in Figure 10.

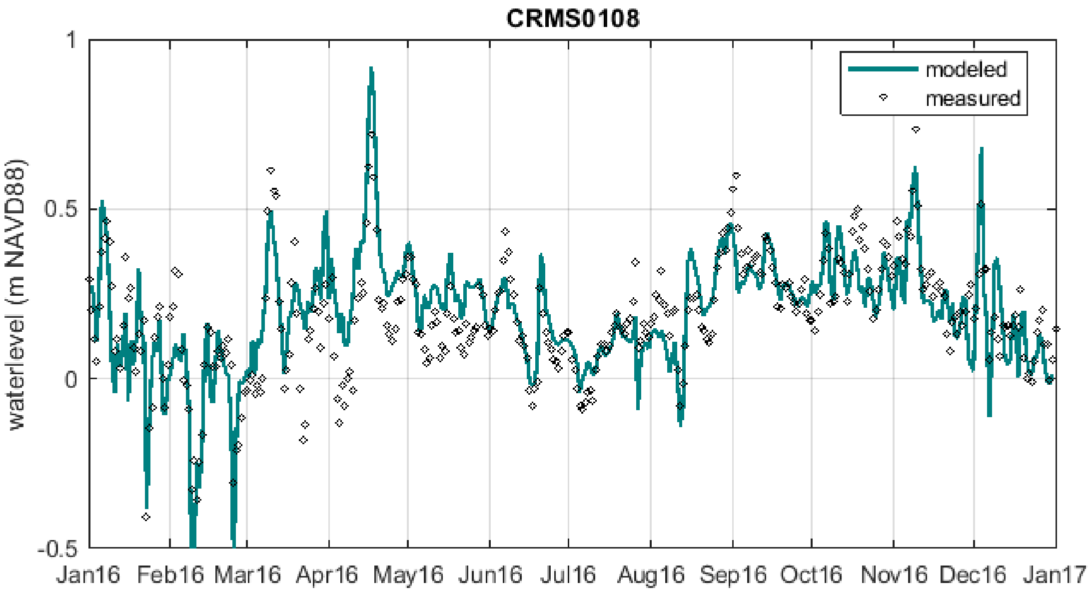

Figure A-5. Simulated daily averaged water levels by the Hydrodynamic Model (green line) compared to observations at CRMS0108 (black dots). The station location is displayed in Figure 10.

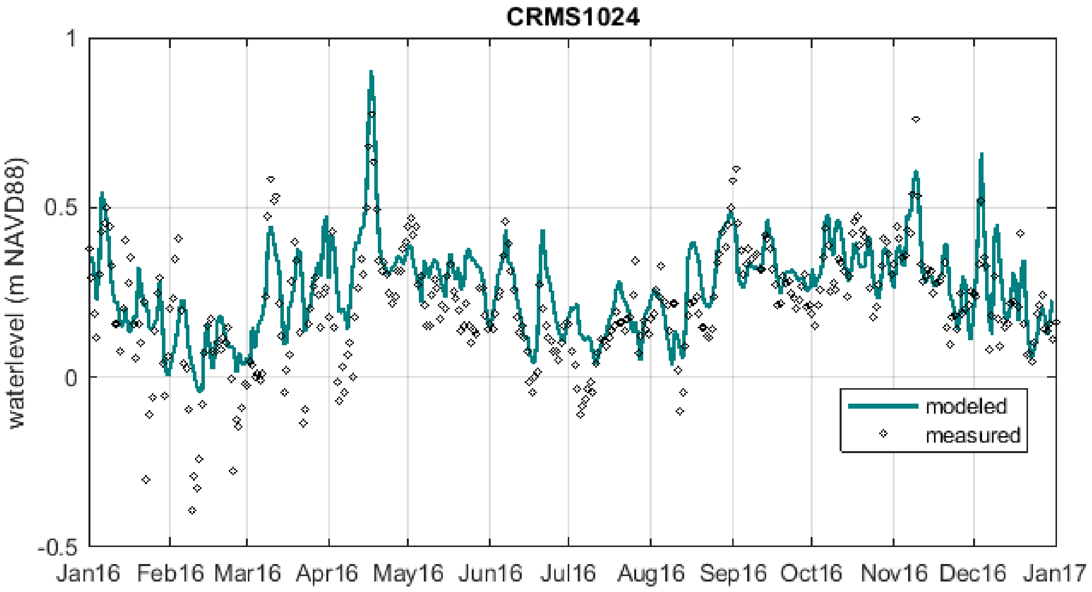

Figure A-6. Simulated daily averaged water levels by the Hydrodynamic Model (green line) compared to observations at CRMS1024 (black dots). The station location is displayed in Figure 10.

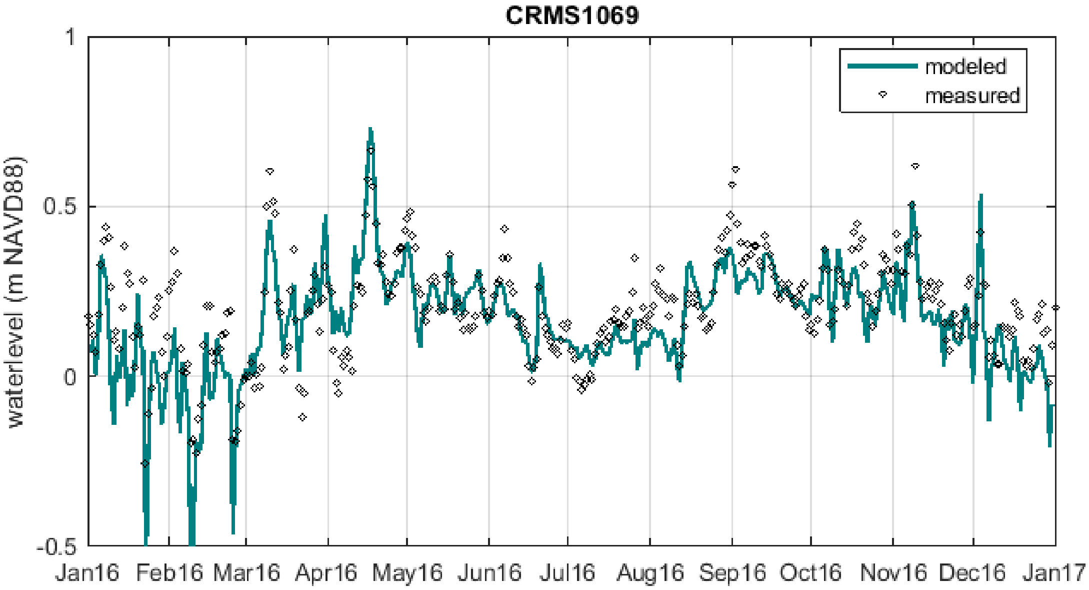

Figure A-7. Simulated daily averaged water levels by the Hydrodynamic Model (green line) compared to observations at CRMS1069 (black dots). The station location is displayed in Figure 10.

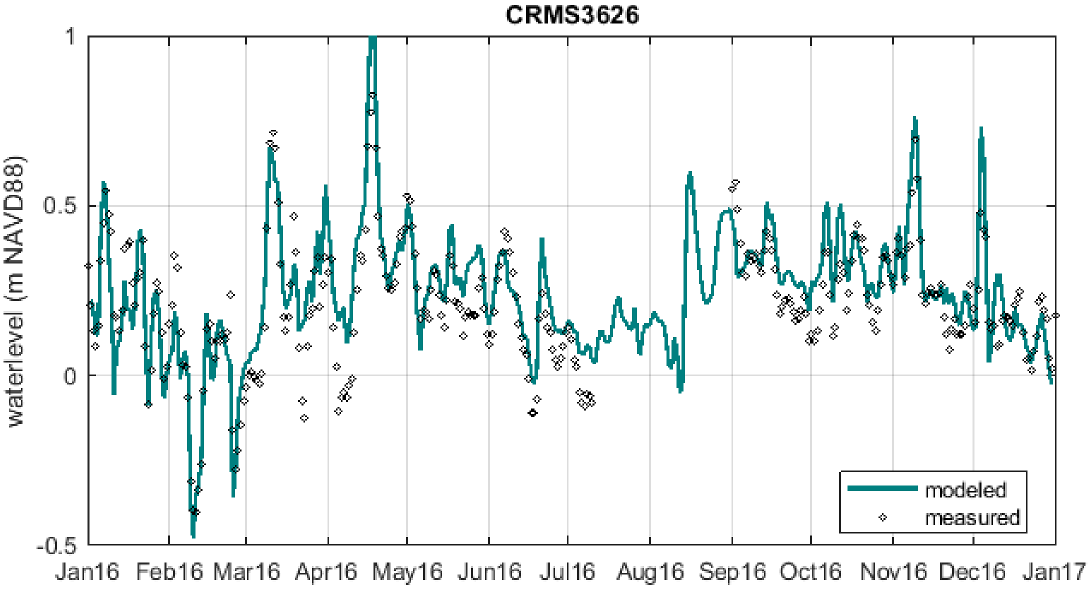

Figure A-8. Simulated daily averaged water levels by the Hydrodynamic Model (green line) compared to observations at CRMS3626 (black dots). The station location is displayed in Figure 10.

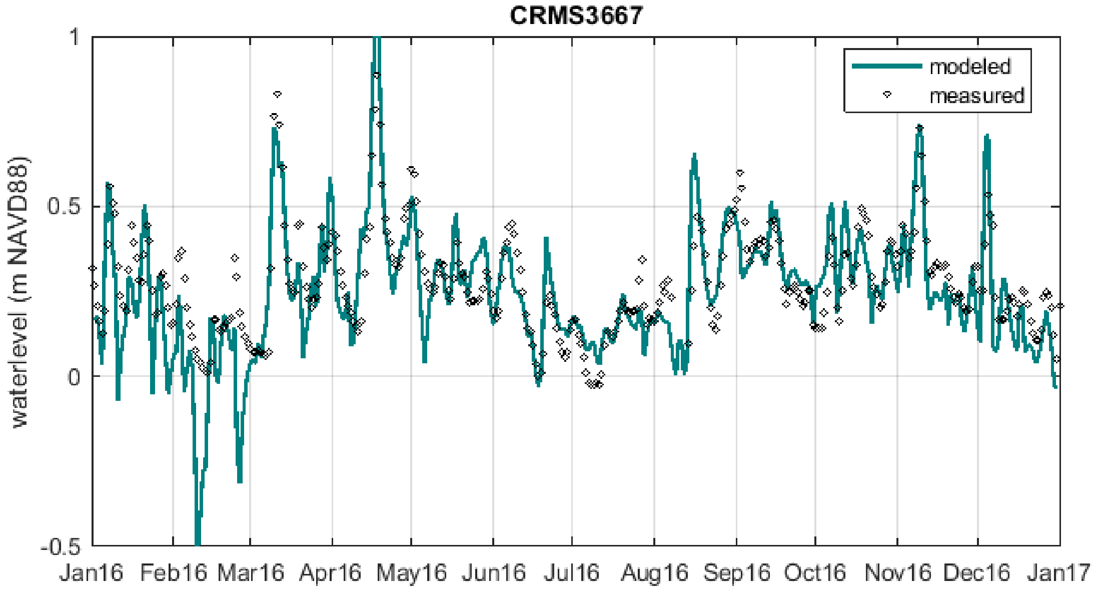

Figure A-9. Simulated daily averaged water levels by the Hydrodynamic Model (green line) compared to observations at CRMS3667 (black dots). The station location is displayed in Figure 10.

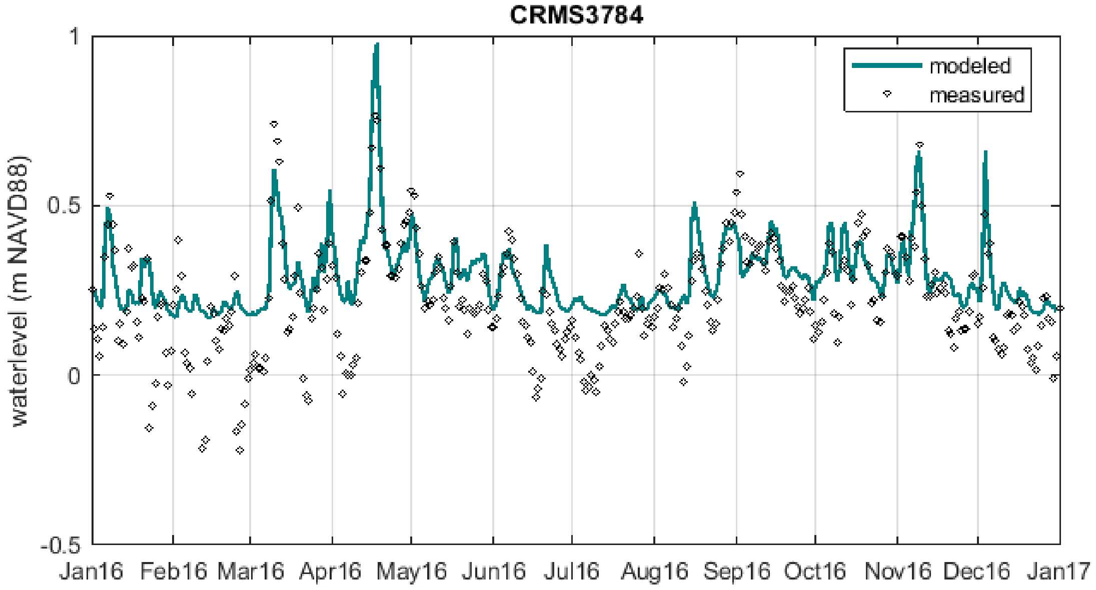

Figure A-10. Simulated daily averaged water levels by the Hydrodynamic Model (green line) compared to observations at CRMS3784 (black dots). The station location is displayed in Figure 10.

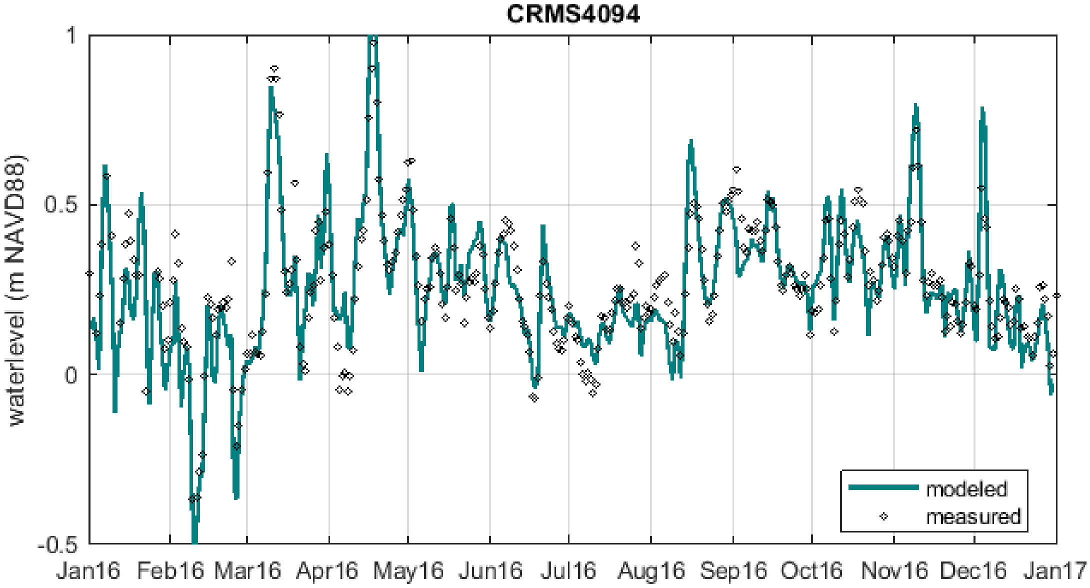

Figure A-11. Simulated daily averaged water levels by the Hydrodynamic Model (green line) compared to observations at CRMS4094 (black dots). The station location is displayed in Figure 10.

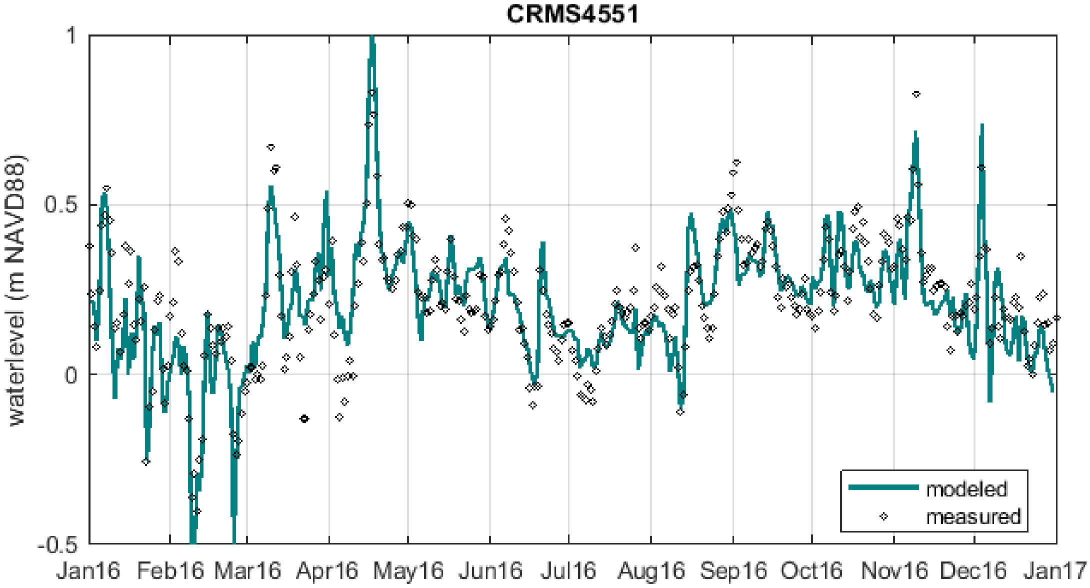

Figure A-12. Simulated daily averaged water levels by the Hydrodynamic Model (green line) compared to observations at CRMS4551 (black dots). The station location is displayed in Figure 10.

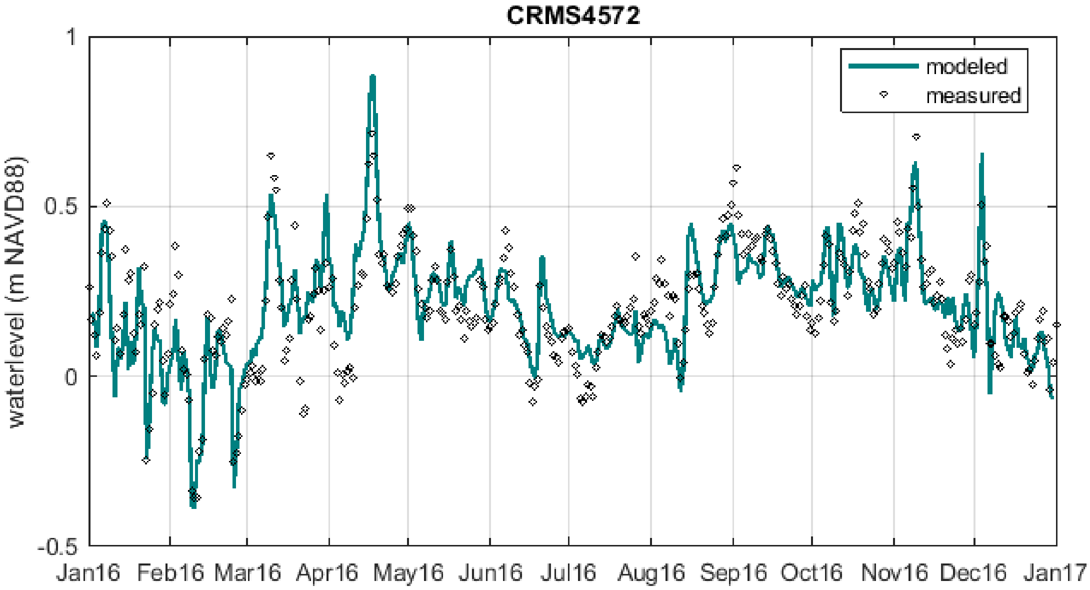

Figure A-13. Simulated daily averaged water levels by the Hydrodynamic Model (green line) compared to observations at CRMS4572 (black dots). The station location is displayed in Figure 10.

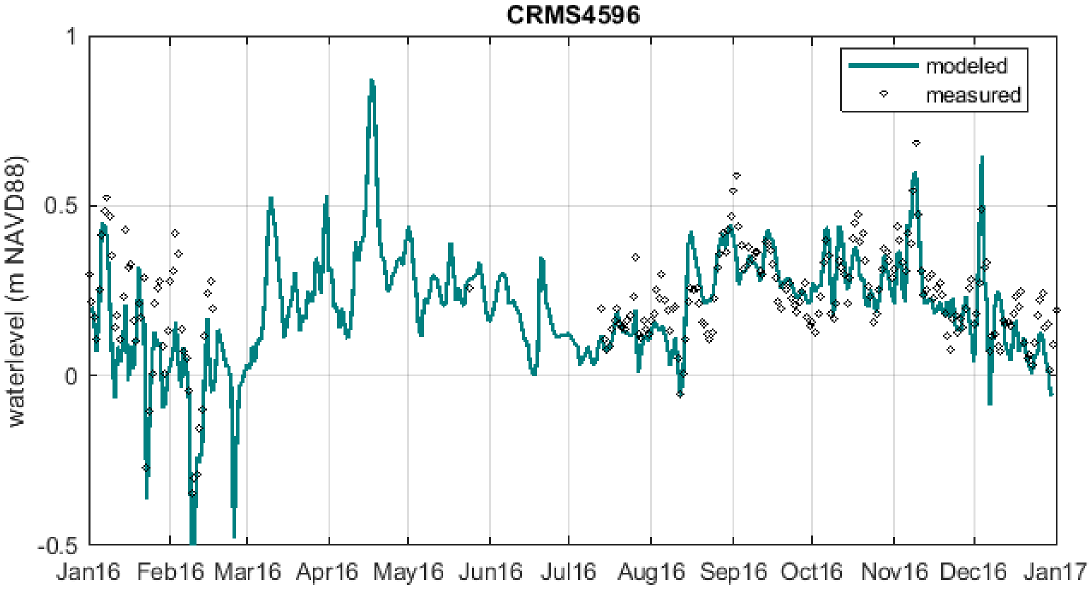

Figure A-14. Simulated daily averaged water levels by the Hydrodynamic Model (green line) compared to observations at CRMS4596 (black dots). The station location is displayed in Figure 10.

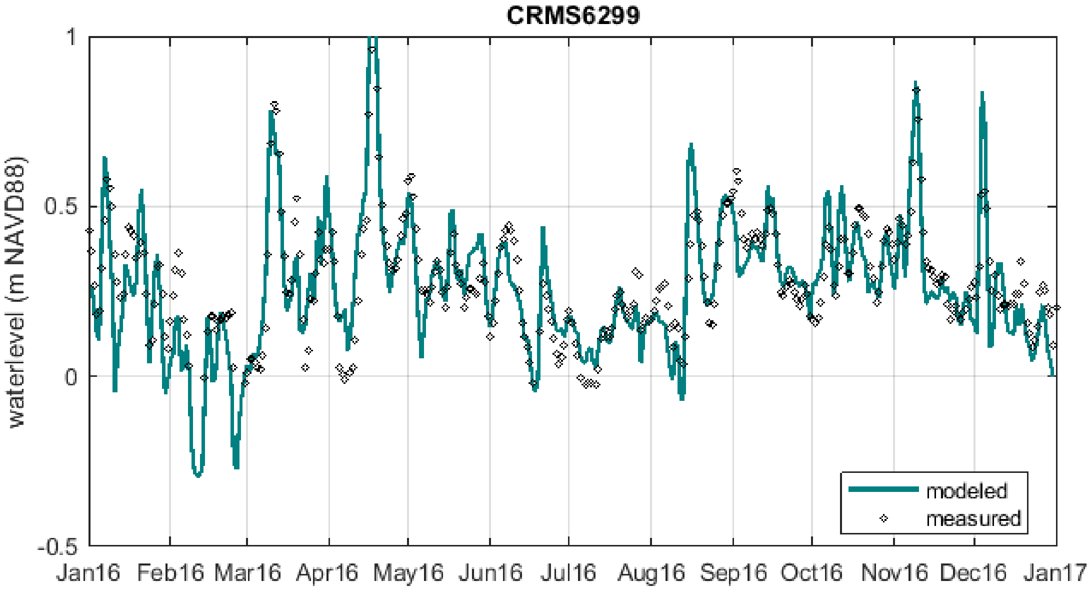

Figure A-15. Simulated daily averaged water levels by the Hydrodynamic Model (green line) compared to observations at CRMS629 (black dots). The station location is displayed in Figure 10.

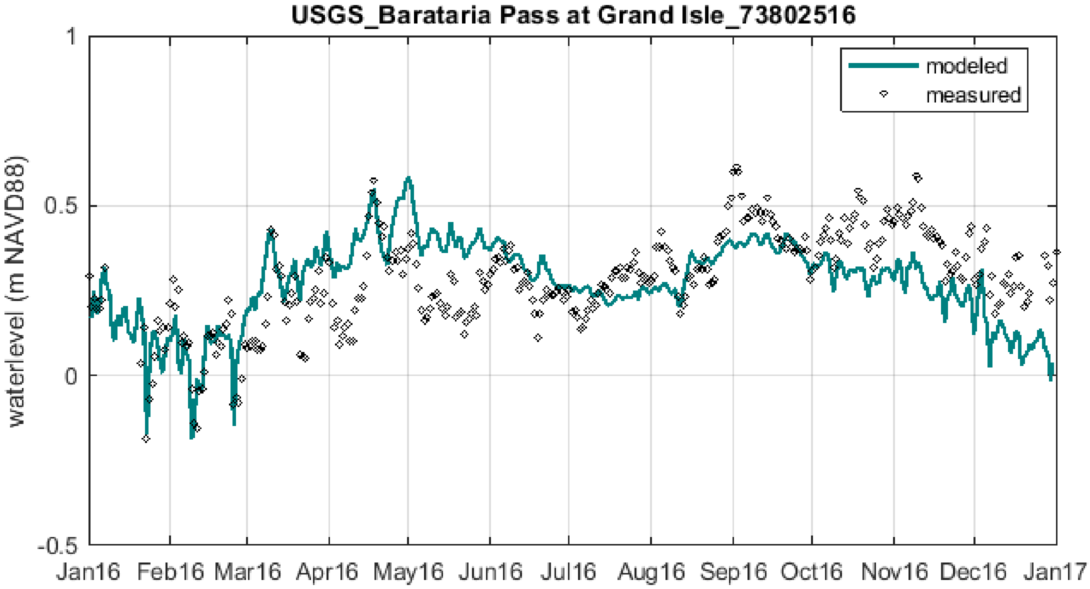

Figure A-16. Simulated daily averaged water levels by the Hydrodynamic Model (green line) compared to observations at USGS station 73802516 (black dots). The station location is displayed in Figure 10.

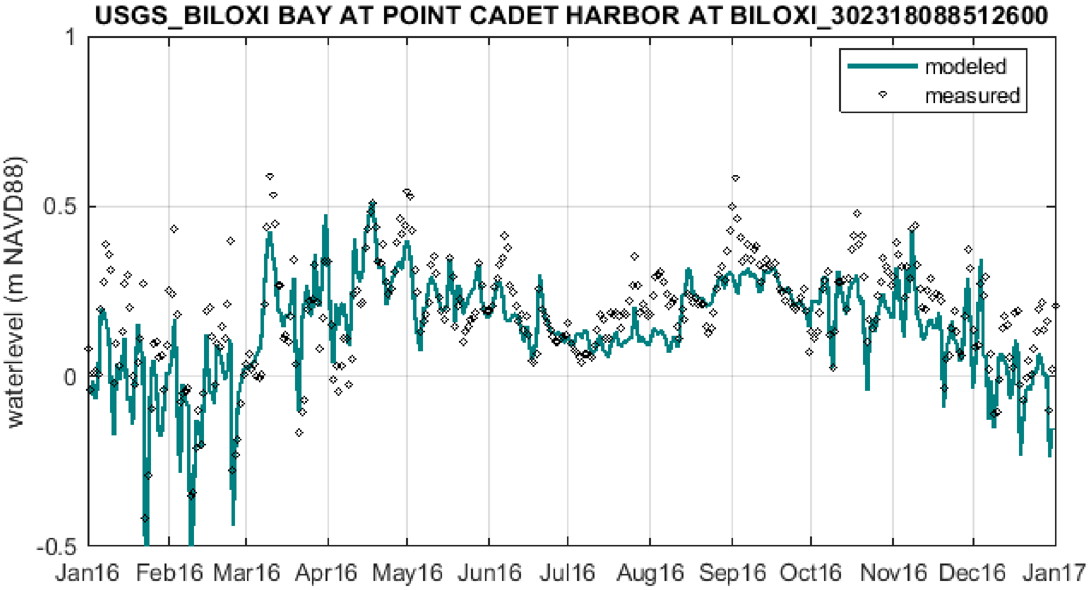

Figure A-17. Simulated daily averaged water levels by the Hydrodynamic Model (green line) compared to observations at USGS station 302318088512600 (black dots). The station location is displayed in Figure 10.

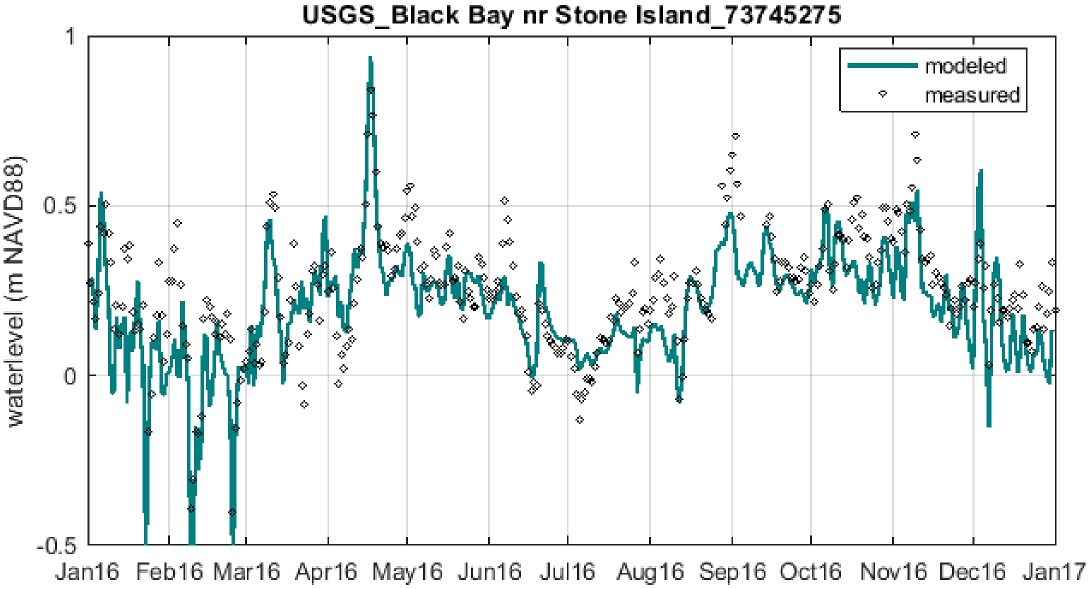

Figure A-18. Simulated daily averaged water levels by the Hydrodynamic Model (green line) compared to observations at USGS station 73745275 (black dots). The station location is displayed in Figure 10.

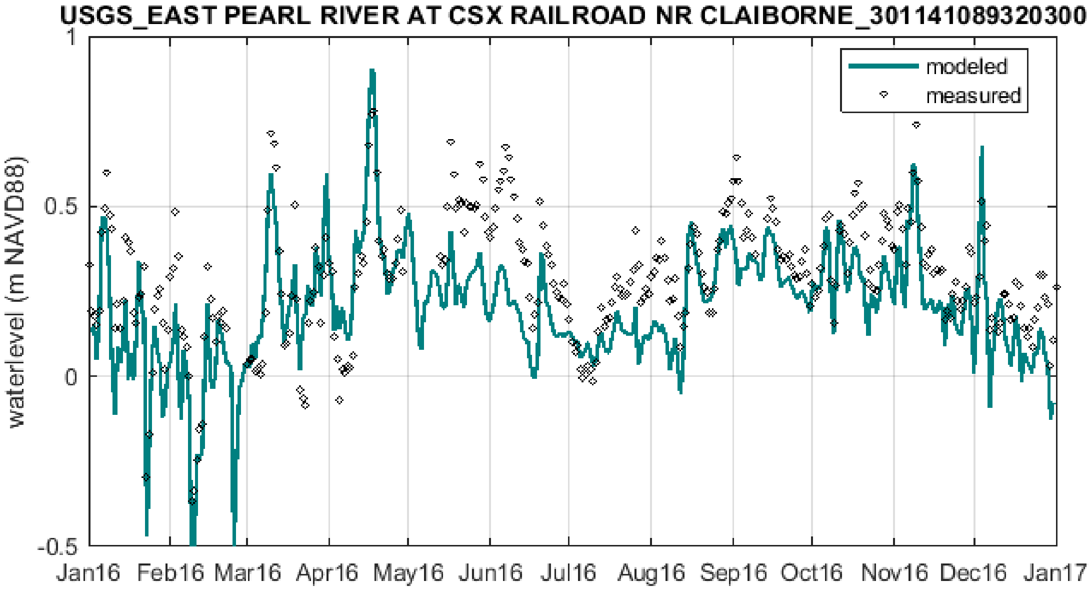

Figure A-19. Simulated daily averaged water levels by the Hydrodynamic Model (green line) compared to observations at USGS station 301141089320300 (black dots). The station location is displayed in Figure 10.

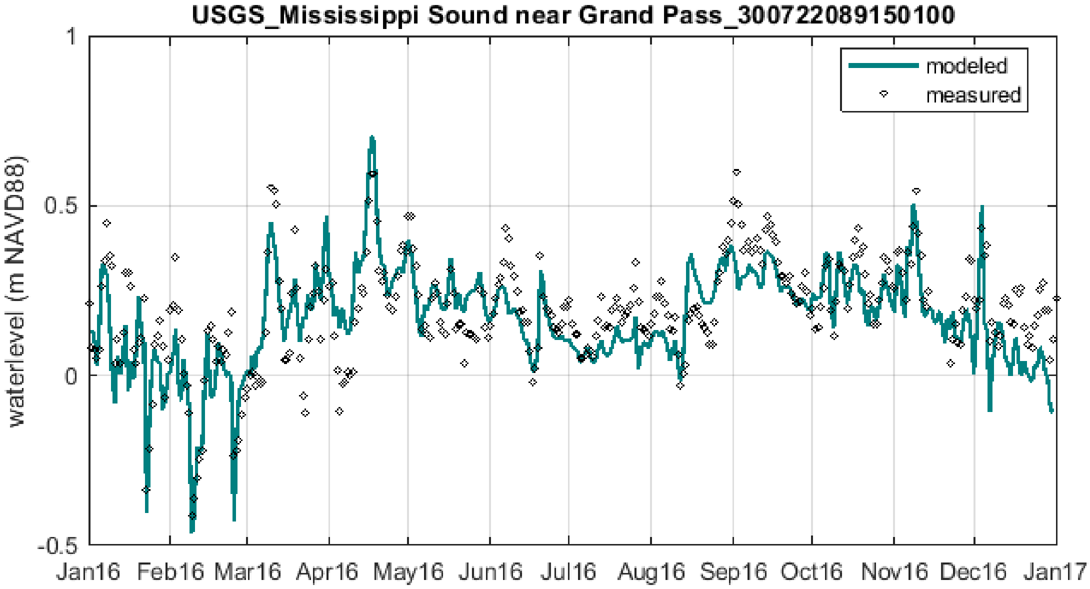

Figure A-20. Simulated daily averaged water levels by the Hydrodynamic Model (green line) compared to observations at USGS station 300722089150100 (black dots). The station location is displayed in Figure 10.

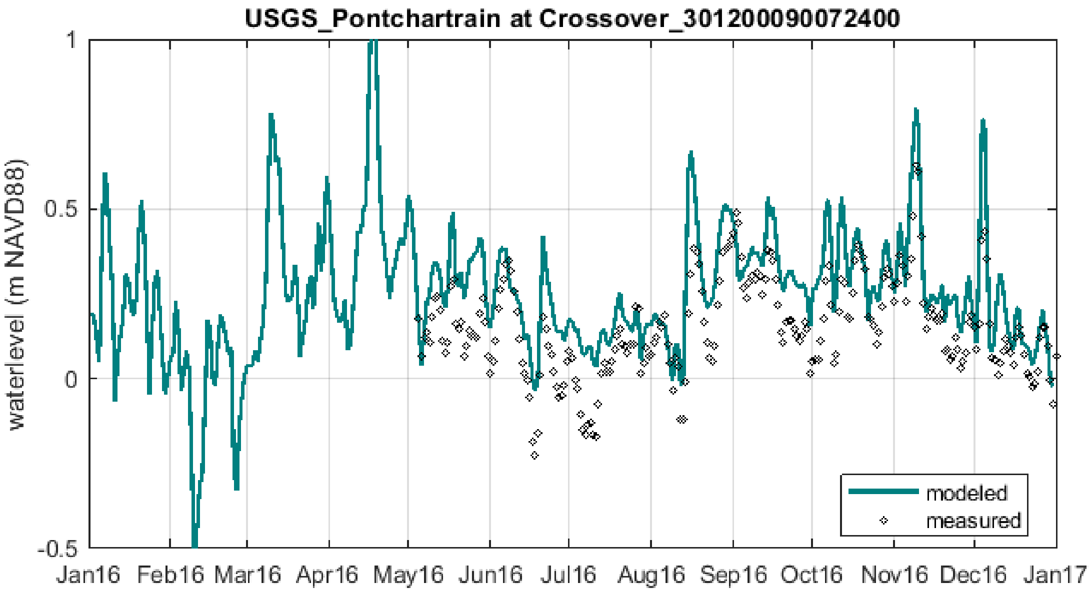

Figure A-21. Simulated daily averaged water levels by the Hydrodynamic Model (green line) compared to observations at USGS station 301200090072400 (black dots). The station location is displayed in Figure 10.

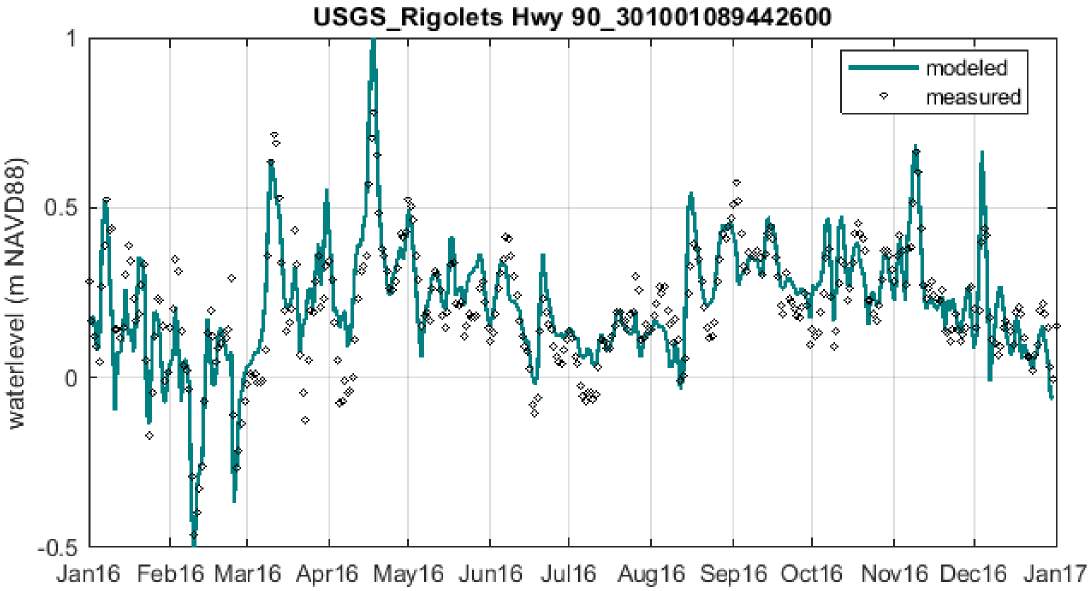

Figure A-22. Simulated daily averaged water levels by the Hydrodynamic Model (green line) compared to observations at USGS station 301001089442600 (black dots). The station location is displayed in Figure 10.

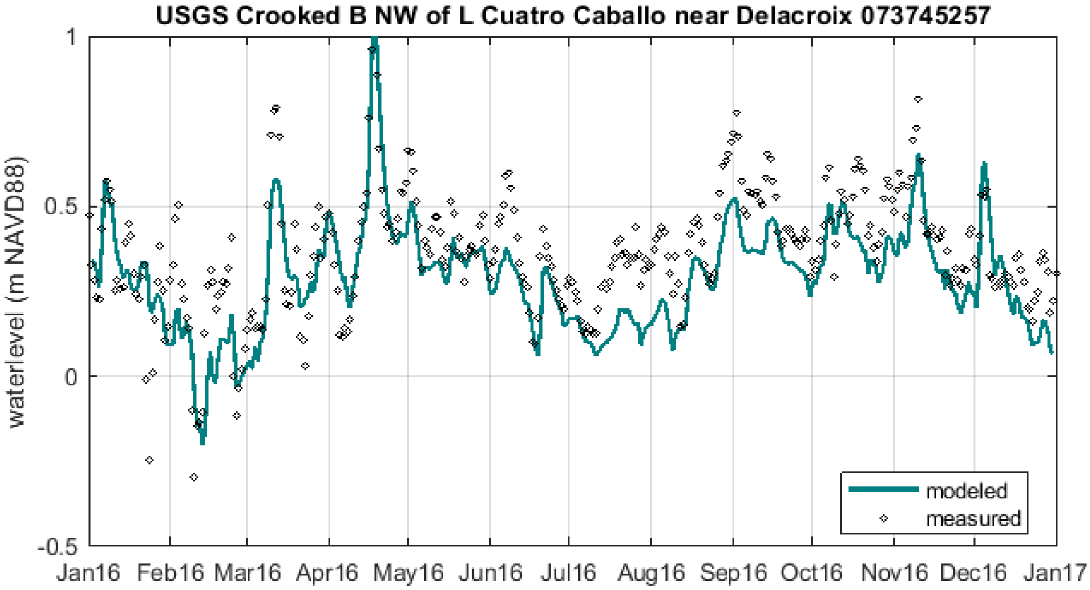

Figure A-23. Simulated daily averaged water levels by the Hydrodynamic Model (green line) compared to observations at USGS station 073745257 (black dots). The station location is displayed in Figure 10.

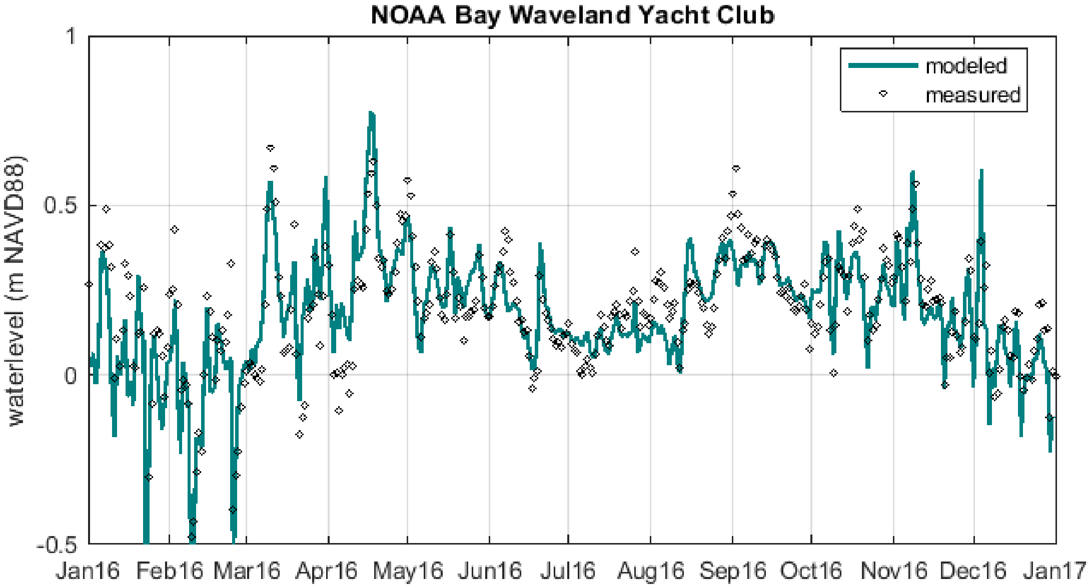

Figure A-24. Simulated daily averaged water levels by the Hydrodynamic Model (green line) compared to observations at NOAA station Bay Waveland Yacht Club (black dots). The station location is displayed in Figure 10.

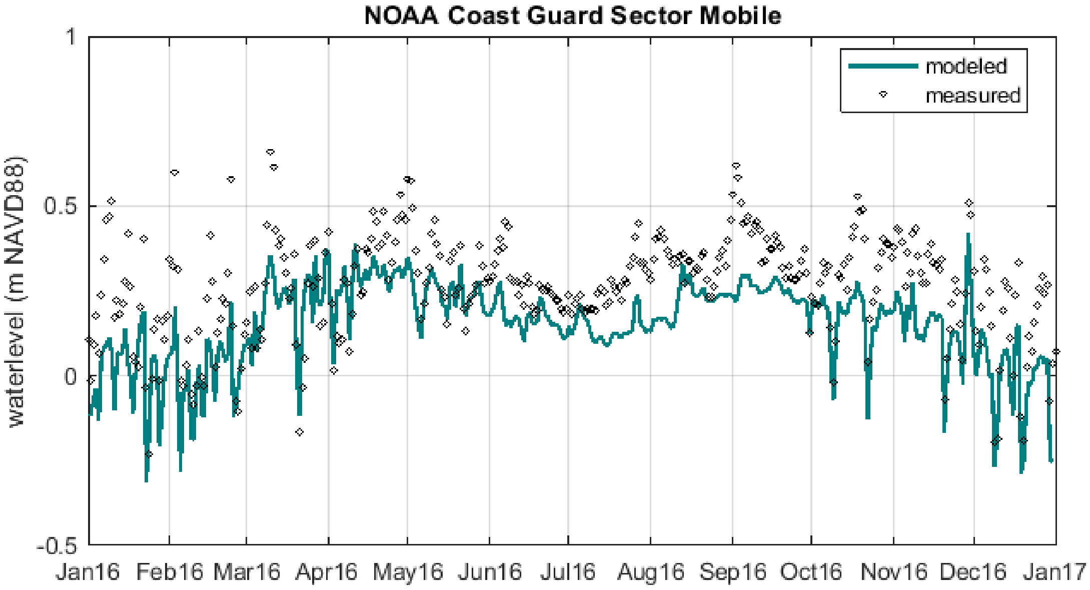

Figure A-25. Simulated daily averaged water levels by the Hydrodynamic Model (green line) compared to observations at NOAA station Coast Guard Sector Mobile (black dots). The station location is displayed in Figure 10.

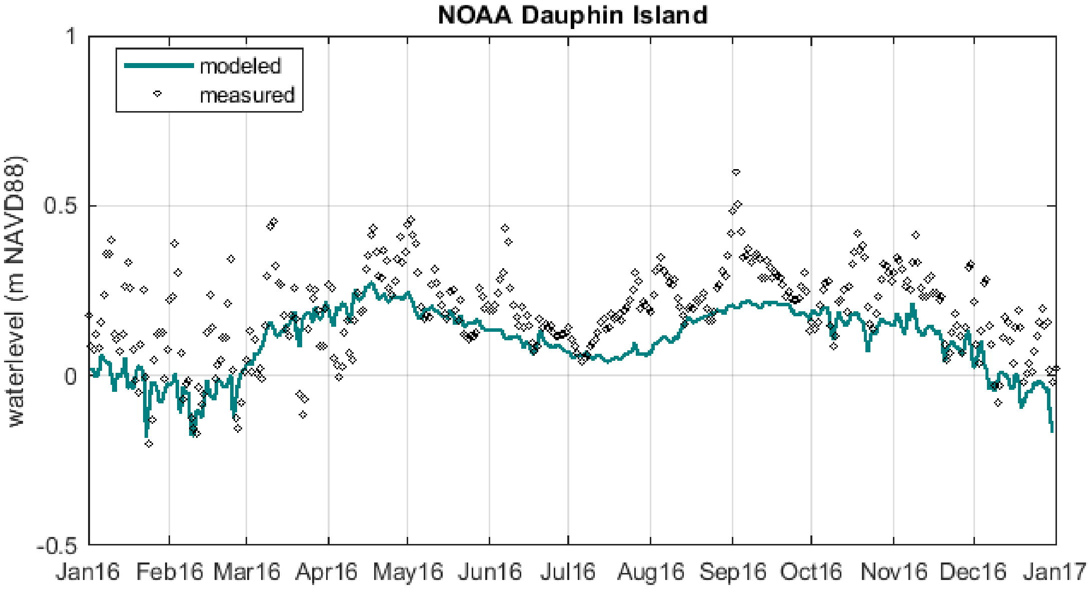

Figure A-26. Simulated daily averaged water levels by the Hydrodynamic Model (green line) compared to observations at NOAA station Dauphin Island (black dots). The station location is displayed in Figure 10.

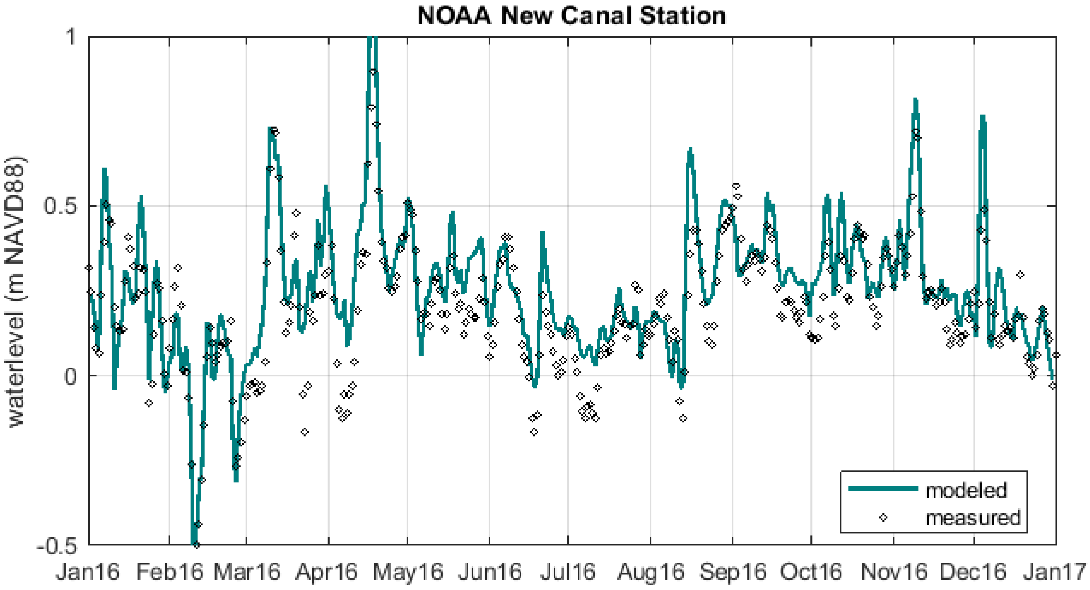

Figure A-27. Simulated daily averaged water levels by the Hydrodynamic Model (green line) compared to observations at NOAA station New Canal (black dots). The station location is displayed in Figure 10.

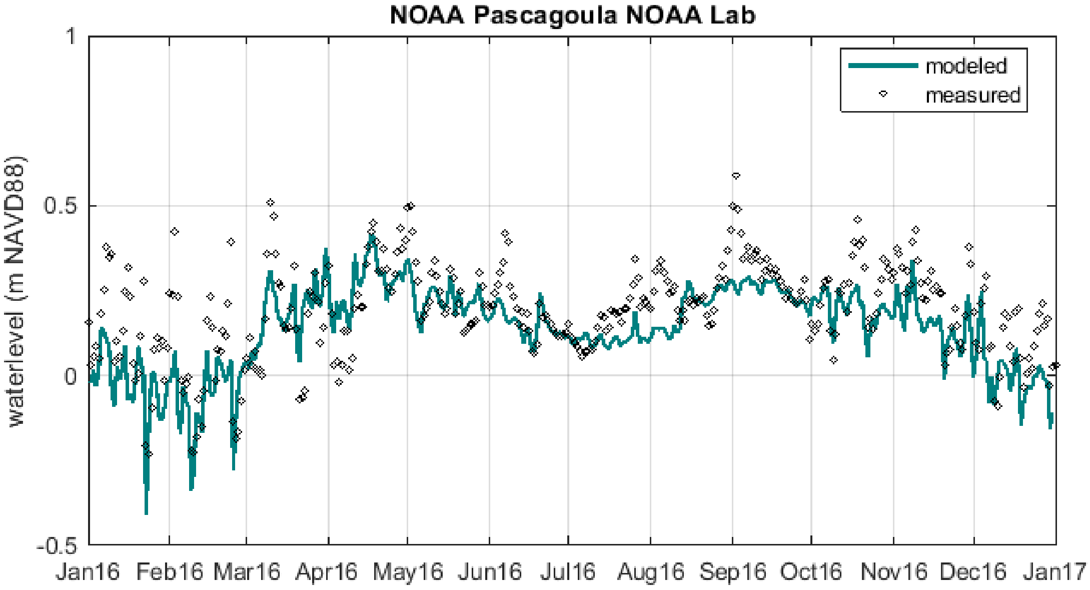

Figure A-28. Simulated daily averaged water levels by the Hydrodynamic Model (green line) compared to observations at NOAA station Pascagoula Lab (black dots). The station location is displayed in Figure 10.

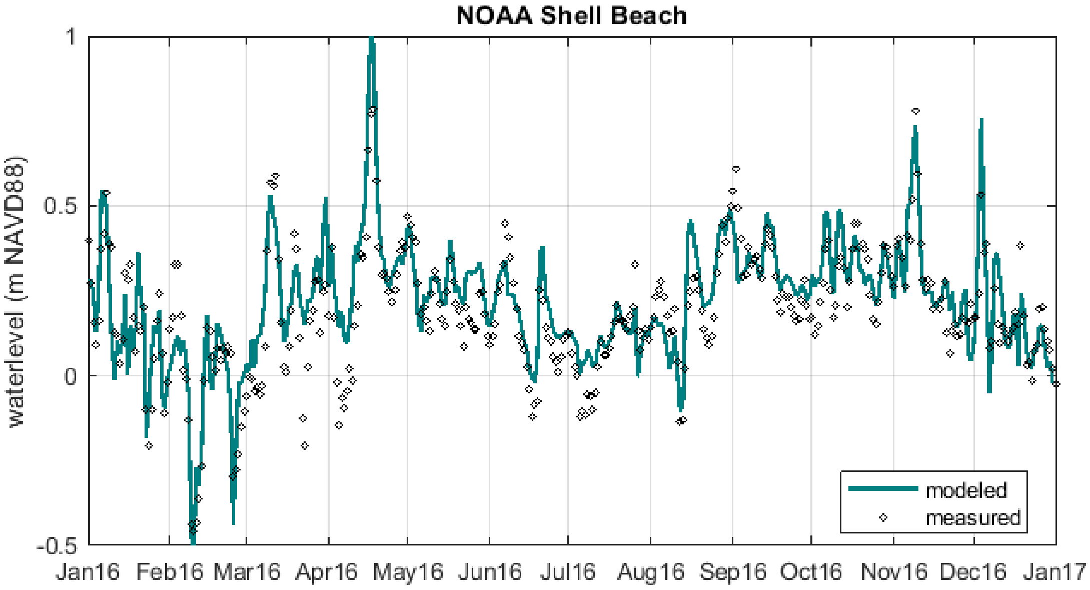

Figure A-29. Simulated daily averaged water levels by the Hydrodynamic Model (green line) compared to observations at NOAA station Shell Beach (black dots). The station location is displayed in Figure 10.

APPENDIX B. SALINITY CALIBRATION

Figure B-1 through Figure show the comparison between daily averaged salinity predicted by the Hydrodynamic Model and observations at all CRMS and USGS stations used for calibration. The location of all stations is displayed in Figure 10. USGS stations for which salinity observation were not available were not included.

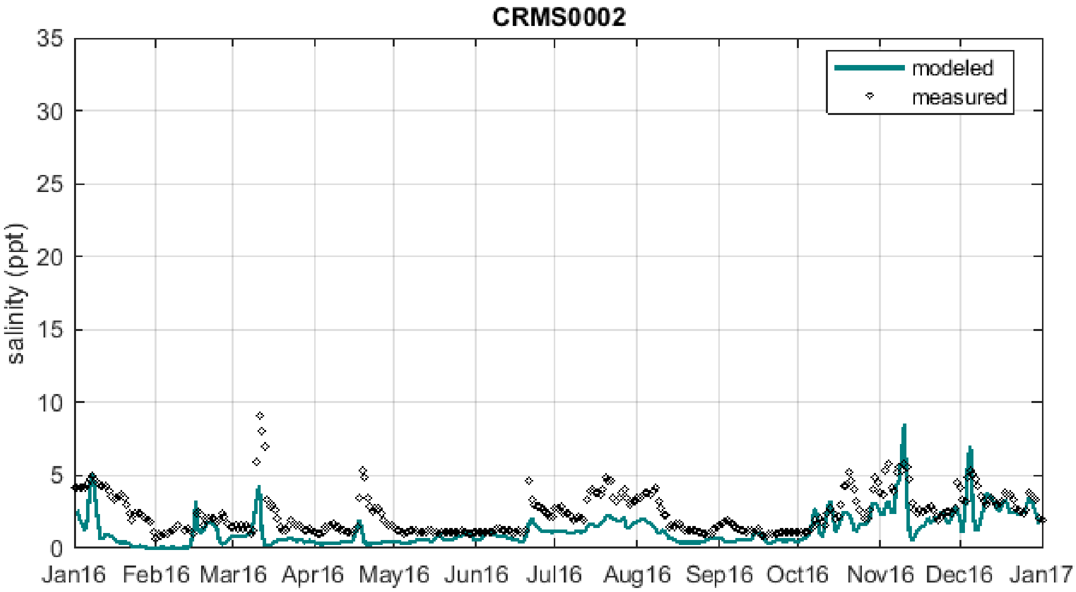

Figure B-1. Simulated daily averaged salinity by the Hydrodynamic Model (green line) compared to observations at CRMS0002 (black dots). The station location is displayed in Figure 10.

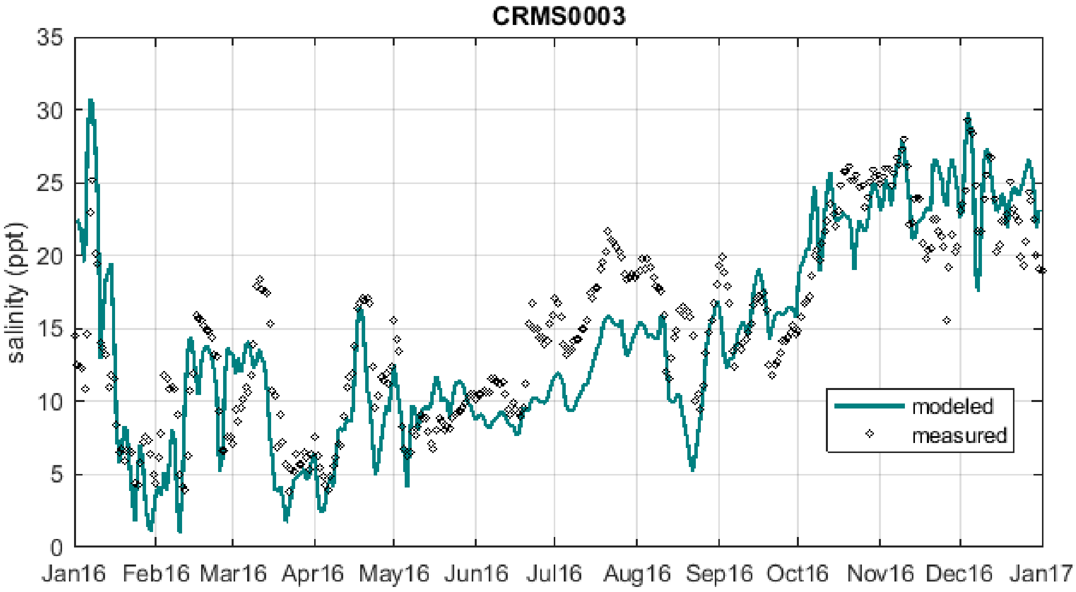

Figure B-2. Simulated daily averaged salinity by the Hydrodynamic Model (green line) compared to observations at CRMS0003 (black dots). The station location is displayed in Figure 10.

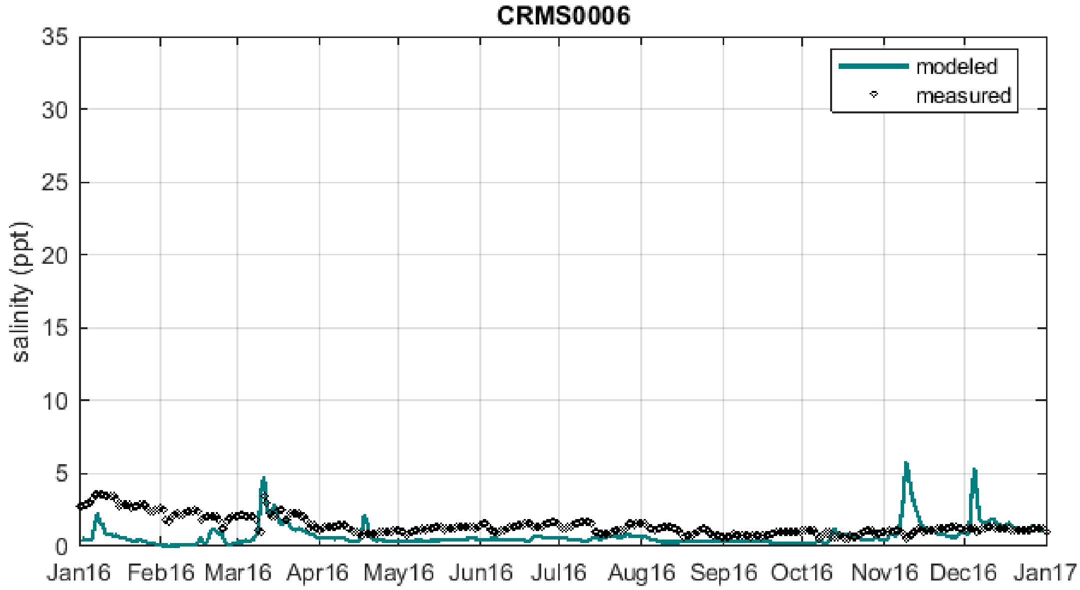

Figure B-3. Simulated daily averaged salinity by the Hydrodynamic Model (green line) compared to observations at CRMS0006 (black dots). The station location is displayed in Figure 10.

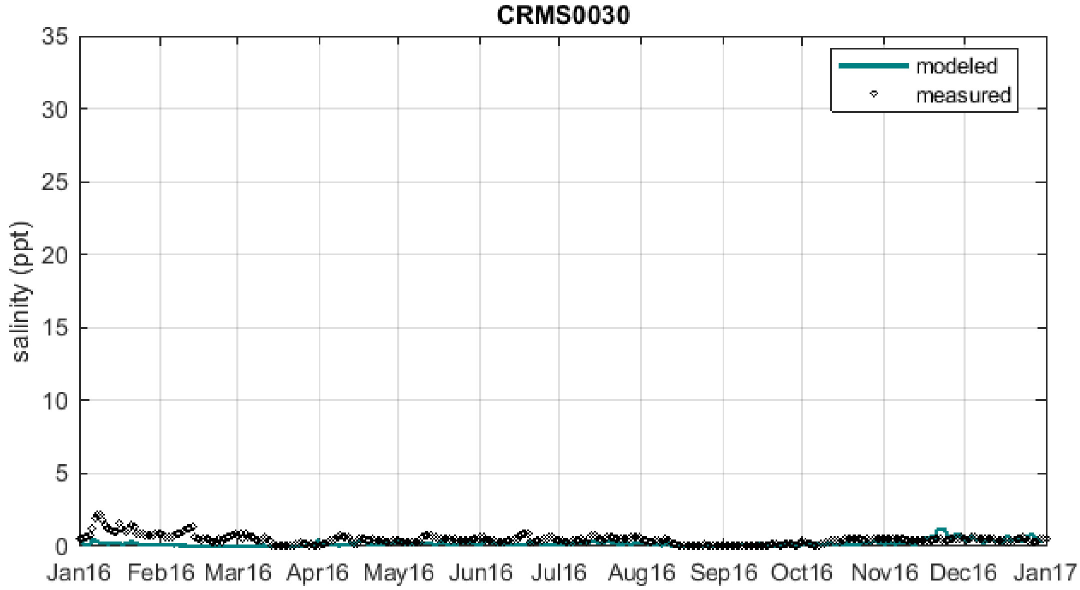

Figure B-4. Simulated daily averaged salinity by the Hydrodynamic Model (green line) compared to observations at CRMS0030 (black dots). The station location is displayed in Figure 10.

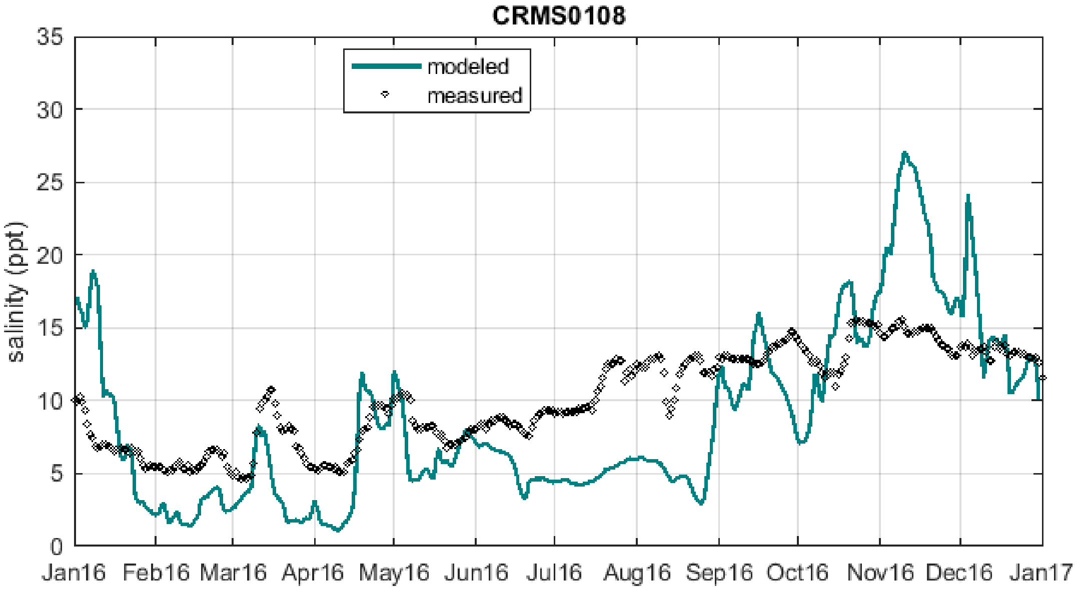

Figure B-5. Simulated daily averaged salinity by the Hydrodynamic Model (green line) compared to observations at CRMS0108 (black dots). The station location is displayed in Figure 10.

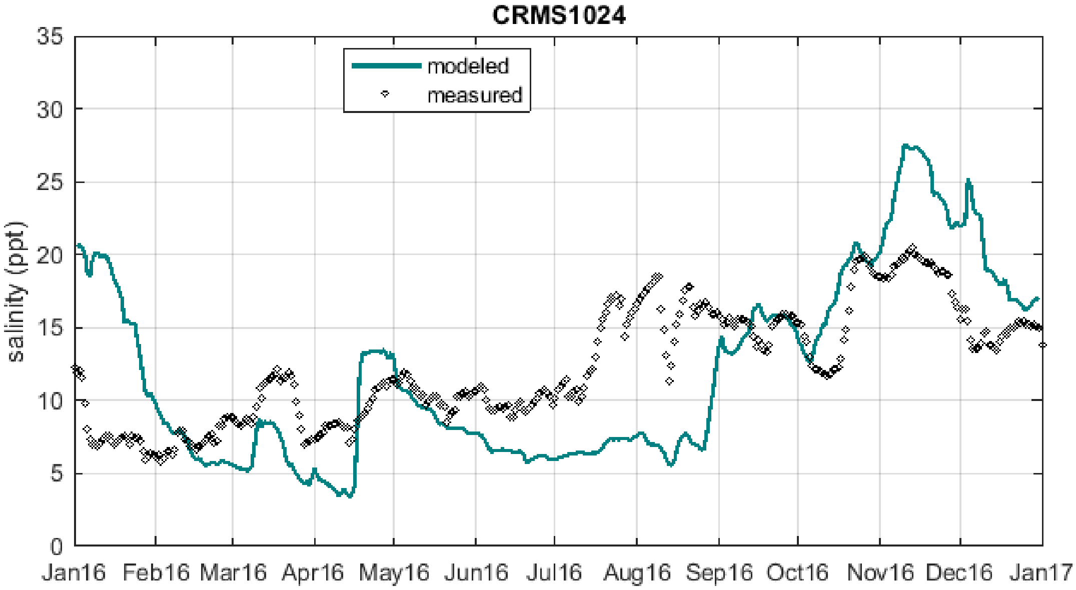

Figure B-6. Simulated daily averaged salinity by the Hydrodynamic Model (green line) compared to observations at CRMS1024 (black dots). The station location is displayed in Figure 10.

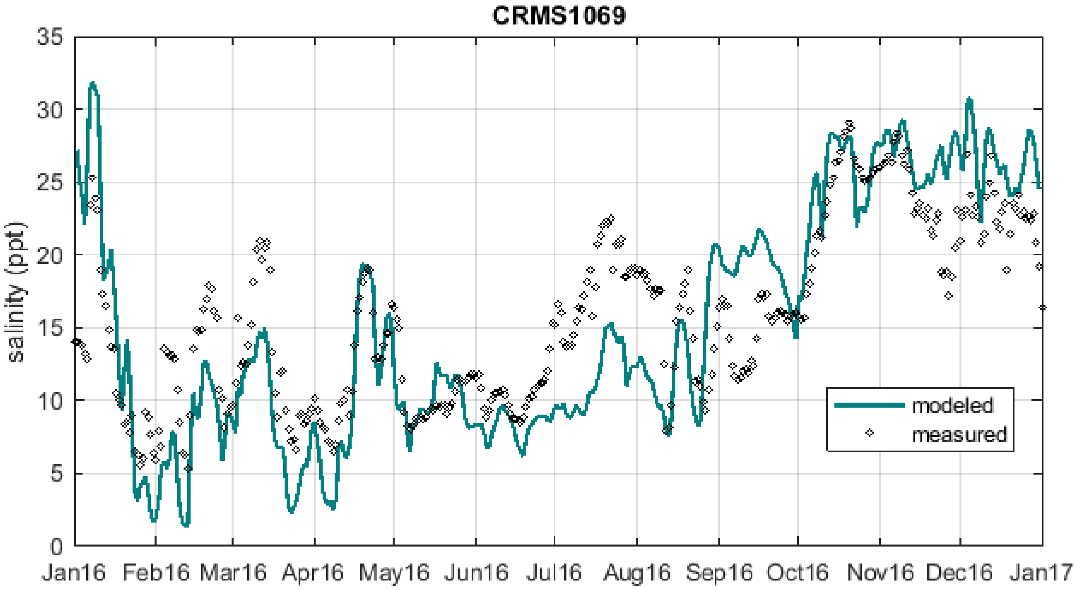

Figure B-7. Simulated daily averaged salinity by the Hydrodynamic Model (green line) compared to observations at CRMS1069 (black dots). The station location is displayed in Figure 10.

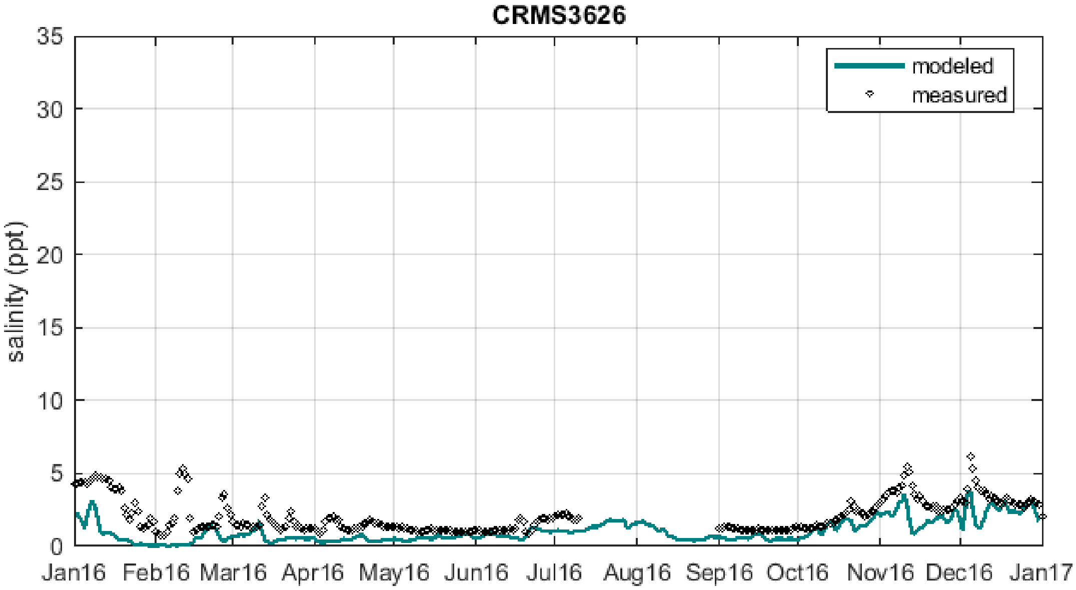

Figure B-8. Simulated daily averaged salinity by the Hydrodynamic Model (green line) compared to observations at CRMS3626 (black dots). The station location is displayed in Figure 10.

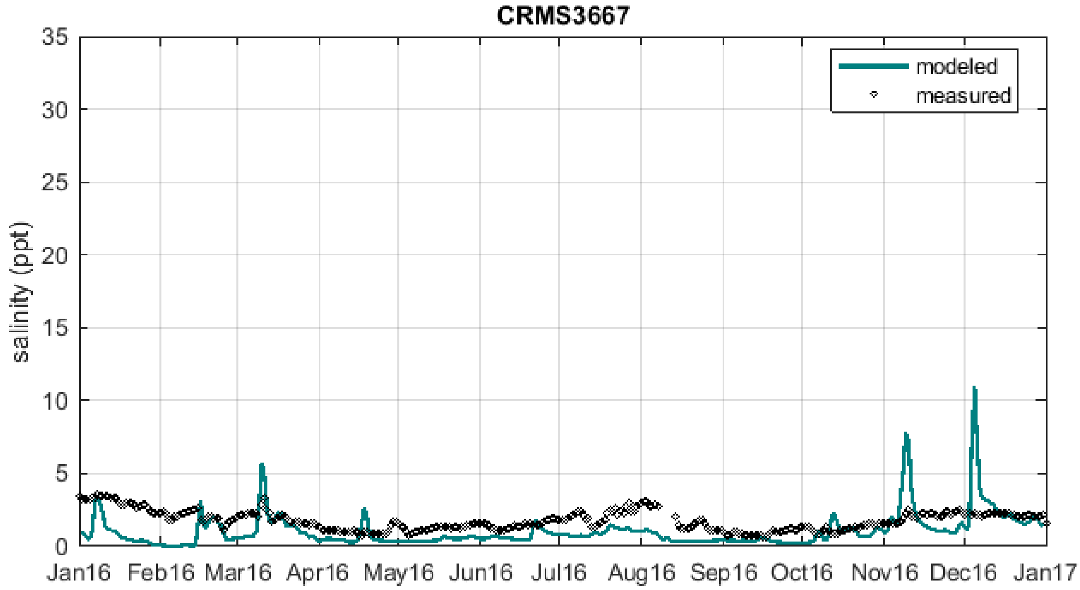

Figure B-9. Simulated daily averaged salinity by the Hydrodynamic Model (green line) compared to observations at CRMS3667 (black dots). The station location is displayed in Figure 10.

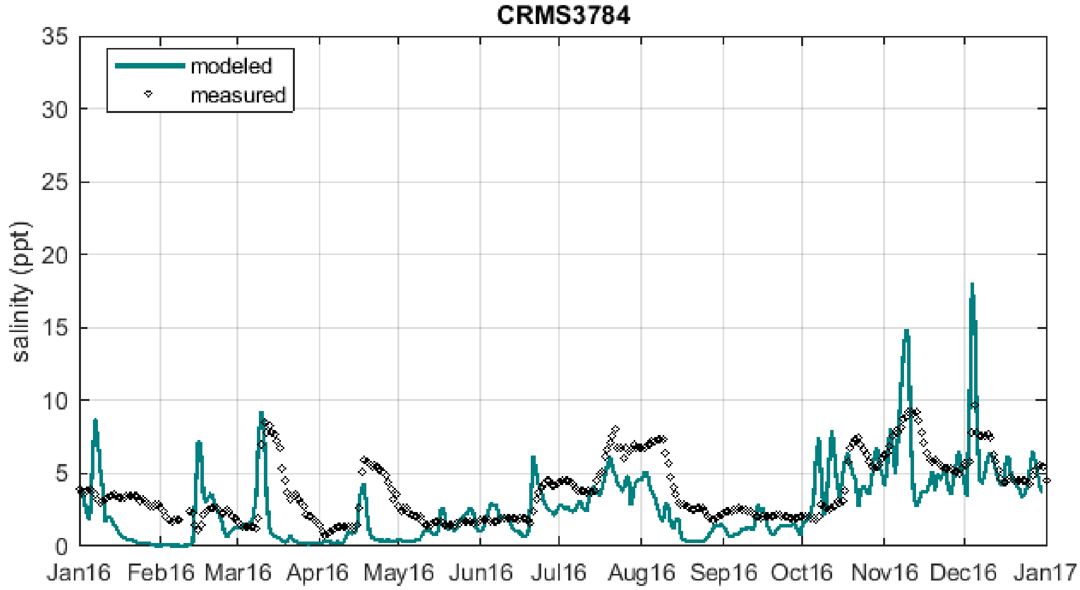

Figure B-10. Simulated daily averaged salinity by the Hydrodynamic Model (green line) compared to observations at CRMS3784 (black dots). The station location is displayed in Figure 10.

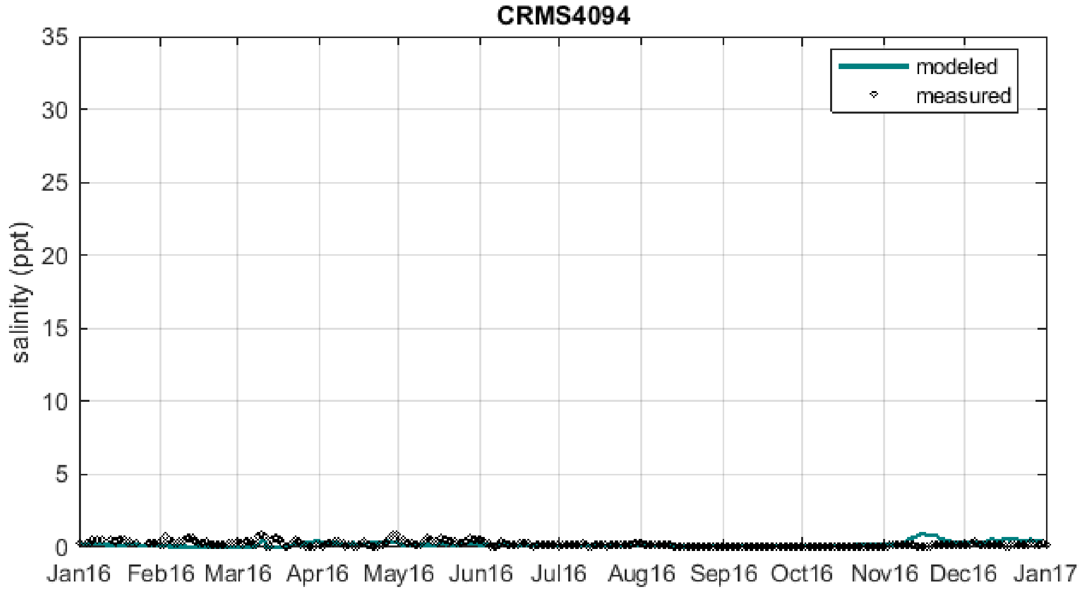

Figure B-11. Simulated daily averaged salinity by the Hydrodynamic Model (green line) compared to observations at CRMS4094 (black dots). The station location is displayed in Figure 10.

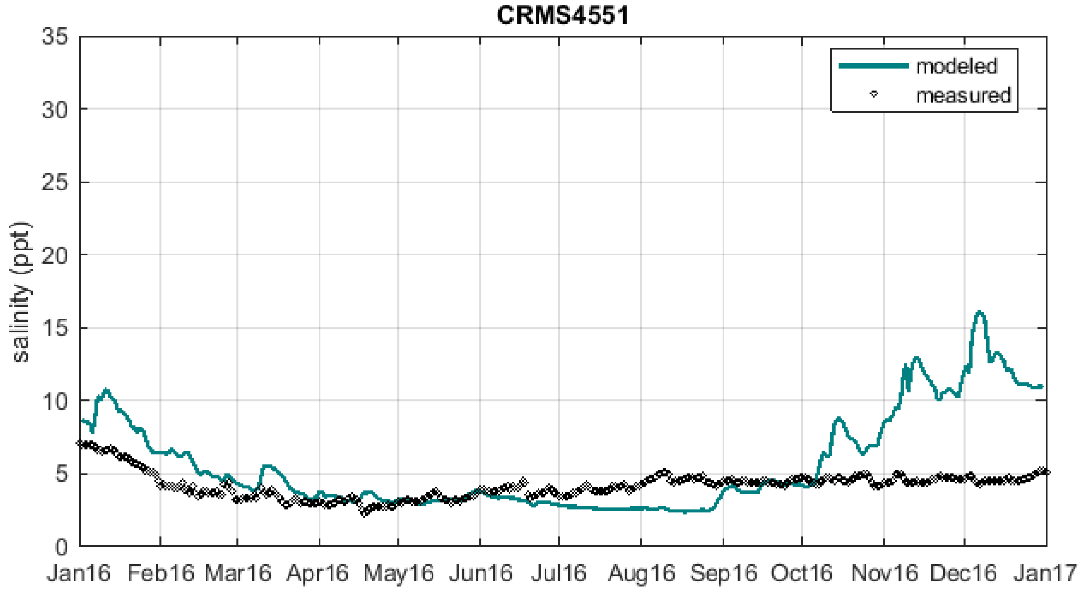

Figure B-12. Simulated daily averaged salinity by the Hydrodynamic Model (green line) compared to observations at CRMS4551 (black dots). The station location is displayed in Figure 10.

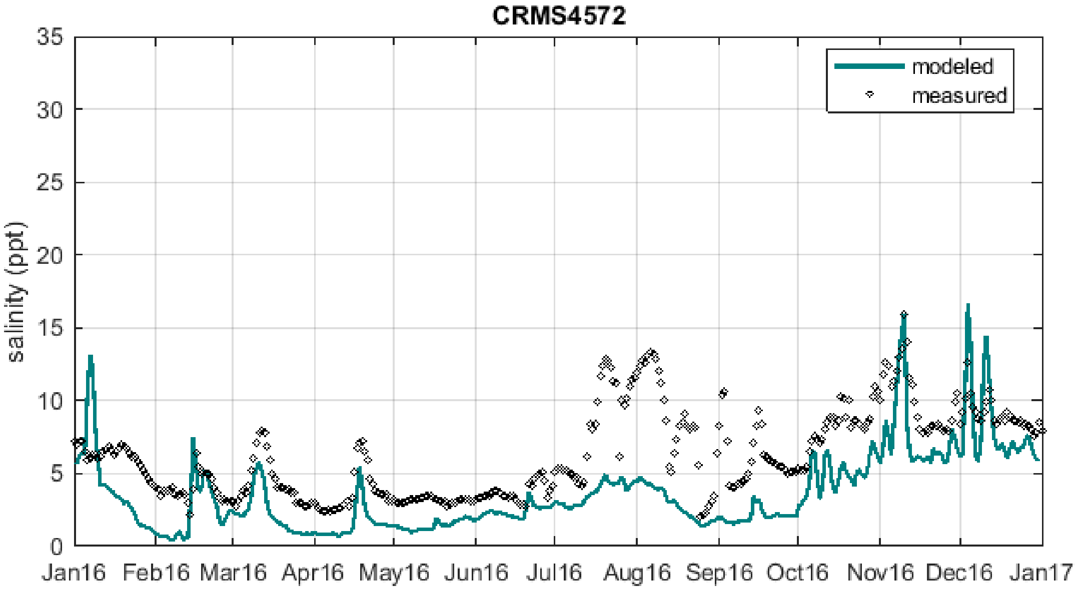

Figure B-13. Simulated daily averaged salinity by the Hydrodynamic Model (green line) compared to observations at CRMS4572 (black dots). The station location is displayed in Figure 10.

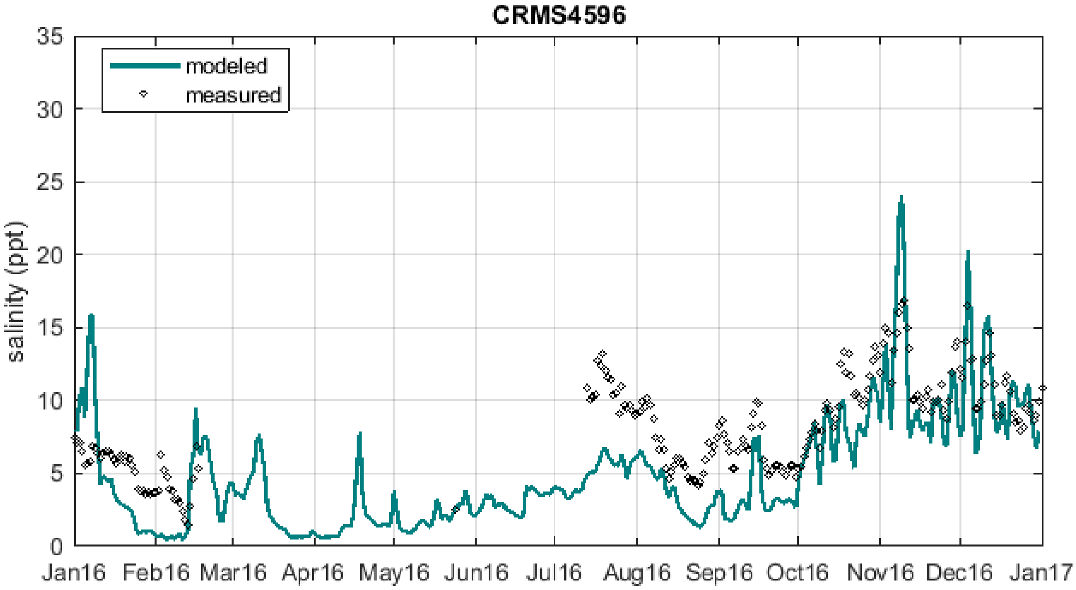

Figure B-14. Simulated daily averaged salinity by the Hydrodynamic Model (green line) compared to observations at CRMS4596 (black dots). The station location is displayed in Figure 10.

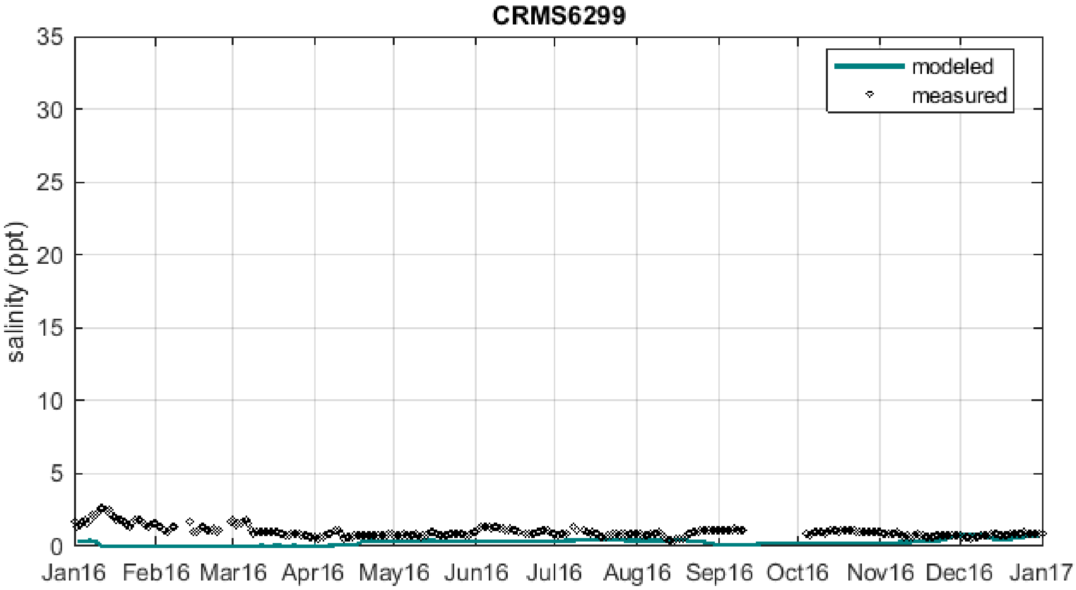

Figure B-15. Simulated daily averaged salinity by the Hydrodynamic Model (green line) compared to observations at CRMS629 (black dots). The station location is displayed in Figure 10.

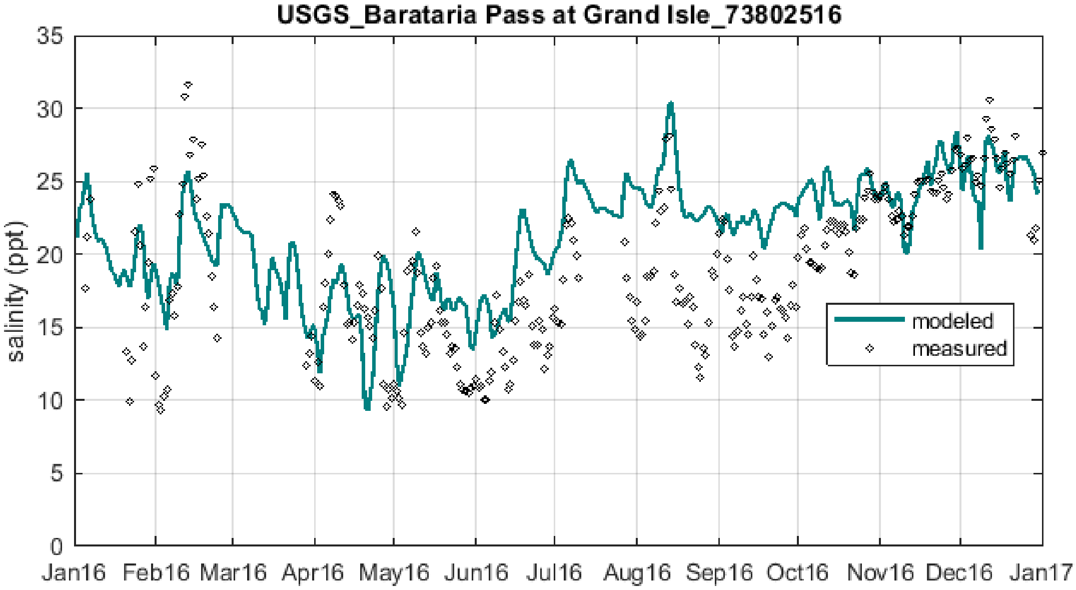

Figure B-16. Simulated daily averaged water levels by the Hydrodynamic Model (green line) compared to observations at USGS station 73802516 (black dots). The station location is displayed in Figure 10

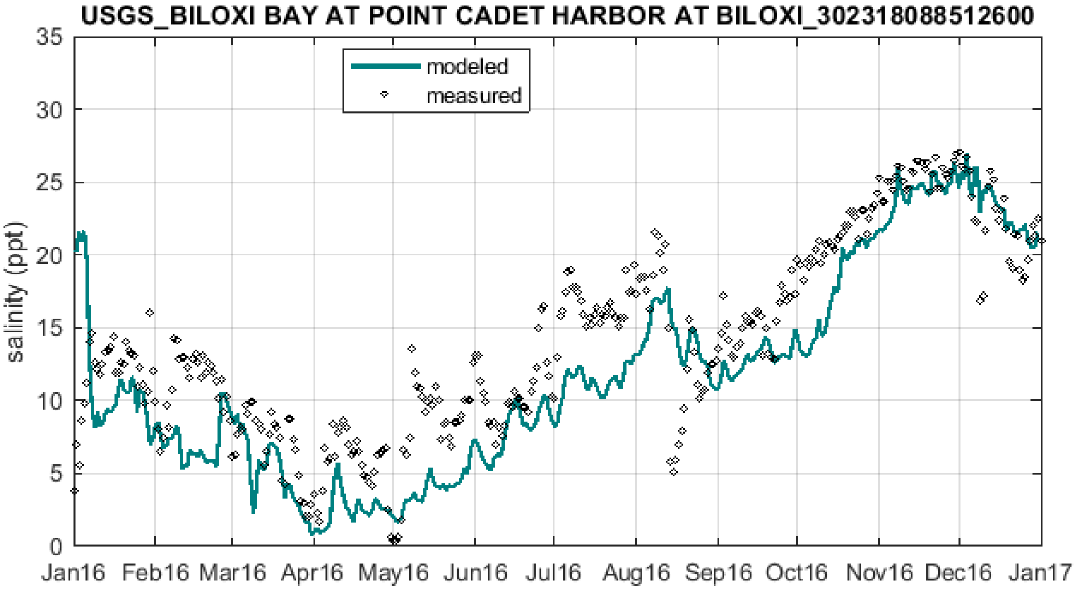

Figure B-17. Simulated daily averaged water levels by the Hydrodynamic Model (green line) compared to observations at USGS station 302318088512600 (black dots). The station location is displayed in Figure 10

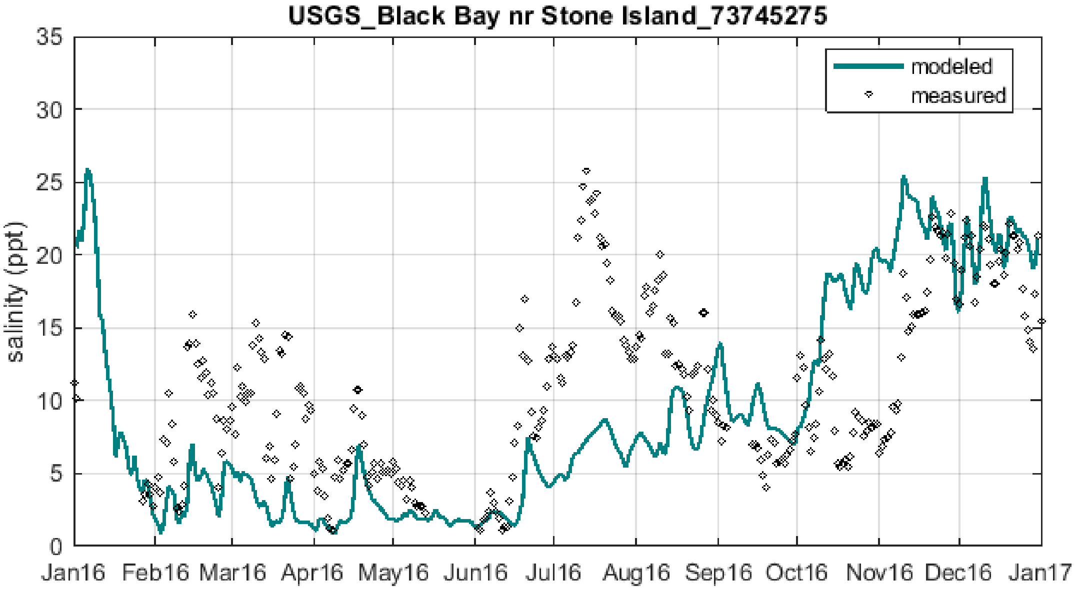

Figure B-18. Simulated daily averaged water levels by the Hydrodynamic Model (green line) compared to observations at USGS station 73745275 (black dots). The station location is displayed in Figure 10

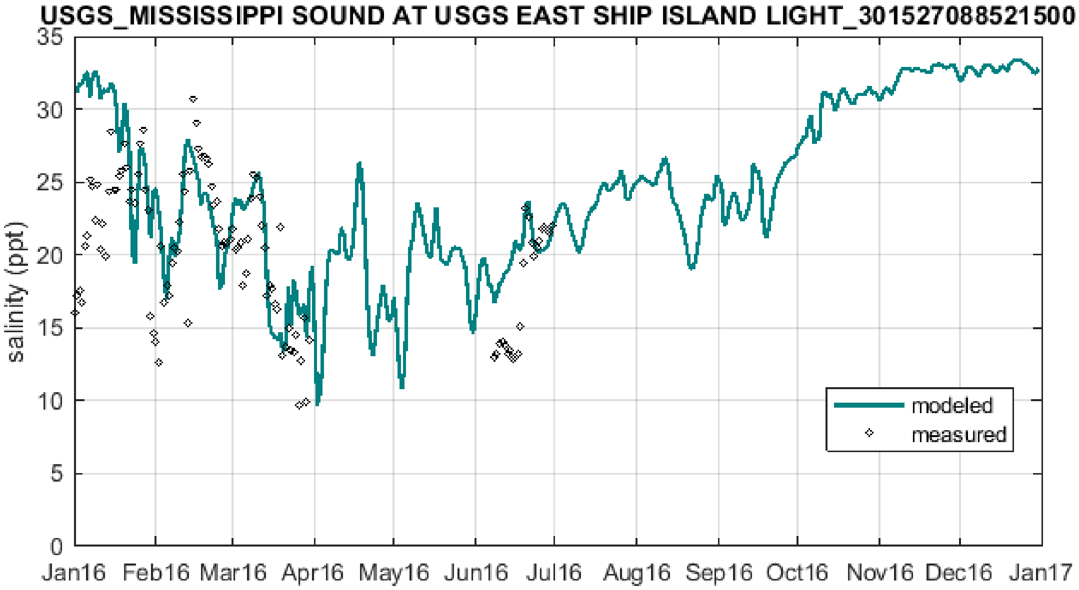

Figure B-19. Simulated daily averaged water levels by the Hydrodynamic Model (green line) compared to observations at USGS station 301527088521500 (black dots). The station location is displayed in Figure 10

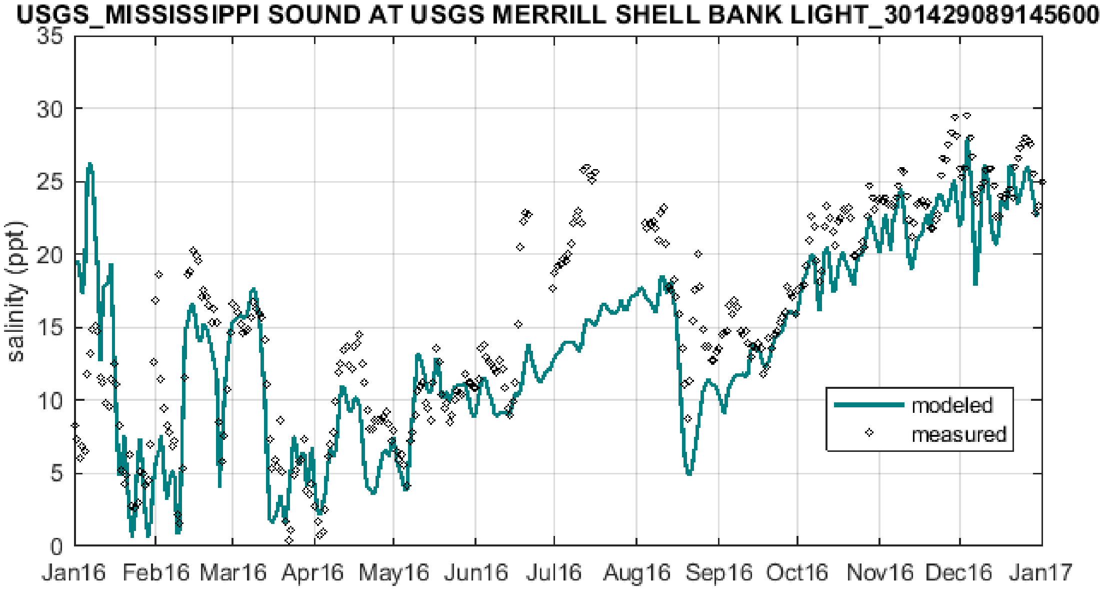

Figure B-20. Simulated daily averaged water levels by the Hydrodynamic Model (green line) compared to observations at USGS station 301429089145600 (black dots). The station location is displayed in Figure 10

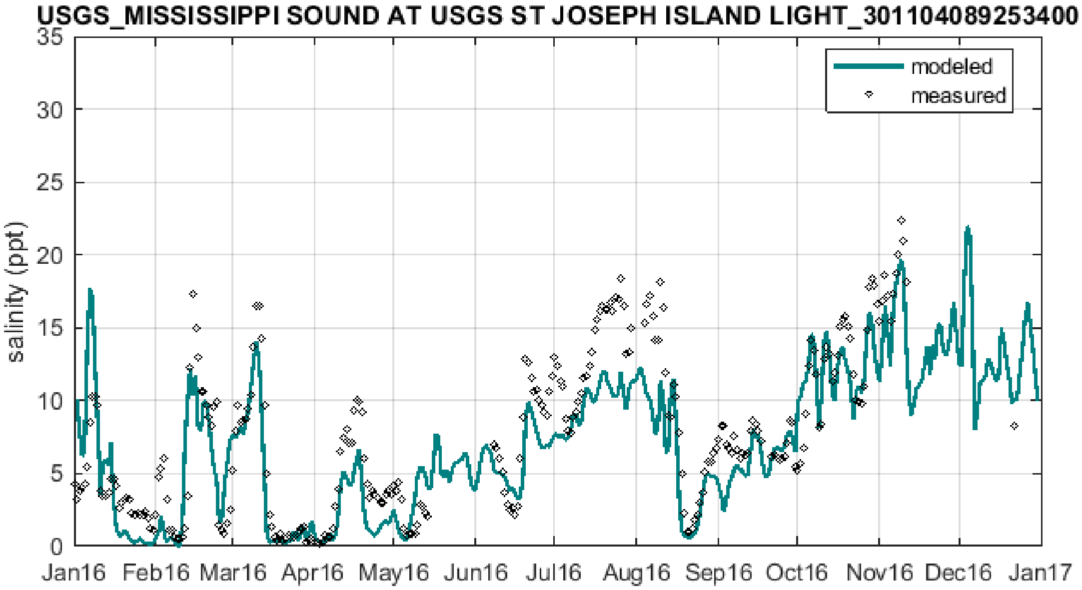

Figure B-21. Simulated daily averaged water levels by the Hydrodynamic Model (green line) compared to observations at USGS station 301104089253400 (black dots). The station location is displayed in Figure 10

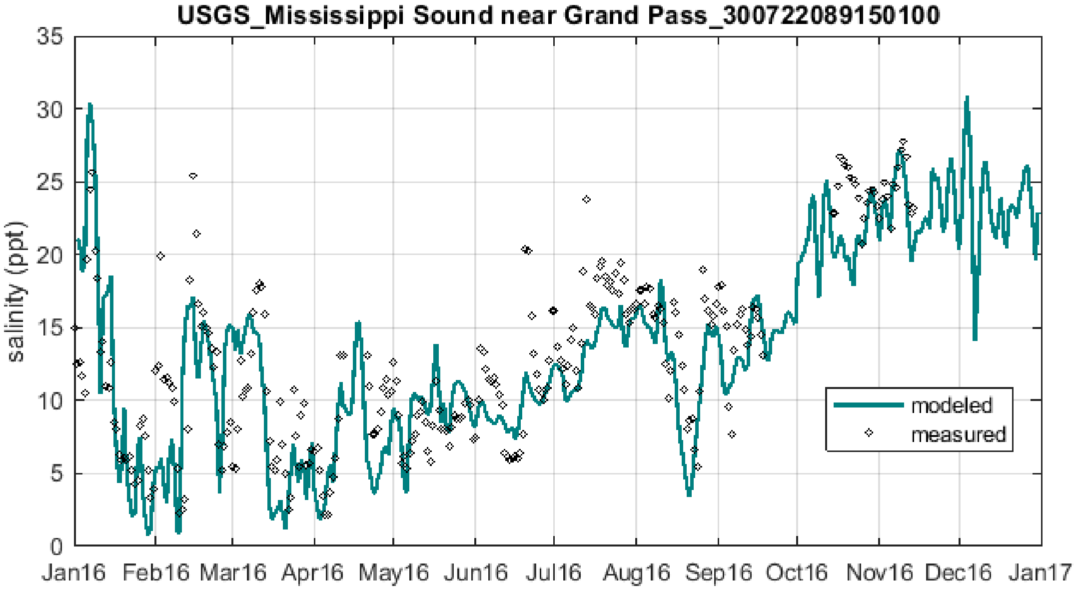

Figure B-22. Simulated daily averaged water levels by the Hydrodynamic Model (green line) compared to observations at USGS station 300722089150100 (black dots). The station location is displayed in Figure 10

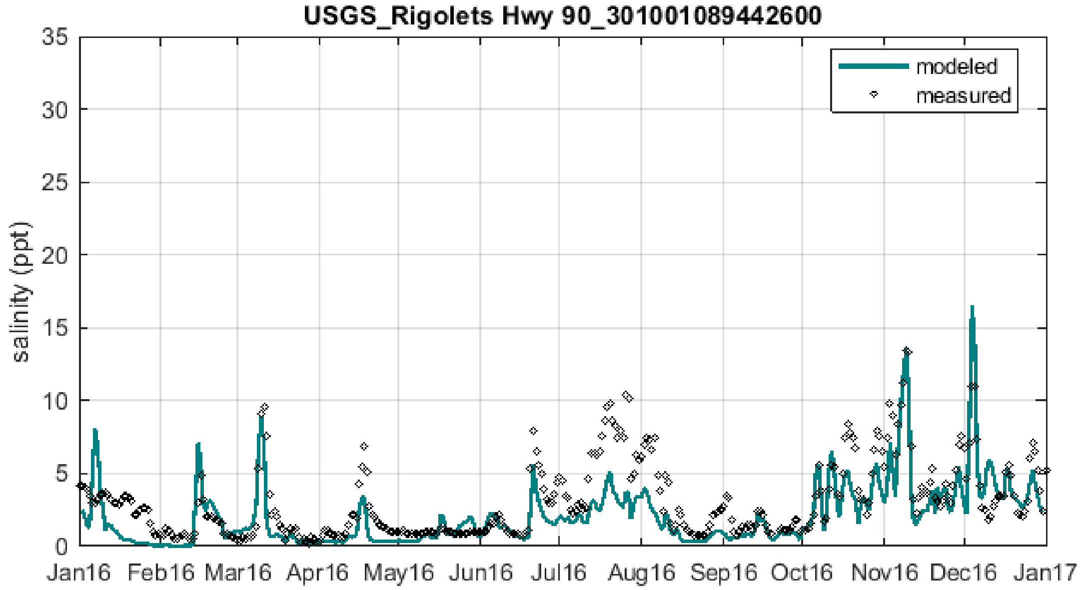

Figure B-23. Simulated daily averaged water levels by the Hydrodynamic Model (green line) compared to observations at USGS station 301001089442600 (black dots). The station location is displayed in Figure 10

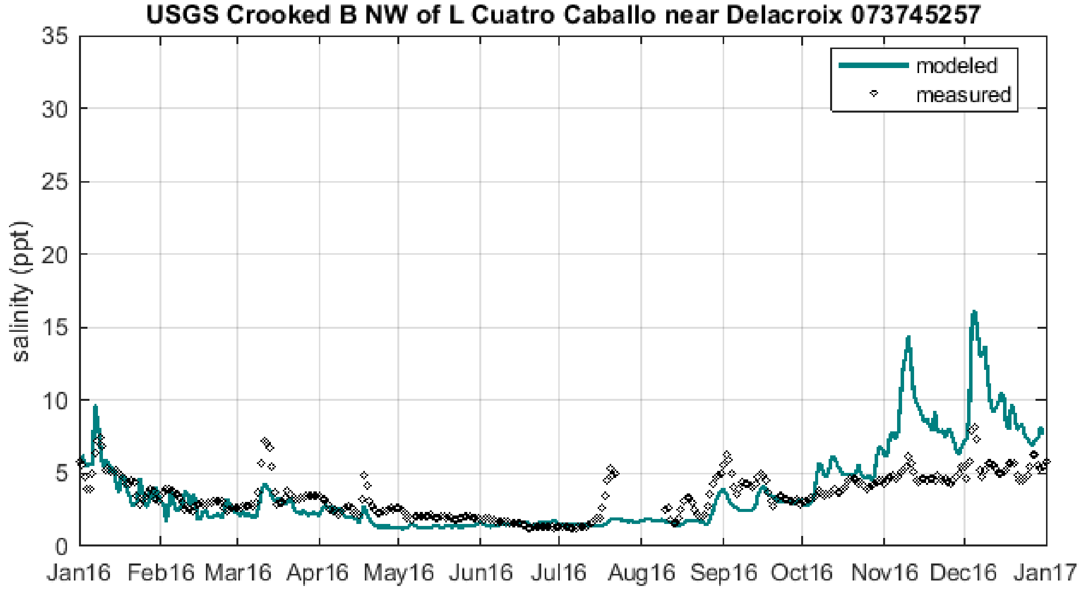

Figure B-24. Simulated daily averaged water levels by the Hydrodynamic Model (green line) compared to observations at USGS station 073745257 (black dots). The station location is displayed in Figure 10

APPENDIX C. TEMPERATURE CALIBRATION

Figure C-1 through Figure C-24 show the comparison between daily averaged temperature predicted by the Hydrodynamic Model and observations at all CRMS and USGS stations used for calibration. The location of all stations is displayed in Figure 10.

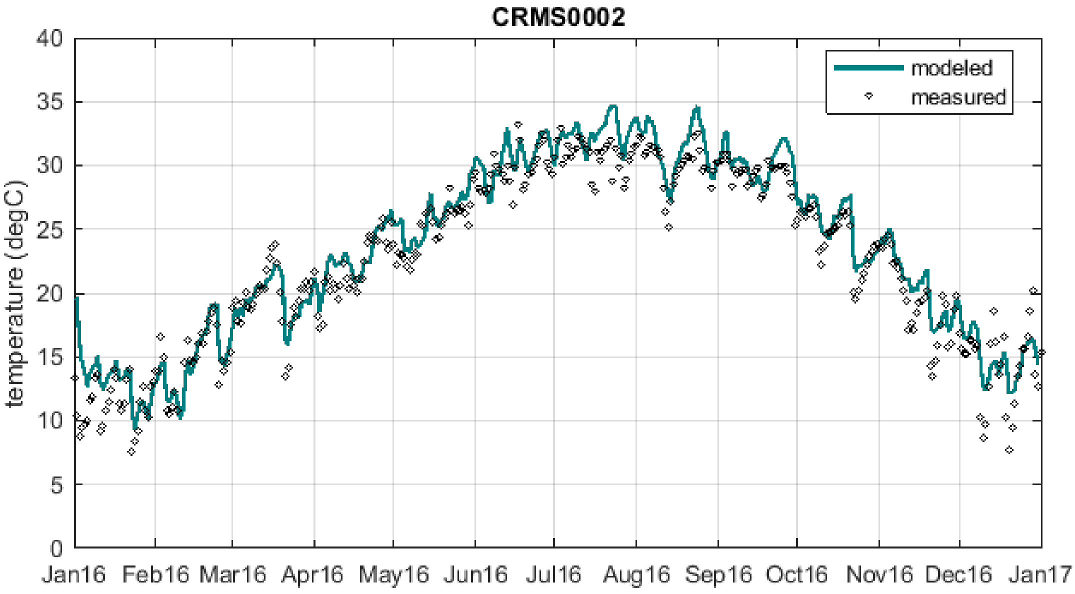

Figure C-1. Simulated daily averaged salinity by the Hydrodynamic Model (green line) compared to observations at CRMS0002 (black dots). The station location is displayed in Figure 10

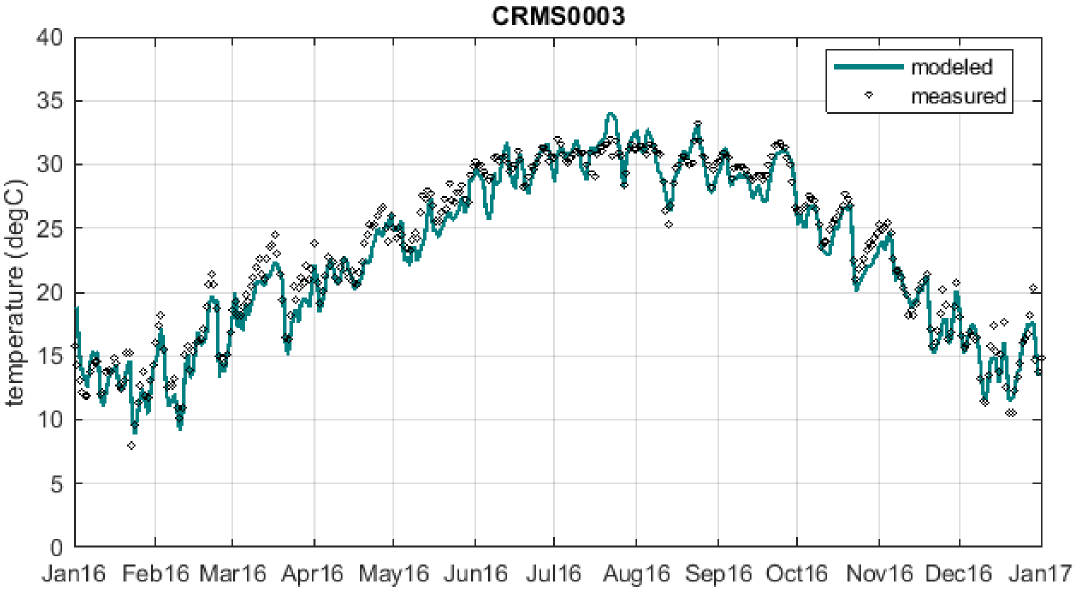

Figure C-2. Simulated daily averaged salinity by the Hydrodynamic Model (green line) compared to observations at CRMS0003 (black dots). The station location is displayed in Figure 10

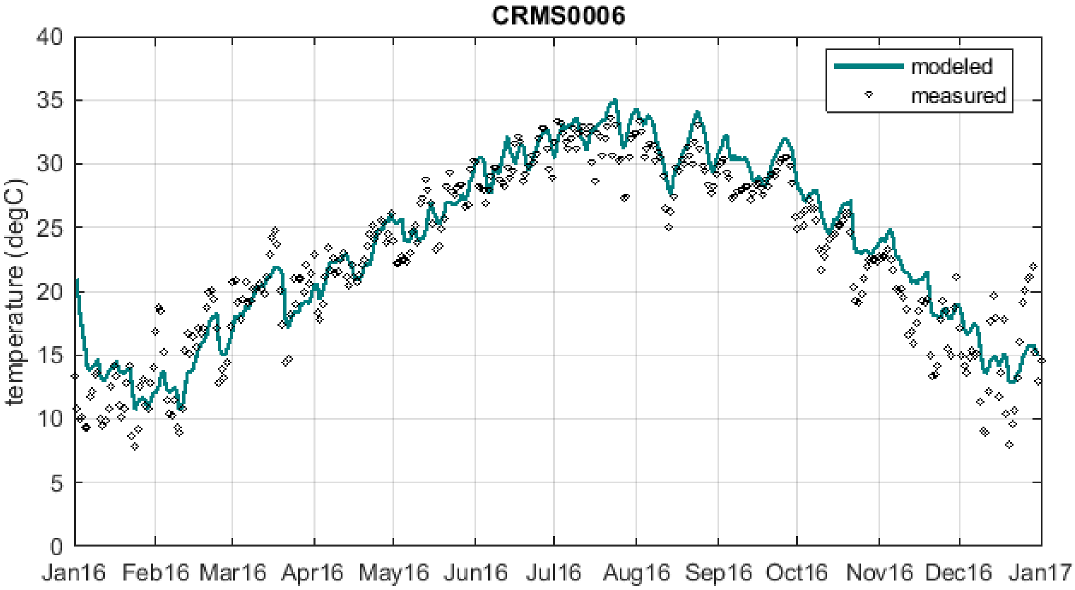

Figure C-3. Simulated daily averaged salinity by the Hydrodynamic Model (green line) compared to observations at CRMS0006 (black dots). The station location is displayed in Figure 10

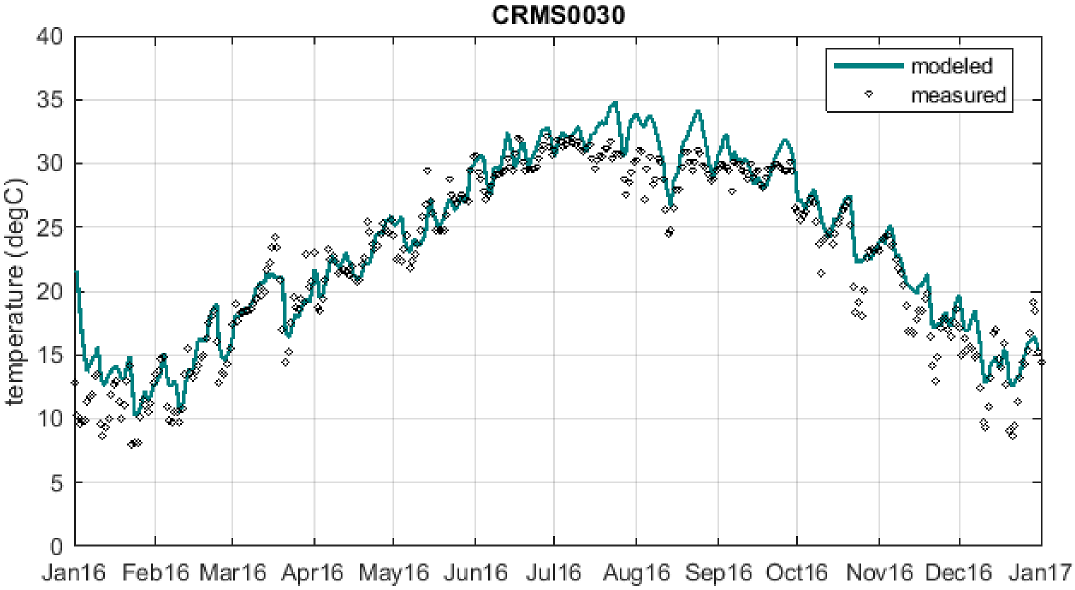

Figure C-4. Simulated daily averaged salinity by the Hydrodynamic Model (green line) compared to observations at CRMS0030 (black dots). The station location is displayed in Figure 10

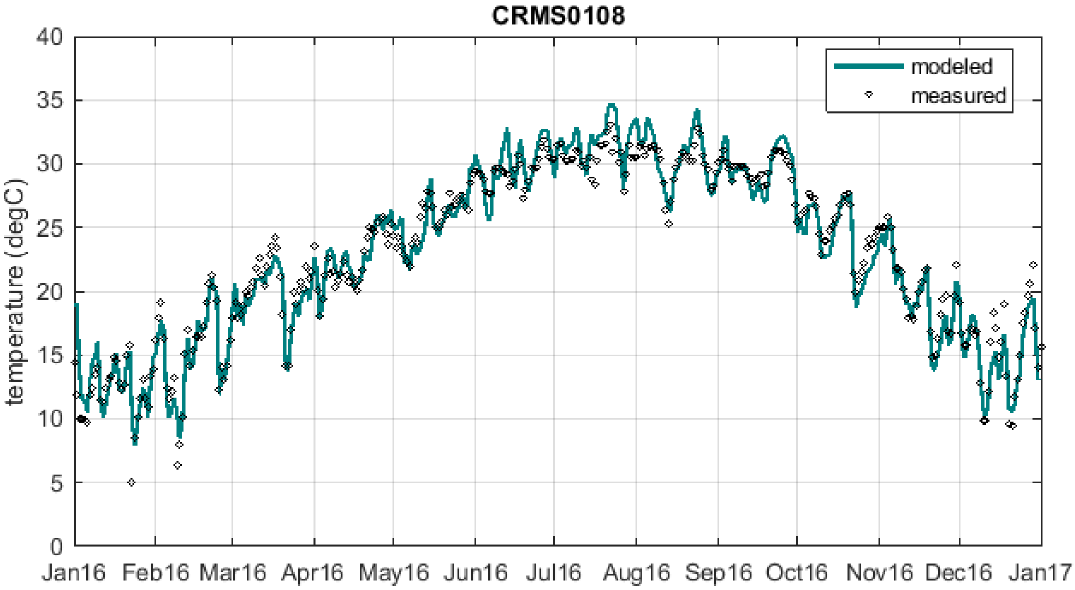

Figure C-5. Simulated daily averaged salinity by the Hydrodynamic Model (green line) compared to observations at CRMS0108 (black dots). The station location is displayed in Figure 10

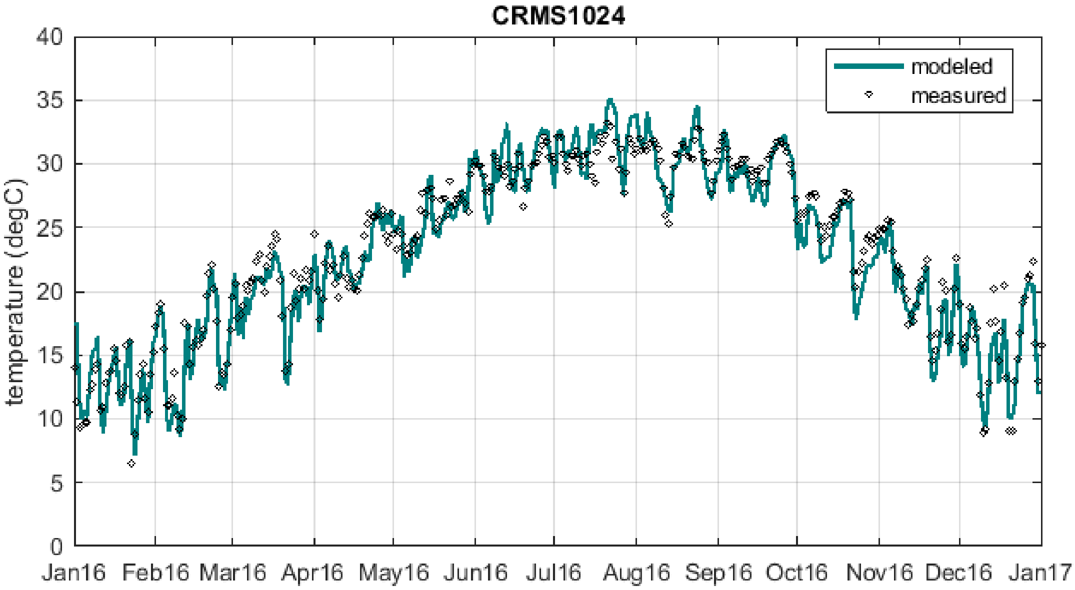

Figure C-6. Simulated daily averaged salinity by the Hydrodynamic Model (green line) compared to observations at CRMS1024 (black dots). The station location is displayed in Figure 10

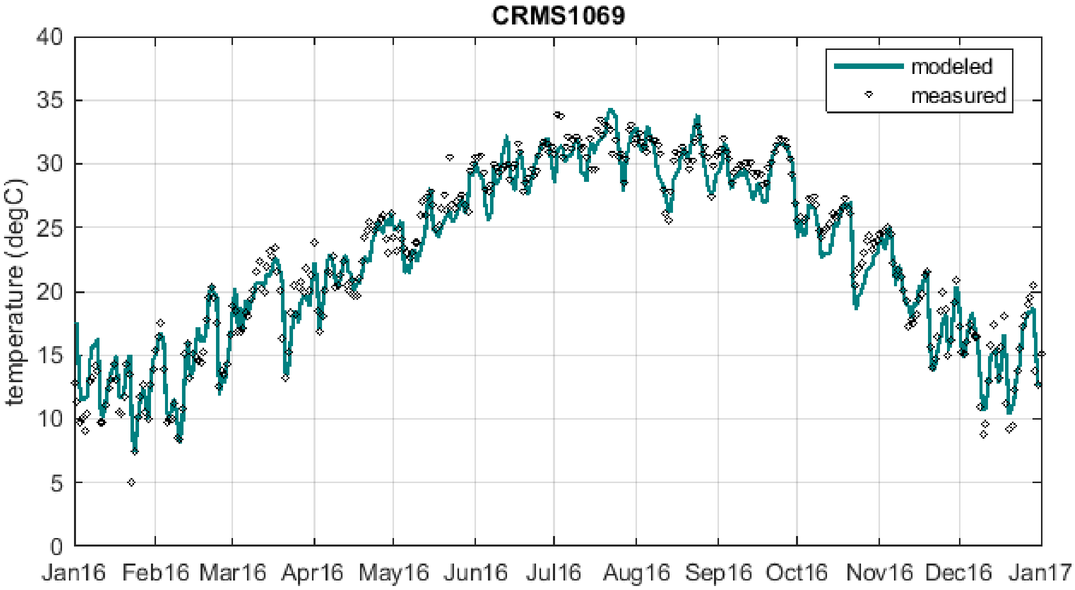

Figure C-7. Simulated daily averaged salinity by the Hydrodynamic Model (green line) compared to observations at CRMS1069 (black dots). The station location is displayed in Figure 10

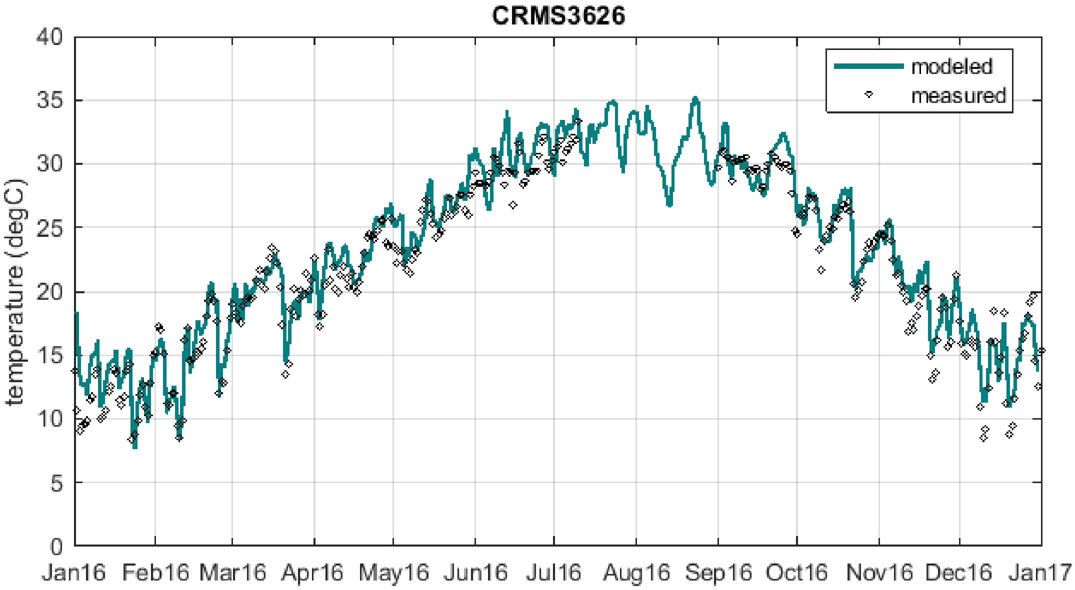

Figure C-8. Simulated daily averaged salinity by the Hydrodynamic Model (green line) compared to observations at CRMS3626 (black dots). The station location is displayed in Figure 10

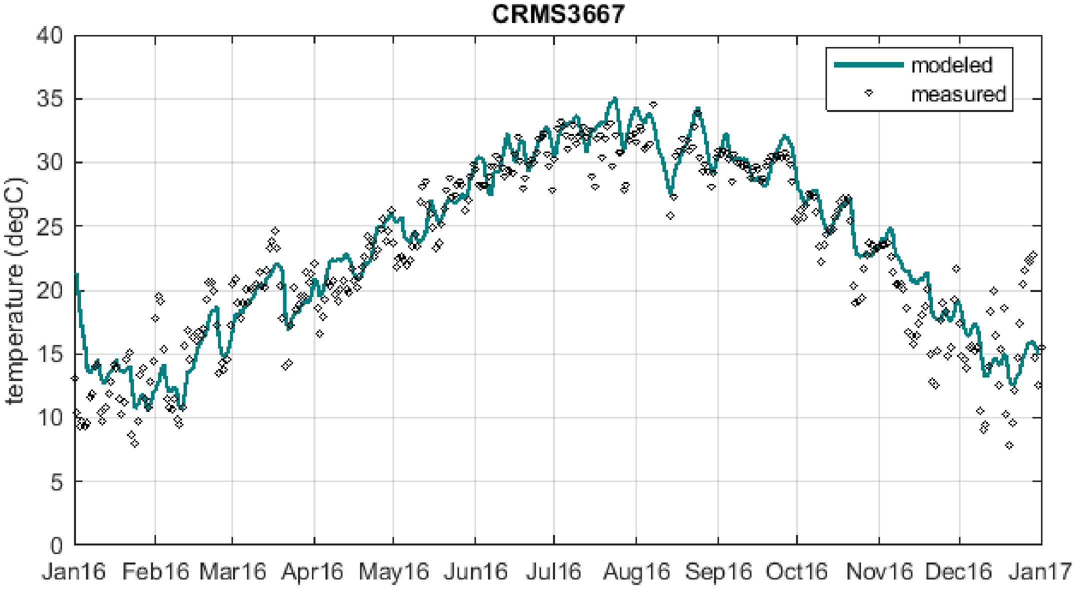

Figure C-9. Simulated daily averaged salinity by the Hydrodynamic Model (green line) compared to observations at CRMS3667 (black dots). The station location is displayed in Figure 10

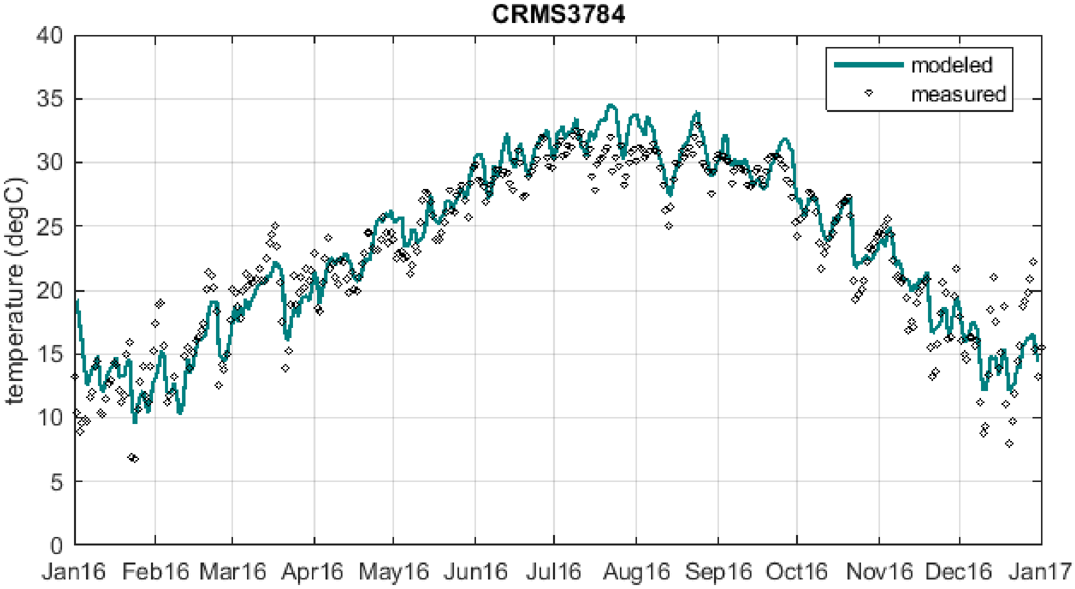

Figure C-10. Simulated daily averaged salinity by the Hydrodynamic Model (green line) compared to observations at CRMS3784 (black dots). The station location is displayed in Figure 10

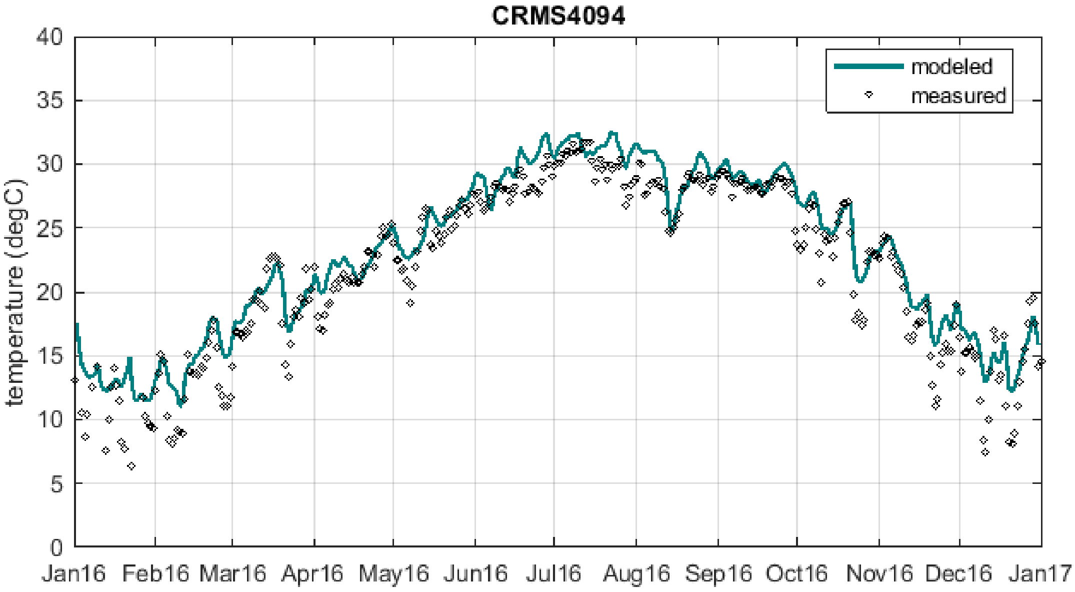

Figure C-11. Simulated daily averaged salinity by the Hydrodynamic Model (green line) compared to observations at CRMS4094 (black dots). The station location is displayed in Figure 10

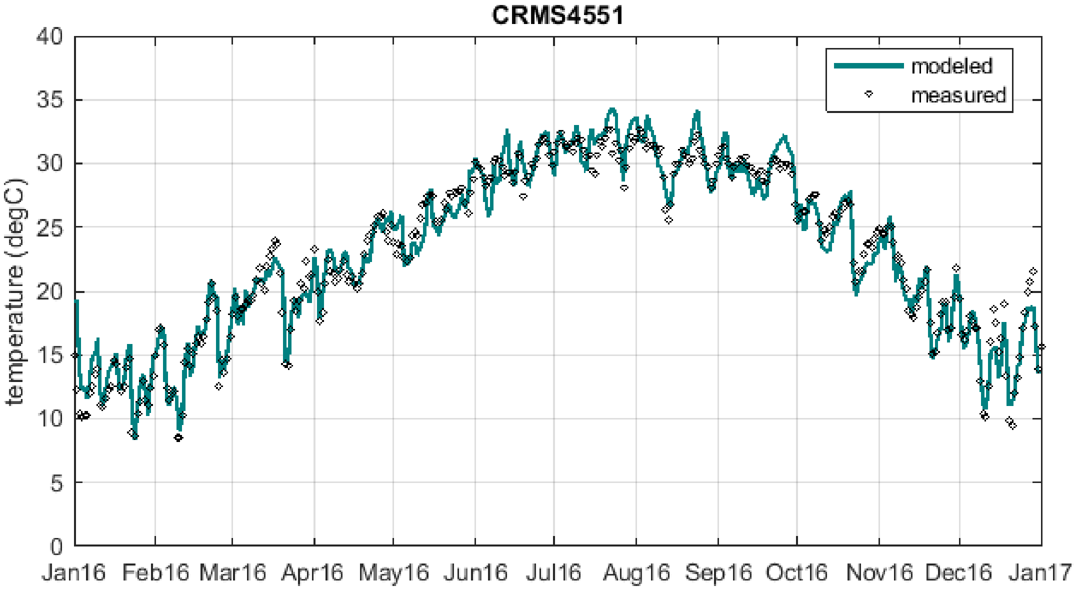

Figure C-12. Simulated daily averaged salinity by the Hydrodynamic Model (green line) compared to observations at CRMS4551 (black dots). The station location is displayed in Figure 10

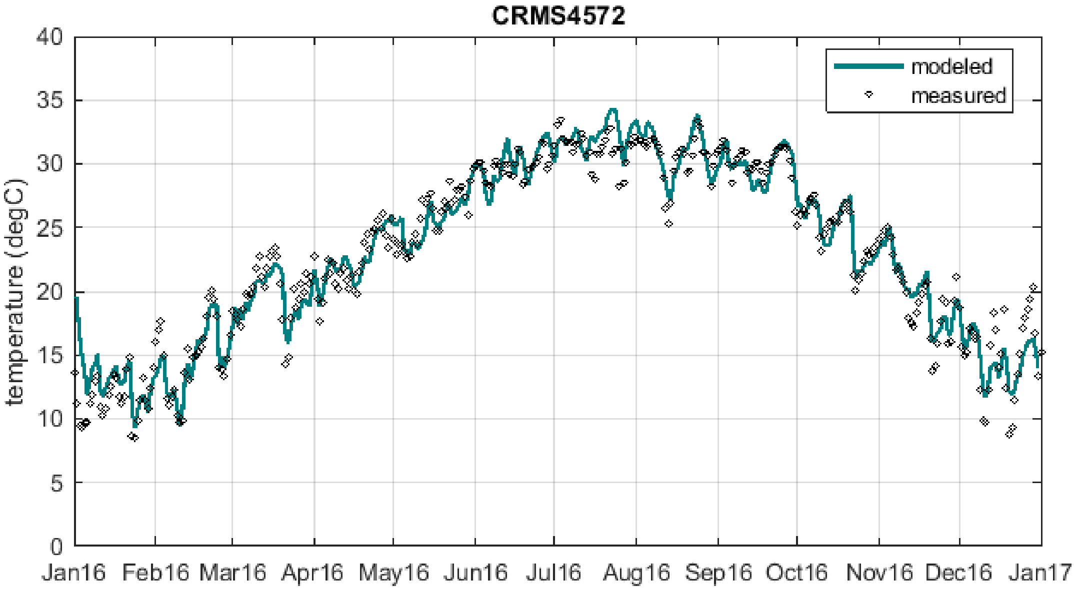

Figure C-13. Simulated daily averaged salinity by the Hydrodynamic Model (green line) compared to observations at CRMS4572 (black dots). The station location is displayed in Figure 10

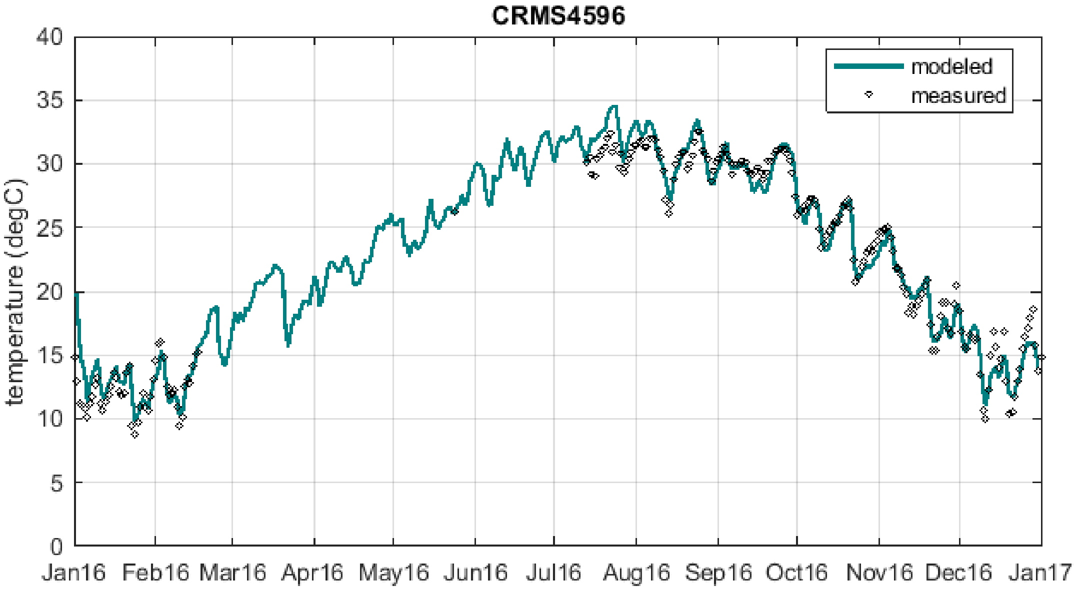

Figure C-14. Simulated daily averaged salinity by the Hydrodynamic Model (green line) compared to observations at CRMS4596 (black dots). The station location is displayed in Figure 10

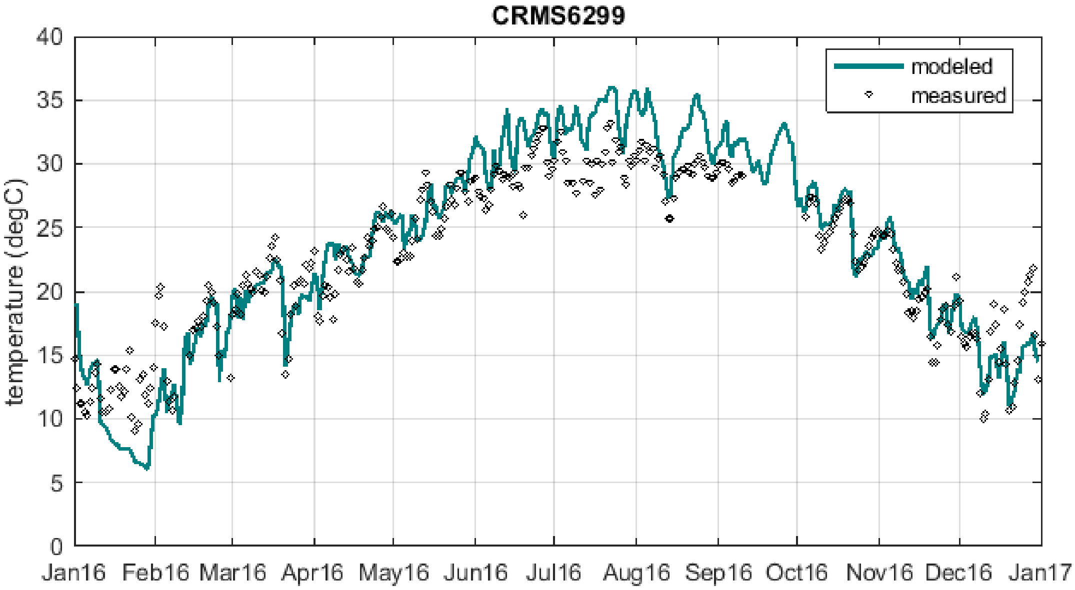

Figure C-15. Simulated daily averaged salinity by the Hydrodynamic Model (green line) compared to observations at CRMS6299 (black dots). The station location is displayed in Figure 10

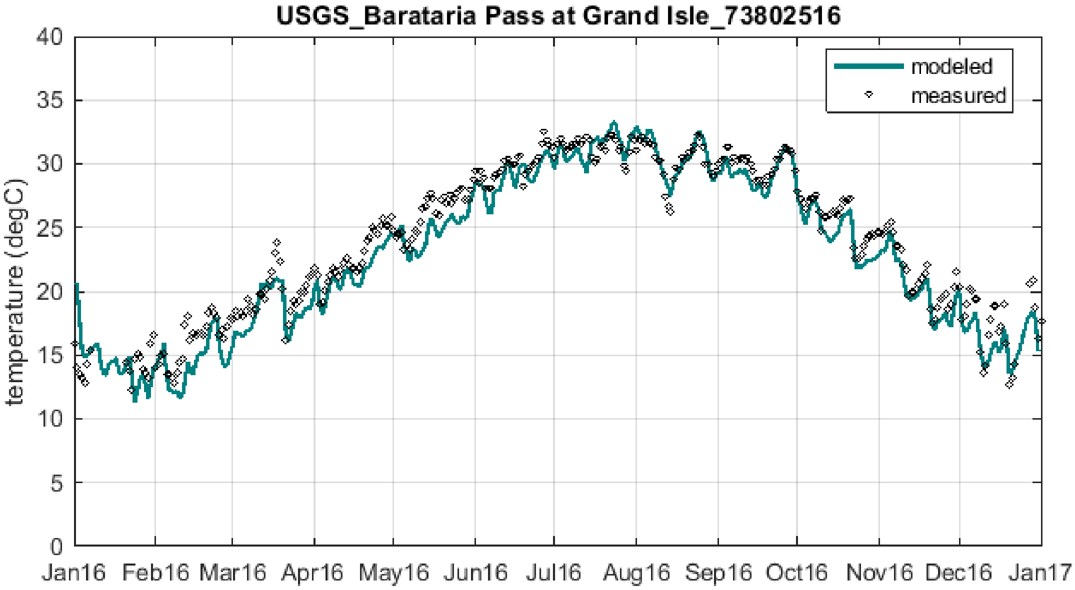

Figure C-16. Simulated daily averaged water levels by the Hydrodynamic Model (green line) compared to observations at USGS station 73802516 (black dots). The station location is displayed in Figure 10

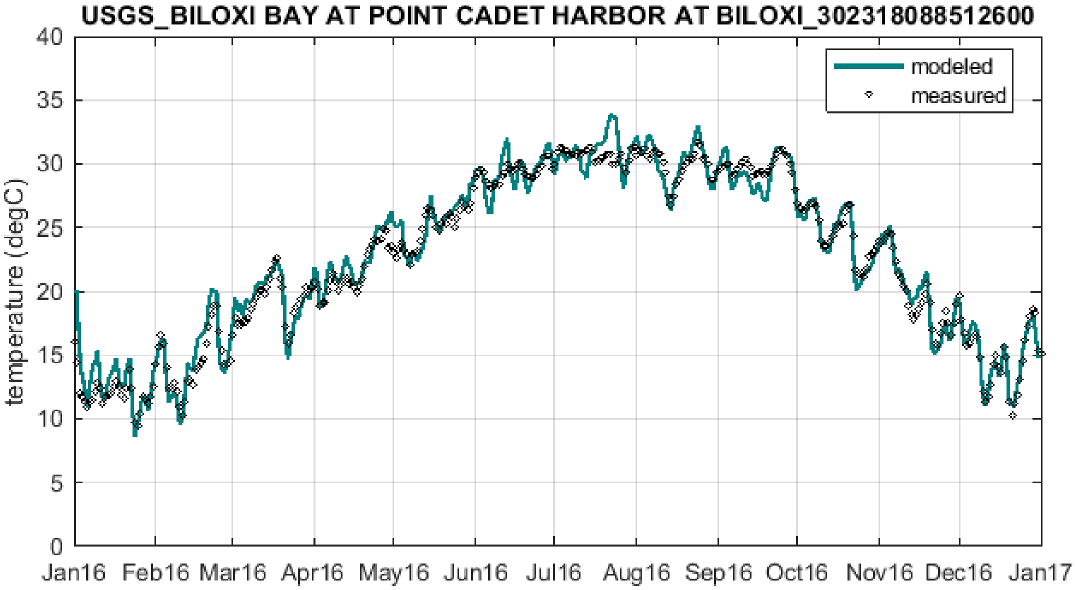

Figure C-17. Simulated daily averaged water levels by the Hydrodynamic Model (green line) compared to observations at USGS station 302318088512600 (black dots). The station location is displayed in Figure 10

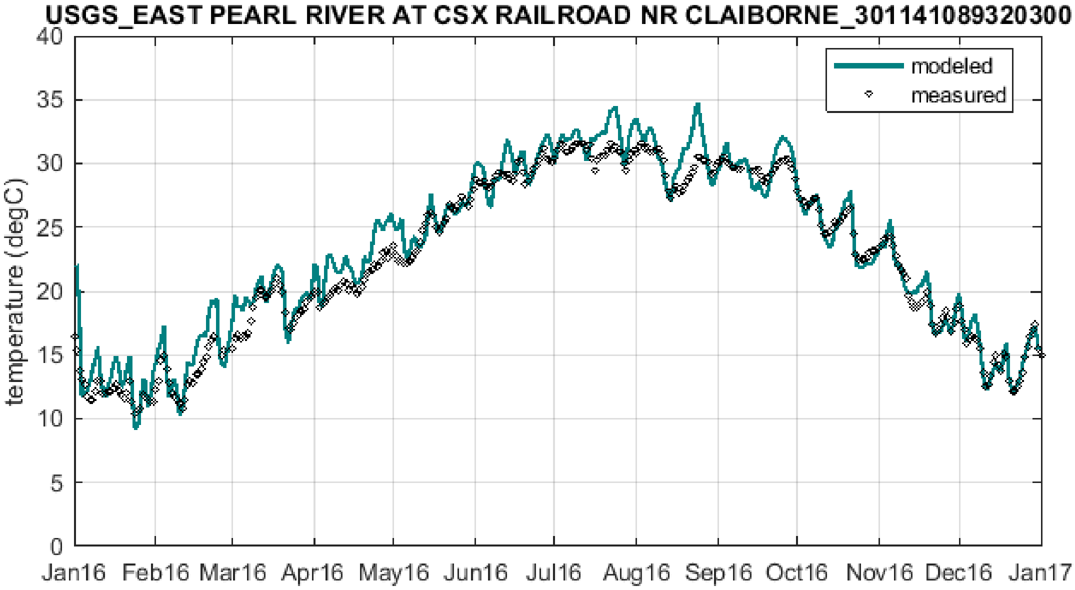

Figure C-18. Simulated daily averaged water levels by the Hydrodynamic Model (green line) compared to observations at USGS station 301141089320300 (black dots). The station location is displayed in Figure 10

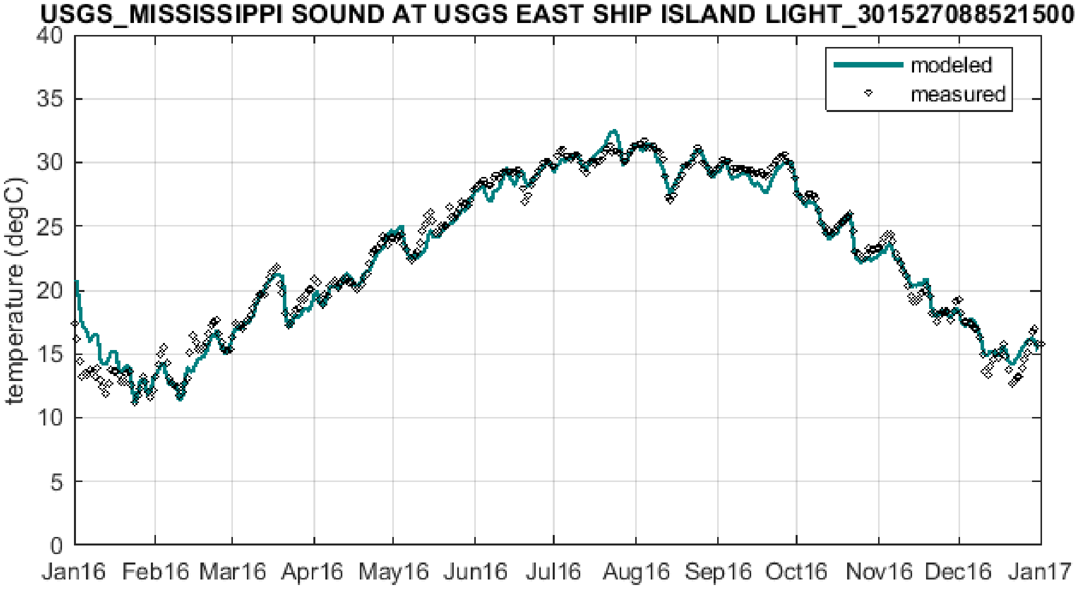

Figure C-19. Simulated daily averaged water levels by the Hydrodynamic Model (green line) compared to observations at USGS station 301527088521500 (black dots). The station location is displayed in Figure 10

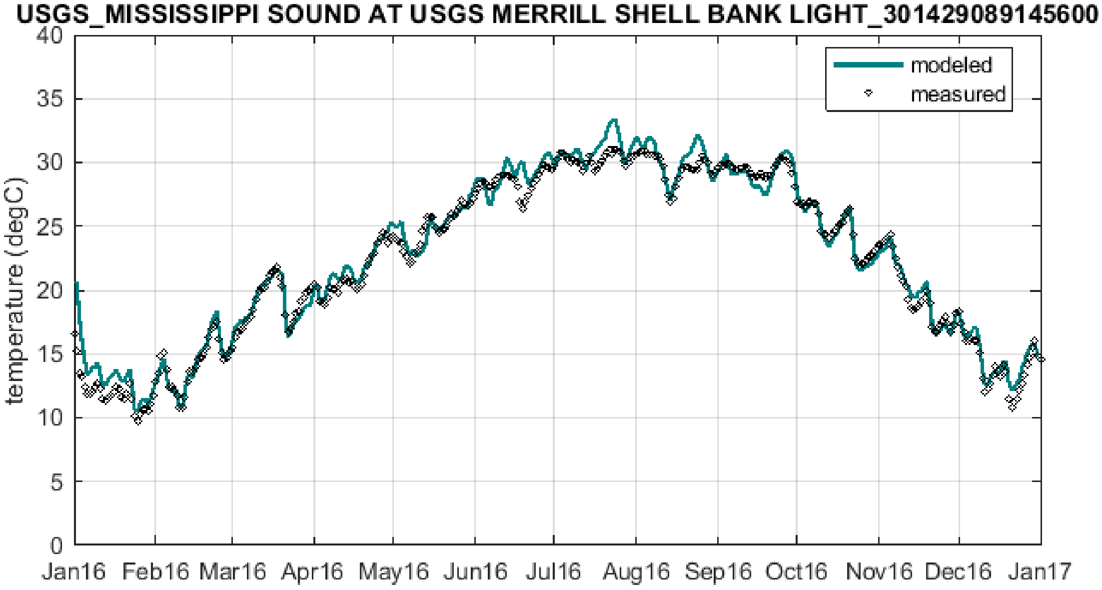

Figure C-20. Simulated daily averaged water levels by the Hydrodynamic Model (green line) compared to observations at USGS station 301429089145600 (black dots). The station location is displayed in Figure 10

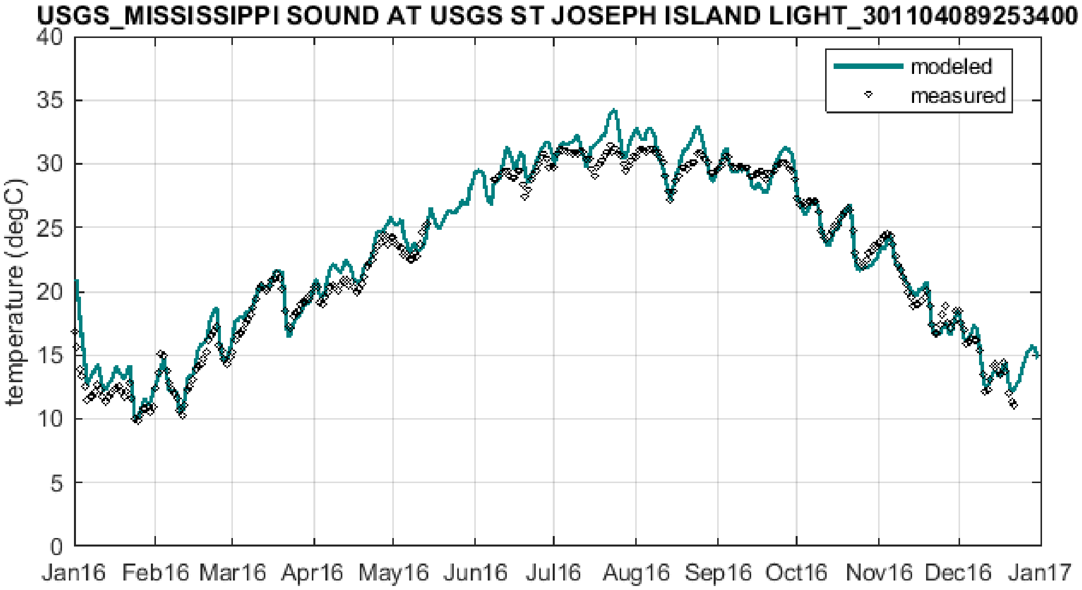

Figure C-21. Simulated daily averaged water levels by the Hydrodynamic Model (green line) compared to observations at USGS station 301104089253400 (black dots). The station location is displayed in Figure 10

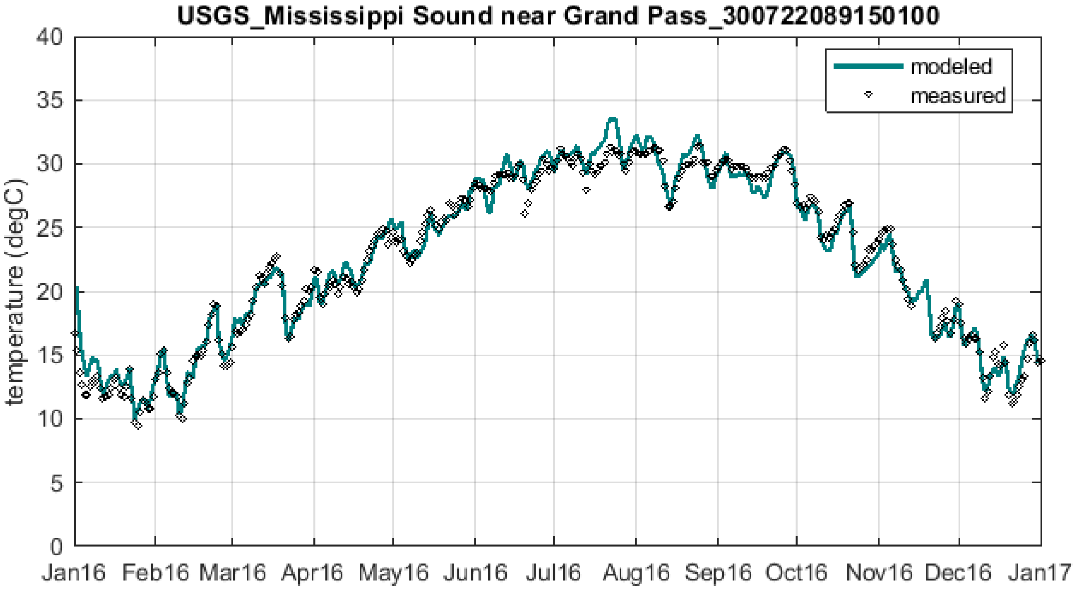

Figure C-22. Simulated daily averaged water levels by the Hydrodynamic Model (green line) compared to observations at USGS station 300722089150100 (black dots). The station location is displayed in Figure 10

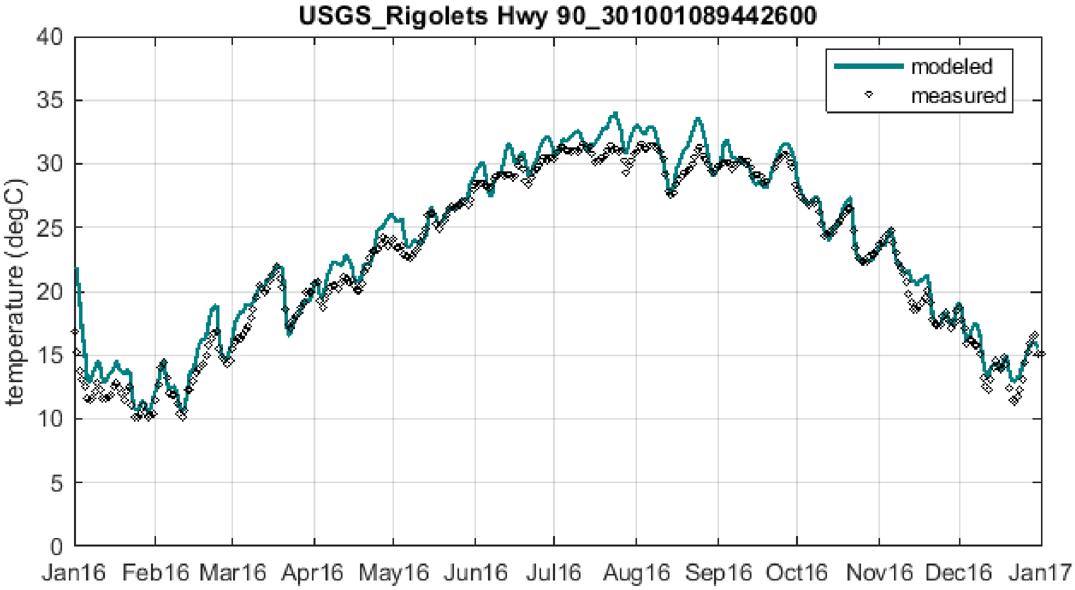

Figure C-23. Simulated daily averaged water levels by the Hydrodynamic Model (green line) compared to observations at USGS station 301001089442600 (black dots). The station location is displayed in Figure 10

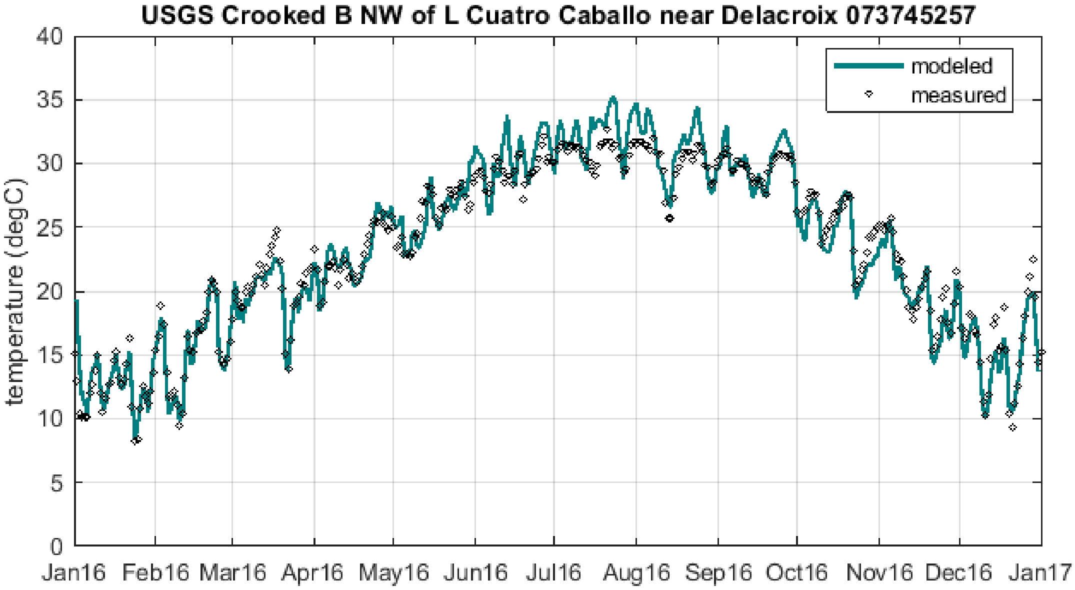

Figure C-24. Simulated daily averaged water levels by the Hydrodynamic Model (green line) compared to observations at USGS station 073745257 (black dots). The station location is displayed in Figure 10

APPENDIX D. SALINITY VALIDATION WITH CTD CASTS

Figure D-1 through Figure D-49 show the comparison between daily averaged salinity projected by the Hydrodynamic Model and available CTD casts used for validation. The location of all stations is displayed in Figure 37.

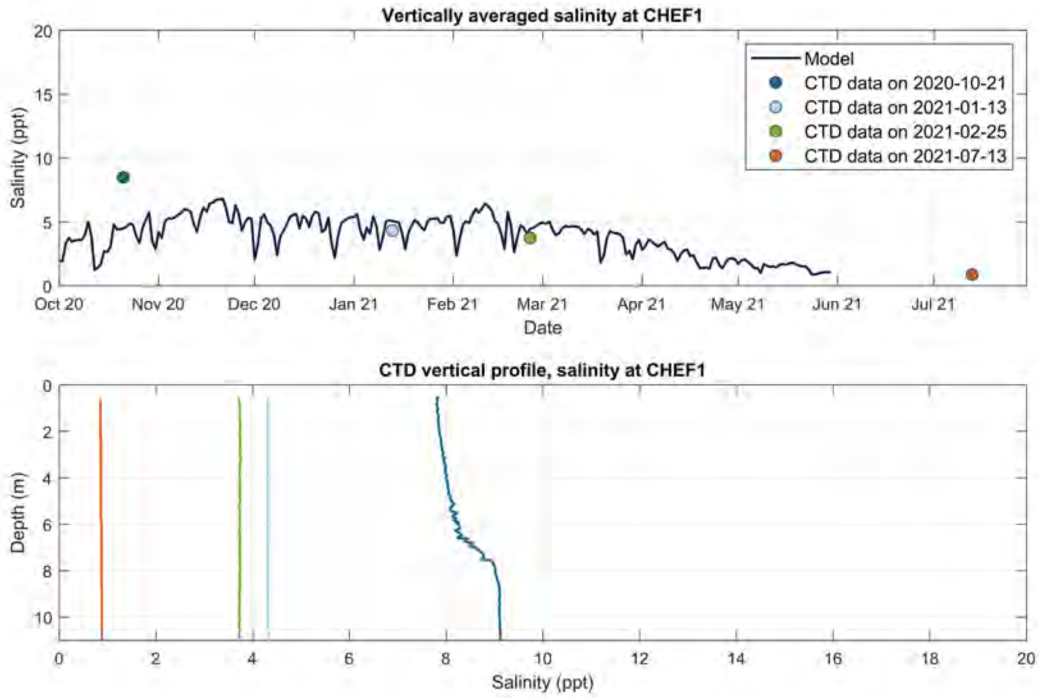

Figure D-1. Salinity validation using CTD casts at CHEF1. Top graph: simulated daily averaged salinity by the Hydrodynamic Model (blue line) compared to depth averaged CTD casts at CHEF1. Bottom graph: vertical salinity CTD profiles collected at CHEF1. The colors of the CTD vertical profiles in the bottom graph match the color of the depth averaged CTD observation in the top graph.

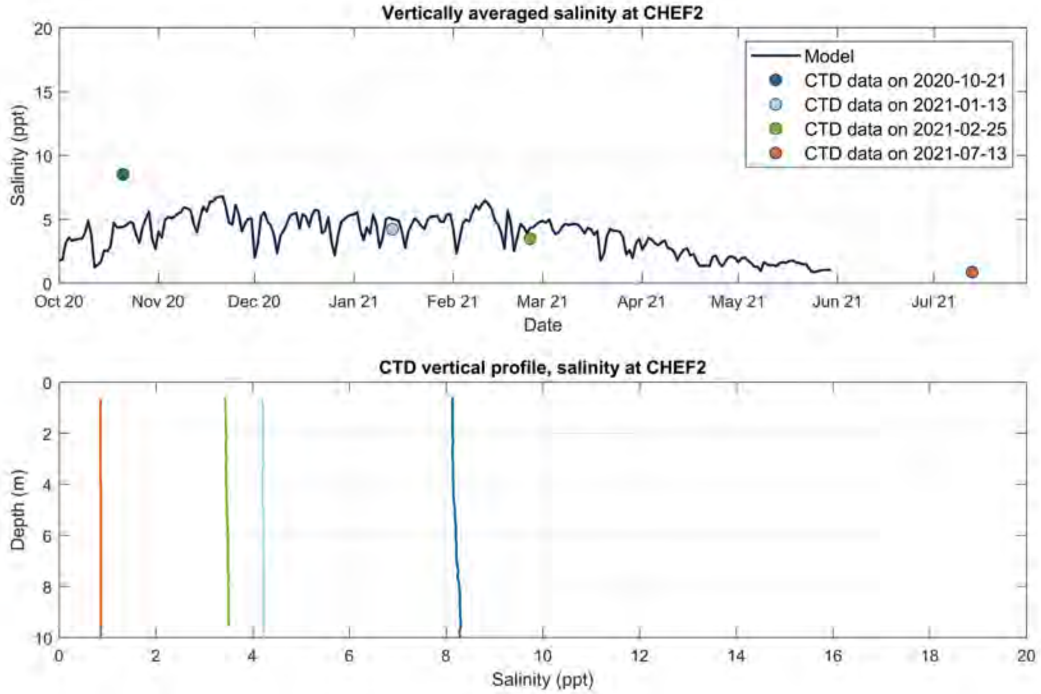

Figure D-2. Salinity validation using CTD casts at CHEF2. Top graph: simulated daily averaged salinity by the Hydrodynamic Model (blue line) compared to depth averaged CTD casts at CHEF2. Bottom graph: vertical salinity CTD profiles collected at CHEF2. The colors of the CTD vertical profiles in the bottom graph match the color of the depth averaged CTD observation in the top graph.

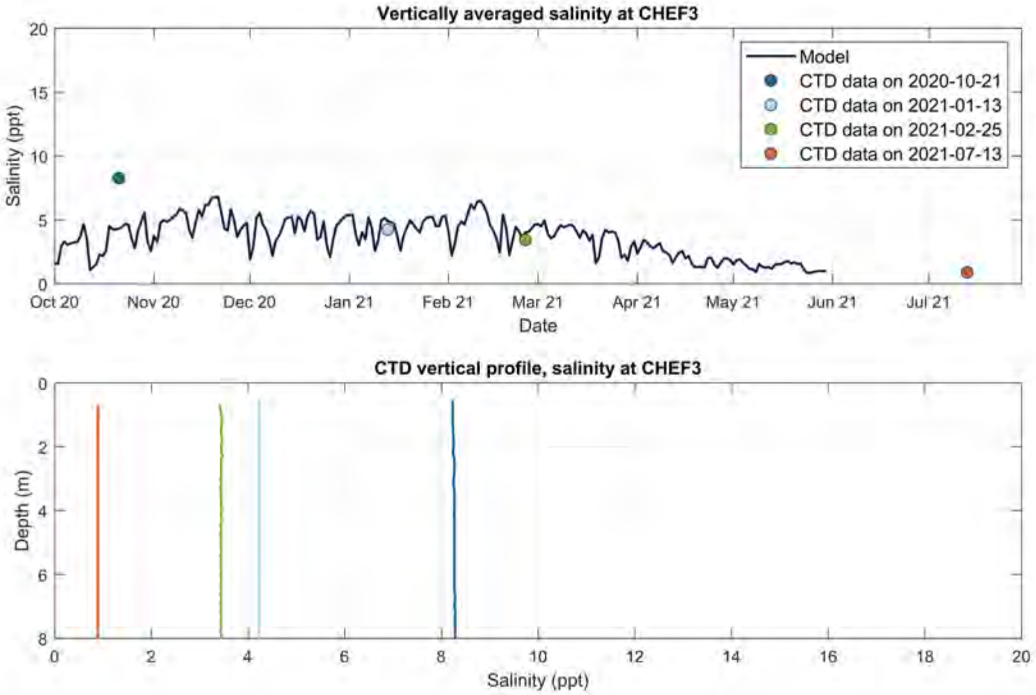

Figure D-3. Salinity validation using CTD casts at CHEF3. Top graph: simulated daily averaged salinity by the Hydrodynamic Model (blue line) compared to depth averaged CTD casts at CHEF3. Bottom graph: vertical salinity CTD profiles collected at CHEF3. The colors of the CTD vertical profiles in the bottom graph match the color of the depth averaged CTD observation in the top graph.

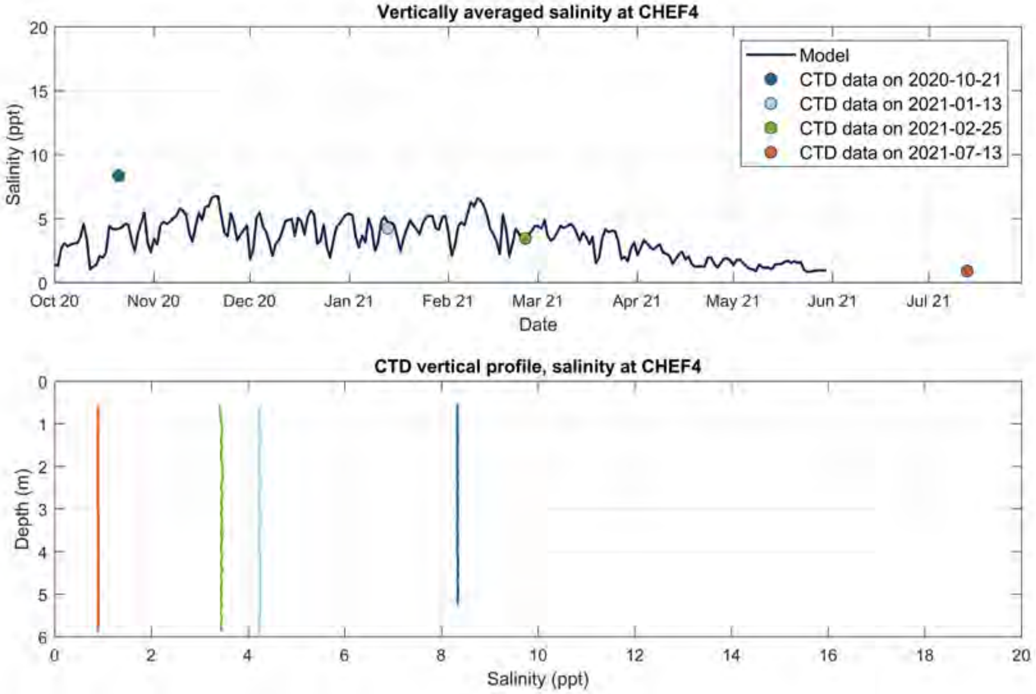

Figure D-4. Salinity validation using CTD casts at CHEF4. Top graph: simulated daily averaged salinity by the Hydrodynamic Model (blue line) compared to depth averaged CTD casts at CHEF4. Bottom graph: vertical salinity CTD profiles collected at CHEF4. The colors of the CTD vertical profiles in the bottom graph match the color of the depth averaged CTD observation in the top graph.

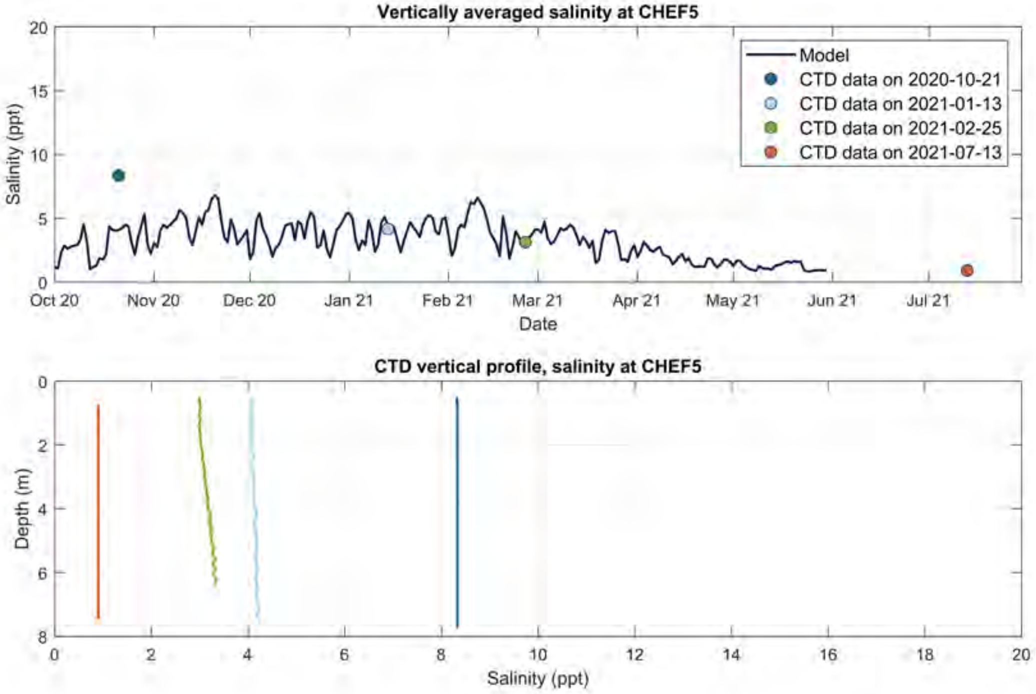

Figure D-5. Salinity validation using CTD casts at CHEF5. Top graph: simulated daily averaged salinity by the Hydrodynamic Model (blue line) compared to depth averaged CTD casts at CHEF5. Bottom graph: vertical salinity CTD profiles collected at CHEF5. The colors of the CTD vertical profiles in the bottom graph match the color of the depth averaged CTD observation in the top graph.

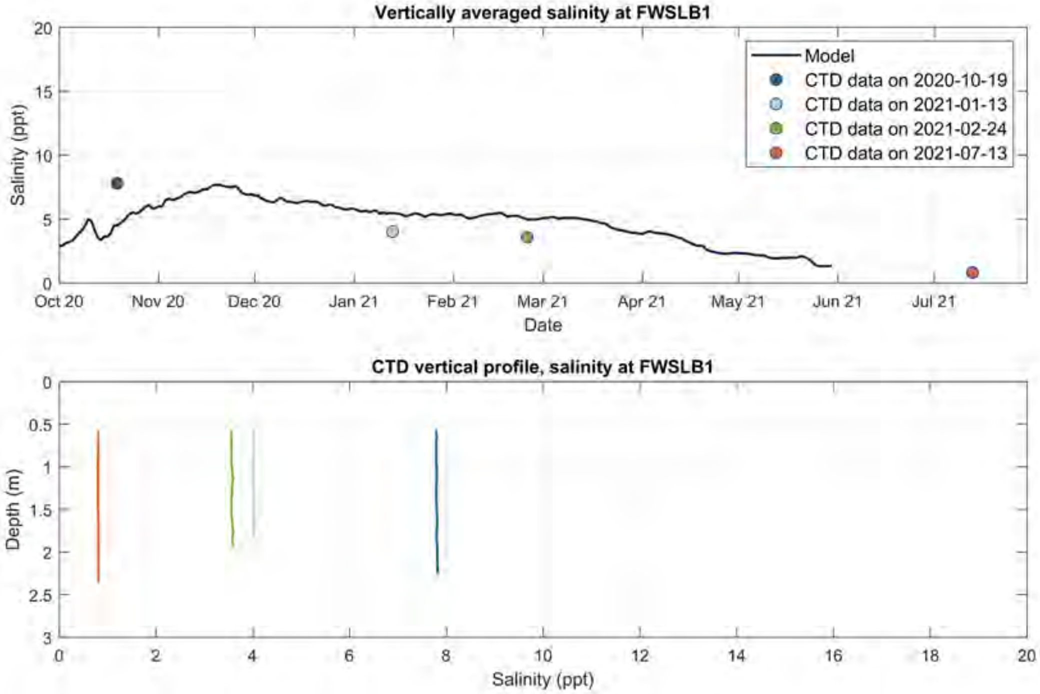

Figure D-6. Salinity validation using CTD casts at FWSLB1. Top graph: simulated daily averaged salinity by the Hydrodynamic Model (blue line) compared to depth averaged CTD casts at FWSLB1. Bottom graph: vertical salinity CTD profiles collected at FWSLB1. The colors of the CTD vertical profiles in the bottom graph match the color of the depth averaged CTD observation in the top graph.

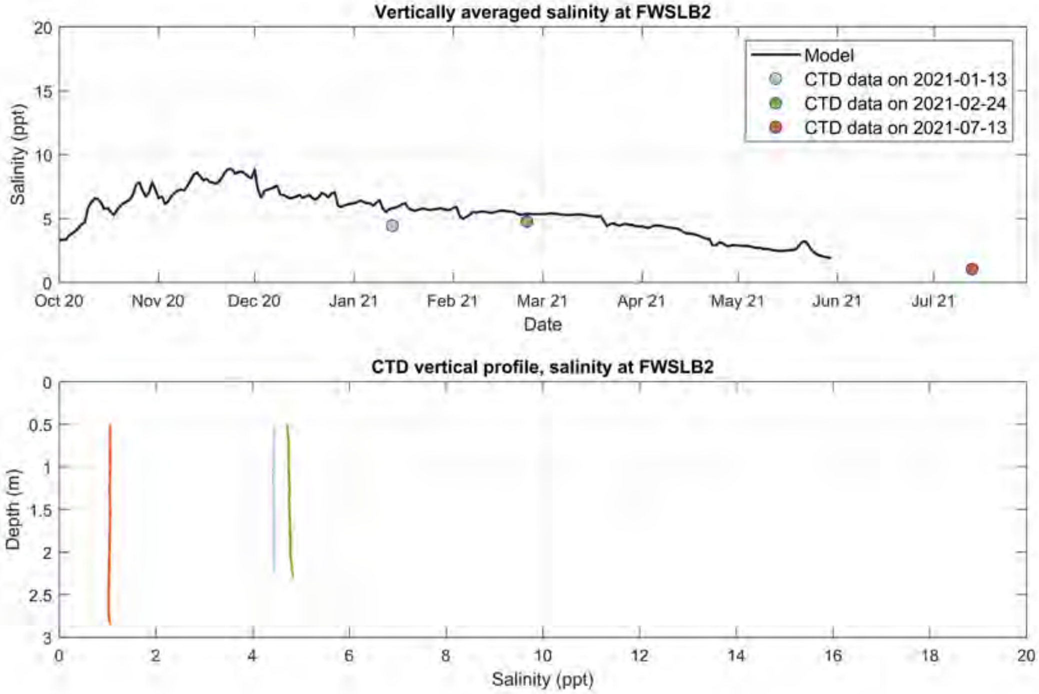

Figure D-7. Salinity validation using CTD casts at FWSLB2. Top graph: simulated daily averaged salinity by the Hydrodynamic Model (blue line) compared to depth averaged CTD casts at FWSLB2. Bottom graph: vertical salinity CTD profiles collected at FWSLB2. The colors of the CTD vertical profiles in the bottom graph match the color of the depth averaged CTD observation in the top graph.

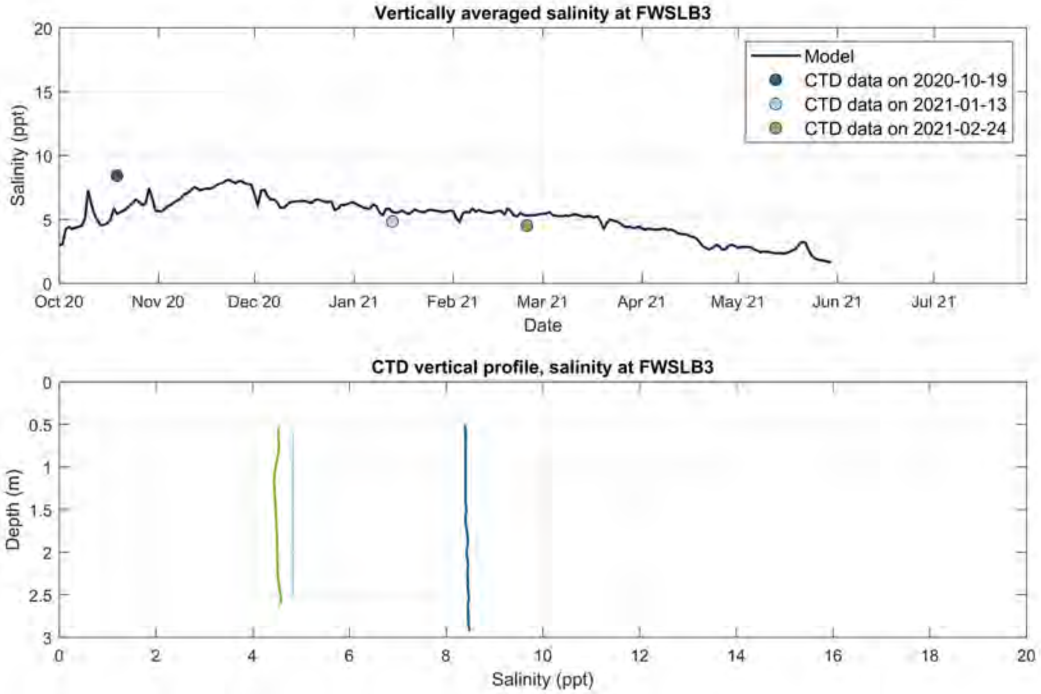

Figure D-8. Salinity validation using CTD casts at FWSLB3. Top graph: simulated daily averaged salinity by the Hydrodynamic Model (blue line) compared to depth averaged CTD casts at FWSLB3. Bottom graph: vertical salinity CTD profiles collected at FWSLB3. The colors of the CTD vertical profiles in the bottom graph match the color of the depth averaged CTD observation in the top graph.

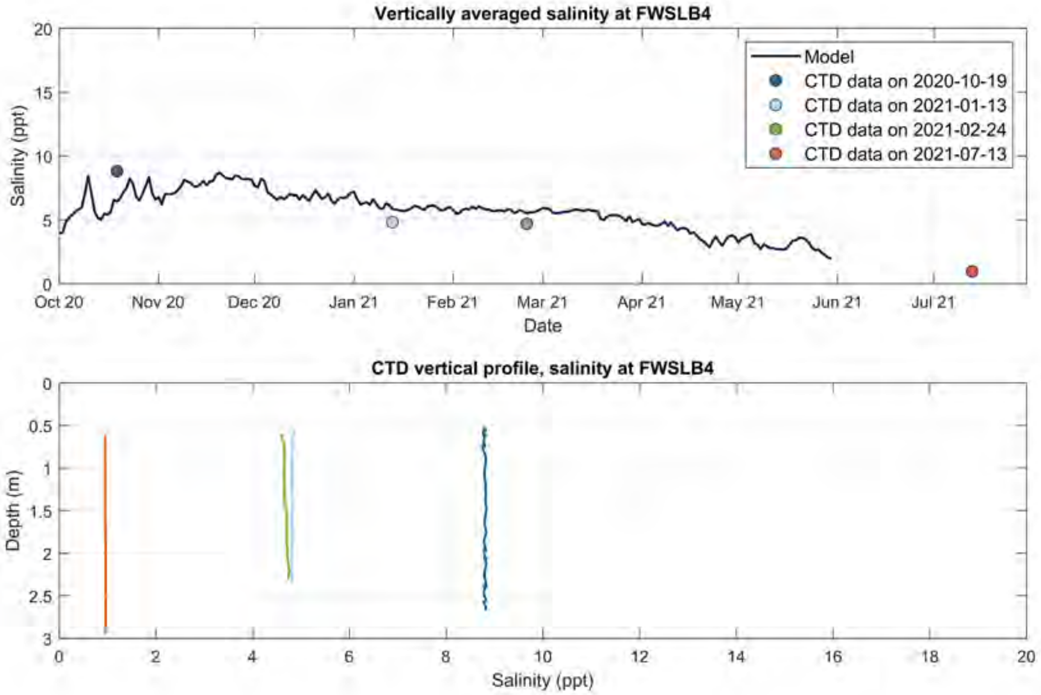

Figure D-9. Salinity validation using CTD casts at FWSLB4. Top graph: simulated daily averaged salinity by the Hydrodynamic Model (blue line) compared to depth averaged CTD casts at FWSLB4. Bottom graph: vertical salinity CTD profiles collected at FWSLB4. The colors of the CTD vertical profiles in the bottom graph match the color of the depth averaged CTD observation in the top graph.

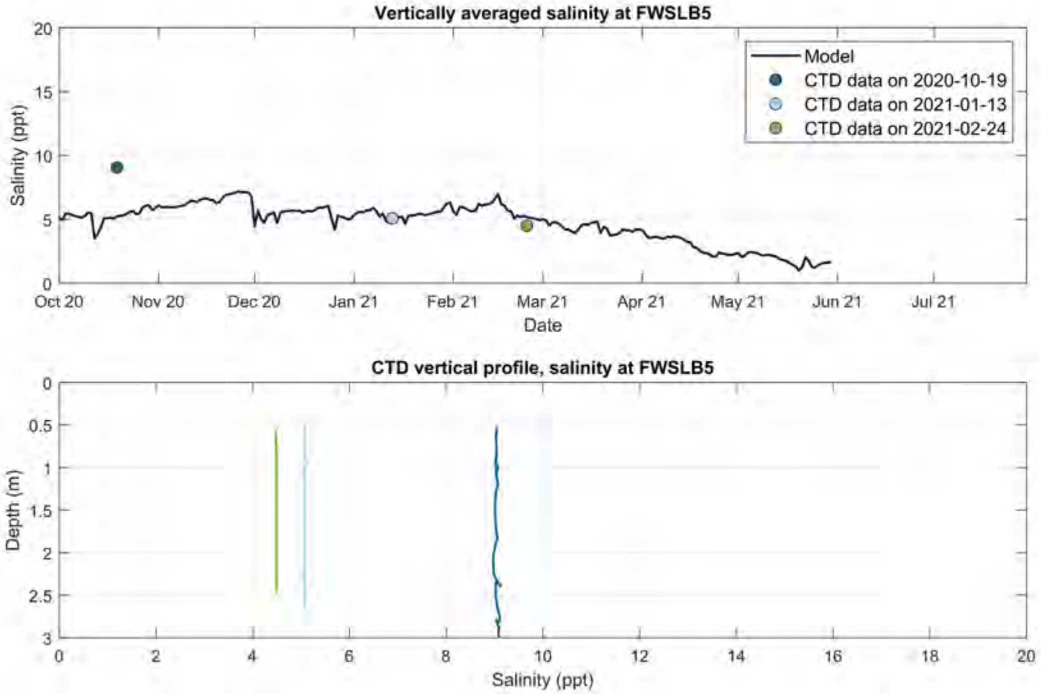

Figure D-10. Salinity validation using CTD casts at FWSLB5. Top graph: simulated daily averaged salinity by the Hydrodynamic Model (blue line) compared to depth averaged CTD casts at FWSLB5. Bottom graph: vertical salinity CTD profiles collected at FWSLB5. The colors of the CTD vertical profiles in the bottom graph match the color of the depth averaged CTD observation in the top graph.

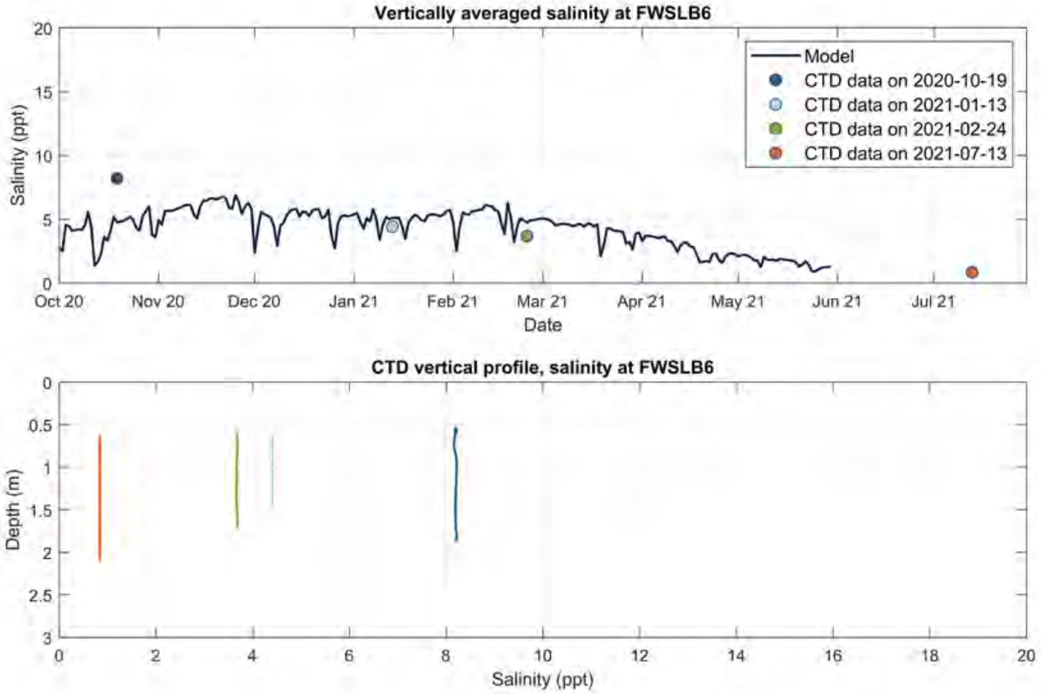

Figure D-11. Salinity validation using CTD casts at FWSLB6. Top graph: simulated daily averaged salinity by the Hydrodynamic Model (blue line) compared to depth averaged CTD casts at FWSLB6. Bottom graph: vertical salinity CTD profiles collected at FWSLB6. The colors of the CTD vertical profiles in the bottom graph match the color of the depth averaged CTD observation in the top graph.

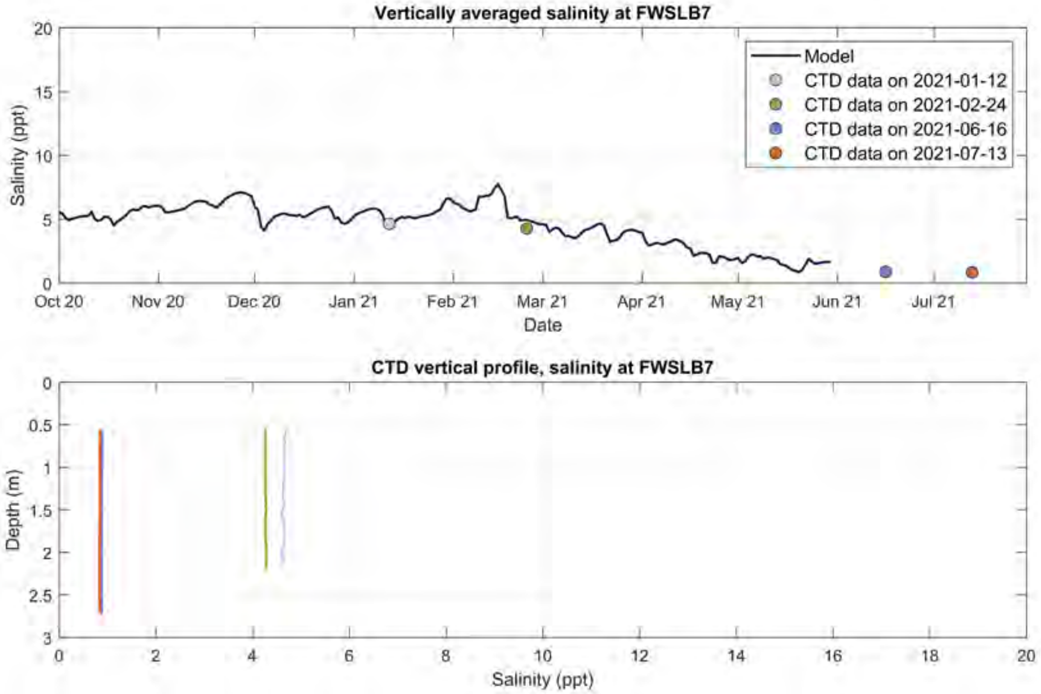

Figure D-12. Salinity validation using CTD casts at FWSLB7. Top graph: simulated daily averaged salinity by the Hydrodynamic Model (blue line) compared to depth averaged CTD casts at FWSLB7. Bottom graph: vertical salinity CTD profiles collected at FWSLB7. The colors of the CTD vertical profiles in the bottom graph match the color of the depth averaged CTD observation in the top graph.

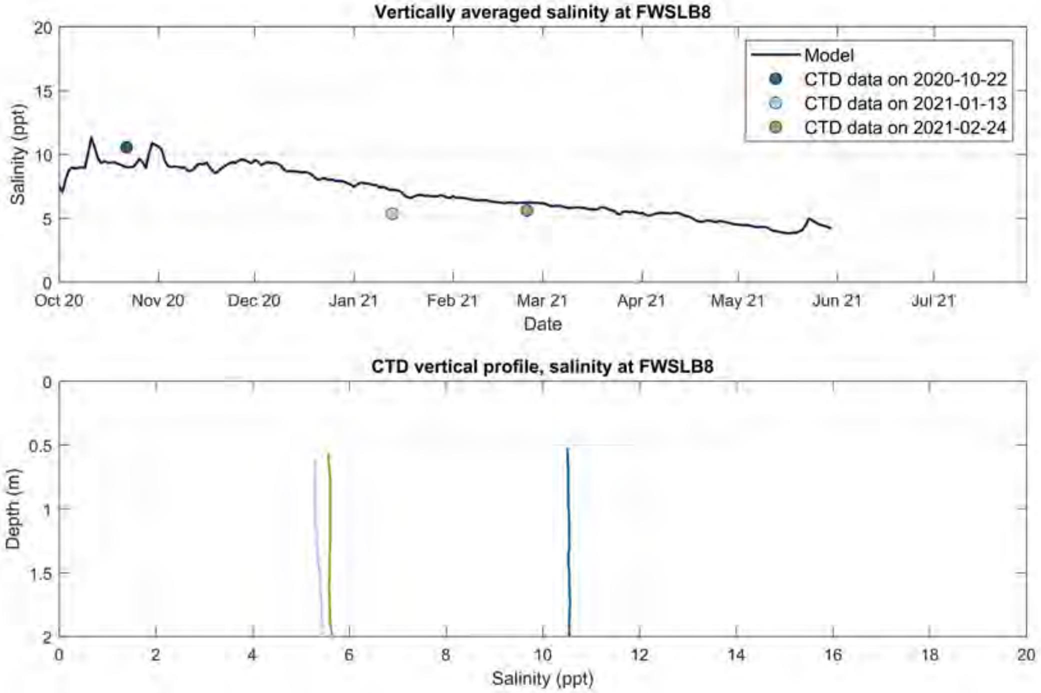

Figure D-13. Salinity validation using CTD casts at FWSLB8. Top graph: simulated daily averaged salinity by the Hydrodynamic Model (blue line) compared to depth averaged CTD casts at FWSLB8. Bottom graph: vertical salinity CTD profiles collected at FWSLB8. The colors of the CTD vertical profiles in the bottom graph match the color of the depth averaged CTD observation in the top graph.

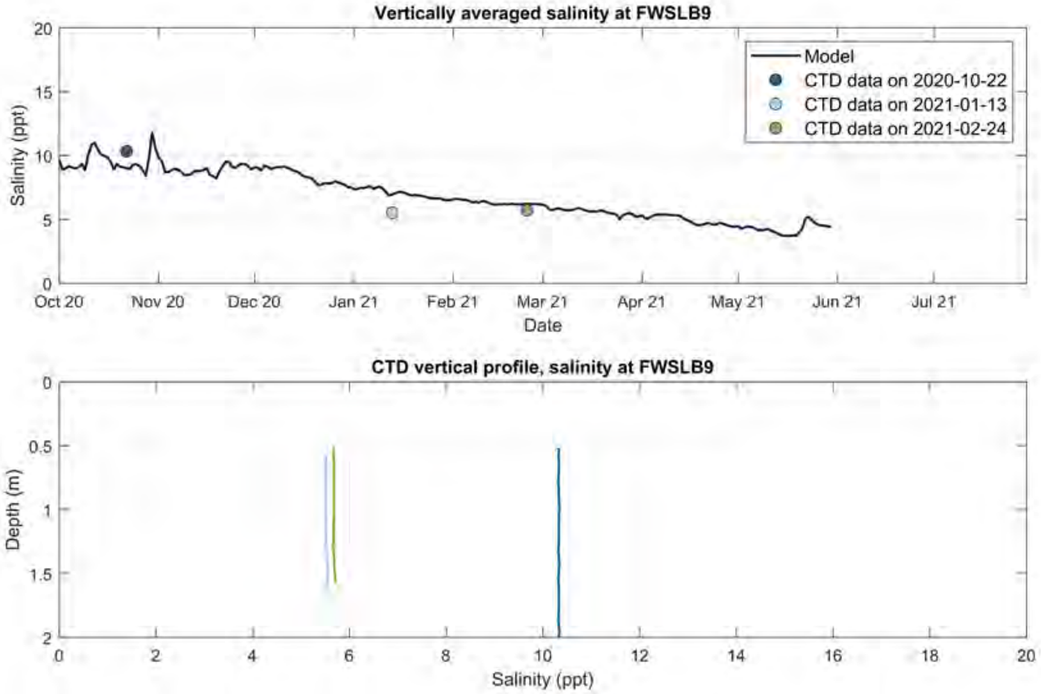

Figure D-14. Salinity validation using CTD casts at FWSLB9. Top graph: simulated daily averaged salinity by the Hydrodynamic Model (blue line) compared to depth averaged CTD casts at FWSLB9. Bottom graph: vertical salinity CTD profiles collected at FWSLB9. The colors of the CTD vertical profiles in the bottom graph match the color of the depth averaged CTD observation in the top graph.

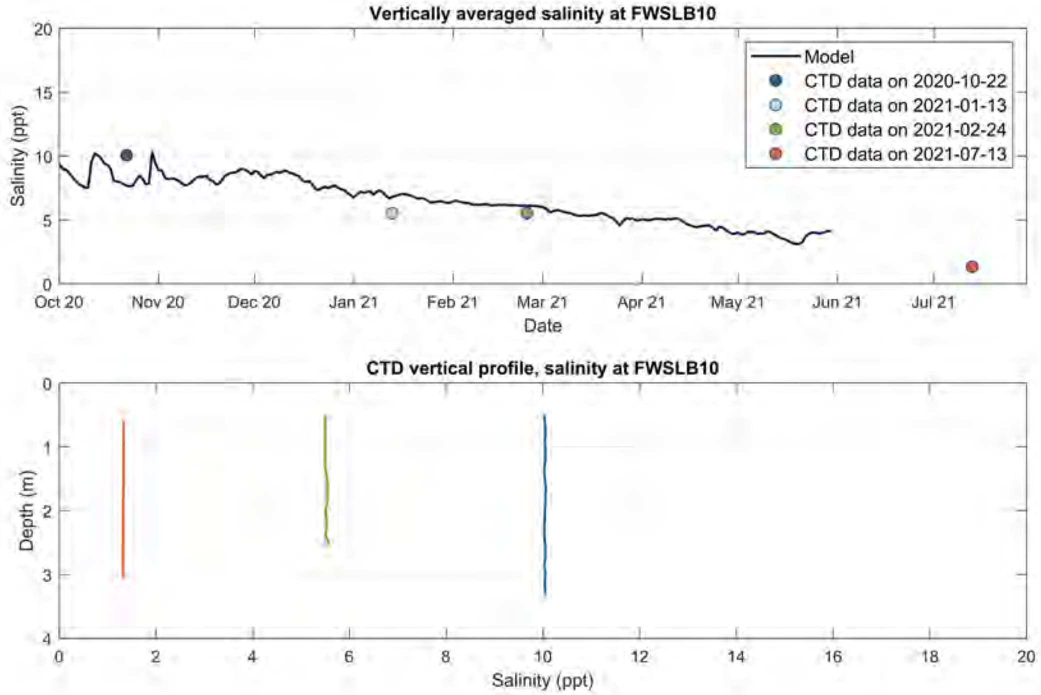

Figure D-15. Salinity validation using CTD casts at FWSLB10. Top graph: simulated daily averaged salinity by the Hydrodynamic Model (blue line) compared to depth averaged CTD casts at FWSLB10. Bottom graph: vertical salinity CTD profiles collected at FWSLB10. The colors of the CTD vertical profiles in the bottom graph match the color of the depth averaged CTD observation in the top graph.

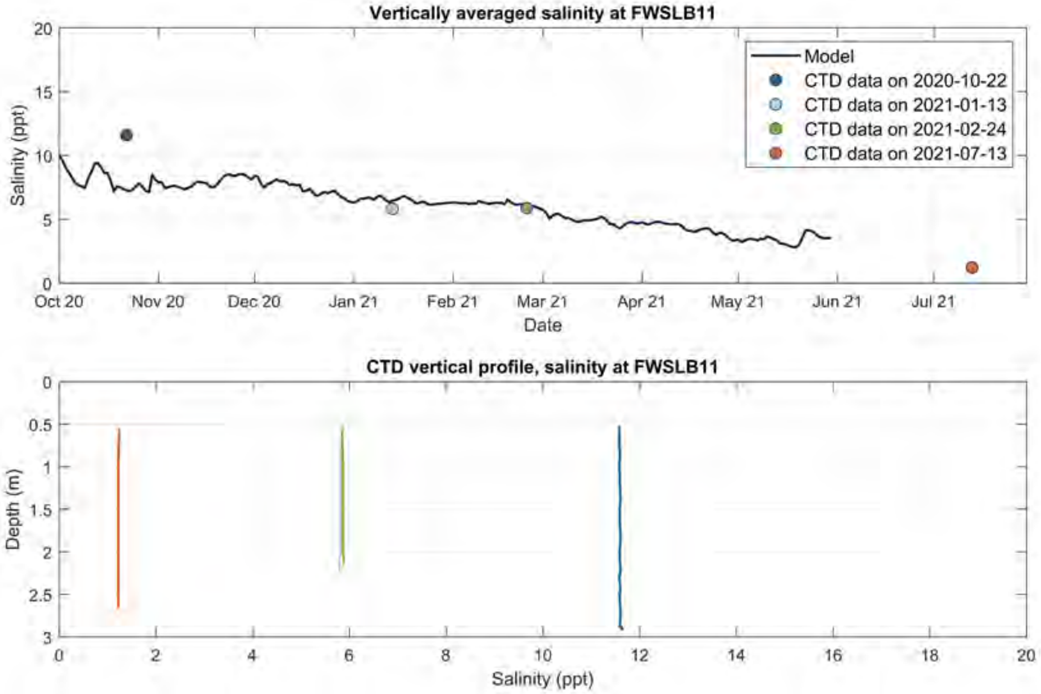

Figure D-16. Salinity validation using CTD casts at FWSLB11. Top graph: simulated daily averaged salinity by the Hydrodynamic Model (blue line) compared to depth averaged CTD casts at FWSLB11. Bottom graph: vertical salinity CTD profiles collected at FWSLB11. The colors of the CTD vertical profiles in the bottom graph match the color of the depth averaged CTD observation in the top graph.

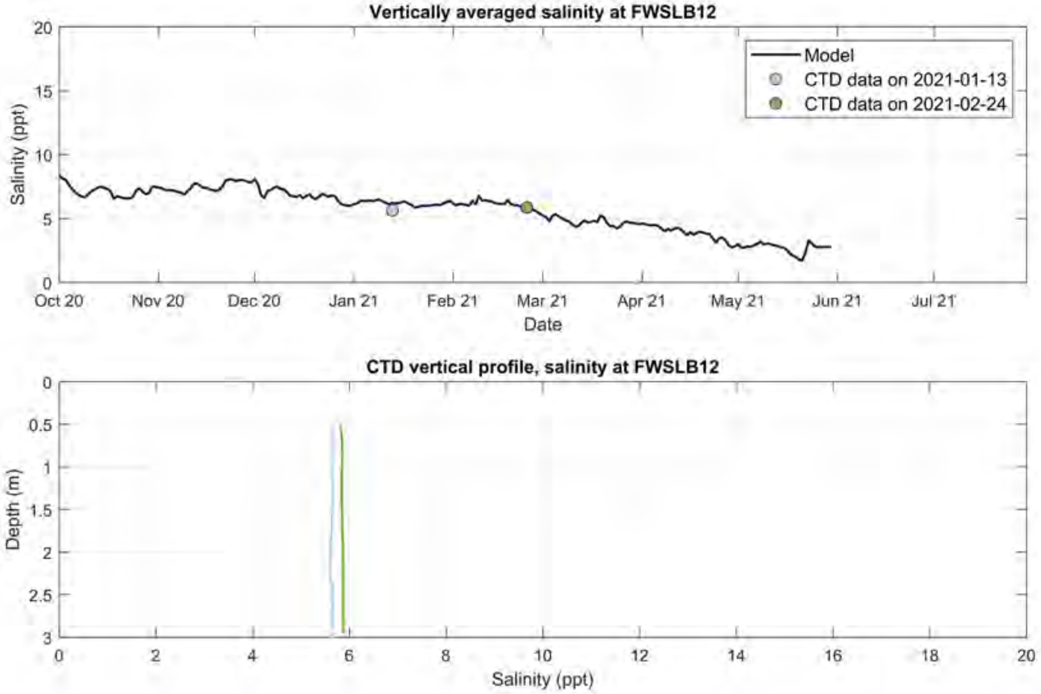

Figure D-17. Salinity validation using CTD casts at FWSLB12. Top graph: simulated daily averaged salinity by the Hydrodynamic Model (blue line) compared to depth averaged CTD casts at FWSLB12. Bottom graph: vertical salinity CTD profiles collected at FWSLB12. The colors of the CTD vertical profiles in the bottom graph match the color of the depth averaged CTD observation in the top graph.

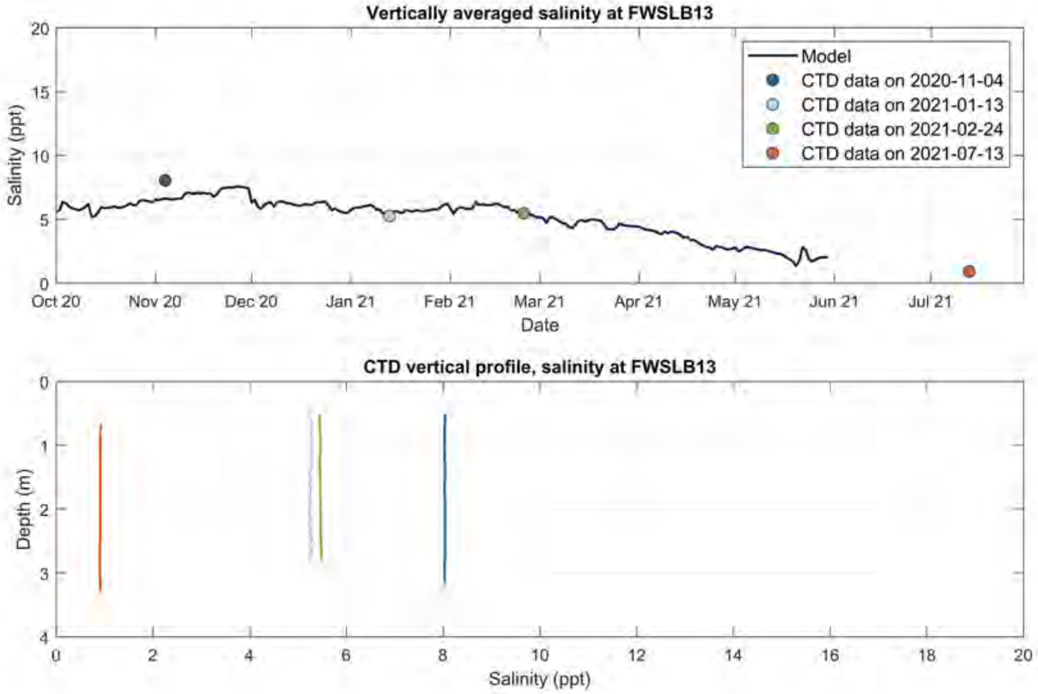

Figure D-18. Salinity validation using CTD casts at FWSLB13. Top graph: simulated daily averaged salinity by the Hydrodynamic Model (blue line) compared to depth averaged CTD casts at FWSLB13. Bottom graph: vertical salinity CTD profiles collected at FWSLB13. The colors of the CTD vertical profiles in the bottom graph match the color of the depth averaged CTD observation in the top graph.

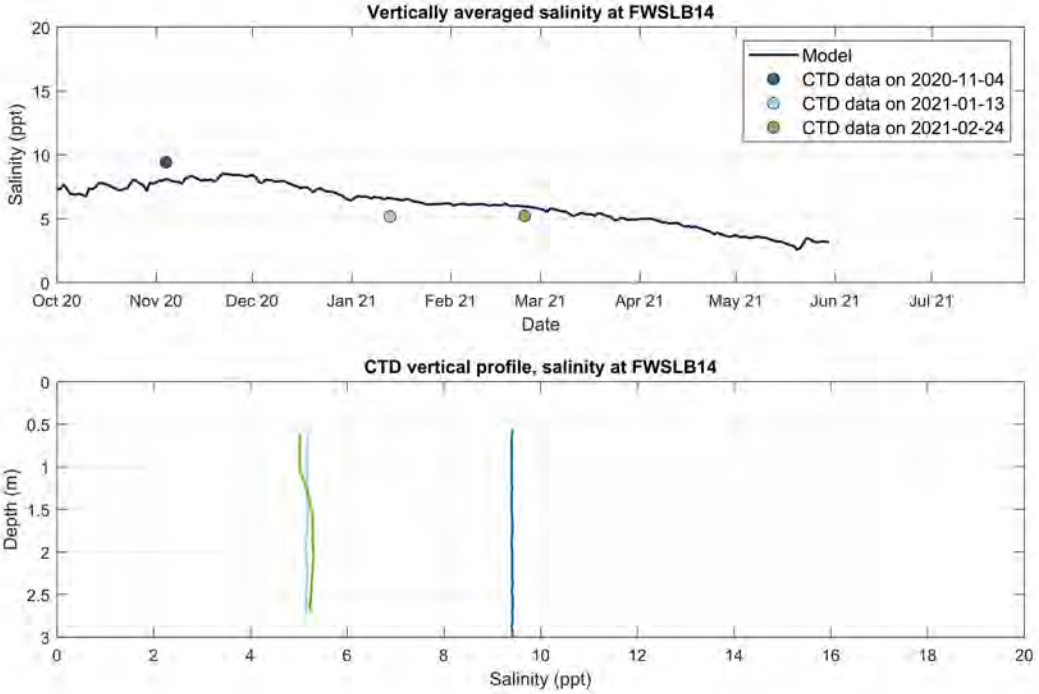

Figure D-19. Salinity validation using CTD casts at FWSLB14. Top graph: simulated daily averaged salinity by the Hydrodynamic Model (blue line) compared to depth averaged CTD casts at FWSLB14. Bottom graph: vertical salinity CTD profiles collected at FWSLB14. The colors of the CTD vertical profiles in the bottom graph match the color of the depth averaged CTD observation in the top graph.

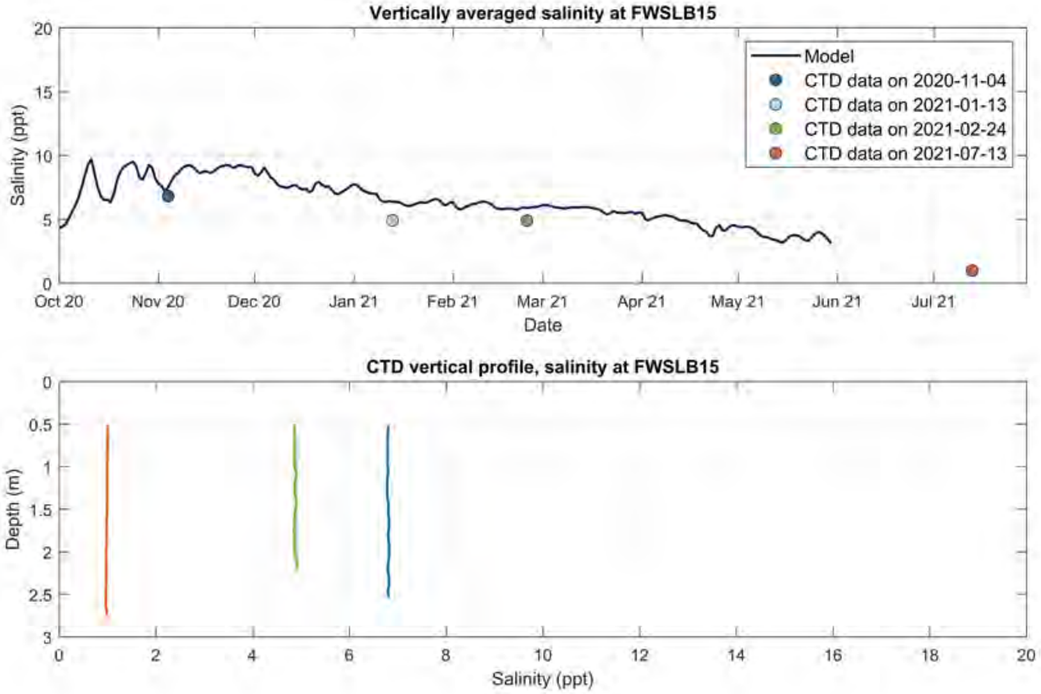

Figure D-20. Salinity validation using CTD casts at FWSLB15. Top graph: simulated daily averaged salinity by the Hydrodynamic Model (blue line) compared to depth averaged CTD casts at FWSLB15. Bottom graph: vertical salinity CTD profiles collected at FWSLB15. The colors of the CTD vertical profiles in the bottom graph match the color of the depth averaged CTD observation in the top graph.

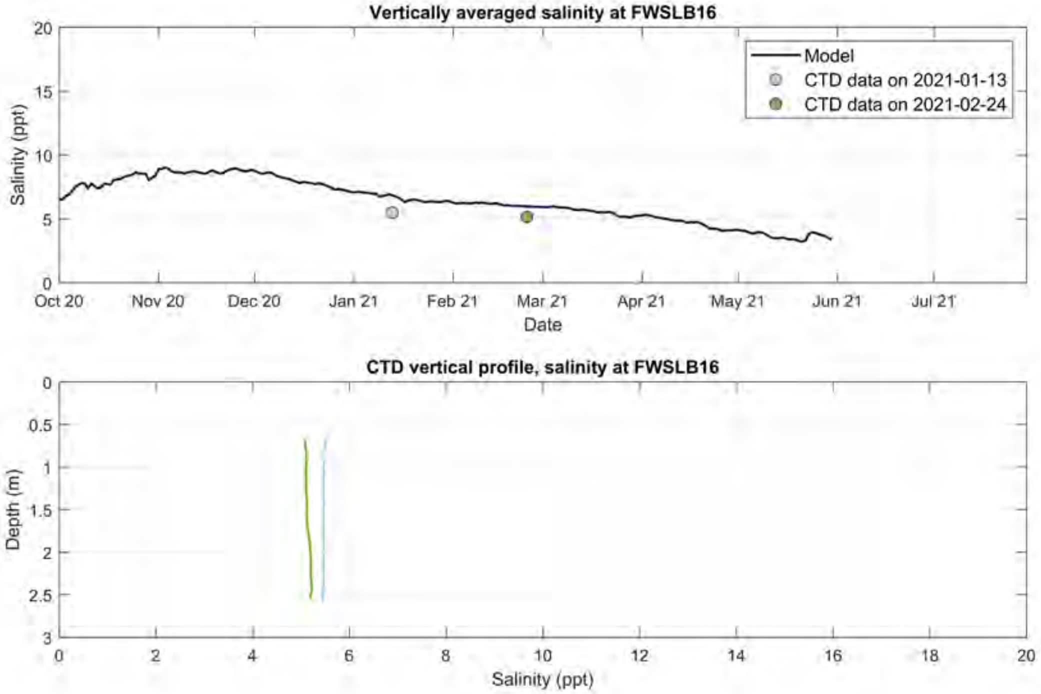

Figure D-21. Salinity validation using CTD casts at FWSLB16. Top graph: simulated daily averaged salinity by the Hydrodynamic Model (blue line) compared to depth averaged CTD casts at FWSLB16. Bottom graph: vertical salinity CTD profiles collected at FWSLB16. The colors of the CTD vertical profiles in the bottom graph match the color of the depth averaged CTD observation in the top graph.

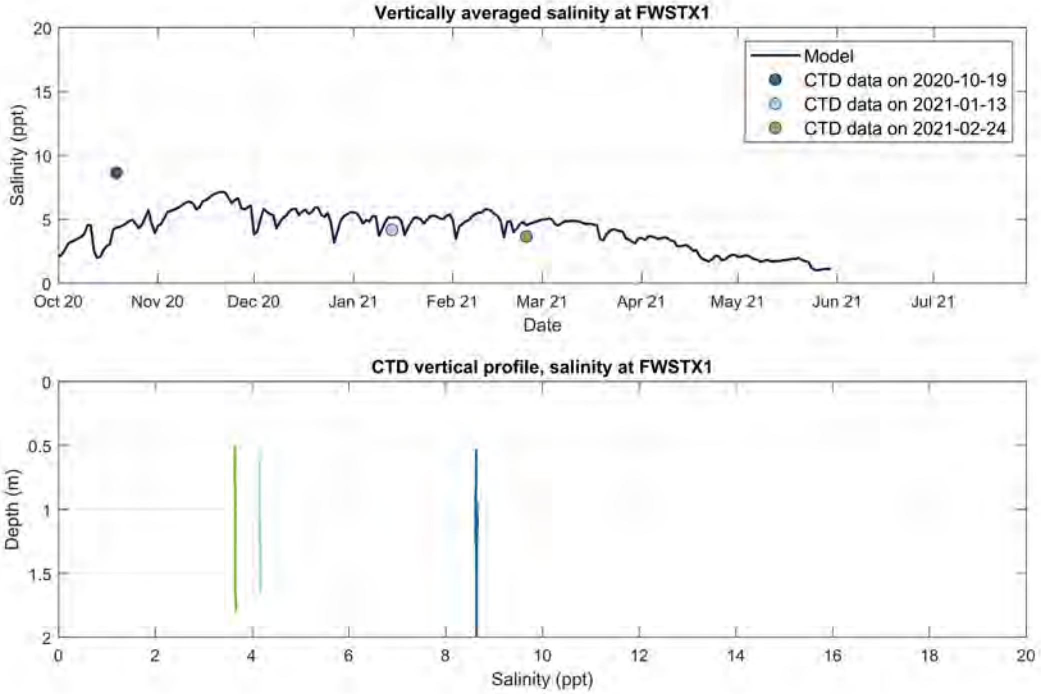

Figure D-22. Salinity validation using CTD casts at FWSTX1. Top graph: simulated daily averaged salinity by the Hydrodynamic Model (blue line) compared to depth averaged CTD casts at FWSTX1. Bottom graph: vertical salinity CTD profiles collected at FWSTX1. The colors of the CTD vertical profiles in the bottom graph match the color of the depth averaged CTD observation in the top graph.

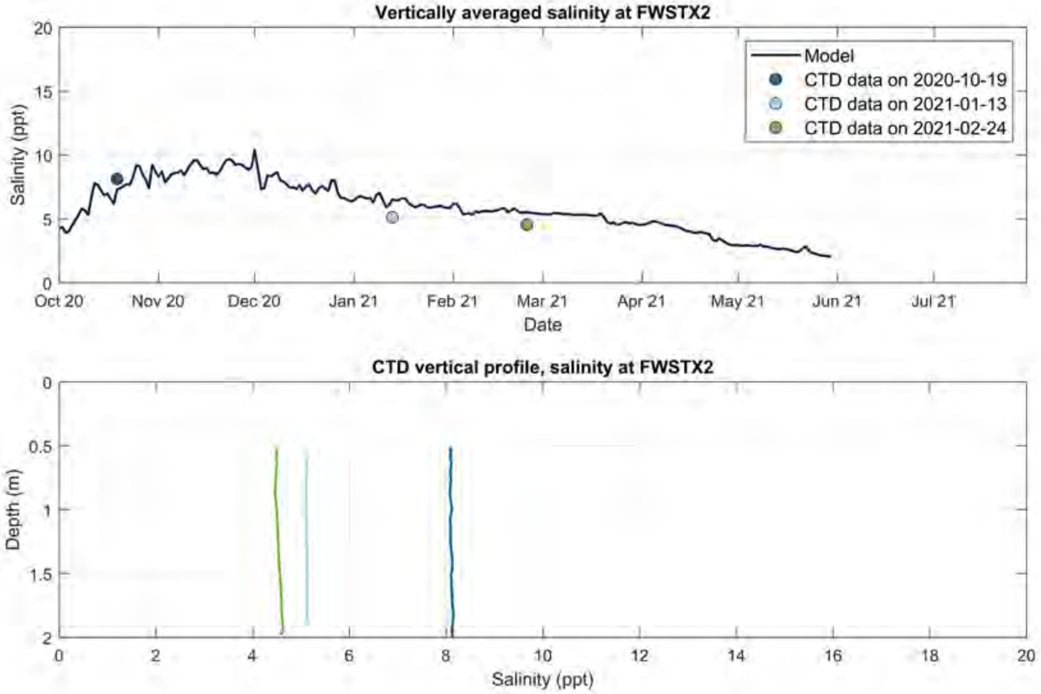

Figure D-23. Salinity validation using CTD casts at FWSTX2. Top graph: simulated daily averaged salinity by the Hydrodynamic Model (blue line) compared to depth averaged CTD casts at FWSTX2. Bottom graph: vertical salinity CTD profiles collected at FWSTX2. The colors of the CTD vertical profiles in the bottom graph match the color of the depth averaged CTD observation in the top graph.

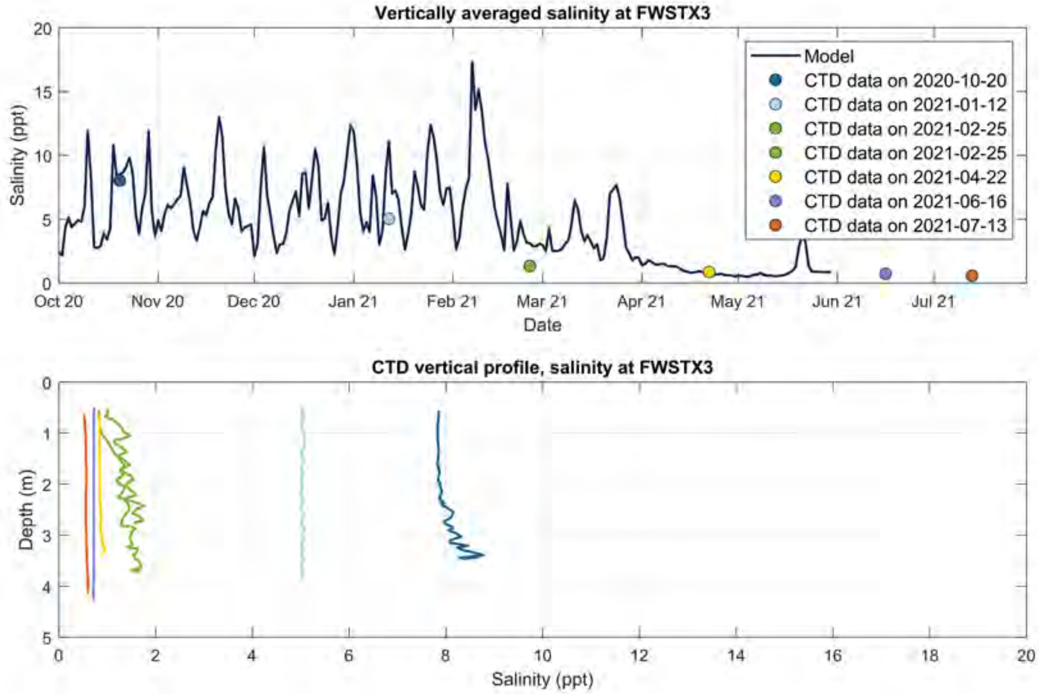

Figure D-24. Salinity validation using CTD casts at FWSTX3. Top graph: simulated daily averaged salinity by the Hydrodynamic Model (blue line) compared to depth averaged CTD casts at FWSTX3. Bottom graph: vertical salinity CTD profiles collected at FWSTX3. The colors of the CTD vertical profiles in the bottom graph match the color of the depth averaged CTD observation in the top graph.

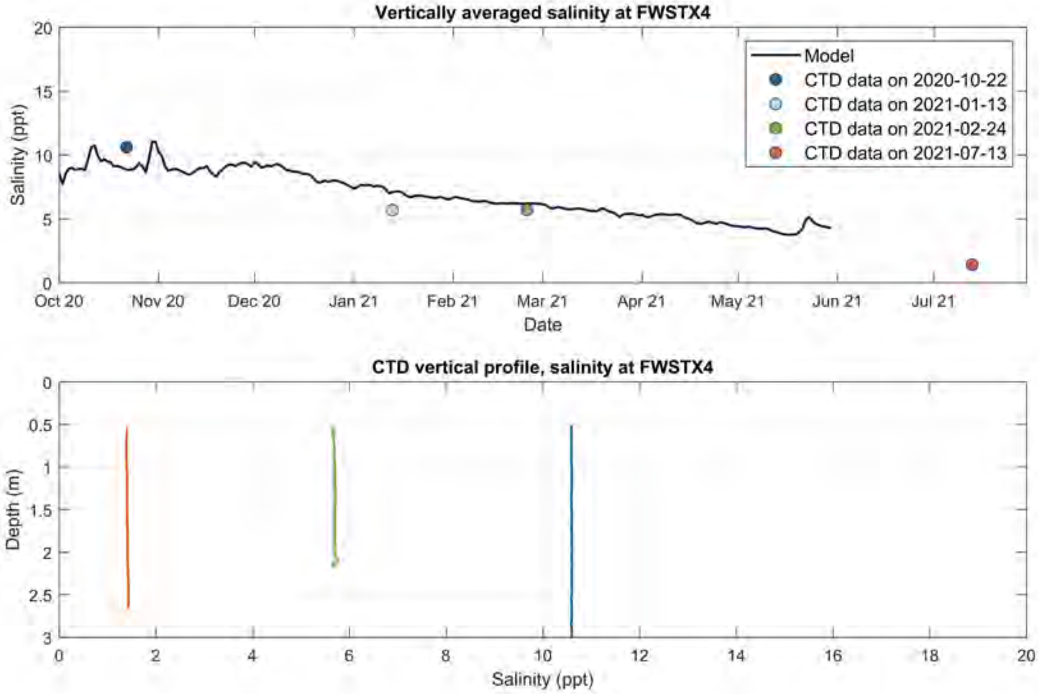

Figure D-25. Salinity validation using CTD casts at FWSTX4. Top graph: simulated daily averaged salinity by the Hydrodynamic Model (blue line) compared to depth averaged CTD casts at FWSTX4. Bottom graph: vertical salinity CTD profiles collected at FWSTX4. The colors of the CTD vertical profiles in the bottom graph match the color of the depth averaged CTD observation in the top graph.

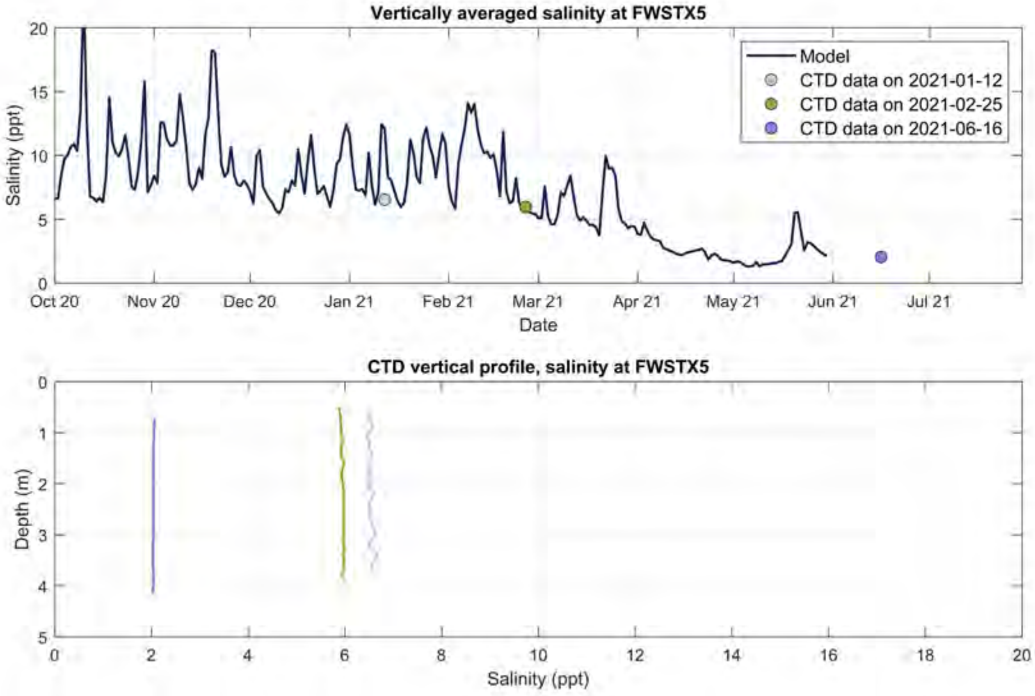

Figure D-26. Salinity validation using CTD casts at FWSTX5. Top graph: simulated daily averaged salinity by the Hydrodynamic Model (blue line) compared to depth averaged CTD casts at FWSTX5. Bottom graph: vertical salinity CTD profiles collected at FWSTX5. The colors of the CTD vertical profiles in the bottom graph match the color of the depth averaged CTD observation in the top graph.

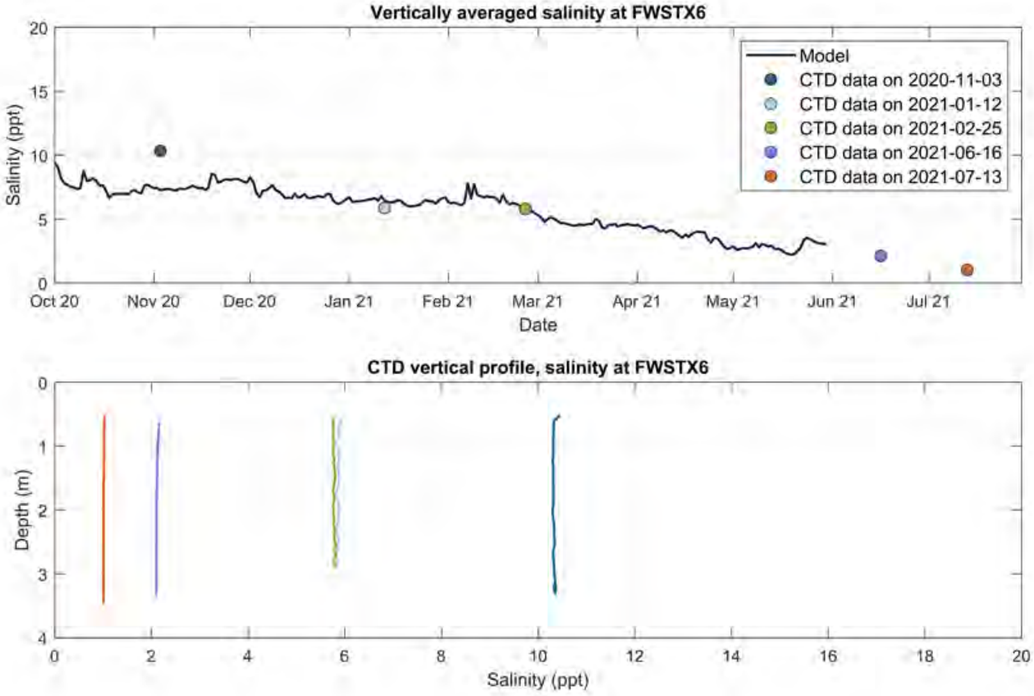

Figure D-27. Salinity validation using CTD casts at FWSTX6. Top graph: simulated daily averaged salinity by the Hydrodynamic Model (blue line) compared to depth averaged CTD casts at FWSTX6. Bottom graph: vertical salinity CTD profiles collected at FWSTX6. The colors of the CTD vertical profiles in the bottom graph match the color of the depth averaged CTD observation in the top graph.

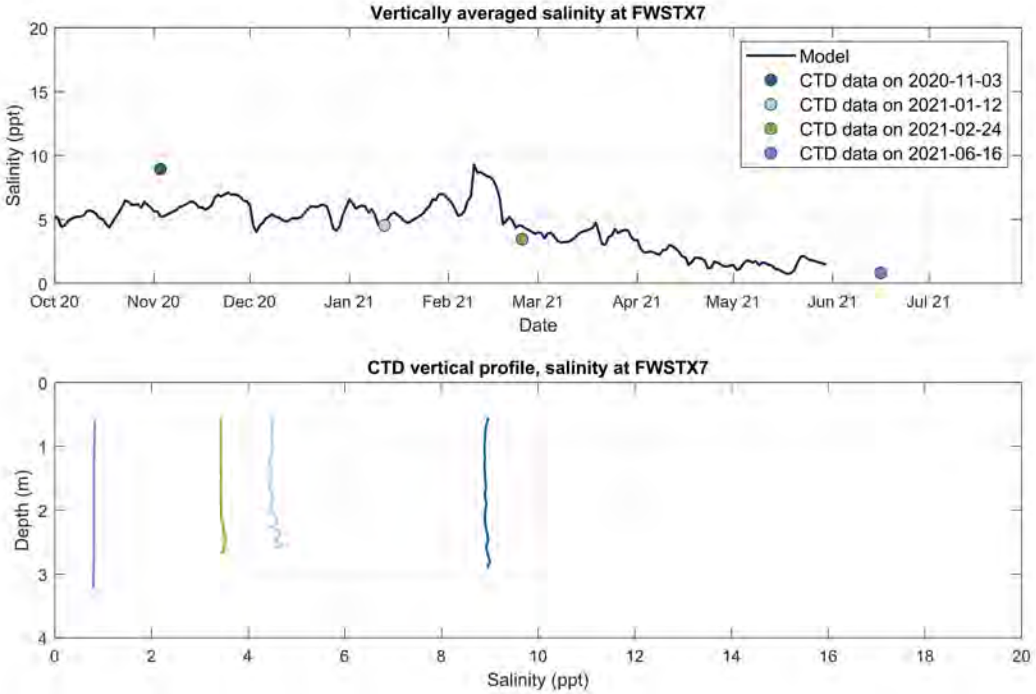

Figure D-28. Salinity validation using CTD casts at FWSTX7. Top graph: simulated daily averaged salinity by the Hydrodynamic Model (blue line) compared to depth averaged CTD casts at FWSTX7. Bottom graph: vertical salinity CTD profiles collected at FWSTX7. The colors of the CTD vertical profiles in the bottom graph match the color of the depth averaged CTD observation in the top graph.

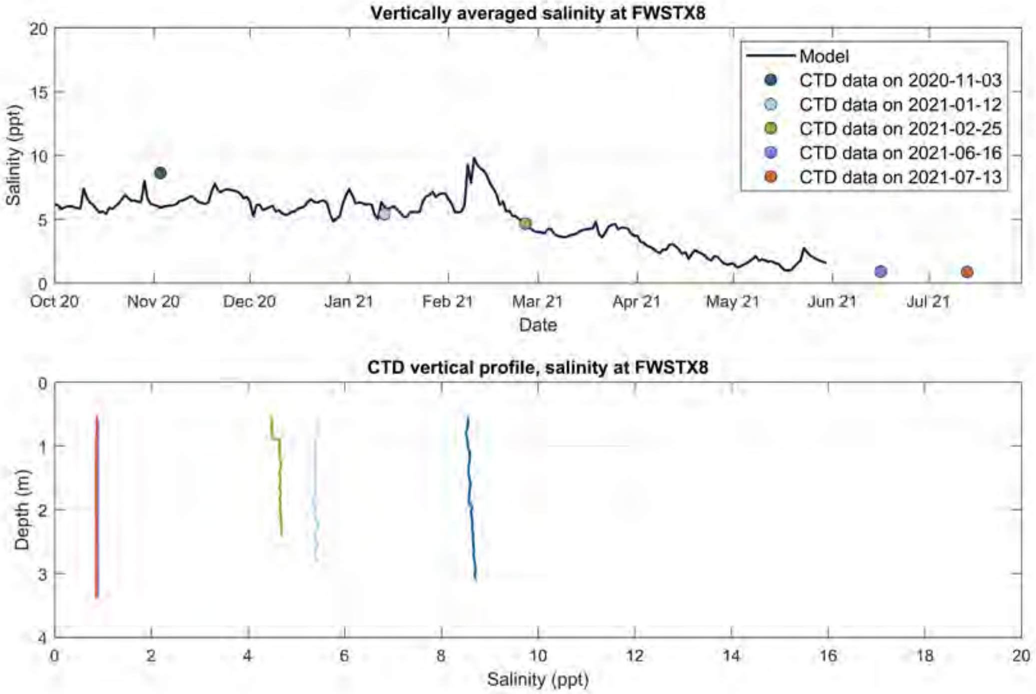

Figure D-29. Salinity validation using CTD casts at FWSTX8. Top graph: simulated daily averaged salinity by the Hydrodynamic Model (blue line) compared to depth averaged CTD casts at FWSTX8. Bottom graph: vertical salinity CTD profiles collected at FWSTX8. The colors of the CTD vertical profiles in the bottom graph match the color of the depth averaged CTD observation in the top graph.

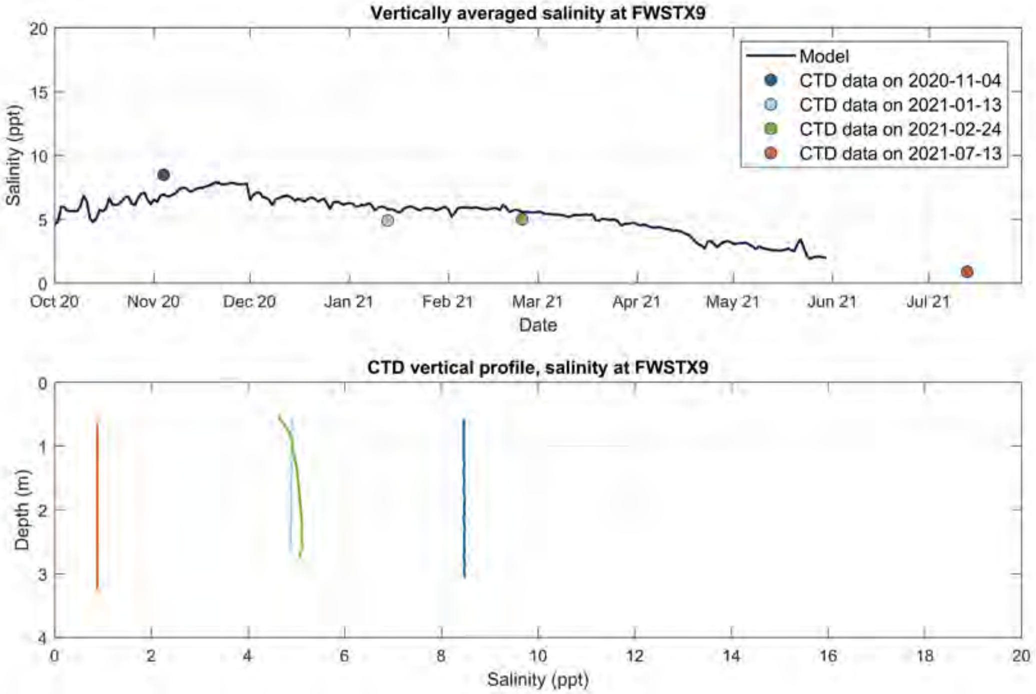

Figure D-30. Salinity validation using CTD casts at FWSTX9. Top graph: simulated daily averaged salinity by the Hydrodynamic Model (blue line) compared to depth averaged CTD casts at FWSTX9. Bottom graph: vertical salinity CTD profiles collected at FWSTX9. The colors of the CTD vertical profiles in the bottom graph match the color of the depth averaged CTD observation in the top graph.

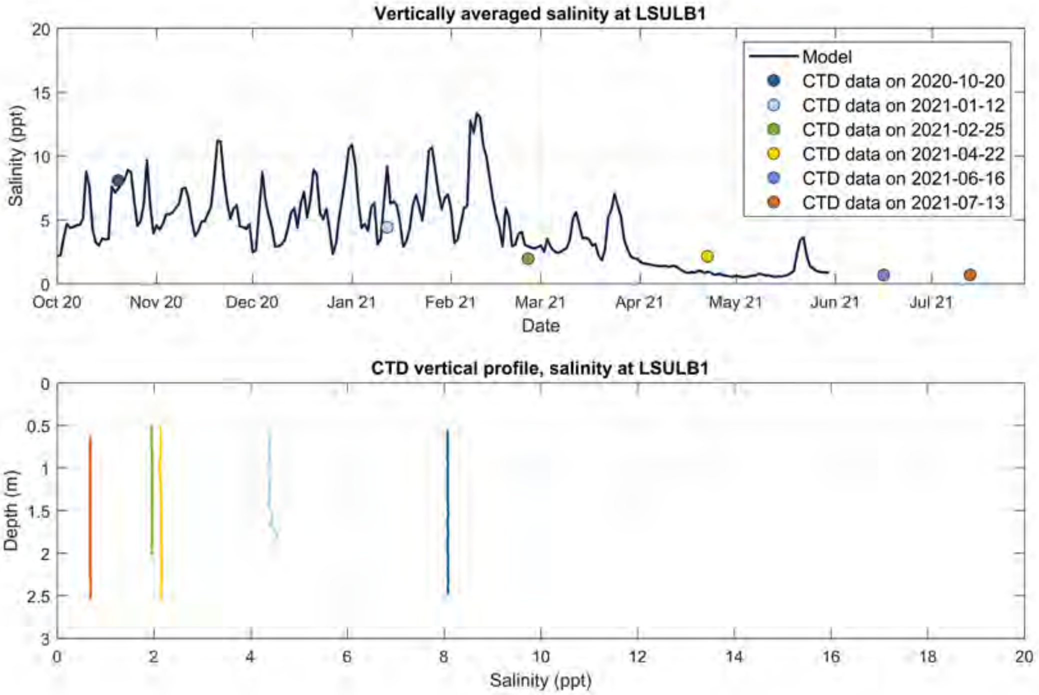

Figure D-31. Salinity validation using CTD casts at LSULB1. Top graph: simulated daily averaged salinity by the Hydrodynamic Model (blue line) compared to depth averaged CTD casts at LSULB1. Bottom graph: vertical salinity CTD profiles collected at LSULB1. The colors of the CTD vertical profiles in the bottom graph match the color of the depth averaged CTD observation in the top graph.

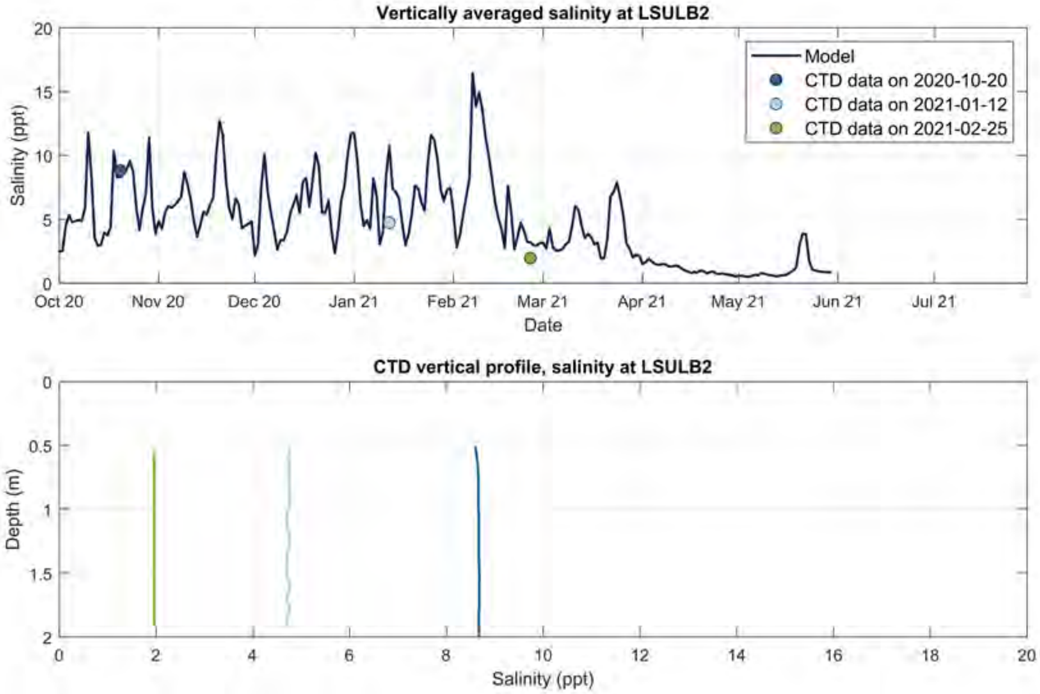

Figure D-32. Salinity validation using CTD casts at LSULB2. Top graph: simulated daily averaged salinity by the Hydrodynamic Model (blue line) compared to depth averaged CTD casts at LSULB2. Bottom graph: vertical salinity CTD profiles collected at LSULB2. The colors of the CTD vertical profiles in the bottom graph match the color of the depth averaged CTD observation in the top graph.

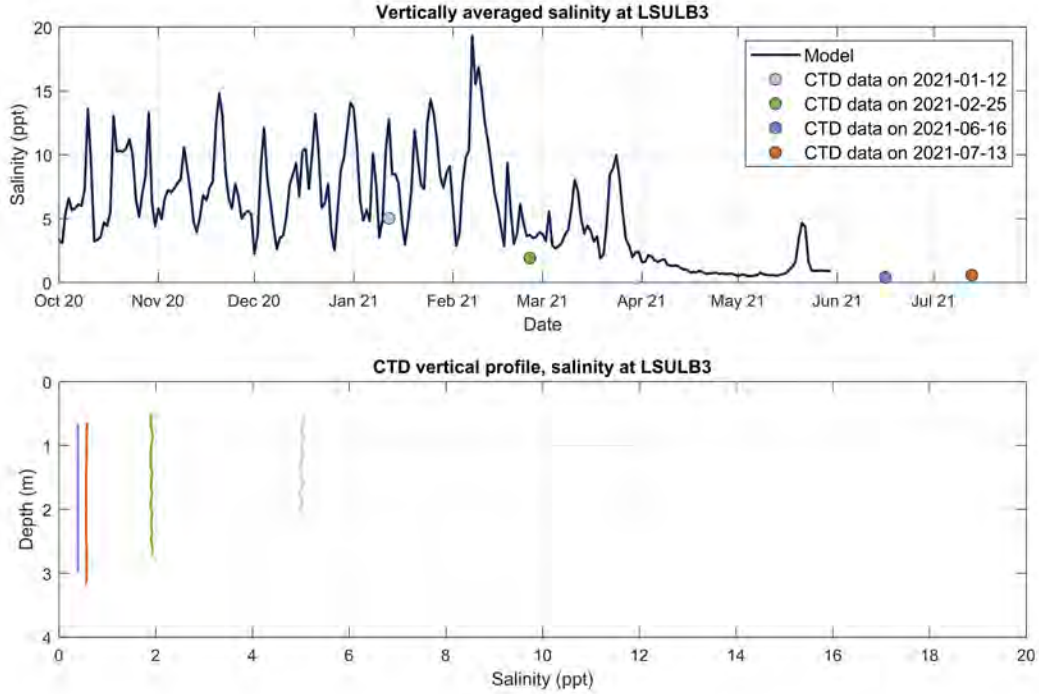

Figure D-33. Salinity validation using CTD casts at LSULB3. Top graph: simulated daily averaged salinity by the Hydrodynamic Model (blue line) compared to depth averaged CTD casts at LSULB3. Bottom graph: vertical salinity CTD profiles collected at LSULB3. The colors of the CTD vertical profiles in the bottom graph match the color of the depth averaged CTD observation in the top graph.

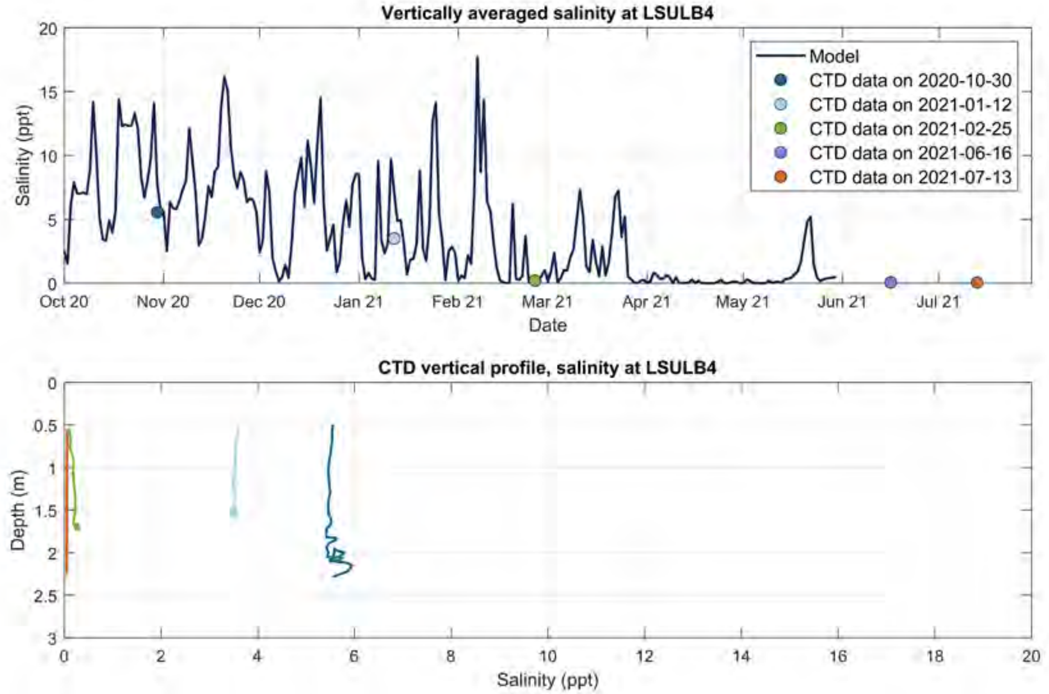

Figure D-34. Salinity validation using CTD casts at LSULB4. Top graph: simulated daily averaged salinity by the Hydrodynamic Model (blue line) compared to depth averaged CTD casts at LSULB4. Bottom graph: vertical salinity CTD profiles collected at LSULB4. The colors of the CTD vertical profiles in the bottom graph match the color of the depth averaged CTD observation in the top graph.

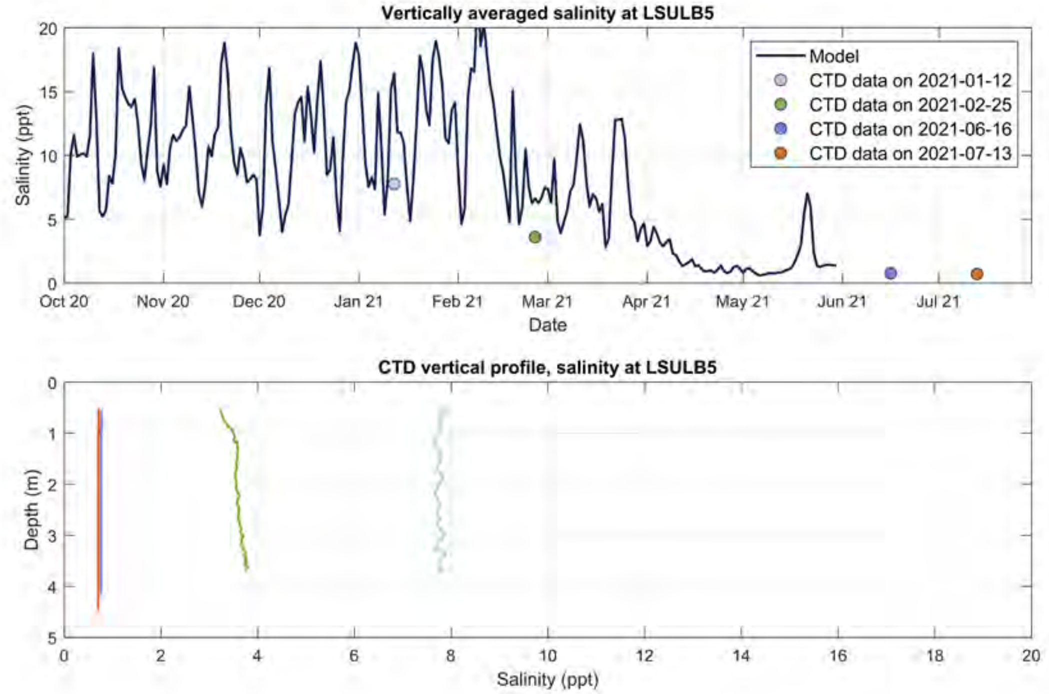

Figure D-35. Salinity validation using CTD casts at LSULB5. Top graph: simulated daily averaged salinity by the Hydrodynamic Model (blue line) compared to depth averaged CTD casts at LSULB5. Bottom graph: vertical salinity CTD profiles collected at LSULB5. The colors of the CTD vertical profiles in the bottom graph match the color of the depth averaged CTD observation in the top graph.

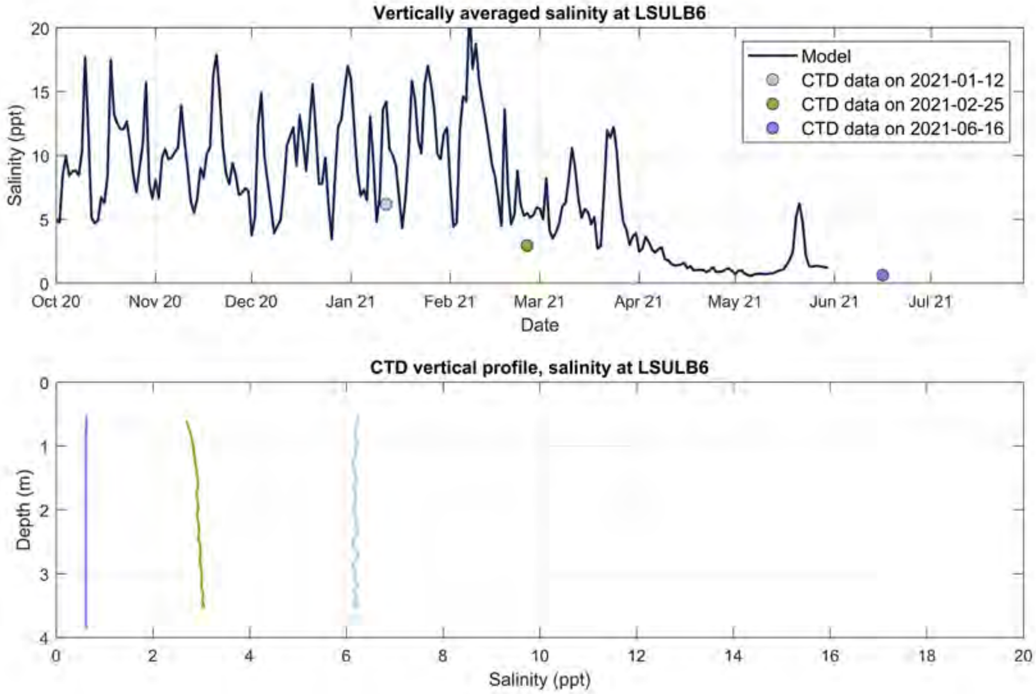

Figure D-36. Salinity validation using CTD casts at LSULB6. Top graph: simulated daily averaged salinity by the Hydrodynamic Model (blue line) compared to depth averaged CTD casts at LSULB6. Bottom graph: vertical salinity CTD profiles collected at LSULB6. The colors of the CTD vertical profiles in the bottom graph match the color of the depth averaged CTD observation in the top graph.

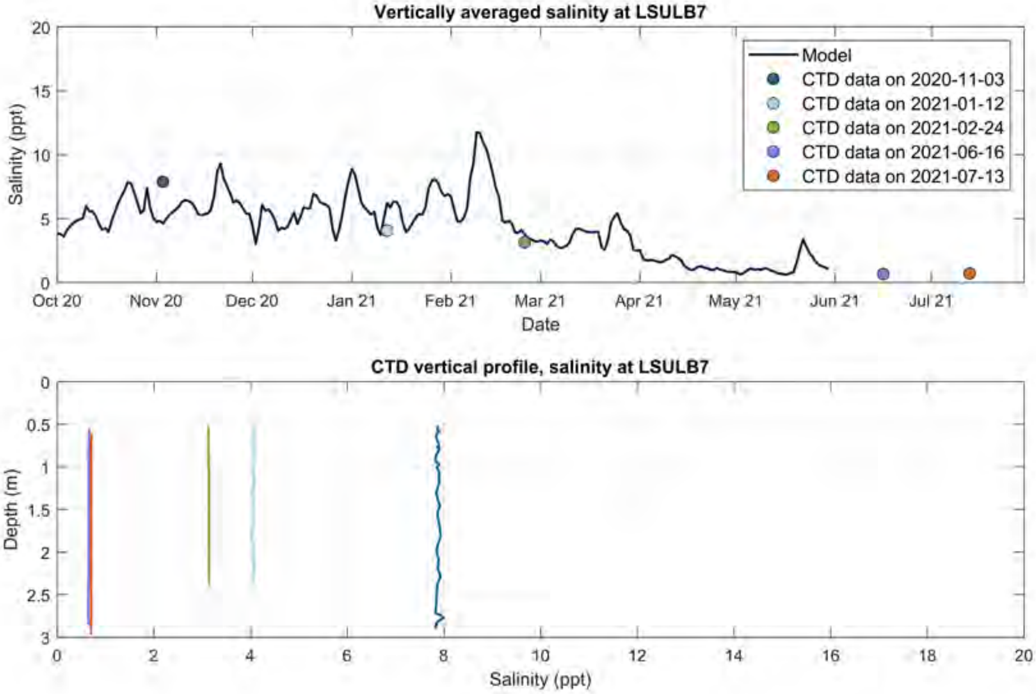

Figure D-37. Salinity validation using CTD casts at LSULB7. Top graph: simulated daily averaged salinity by the Hydrodynamic Model (blue line) compared to depth averaged CTD casts at LSULB7. Bottom graph: vertical salinity CTD profiles collected at LSULB7. The colors of the CTD vertical profiles in the bottom graph match the color of the depth averaged CTD observation in the top graph.

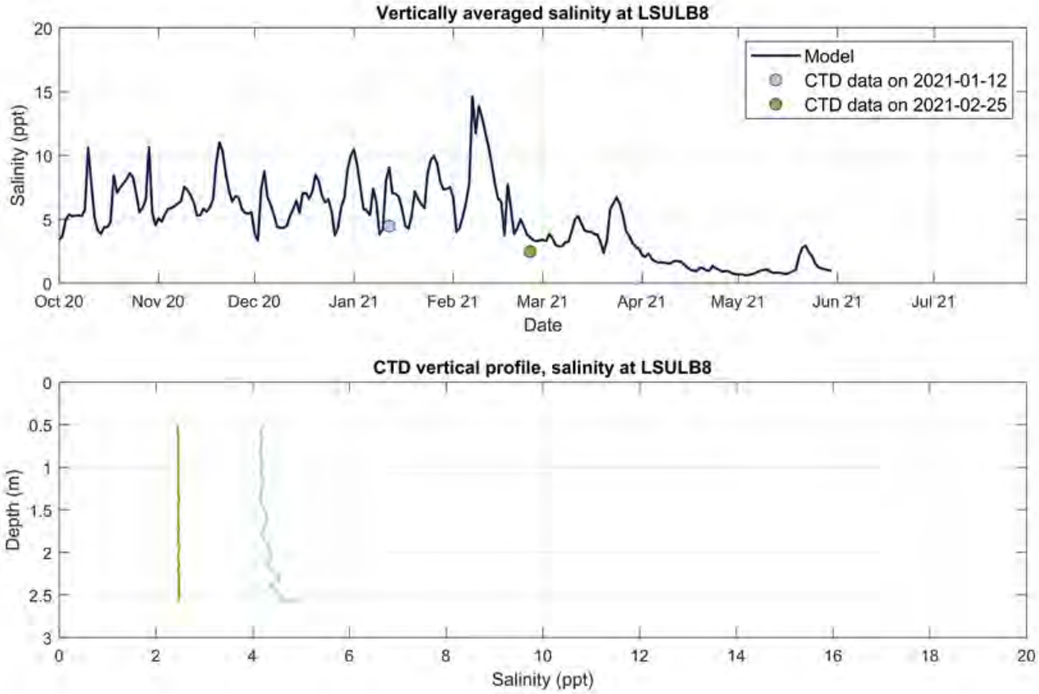

Figure D-38. Salinity validation using CTD casts at LSULB8. Top graph: simulated daily averaged salinity by the Hydrodynamic Model (blue line) compared to depth averaged CTD casts at LSULB8. Bottom graph: vertical salinity CTD profiles collected at LSULB8. The colors of the CTD vertical profiles in the bottom graph match the color of the depth averaged CTD observation in the top graph.

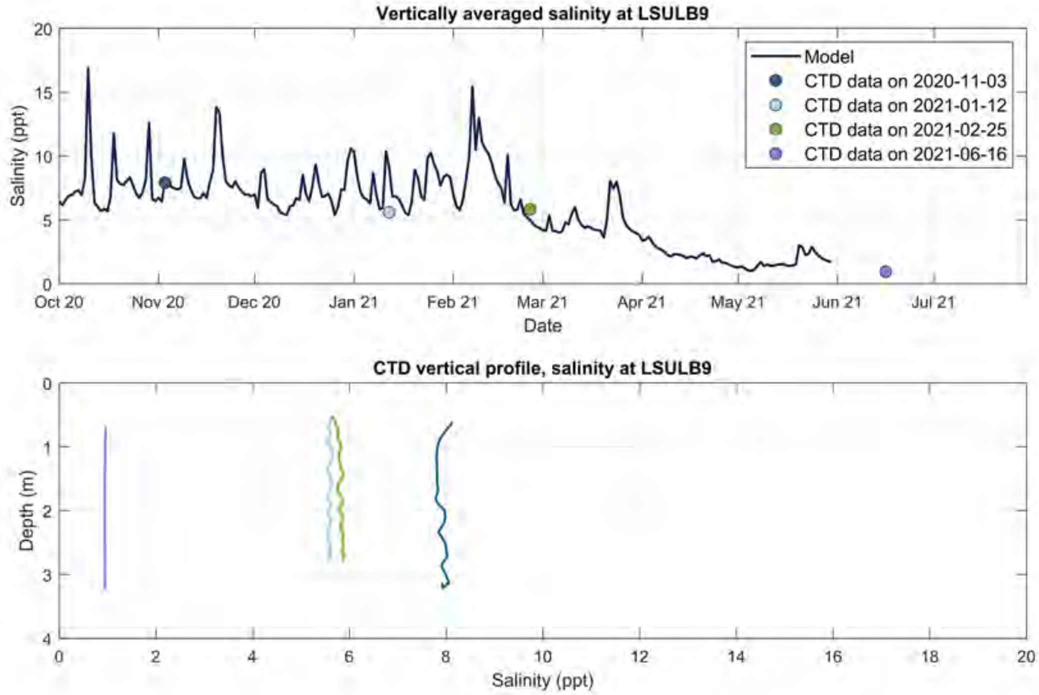

Figure D-39. Salinity validation using CTD casts at LSULB9. Top graph: simulated daily averaged salinity by the Hydrodynamic Model (blue line) compared to depth averaged CTD casts at LSULB9. Bottom graph: vertical salinity CTD profiles collected at LSULB9. The colors of the CTD vertical profiles in the bottom graph match the color of the depth averaged CTD observation in the top graph.

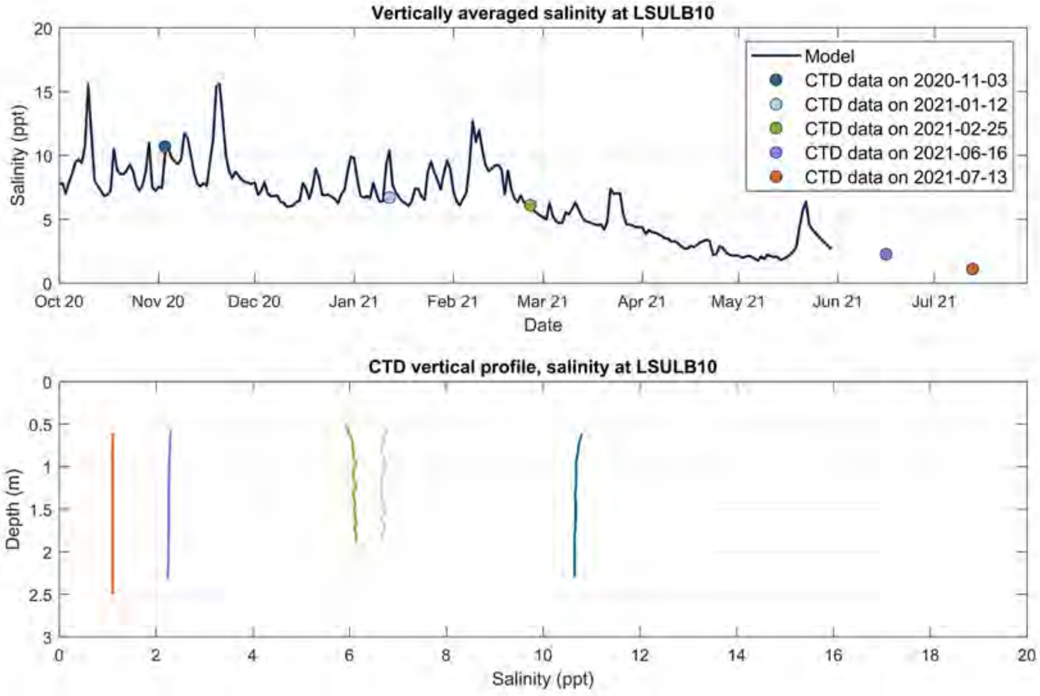

Figure D-40. Salinity validation using CTD casts at LSULB10. Top graph: simulated daily averaged salinity by the Hydrodynamic Model (blue line) compared to depth averaged CTD casts at LSULB10. Bottom graph: vertical salinity CTD profiles collected at LSULB10. The colors of the CTD vertical profiles in the bottom graph match the color of the depth averaged CTD observation in the top graph.

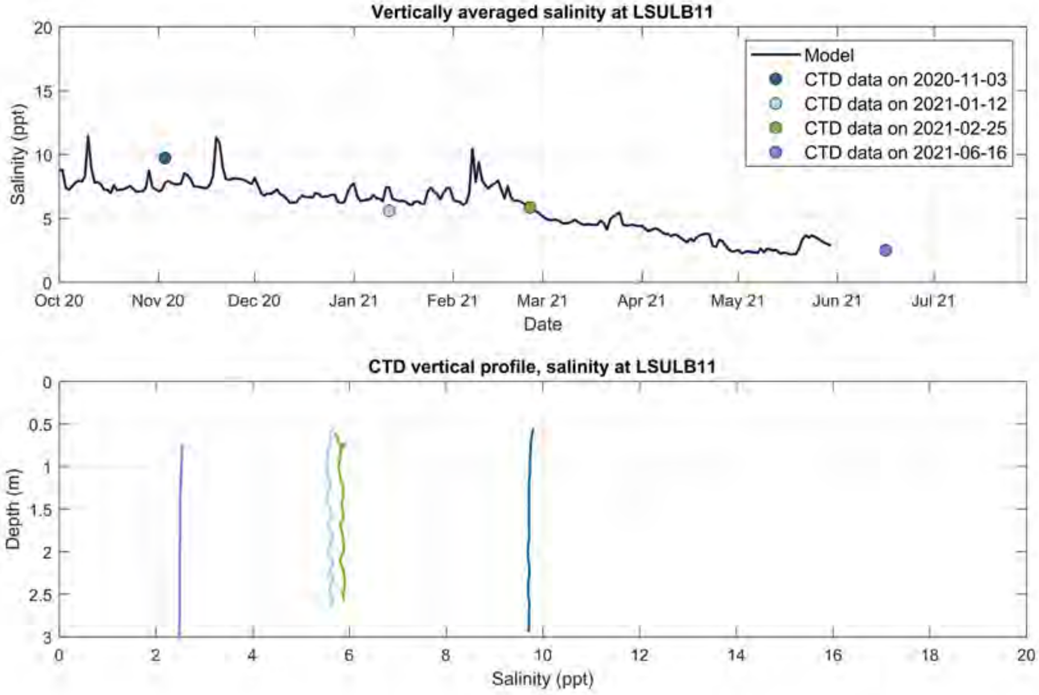

Figure D-41. Salinity validation using CTD casts at LSULB11. Top graph: simulated daily averaged salinity by the Hydrodynamic Model (blue line) compared to depth averaged CTD casts at LSULB11. Bottom graph: vertical salinity CTD profiles collected at LSULB11. The colors of the CTD vertical profiles in the bottom graph match the color of the depth averaged CTD observation in the top graph.

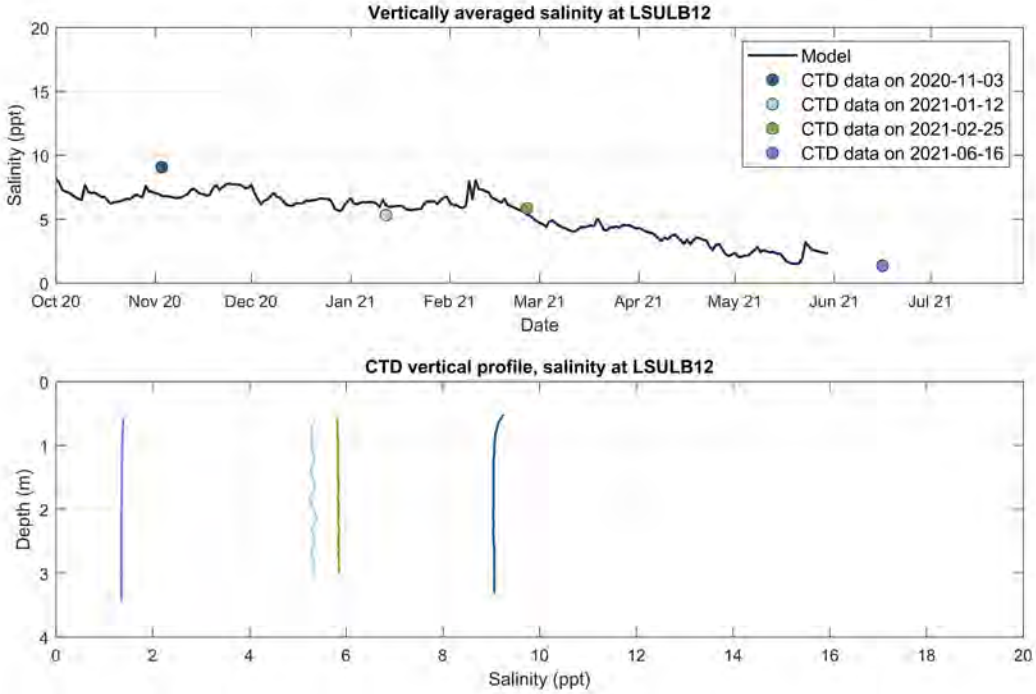

Figure D-42. Salinity validation using CTD casts at LSULB12. Top graph: simulated daily averaged salinity by the Hydrodynamic Model (blue line) compared to depth averaged CTD casts at LSULB12. Bottom graph: vertical salinity CTD profiles collected at LSULB12. The colors of the CTD vertical profiles in the bottom graph match the color of the depth averaged CTD observation in the top graph.

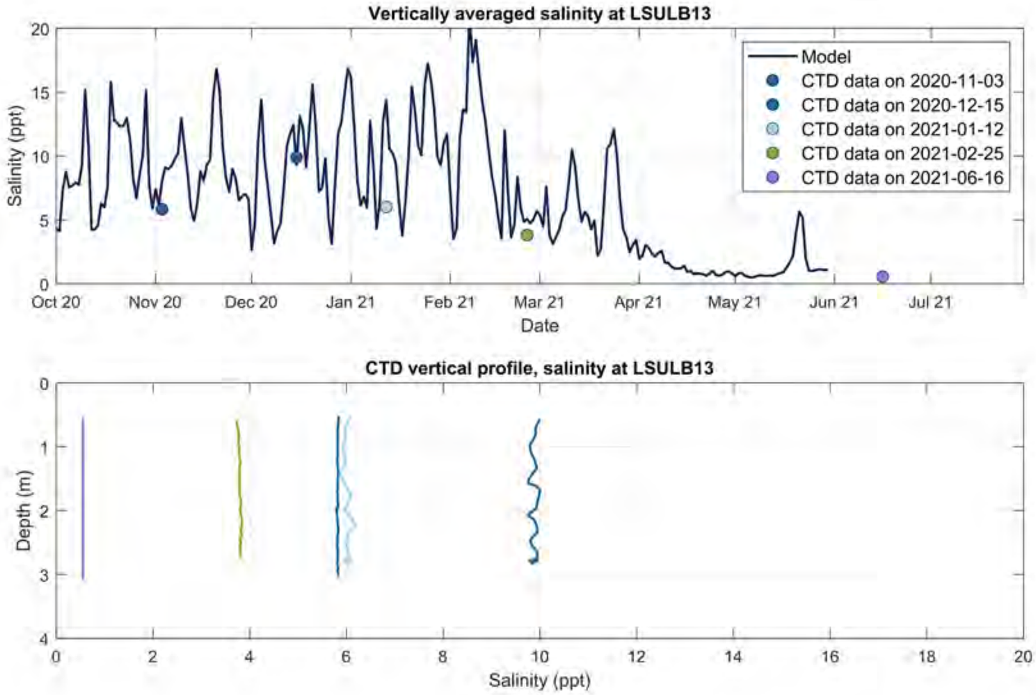

Figure D-43. Salinity validation using CTD casts at LSULB13. Top graph: simulated daily averaged salinity by the Hydrodynamic Model (blue line) compared to depth averaged CTD casts at LSULB13. Bottom graph: vertical salinity CTD profiles collected at LSULB13. The colors of the CTD vertical profiles in the bottom graph match the color of the depth averaged CTD observation in the top graph.

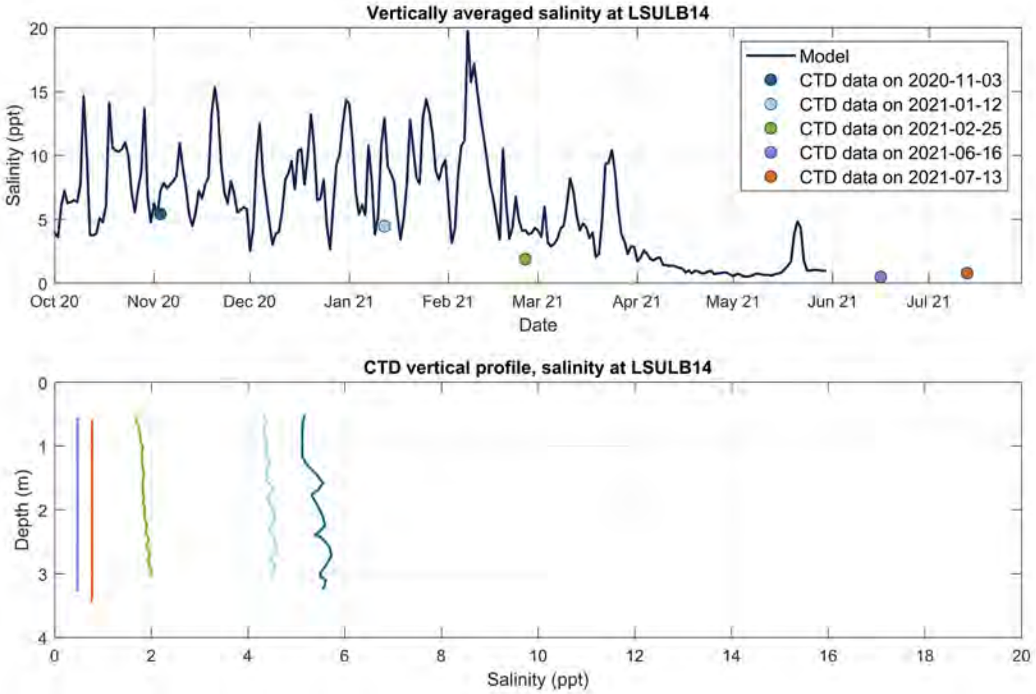

Figure D-44. Salinity validation using CTD casts at LSULB14. Top graph: simulated daily averaged salinity by the Hydrodynamic Model (blue line) compared to depth averaged CTD casts at LSULB14. Bottom graph: vertical salinity CTD profiles collected at LSULB14. The colors of the CTD vertical profiles in the bottom graph match the color of the depth averaged CTD observation in the top graph.

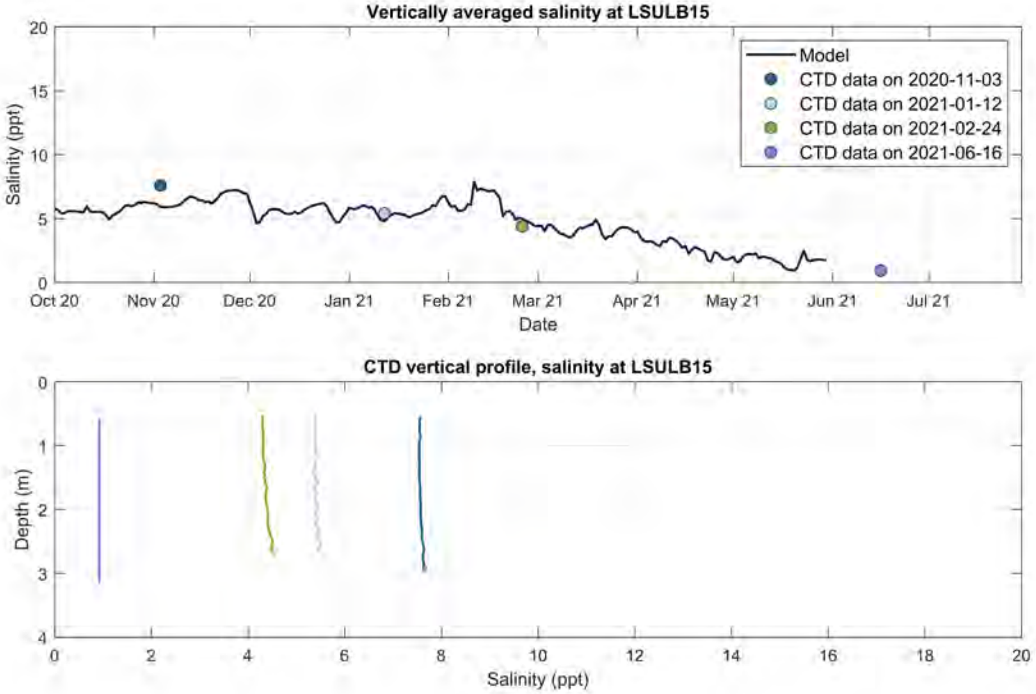

Figure D-45. Salinity validation using CTD casts at LSULB15. Top graph: simulated daily averaged salinity by the Hydrodynamic Model (blue line) compared to depth averaged CTD casts at LSULB15. Bottom graph: vertical salinity CTD profiles collected at LSULB15. The colors of the CTD vertical profiles in the bottom graph match the color of the depth averaged CTD observation in the top graph.

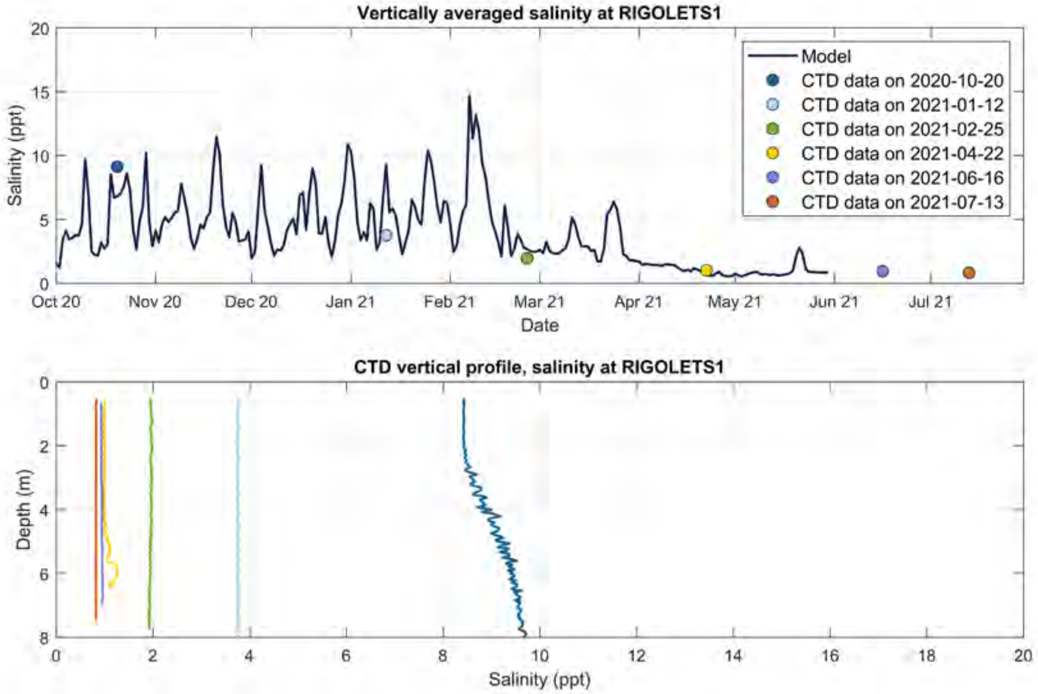

Figure D-46. Salinity validation using CTD casts at RIGOLETS1. Top graph: simulated daily averaged salinity by the Hydrodynamic Model (blue line) compared to depth averaged CTD casts at RIGOLETS1. Bottom graph: vertical salinity CTD profiles collected at RIGOLETS1. The colors of the CTD vertical profiles in the bottom graph match the color of the depth averaged CTD observation in the top graph.

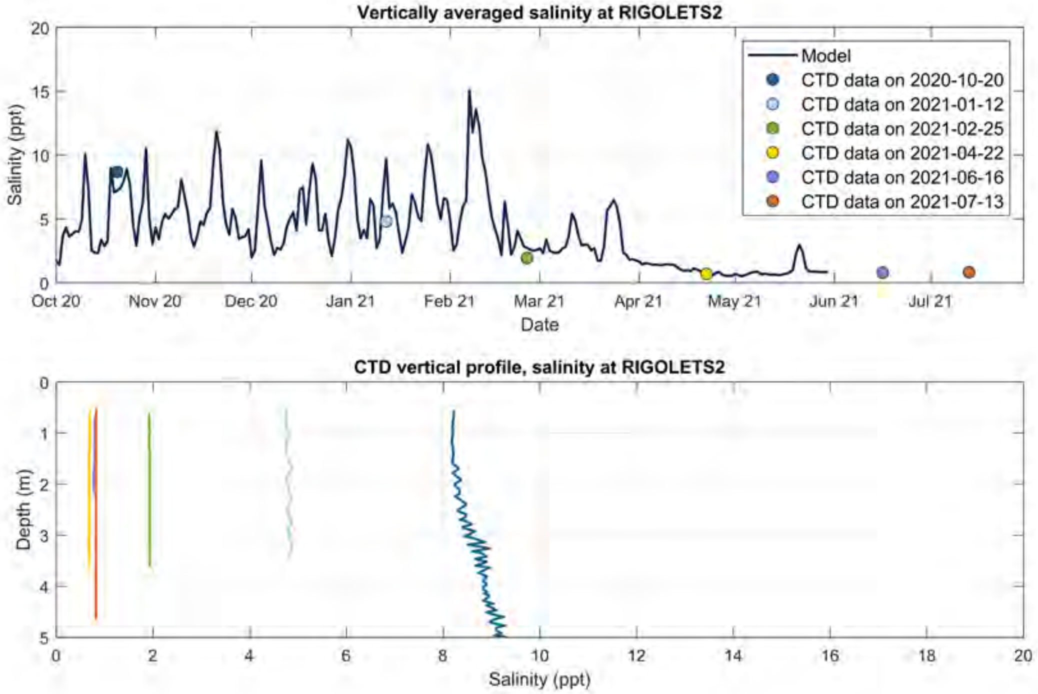

Figure D-47. Salinity validation using CTD casts at RIGOLETS2. Top graph: simulated daily averaged salinity by the Hydrodynamic Model (blue line) compared to depth averaged CTD casts at RIGOLETS2. Bottom graph: vertical salinity CTD profiles collected at RIGOLETS2. The colors of the CTD vertical profiles in the bottom graph match the color of the depth averaged CTD observation in the top graph.

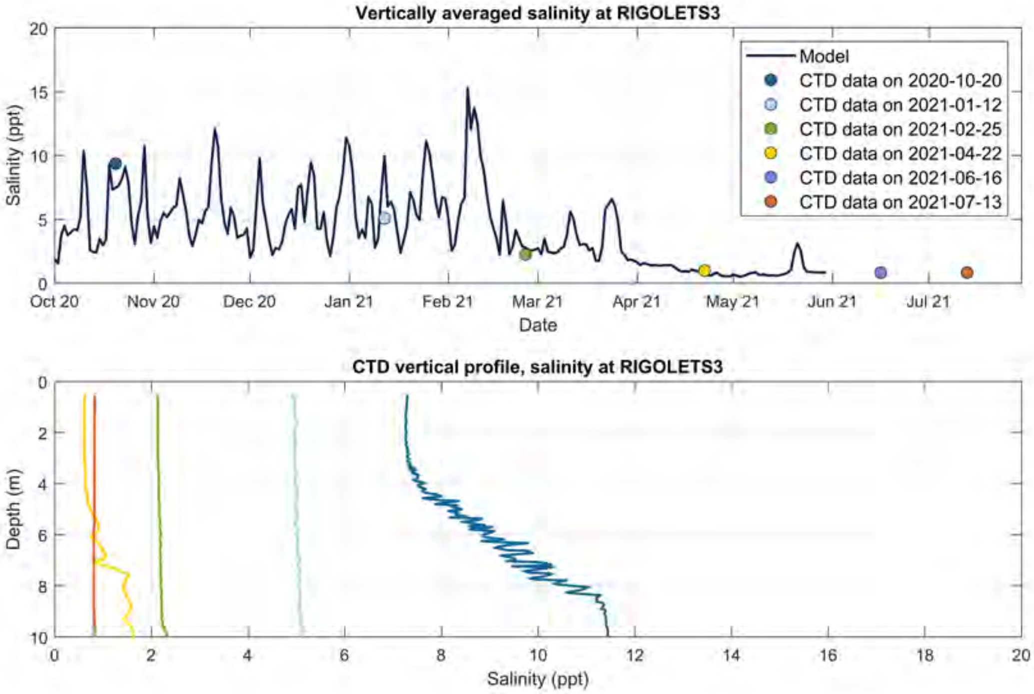

Figure D-48. Salinity validation using CTD casts at RIGOLETS3. Top graph: simulated daily averaged salinity by the Hydrodynamic Model (blue line) compared to depth averaged CTD casts at RIGOLETS3. Bottom graph: vertical salinity CTD profiles collected at RIGOLETS3. The colors of the CTD vertical profiles in the bottom graph match the color of the depth averaged CTD observation in the top graph.

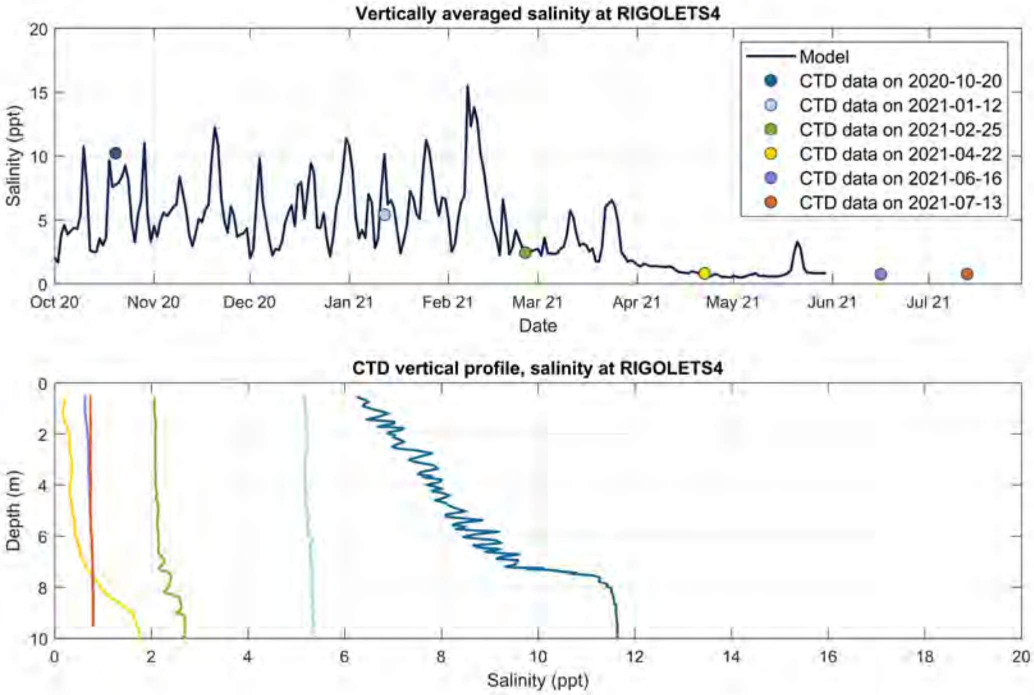

Figure D-49. Salinity validation using CTD casts at RIGOLETS4. Top graph: simulated daily averaged salinity by the Hydrodynamic Model (blue line) compared to depth averaged CTD casts at RIGOLETS4. Bottom graph: vertical salinity CTD profiles collected at RIGOLETS4. The colors of the CTD vertical profiles in the bottom graph match the color of the depth averaged CTD observation in the top graph.

APPENDIX E. TEMPERATURE VALIDATION WITH CTD CASTS

Figure E-1 through Figure E-49 show the comparison between daily averaged temperature projected by the Hydrodynamic Model and CTD casts used for validation. The location of all stations is displayed in Figure 37.

Figure E-1.Temperature validation with CTD casts at CHEF1. Top graph: simulated daily averaged temperature by the Hydrodynamic Model (blue line) compared to depth averaged CTD casts at CHEF1. Bottom graph: vertical temperature CTD profiles collected at CHEF1. The colors of the CTD vertical profiles in the bottom graph match the color of the depth averaged CTD observation in the top graph.

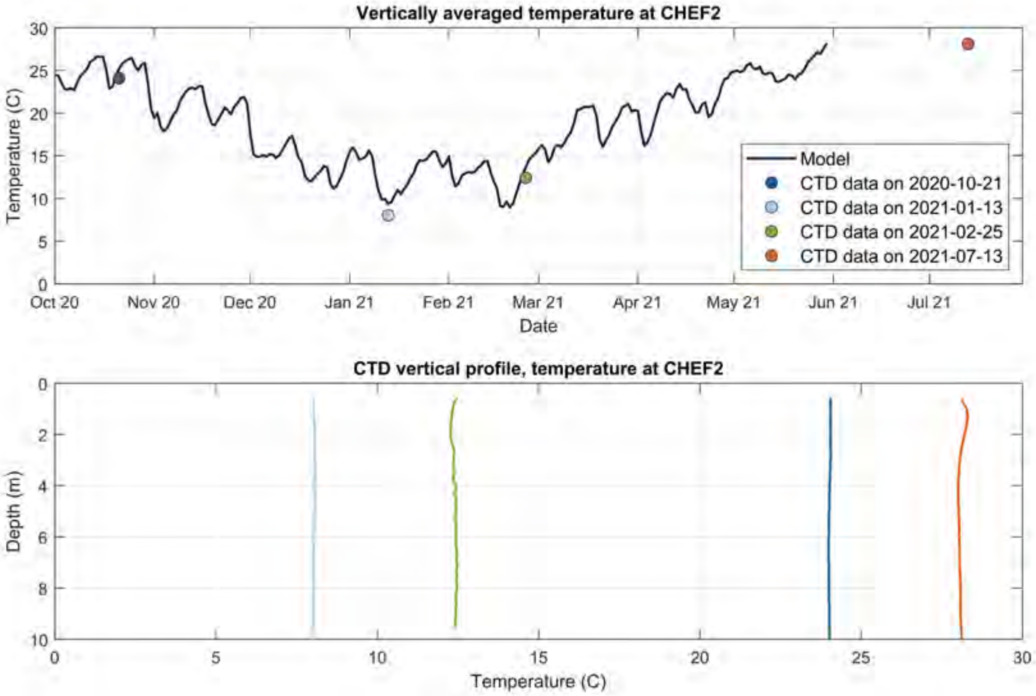

Figure E-2.Temperature validation with CTD casts at CHEF2. Top graph: simulated daily averaged temperature by the Hydrodynamic Model (blue line) compared to depth averaged CTD casts at CHEF2. Bottom graph: vertical temperature CTD profiles collected at CHEF2. The colors of the CTD vertical profiles in the bottom graph match the color of the depth averaged CTD observation in the top graph.

Figure E-3.Temperature validation with CTD casts at CHEF3. Top graph: simulated daily averaged temperature by the Hydrodynamic Model (blue line) compared to depth averaged CTD casts at CHEF3. Bottom graph: vertical temperature CTD profiles collected at CHEF3. The colors of the CTD vertical profiles in the bottom graph match the color of the depth averaged CTD observation in the top graph.

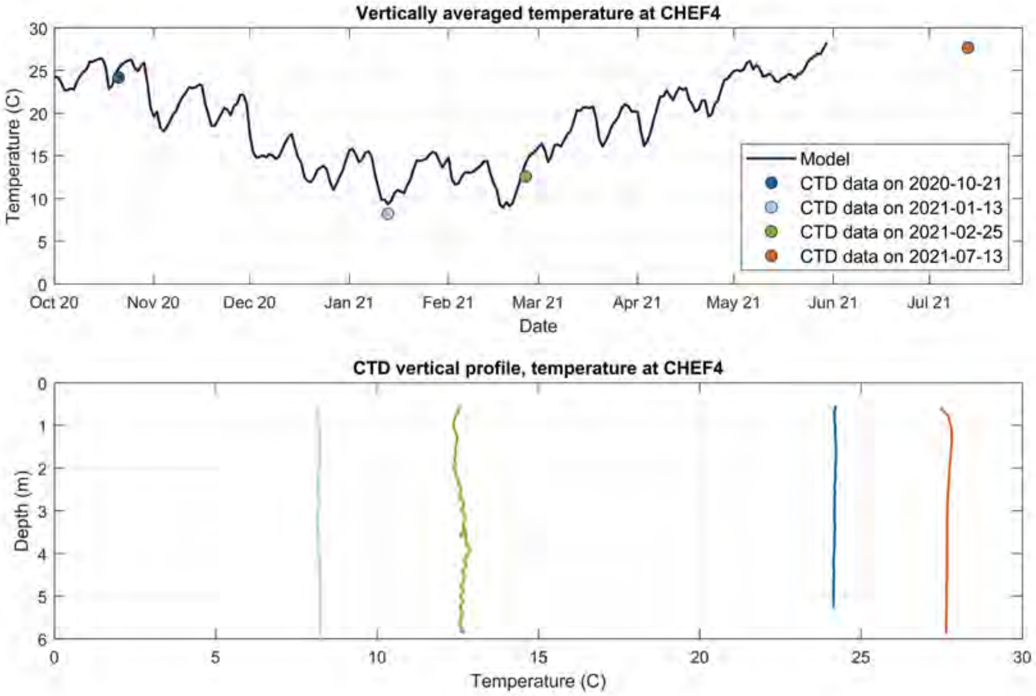

Figure E-4.Temperature validation with CTD casts at CHEF4. Top graph: simulated daily averaged temperature by the Hydrodynamic Model (blue line) compared to depth averaged CTD casts at CHEF4. Bottom graph: vertical temperature CTD profiles collected at CHEF4. The colors of the CTD vertical profiles in the bottom graph match the color of the depth averaged CTD observation in the top graph.

Figure E-5.Temperature validation with CTD casts at CHEF5. Top graph: simulated daily averaged temperature by the Hydrodynamic Model (blue line) compared to depth averaged CTD casts at CHEF5. Bottom graph: vertical temperature CTD profiles collected at CHEF5. The colors of the CTD vertical profiles in the bottom graph match the color of the depth averaged CTD observation in the top graph.

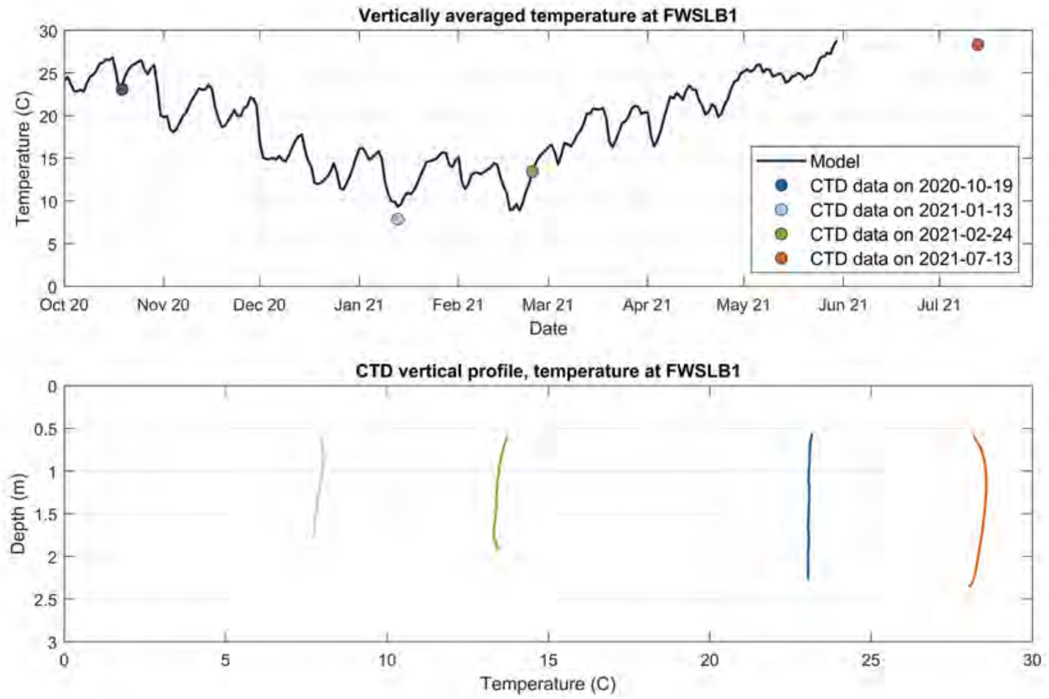

Figure E-6.Temperature validation with CTD casts at FWSLB1. Top graph: simulated daily averaged temperature by the Hydrodynamic Model (blue line) compared to depth averaged CTD casts at FWSLB1. Bottom graph: vertical temperature CTD profiles collected at FWSLB1. The colors of the CTD vertical profiles in the bottom graph match the color of the depth averaged CTD observation in the top graph.

Figure E-7.Temperature validation with CTD casts at FWSLB2. Top graph: simulated daily averaged temperature by the Hydrodynamic Model (blue line) compared to depth averaged CTD casts at FWSLB2. Bottom graph: vertical temperature CTD profiles collected at FWSLB2. The colors of the CTD vertical profiles in the bottom graph match the color of the depth averaged CTD observation in the top graph.

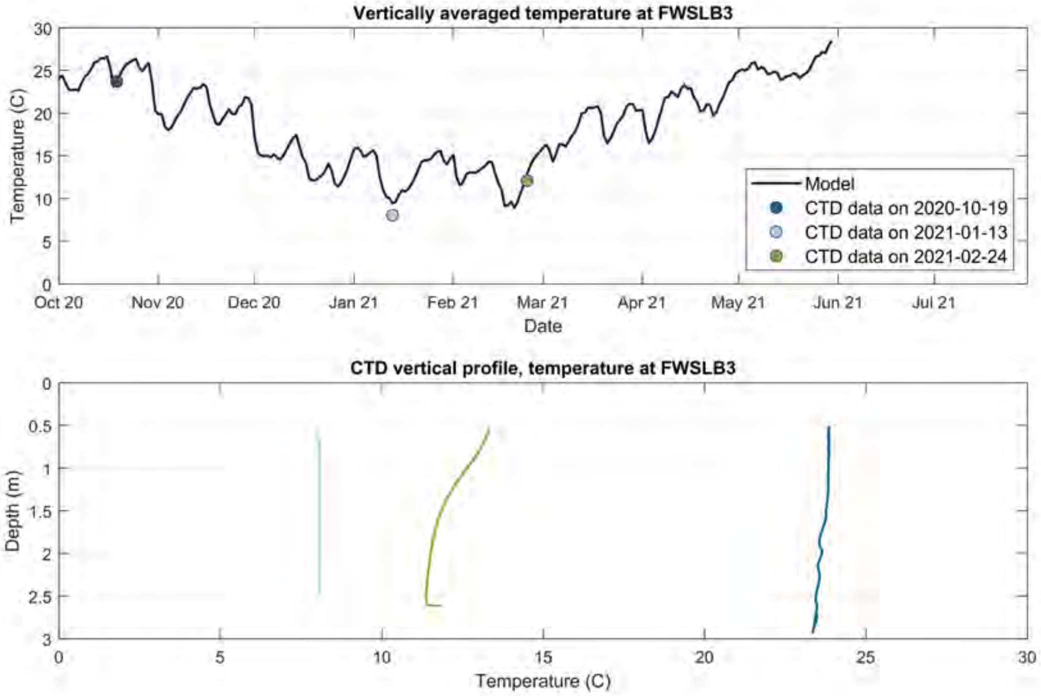

Figure E-8.Temperature validation with CTD casts at FWSLB3. Top graph: simulated daily averaged temperature by the Hydrodynamic Model (blue line) compared to depth averaged CTD casts at FWSLB3. Bottom graph: vertical temperature CTD profiles collected at FWSLB3. The colors of the CTD vertical profiles in the bottom graph match the color of the depth averaged CTD observation in the top graph.

Figure E-9.Temperature validation with CTD casts at FWSLB4. Top graph: simulated daily averaged temperature by the Hydrodynamic Model (blue line) compared to depth averaged CTD casts at FWSLB4. Bottom graph: vertical temperature CTD profiles collected at FWSLB4. The colors of the CTD vertical profiles in the bottom graph match the color of the depth averaged CTD observation in the top graph.

Figure E-10.Temperature validation with CTD casts at FWSLB5. Top graph: simulated daily averaged temperature by the Hydrodynamic Model (blue line) compared to depth averaged CTD casts at FWSLB5. Bottom graph: vertical temperature CTD profiles collected at FWSLB5. The colors of the CTD vertical profiles in the bottom graph match the color of the depth averaged CTD observation in the top graph.

Figure E-11.Temperature validation with CTD casts at FWSLB6. Top graph: simulated daily averaged temperature by the Hydrodynamic Model (blue line) compared to depth averaged CTD casts at FWSLB6. Bottom graph: vertical temperature CTD profiles collected at FWSLB6. The colors of the CTD vertical profiles in the bottom graph match the color of the depth averaged CTD observation in the top graph.

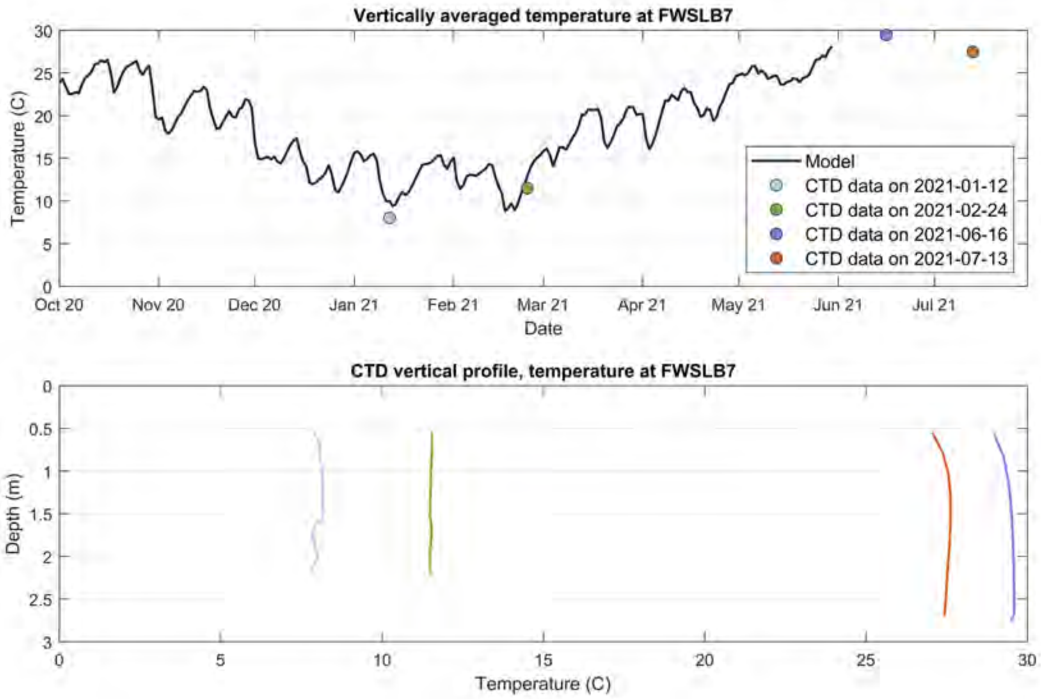

Figure E-12.Temperature validation with CTD casts at FWSLB7. Top graph: simulated daily averaged temperature by the Hydrodynamic Model (blue line) compared to depth averaged CTD casts at FWSLB7. Bottom graph: vertical temperature CTD profiles collected at FWSLB7. The colors of the CTD vertical profiles in the bottom graph match the color of the depth averaged CTD observation in the top graph.

Figure E-13.Temperature validation with CTD casts at FWSLB8. Top graph: simulated daily averaged temperature by the Hydrodynamic Model (blue line) compared to depth averaged CTD casts at FWSLB8. Bottom graph: vertical temperature CTD profiles collected at FWSLB8. The colors of the CTD vertical profiles in the bottom graph match the color of the depth averaged CTD observation in the top graph.

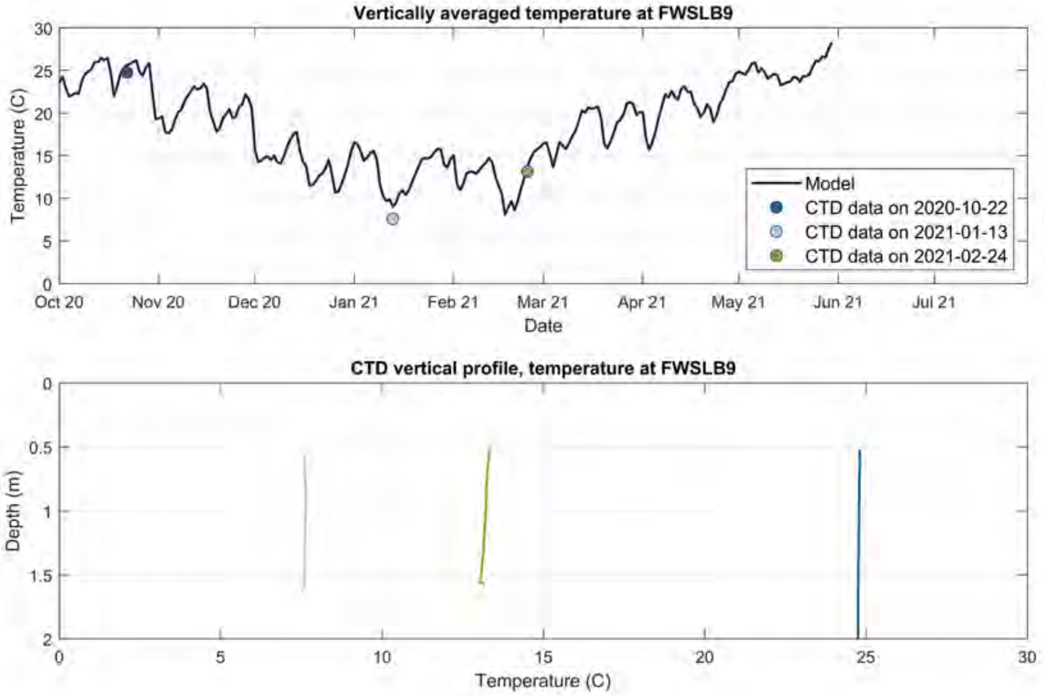

Figure E-14.Temperature validation with CTD casts at FWSLB9. Top graph: simulated daily averaged temperature by the Hydrodynamic Model (blue line) compared to depth averaged CTD casts at FWSLB9. Bottom graph: vertical temperature CTD profiles collected at FWSLB9. The colors of the CTD vertical profiles in the bottom graph match the color of the depth averaged CTD observation in the top graph.

Figure E-15.Temperature validation with CTD casts at FWSLB10. Top graph: simulated daily averaged temperature by the Hydrodynamic Model (blue line) compared to depth averaged CTD casts at FWSLB10. Bottom graph: vertical temperature CTD profiles collected at FWSLB10. The colors of the CTD vertical profiles in the bottom graph match the color of the depth averaged CTD observation in the top graph.

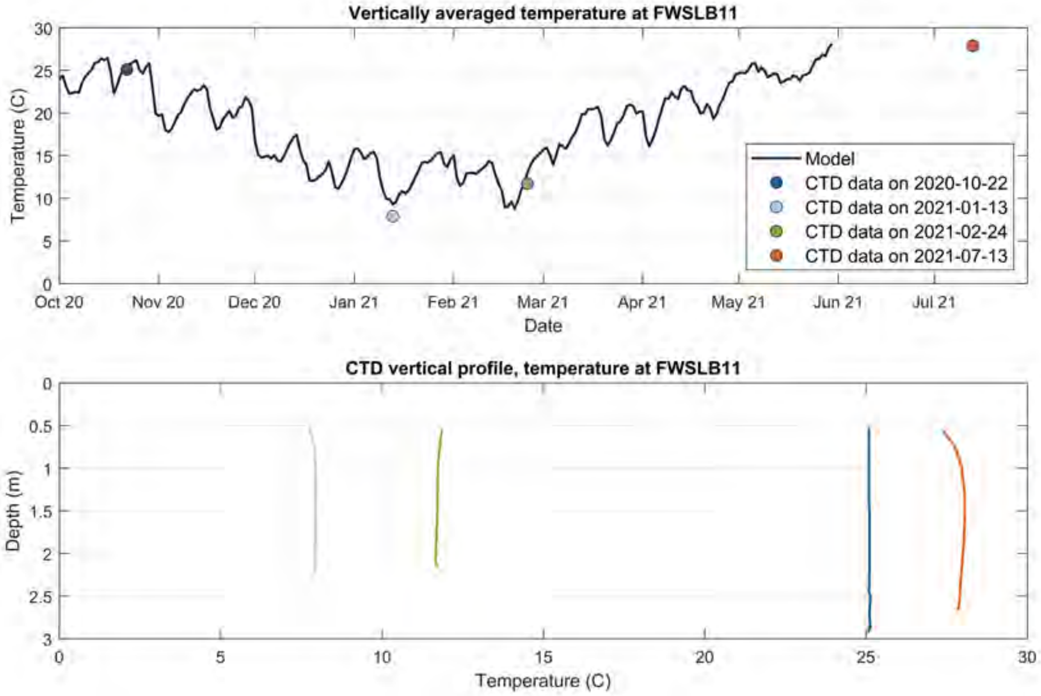

Figure E-16.Temperature validation with CTD casts at FWSLB11. Top graph: simulated daily averaged temperature by the Hydrodynamic Model (blue line) compared to depth averaged CTD casts at FWSLB11. Bottom graph: vertical temperature CTD profiles collected at FWSLB11. The colors of the CTD vertical profiles in the bottom graph match the color of the depth averaged CTD observation in the top graph.

Figure E-17.Temperature validation with CTD casts at FWSLB12. Top graph: simulated daily averaged temperature by the Hydrodynamic Model (blue line) compared to depth averaged CTD casts at FWSLB12. Bottom graph: vertical temperature CTD profiles collected at FWSLB12. The colors of the CTD vertical profiles in the bottom graph match the color of the depth averaged CTD observation in the top graph.

Figure E-18.Temperature validation with CTD casts at FWSLB13. Top graph: simulated daily averaged temperature by the Hydrodynamic Model (blue line) compared to depth averaged CTD casts at FWSLB13. Bottom graph: vertical temperature CTD profiles collected at FWSLB13. The colors of the CTD vertical profiles in the bottom graph match the color of the depth averaged CTD observation in the top graph.

Figure E-19.Temperature validation with CTD casts at FWSLB14. Top graph: simulated daily averaged temperature by the Hydrodynamic Model (blue line) compared to depth averaged CTD casts at FWSLB14. Bottom graph: vertical temperature CTD profiles collected at FWSLB14. The colors of the CTD vertical profiles in the bottom graph match the color of the depth averaged CTD observation in the top graph.

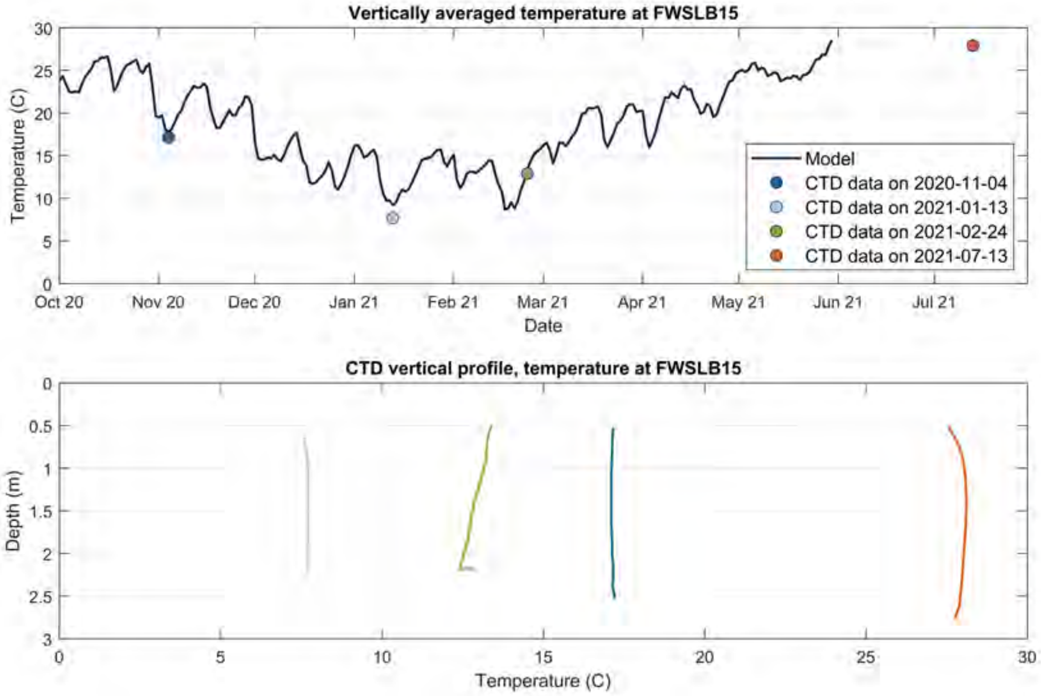

Figure E-20.Temperature validation with CTD casts at FWSLB15. Top graph: simulated daily averaged temperature by the Hydrodynamic Model (blue line) compared to depth averaged CTD casts at FWSLB15. Bottom graph: vertical temperature CTD profiles collected at FWSLB15. The colors of the CTD vertical profiles in the bottom graph match the color of the depth averaged CTD observation in the top graph.

Figure E-21.Temperature validation with CTD casts at FWSLB16. Top graph: simulated daily averaged temperature by the Hydrodynamic Model (blue line) compared to depth averaged CTD casts at FWSLB16. Bottom graph: vertical temperature CTD profiles collected at FWSLB16. The colors of the CTD vertical profiles in the bottom graph match the color of the depth averaged CTD observation in the top graph.

Figure E-22.Temperature validation with CTD casts at FWSTX1. Top graph: simulated daily averaged temperature by the Hydrodynamic Model (blue line) compared to depth averaged CTD casts at FWSTX1. Bottom graph: vertical temperature CTD profiles collected at FWSTX1. The colors of the CTD vertical profiles in the bottom graph match the color of the depth averaged CTD observation in the top graph.

Figure E-23.Temperature validation with CTD casts at FWSTX2. Top graph: simulated daily averaged temperature by the Hydrodynamic Model (blue line) compared to depth averaged CTD casts at FWSTX2. Bottom graph: vertical temperature CTD profiles collected at FWSTX2. The colors of the CTD vertical profiles in the bottom graph match the color of the depth averaged CTD observation in the top graph.

Figure E-24.Temperature validation with CTD casts at FWSTX3. Top graph: simulated daily averaged temperature by the Hydrodynamic Model (blue line) compared to depth averaged CTD casts at FWSTX3. Bottom graph: vertical temperature CTD profiles collected at FWSTX3. The colors of the CTD vertical profiles in the bottom graph match the color of the depth averaged CTD observation in the top graph.

Figure E-25.Temperature validation with CTD casts at FWSTX4. Top graph: simulated daily averaged temperature by the Hydrodynamic Model (blue line) compared to depth averaged CTD casts at FWSTX4. Bottom graph: vertical temperature CTD profiles collected at FWSTX4. The colors of the CTD vertical profiles in the bottom graph match the color of the depth averaged CTD observation in the top graph.

Figure E-26.Temperature validation with CTD casts at FWSTX5. Top graph: simulated daily averaged temperature by the Hydrodynamic Model (blue line) compared to depth averaged CTD casts at FWSTX5. Bottom graph: vertical temperature CTD profiles collected at FWSTX5. The colors of the CTD vertical profiles in the bottom graph match the color of the depth averaged CTD observation in the top graph.

Figure E-27.Temperature validation with CTD casts at FWSTX6. Top graph: simulated daily averaged temperature by the Hydrodynamic Model (blue line) compared to depth averaged CTD casts at FWSTX6. Bottom graph: vertical temperature CTD profiles collected at FWSTX6. The colors of the CTD vertical profiles in the bottom graph match the color of the depth averaged CTD observation in the top graph.

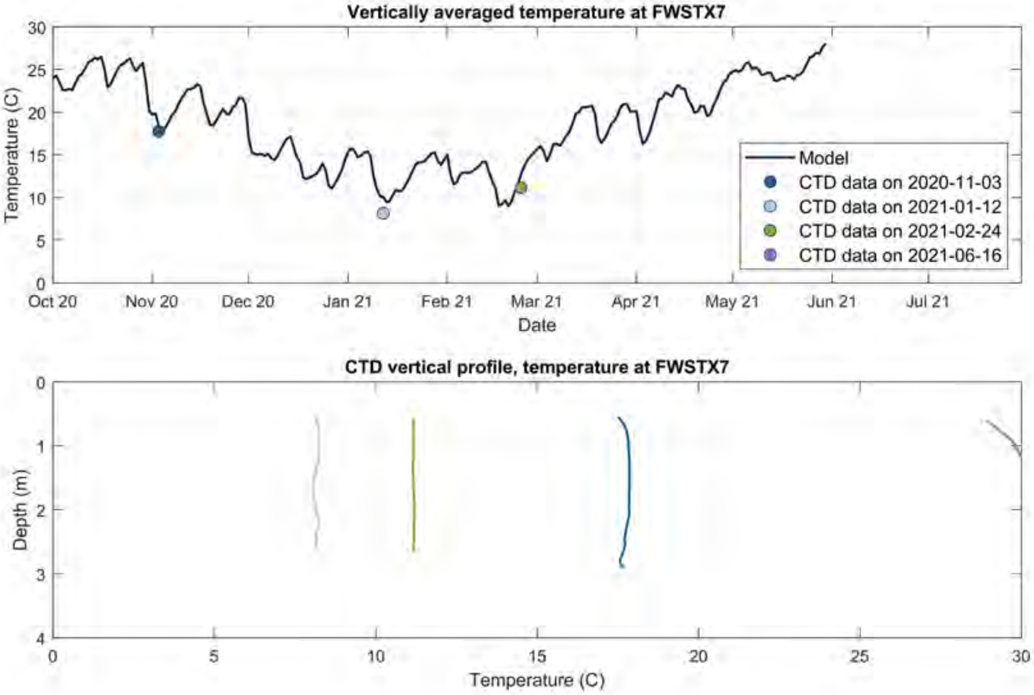

Figure E-28.Temperature validation with CTD casts at FWSTX7. Top graph: simulated daily averaged temperature by the Hydrodynamic Model (blue line) compared to depth averaged CTD casts at FWSTX7. Bottom graph: vertical temperature CTD profiles collected at FWSTX7. The colors of the CTD vertical profiles in the bottom graph match the color of the depth averaged CTD observation in the top graph.

Figure E-29.Temperature validation with CTD casts at FWSTX8. Top graph: simulated daily averaged temperature by the Hydrodynamic Model (blue line) compared to depth averaged CTD casts at FWSTX8. Bottom graph: vertical temperature CTD profiles collected at FWSTX8. The colors of the CTD vertical profiles in the bottom graph match the color of the depth averaged CTD observation in the top graph.

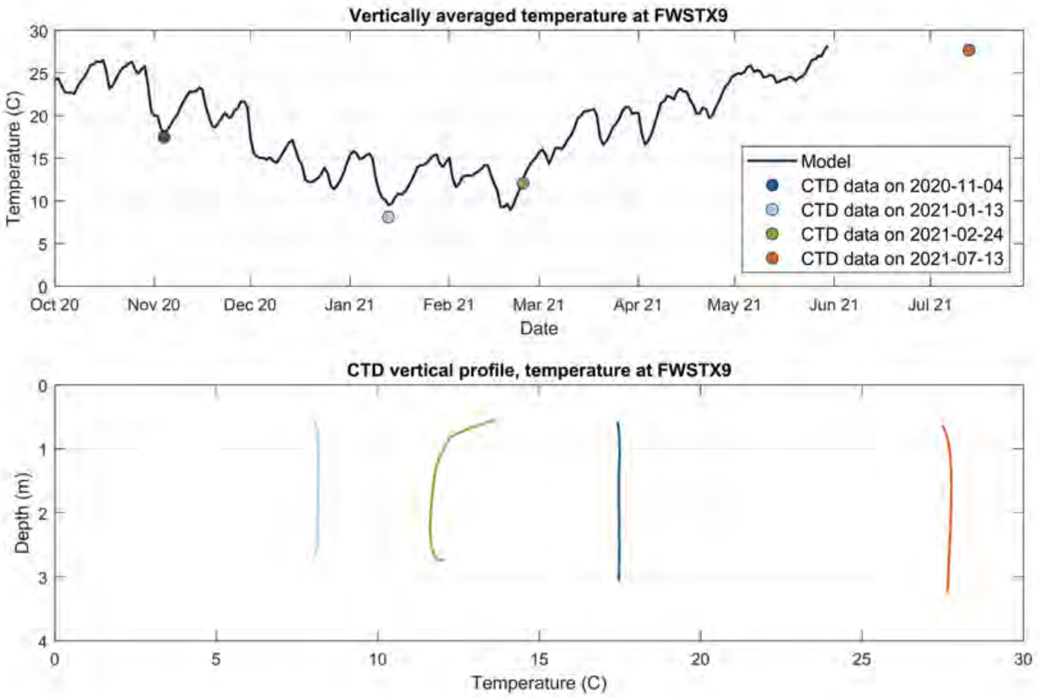

Figure E-30.Temperature validation with CTD casts at FWSTX9. Top graph: simulated daily averaged temperature by the Hydrodynamic Model (blue line) compared to depth averaged CTD casts at FWSTX9. Bottom graph: vertical temperature CTD profiles collected at FWSTX9. The colors of the CTD vertical profiles in the bottom graph match the color of the depth averaged CTD observation in the top graph.

Figure E-31.Temperature validation with CTD casts at LSULB1. Top graph: simulated daily averaged temperature by the Hydrodynamic Model (blue line) compared to depth averaged CTD casts at LSULB1. Bottom graph: vertical temperature CTD profiles collected at LSULB1. The colors of the CTD vertical profiles in the bottom graph match the color of the depth averaged CTD observation in the top graph.

Figure E-32.Temperature validation with CTD casts at LSULB2. Top graph: simulated daily averaged temperature by the Hydrodynamic Model (blue line) compared to depth averaged CTD casts at LSULB2. Bottom graph: vertical temperature CTD profiles collected at LSULB2. The colors of the CTD vertical profiles in the bottom graph match the color of the depth averaged CTD observation in the top graph.

Figure E-33.Temperature validation with CTD casts at LSULB3. Top graph: simulated daily averaged temperature by the Hydrodynamic Model (blue line) compared to depth averaged CTD casts at LSULB3. Bottom graph: vertical temperature CTD profiles collected at LSULB3. The colors of the CTD vertical profiles in the bottom graph match the color of the depth averaged CTD observation in the top graph.

Figure E-34.Temperature validation with CTD casts at LSULB4. Top graph: simulated daily averaged temperature by the Hydrodynamic Model (blue line) compared to depth averaged CTD casts at LSULB4. Bottom graph: vertical temperature CTD profiles collected at LSULB4. The colors of the CTD vertical profiles in the bottom graph match the color of the depth averaged CTD observation in the top graph.

Figure E-35.Temperature validation with CTD casts at LSULB5. Top graph: simulated daily averaged temperature by the Hydrodynamic Model (blue line) compared to depth averaged CTD casts at LSULB5. Bottom graph: vertical temperature CTD profiles collected at LSULB5. The colors of the CTD vertical profiles in the bottom graph match the color of the depth averaged CTD observation in the top graph.

Figure E-36.Temperature validation with CTD casts at LSULB6. Top graph: simulated daily averaged temperature by the Hydrodynamic Model (blue line) compared to depth averaged CTD casts at LSULB6. Bottom graph: vertical temperature CTD profiles collected at LSULB6. The colors of the CTD vertical profiles in the bottom graph match the color of the depth averaged CTD observation in the top graph.

Figure E-37.Temperature validation with CTD casts at LSULB7. Top graph: simulated daily averaged temperature by the Hydrodynamic Model (blue line) compared to depth averaged CTD casts at LSULB7. Bottom graph: vertical temperature CTD profiles collected at LSULB7. The colors of the CTD vertical profiles in the bottom graph match the color of the depth averaged CTD observation in the top graph.

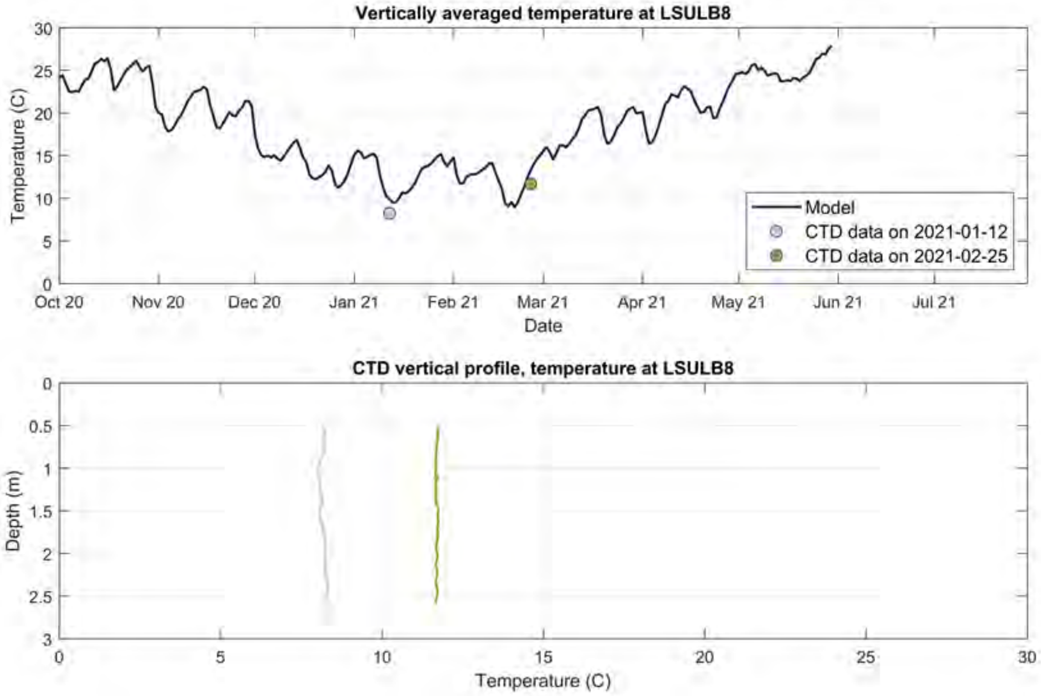

Figure E-38.Temperature validation with CTD casts at LSULB8. Top graph: simulated daily averaged temperature by the Hydrodynamic Model (blue line) compared to depth averaged CTD casts at LSULB8. Bottom graph: vertical temperature CTD profiles collected at LSULB8. The colors of the CTD vertical profiles in the bottom graph match the color of the depth averaged CTD observation in the top graph.

Figure E-39.Temperature validation with CTD casts at LSULB9. Top graph: simulated daily averaged temperature by the Hydrodynamic Model (blue line) compared to depth averaged CTD casts at LSULB9. Bottom graph: vertical temperature CTD profiles collected at LSULB9. The colors of the CTD vertical profiles in the bottom graph match the color of the depth averaged CTD observation in the top graph.

Figure E-40.Temperature validation with CTD casts at LSULB10. Top graph: simulated daily averaged temperature by the Hydrodynamic Model (blue line) compared to depth averaged CTD casts at LSULB10. Bottom graph: vertical temperature CTD profiles collected at LSULB10. The colors of the CTD vertical profiles in the bottom graph match the color of the depth averaged CTD observation in the top graph.

Figure E-41.Temperature validation with CTD casts at LSULB11. Top graph: simulated daily averaged temperature by the Hydrodynamic Model (blue line) compared to depth averaged CTD casts at LSULB11. Bottom graph: vertical temperature CTD profiles collected at LSULB11. The colors of the CTD vertical profiles in the bottom graph match the color of the depth averaged CTD observation in the top graph.

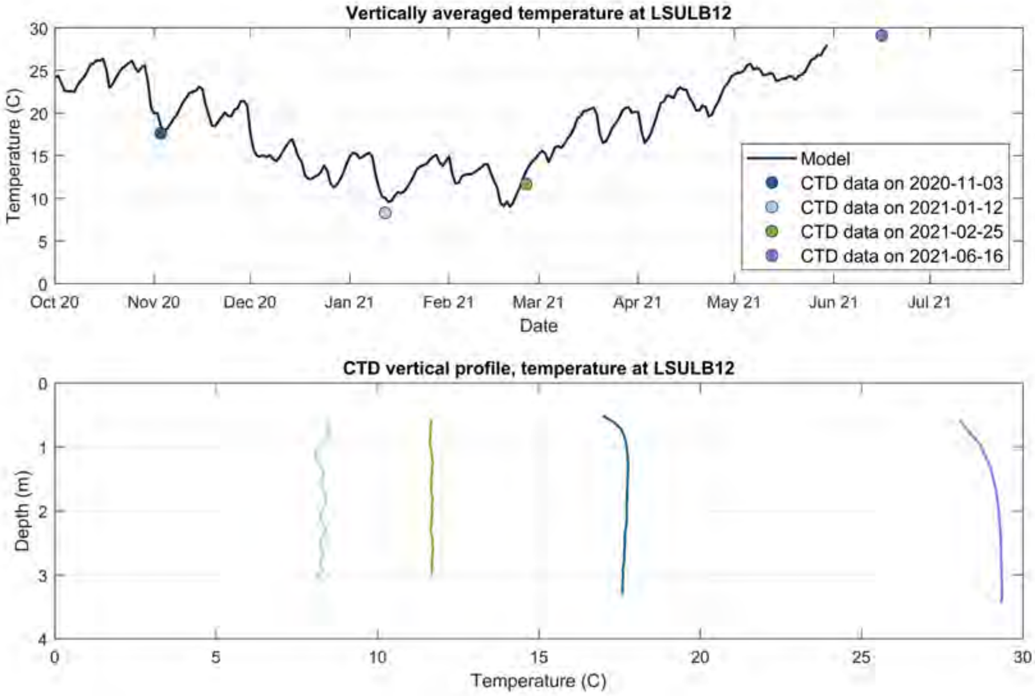

Figure E-42.Temperature validation with CTD casts at LSULB12. Top graph: simulated daily averaged temperature by the Hydrodynamic Model (blue line) compared to depth averaged CTD casts at LSULB12. Bottom graph: vertical temperature CTD profiles collected at LSULB12. The colors of the CTD vertical profiles in the bottom graph match the color of the depth averaged CTD observation in the top graph.

Figure E-43.Temperature validation with CTD casts at LSULB13. Top graph: simulated daily averaged temperature by the Hydrodynamic Model (blue line) compared to depth averaged CTD casts at LSULB13. Bottom graph: vertical temperature CTD profiles collected at LSULB13. The colors of the CTD vertical profiles in the bottom graph match the color of the depth averaged CTD observation in the top graph.

Figure E-44.Temperature validation with CTD casts at LSULB14. Top graph: simulated daily averaged temperature by the Hydrodynamic Model (blue line) compared to depth averaged CTD casts at LSULB14. Bottom graph: vertical temperature CTD profiles collected at LSULB14. The colors of the CTD vertical profiles in the bottom graph match the color of the depth averaged CTD observation in the top graph.

Figure E-45.Temperature validation with CTD casts at LSULB15. Top graph: simulated daily averaged temperature by the Hydrodynamic Model (blue line) compared to depth averaged CTD casts at LSULB15. Bottom graph: vertical temperature CTD profiles collected at LSULB15. The colors of the CTD vertical profiles in the bottom graph match the color of the depth averaged CTD observation in the top graph.

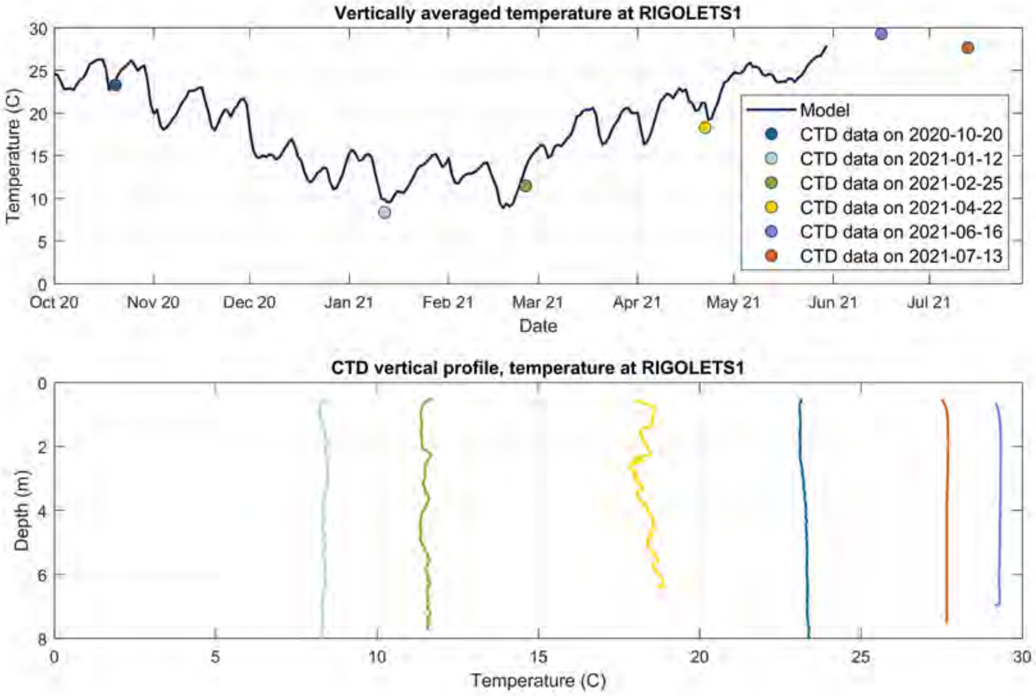

Figure E-46.Temperature validation with CTD casts at RIGOLETS1. Top graph: simulated daily averaged temperature by the Hydrodynamic Model (blue line) compared to depth averaged CTD casts at RIGOLETS1. Bottom graph: vertical temperature CTD profiles collected at RIGOLETS1. The colors of the CTD vertical profiles in the bottom graph match the color of the depth averaged CTD observation in the top graph.

Figure E-47.Temperature validation with CTD casts at RIGOLETS2. Top graph: simulated daily averaged temperature by the Hydrodynamic Model (blue line) compared to depth averaged CTD casts at RIGOLETS2. Bottom graph: vertical temperature CTD profiles collected at RIGOLETS2. The colors of the CTD vertical profiles in the bottom graph match the color of the depth averaged CTD observation in the top graph.

Figure E-48.Temperature validation with CTD casts at RIGOLETS3. Top graph: simulated daily averaged temperature by the Hydrodynamic Model (blue line) compared to depth averaged CTD casts at RIGOLETS3. Bottom graph: vertical temperature CTD profiles collected at RIGOLETS3. The colors of the CTD vertical profiles in the bottom graph match the color of the depth averaged CTD observation in the top graph.

Figure E-49.Temperature validation with CTD casts at RIGOLETS4. Top graph: simulated daily averaged temperature by the Hydrodynamic Model (blue line) compared to depth averaged CTD casts at RIGOLETS4. Bottom graph: vertical temperature CTD profiles collected at RIGOLETS4. The colors of the CTD vertical profiles in the bottom graph match the color of the depth averaged CTD observation in the top graph.

APPENDIX F. DO PROXY VALIDATION WITH CTD CASTS

Figure F-1 through Figure F-48 show the comparison between daily averaged temperature projected by the Hydrodynamic Model and all available CTD casts used for validation. The location of all stations is displayed in Figure 37.

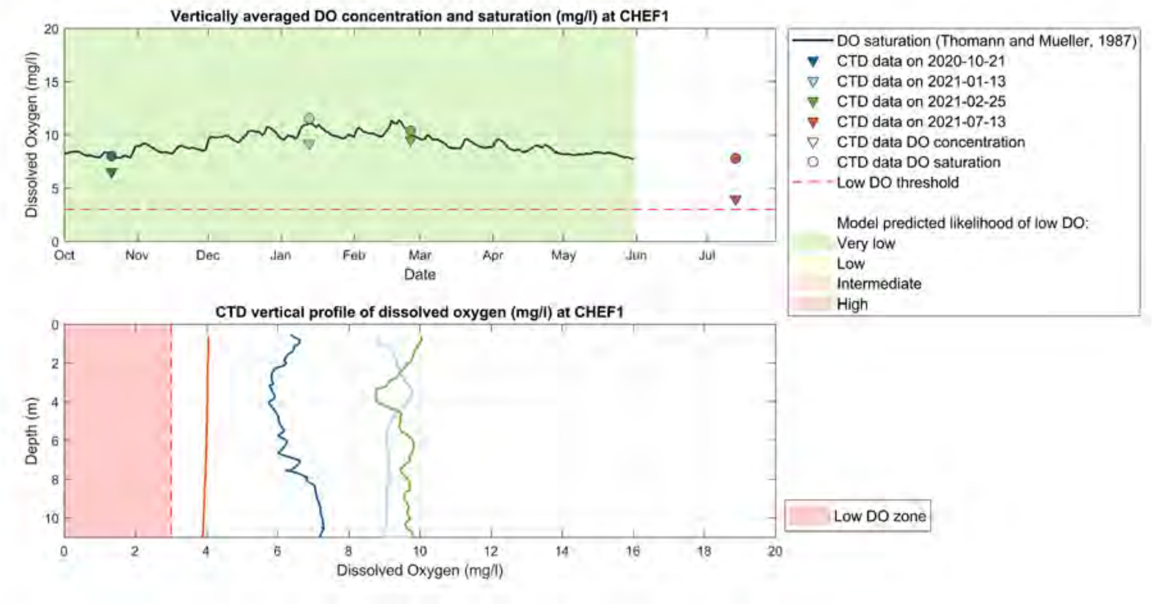

Figure F-1. DO proxy validation with CTD casts at CHEF1. Top graph: DO saturation estimated with Eq.8 (blue line), depth averaged DO saturation (circles) and concentration (triangles) measured by the CTD casts at CHEF1. Background color shows the likelihood of low DO predicted using the Hydrodynamic Model results and the rules in Table 8. Bottom graph: vertical DO concentration CTD profiles collected at CHEF1. The colors of the CTD vertical profiles in the bottom graph match the color of the depth averaged CTD observation in the top graph. The zone of low DO is highlighted in red.

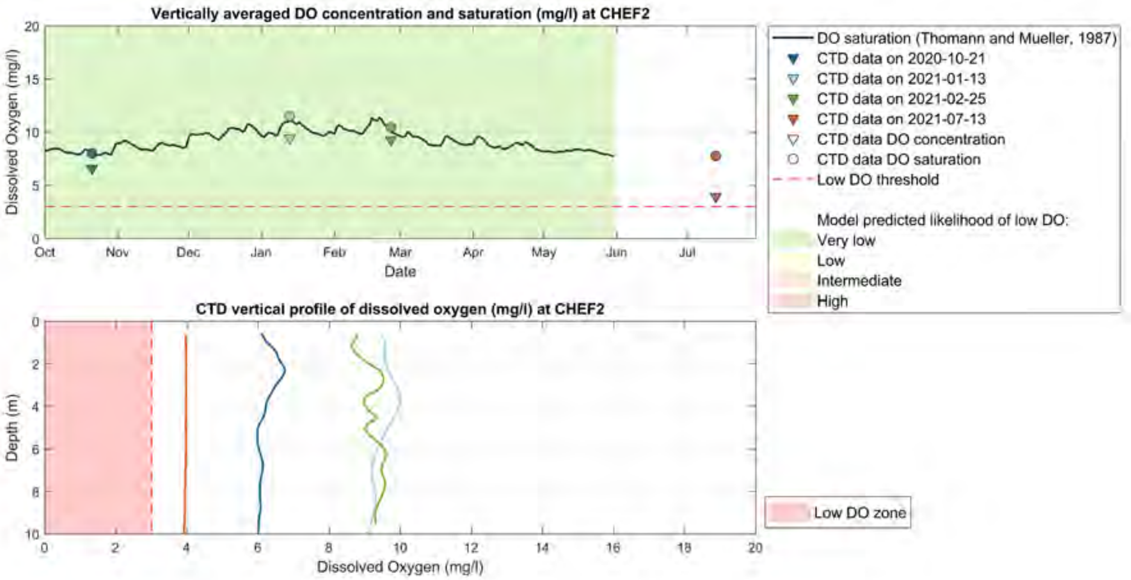

Figure F-2. DO proxy validation with CTD casts at CHEF2. Top graph: DO saturation estimated with Eq.8 (blue line), depth averaged DO saturation (circles) and concentration (triangles) measured by the CTD casts at CHEF2. Background color shows the likelihood of low DO predicted using the Hydrodynamic Model results and the rules in Table 8. Bottom graph: vertical DO concentration CTD profiles collected at CHEF2. The colors of the CTD vertical profiles in the bottom graph match the color of the depth averaged CTD observation in the top graph. The zone of low DO is highlighted in red.

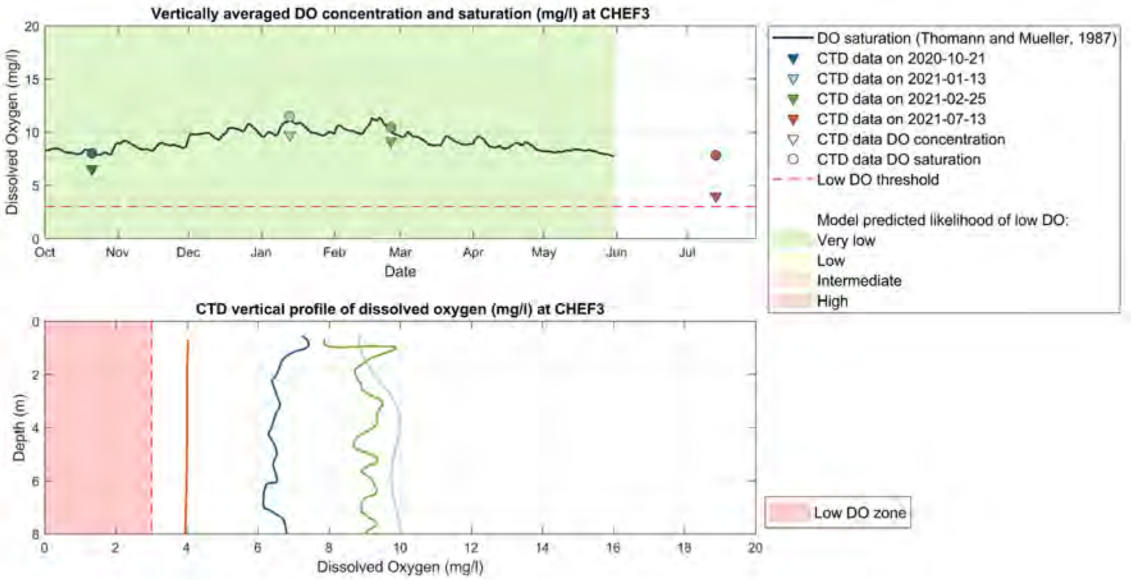

Figure F-3. DO proxy validation with CTD casts at CHEF3. Top graph: DO saturation estimated with Eq.8 (blue line), depth averaged DO saturation (circles) and concentration (triangles) measured by the CTD casts at CHEF3. Background color shows the likelihood of low DO predicted using the Hydrodynamic Model results and the rules in Table 8. Bottom graph: vertical DO concentration CTD profiles collected at CHEF3. The colors of the CTD vertical profiles in the bottom graph match the color of the depth averaged CTD observation in the top graph. The zone of low DO is highlighted in red.

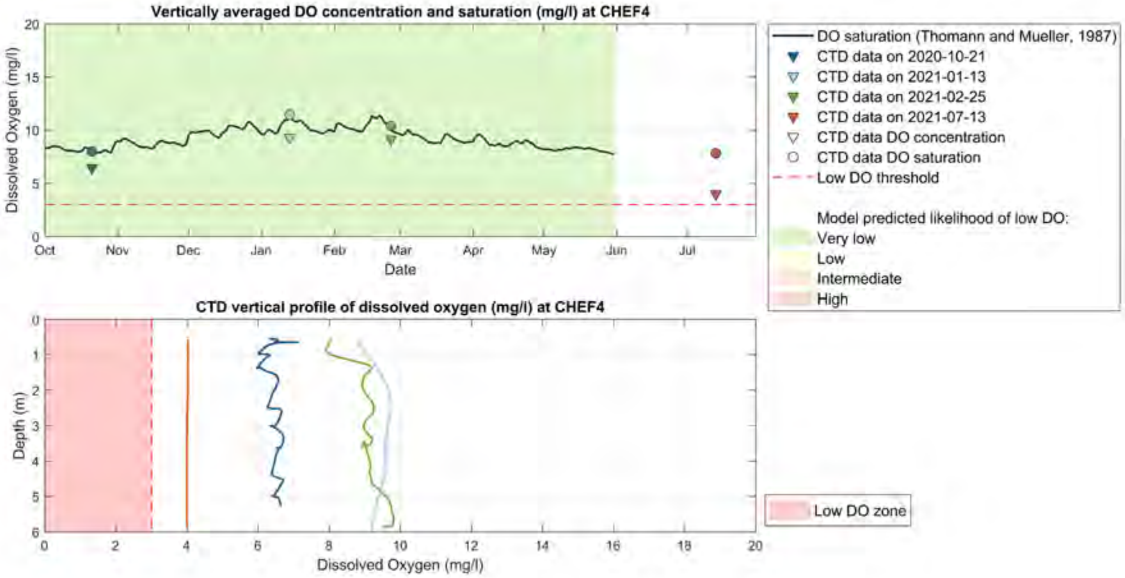

Figure F-4. DO proxy validation with CTD casts at CHEF4. Top graph: DO saturation estimated with Eq.8 (blue line), depth averaged DO saturation (circles) and concentration (triangles) measured by the CTD casts at CHEF4. Background color shows the likelihood of low DO predicted using the Hydrodynamic Model results and the rules in Table 8. Bottom graph: vertical DO concentration CTD profiles collected at CHEF4. The colors of the CTD vertical profiles in the bottom graph match the color of the depth averaged CTD observation in the top graph. The zone of low DO is highlighted in red.

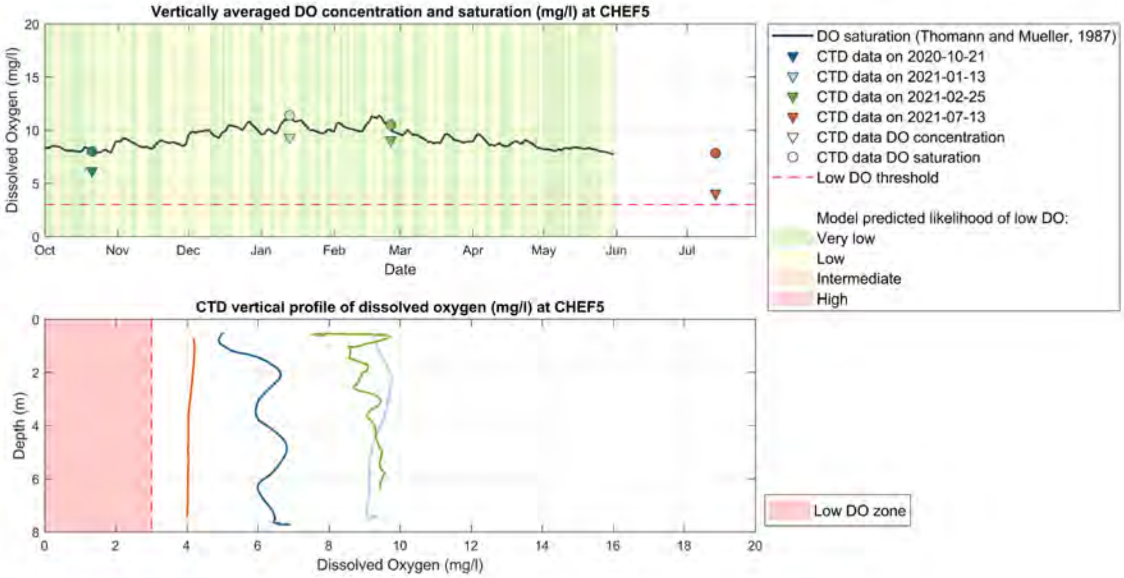

Figure F-5. DO proxy validation with CTD casts at CHEF5. Top graph: DO saturation estimated with Eq.8 (blue line), depth averaged DO saturation (circles) and concentration (triangles) measured by the CTD casts at CHEF5. Background color shows the likelihood of low DO predicted using the Hydrodynamic Model results and the rules in Table 8. Bottom graph: vertical DO concentration CTD profiles collected at CHEF5. The colors of the CTD vertical profiles in the bottom graph match the color of the depth averaged CTD observation in the top graph. The zone of low DO is highlighted in red.

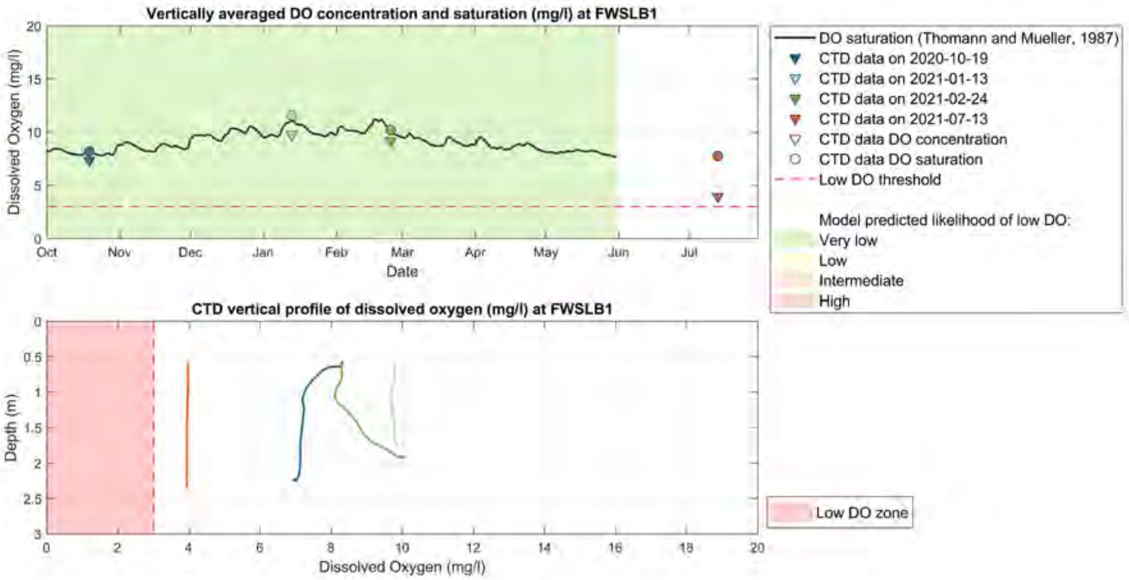

Figure F-6. DO proxy validation with CTD casts at FWSLB1. Top graph: DO saturation estimated with Eq.8 (blue line), depth averaged DO saturation (circles) and concentration (triangles) measured by the CTD casts at FWSLB1. Background color shows the likelihood of low DO predicted using the Hydrodynamic Model results and the rules in Table 8. Bottom graph: vertical DO concentration CTD profiles collected at FWSLB1. The colors of the CTD vertical profiles in the bottom graph match the color of the depth averaged CTD observation in the top graph. The zone of low DO is highlighted in red.

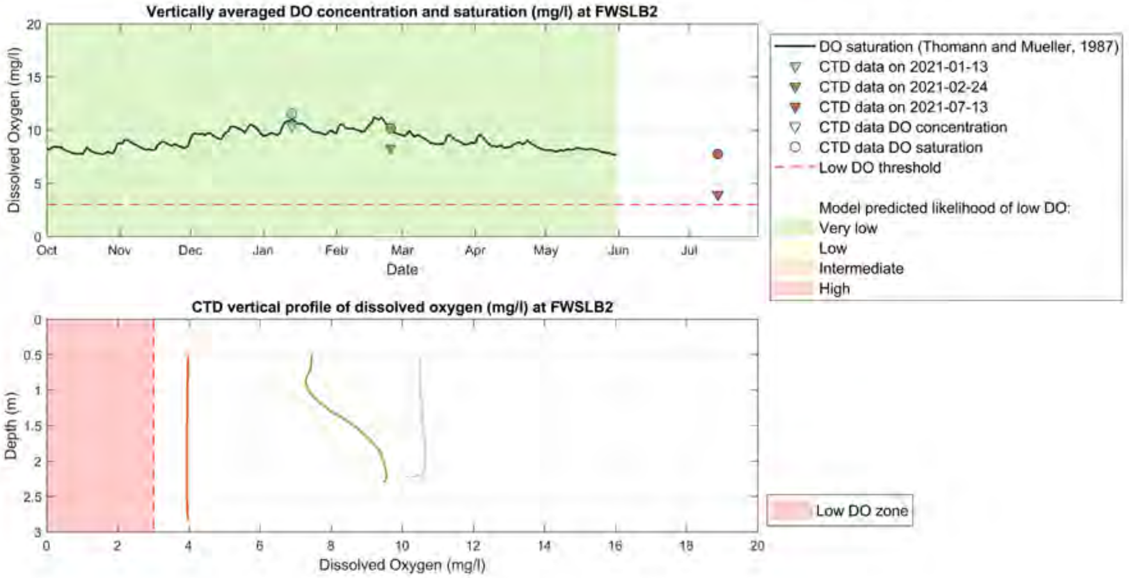

Figure F-7. DO proxy validation with CTD casts at FWSLB2. Top graph: DO saturation estimated with Eq.8 (blue line), depth averaged DO saturation (circles) and concentration (triangles) measured by the CTD casts at FWSLB2. Background color shows the likelihood of low DO predicted using the Hydrodynamic Model results and the rules in Table 8. Bottom graph: vertical DO concentration CTD profiles collected at FWSLB2. The colors of the CTD vertical profiles in the bottom graph match the color of the depth averaged CTD observation in the top graph. The zone of low DO is highlighted in red.

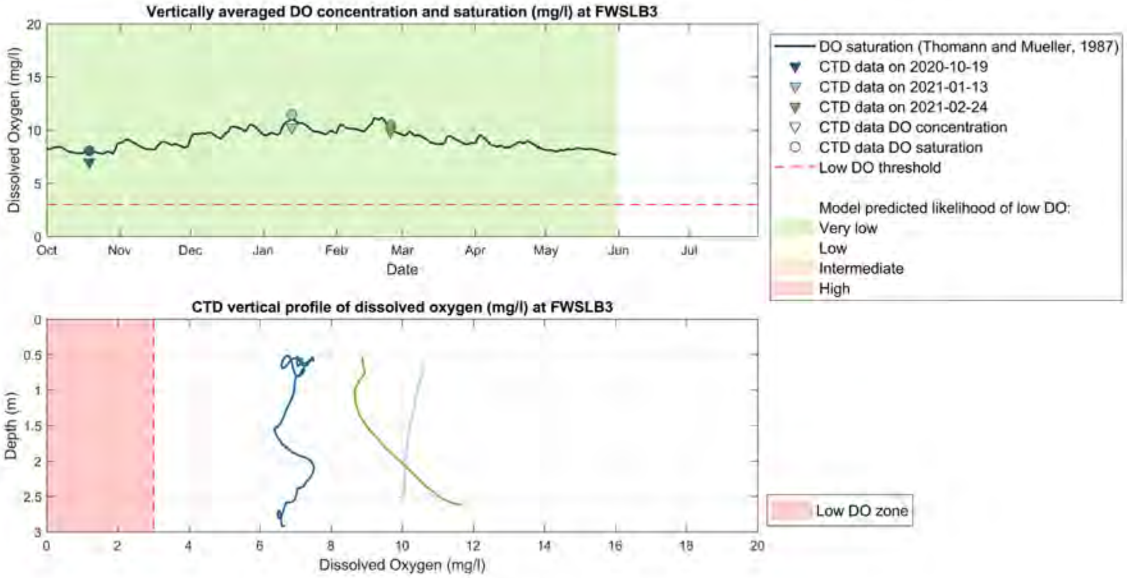

Figure F-8. DO proxy validation with CTD casts at FWSLB3. Top graph: DO saturation estimated with Eq.8 (blue line), depth averaged DO saturation (circles) and concentration (triangles) measured by the CTD casts at FWSLB3. Background color shows the likelihood of low DO predicted using the Hydrodynamic Model results and the rules in Table 8. Bottom graph: vertical DO concentration CTD profiles collected at FWSLB3. The colors of the CTD vertical profiles in the bottom graph match the color of the depth averaged CTD observation in the top graph. The zone of low DO is highlighted in red.

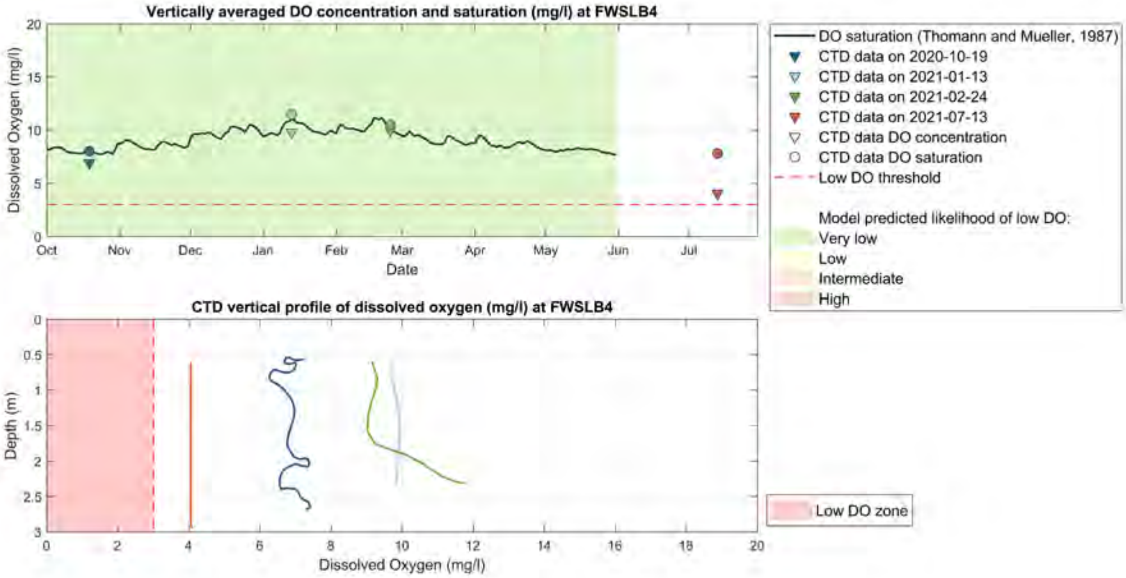

Figure F-9. DO proxy validation with CTD casts at FWSLB4. Top graph: DO saturation estimated with Eq.8 (blue line), depth averaged DO saturation (circles) and concentration (triangles) measured by the CTD casts at FWSLB4. Background color shows the likelihood of low DO predicted using the Hydrodynamic Model results and the rules in Table 8. Bottom graph: vertical DO concentration CTD profiles collected at FWSLB4. The colors of the CTD vertical profiles in the bottom graph match the color of the depth averaged CTD observation in the top graph. The zone of low DO is highlighted in red.

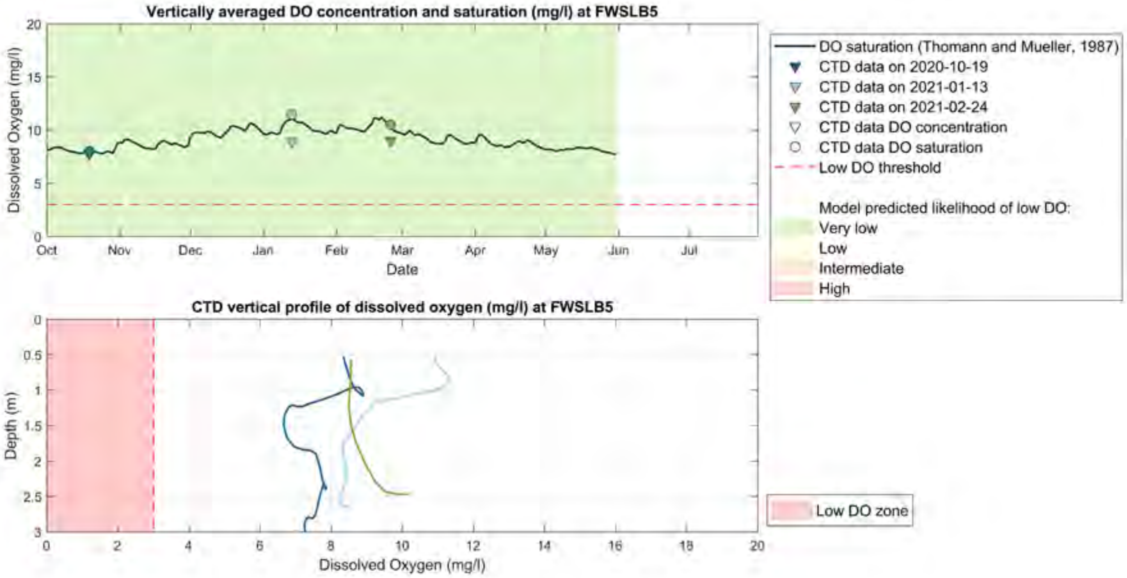

Figure F-10. DO proxy validation with CTD casts at FWSLB5. Top graph: DO saturation estimated with Eq.8 (blue line), depth averaged DO saturation (circles) and concentration (triangles) measured by the CTD casts at FWSLB5. Background color shows the likelihood of low DO predicted using the Hydrodynamic Model results and the rules in Table 8. Bottom graph: vertical DO concentration CTD profiles collected at FWSLB5. The colors of the CTD vertical profiles in the bottom graph match the color of the depth averaged CTD observation in the top graph. The zone of low DO is highlighted in red.

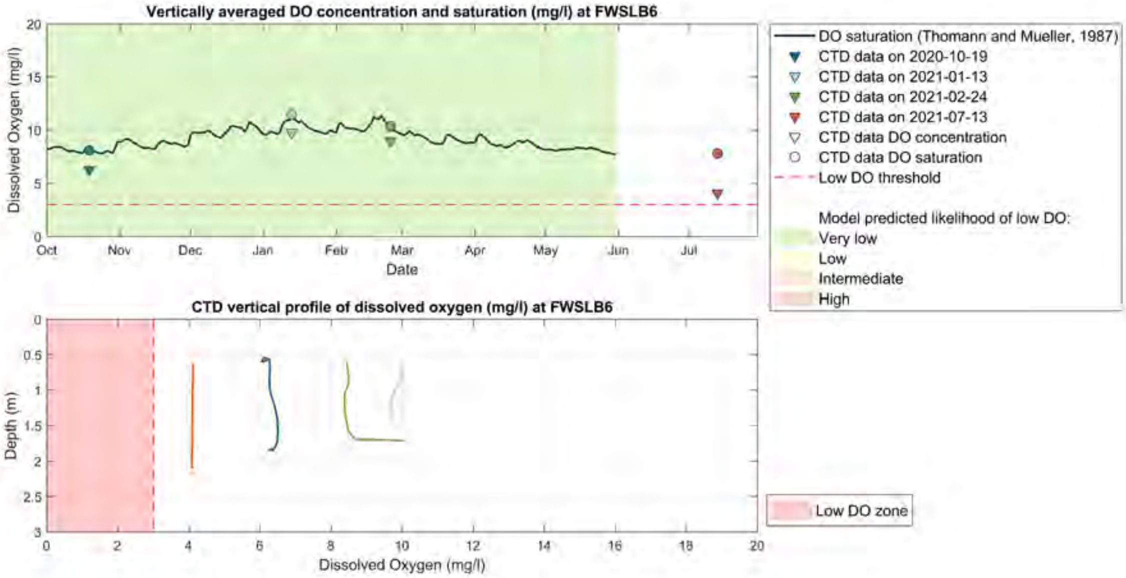

Figure F-11. DO proxy validation with CTD casts at FWSLB6. Top graph: DO saturation estimated with Eq.8 (blue line), depth averaged DO saturation (circles) and concentration (triangles) measured by the CTD casts at FWSLB6. Background color shows the likelihood of low DO predicted using the Hydrodynamic Model results and the rules in Table 8. Bottom graph: vertical DO concentration CTD profiles collected at FWSLB6. The colors of the CTD vertical profiles in the bottom graph match the color of the depth averaged CTD observation in the top graph. The zone of low DO is highlighted in red.

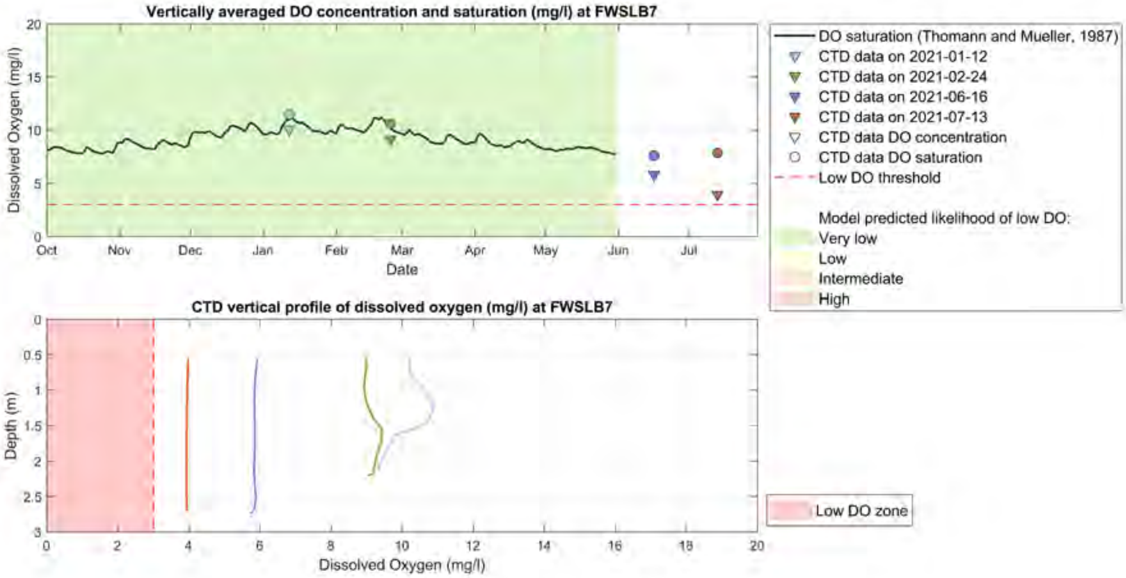

Figure F-12. DO proxy validation with CTD casts at FWSLB7. Top graph: DO saturation estimated with Eq.8 (blue line), depth averaged DO saturation (circles) and concentration (triangles) measured by the CTD casts at FWSLB7. Background color shows the likelihood of low DO predicted using the Hydrodynamic Model results and the rules in Table 8. Bottom graph: vertical DO concentration CTD profiles collected at FWSLB7. The colors of the CTD vertical profiles in the bottom graph match the color of the depth averaged CTD observation in the top graph. The zone of low DO is highlighted in red.

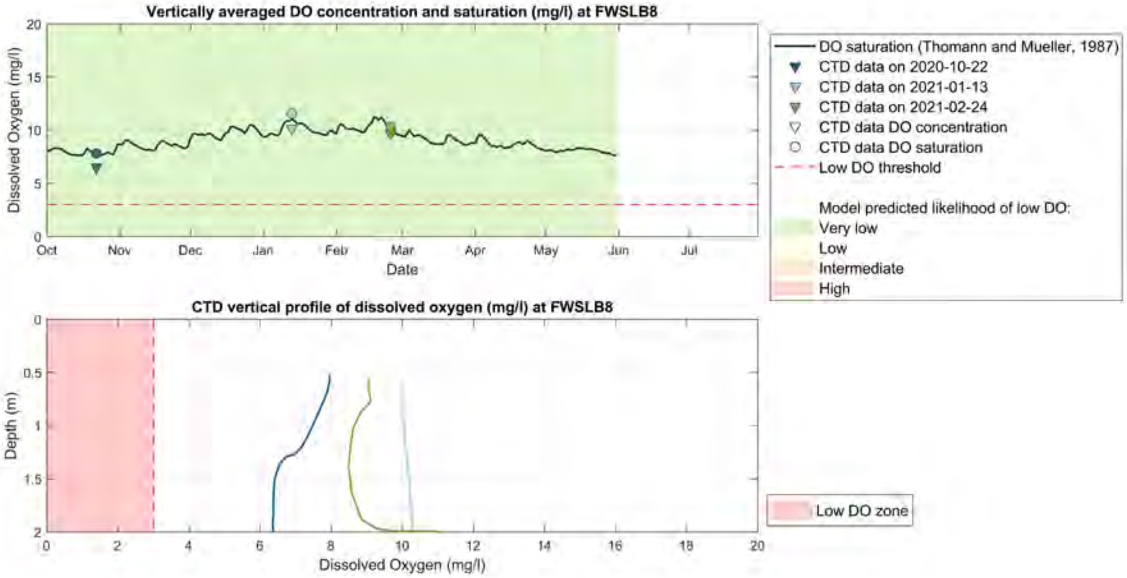

Figure F-13. DO proxy validation with CTD casts at FWSLB8. Top graph: DO saturation estimated with Eq.8 (blue line), depth averaged DO saturation (circles) and concentration (triangles) measured by the CTD casts at FWSLB8. Background color shows the likelihood of low DO predicted using the Hydrodynamic Model results and the rules in Table 8. Bottom graph: vertical DO concentration CTD profiles collected at FWSLB8. The colors of the CTD vertical profiles in the bottom graph match the color of the depth averaged CTD observation in the top graph. The zone of low DO is highlighted in red.

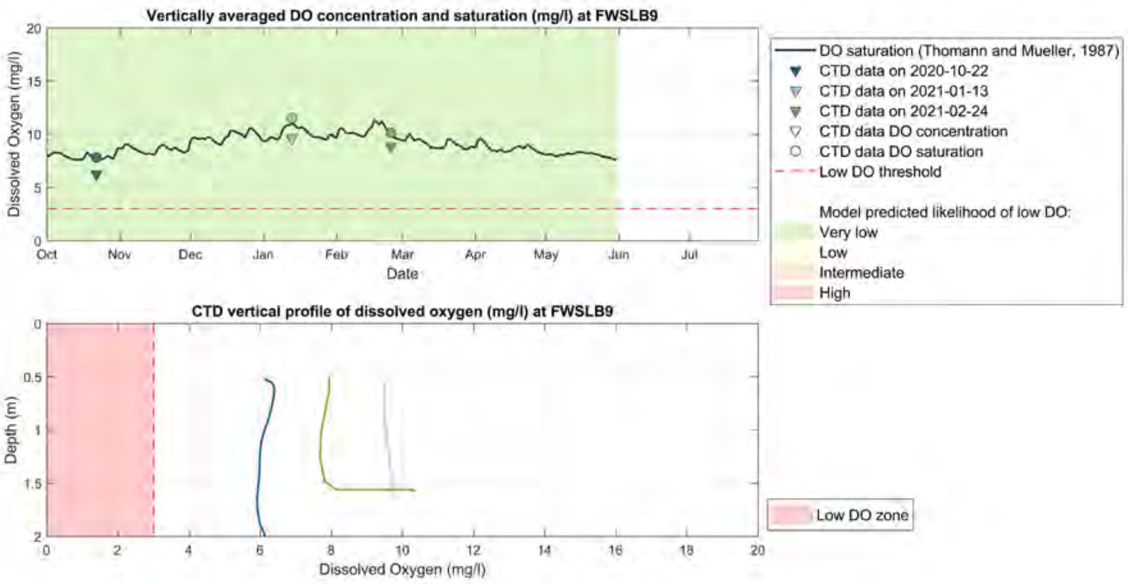

Figure F-14. DO proxy validation with CTD casts at FWSLB9. Top graph: DO saturation estimated with Eq.8 (blue line), depth averaged DO saturation (circles) and concentration (triangles) measured by the CTD casts at FWSLB9. Background color shows the likelihood of low DO predicted using the Hydrodynamic Model results and the rules in Table 8. Bottom graph: vertical DO concentration CTD profiles collected at FWSLB9. The colors of the CTD vertical profiles in the bottom graph match the color of the depth averaged CTD observation in the top graph. The zone of low DO is highlighted in red.

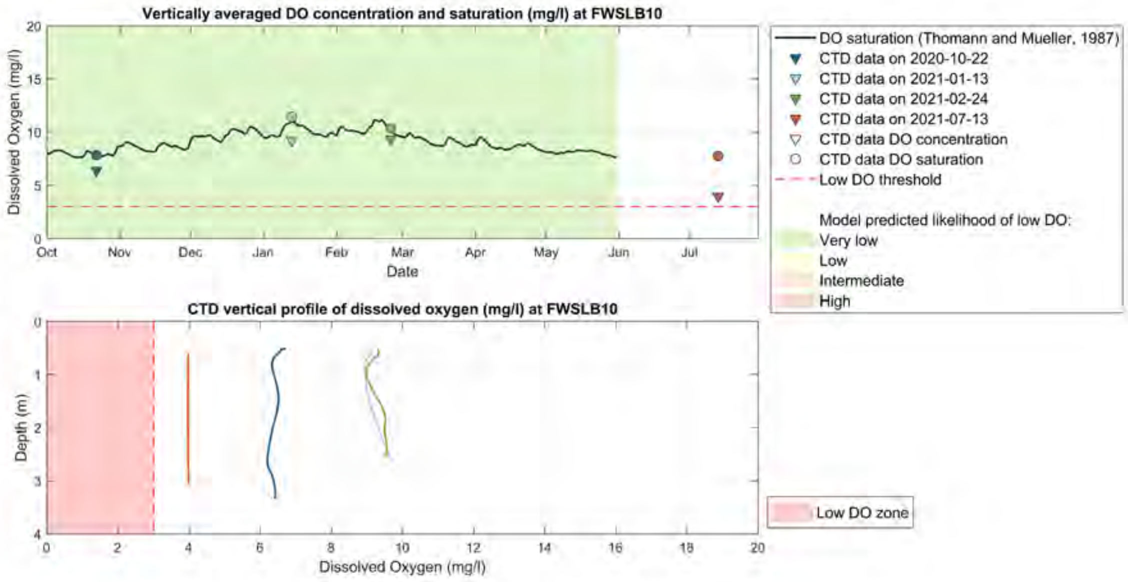

Figure F-15. DO proxy validation with CTD casts at FWSLB10. Top graph: DO saturation estimated with Eq.8 (blue line), depth averaged DO saturation (circles) and concentration (triangles) measured by the CTD casts at FWSLB10. Background color shows the likelihood of low DO predicted using the Hydrodynamic Model results and the rules in Table 8. Bottom graph: vertical DO concentration CTD profiles collected at FWSLB10. The colors of the CTD vertical profiles in the bottom graph match the color of the depth averaged CTD observation in the top graph. The zone of low DO is highlighted in red.

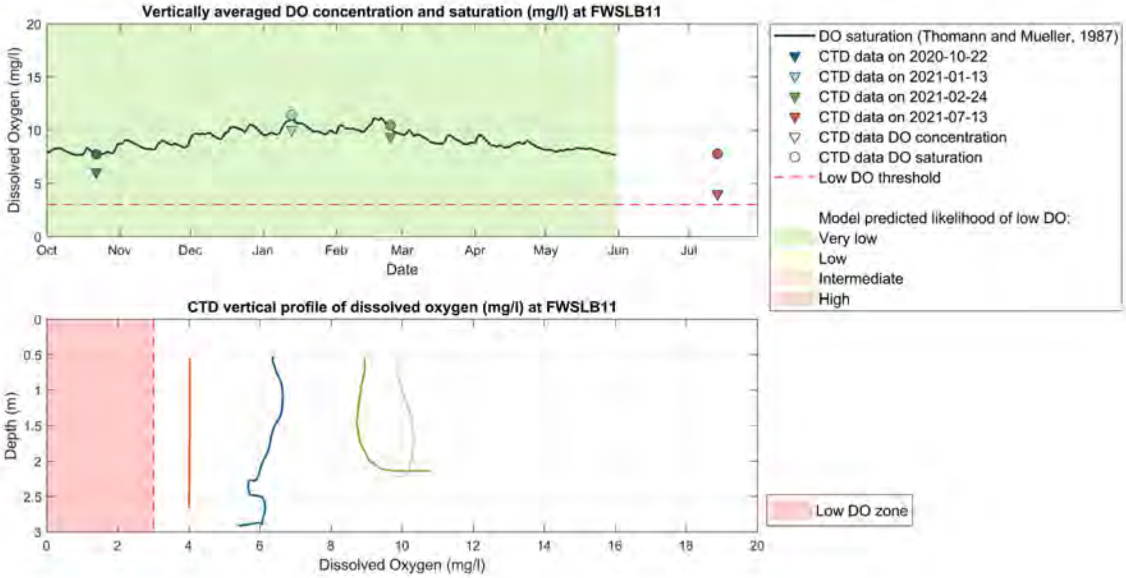

Figure F-16. DO proxy validation with CTD casts at FWSLB11. Top graph: DO saturation estimated with Eq.8 (blue line), depth averaged DO saturation (circles) and concentration (triangles) measured by the CTD casts at FWSLB11. Background color shows the likelihood of low DO predicted using the Hydrodynamic Model results and the rules in Table 8. Bottom graph: vertical DO concentration CTD profiles collected at FWSLB11. The colors of the CTD vertical profiles in the bottom graph match the color of the depth averaged CTD observation in the top graph. The zone of low DO is highlighted in red.

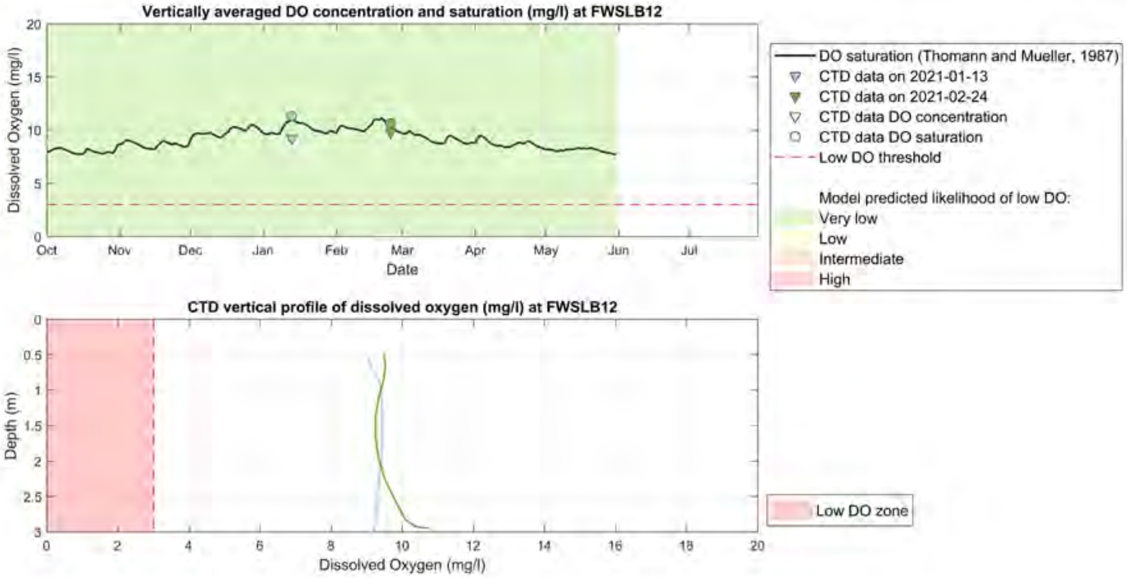

Figure F-17. DO proxy validation with CTD casts at FWSLB12. Top graph: DO saturation estimated with Eq.8 (blue line), depth averaged DO saturation (circles) and concentration (triangles) measured by the CTD casts at FWSLB12. Background color shows the likelihood of low DO predicted using the Hydrodynamic Model results and the rules in Table 8. Bottom graph: vertical DO concentration CTD profiles collected at FWSLB12. The colors of the CTD vertical profiles in the bottom graph match the color of the depth averaged CTD observation in the top graph. The zone of low DO is highlighted in red.

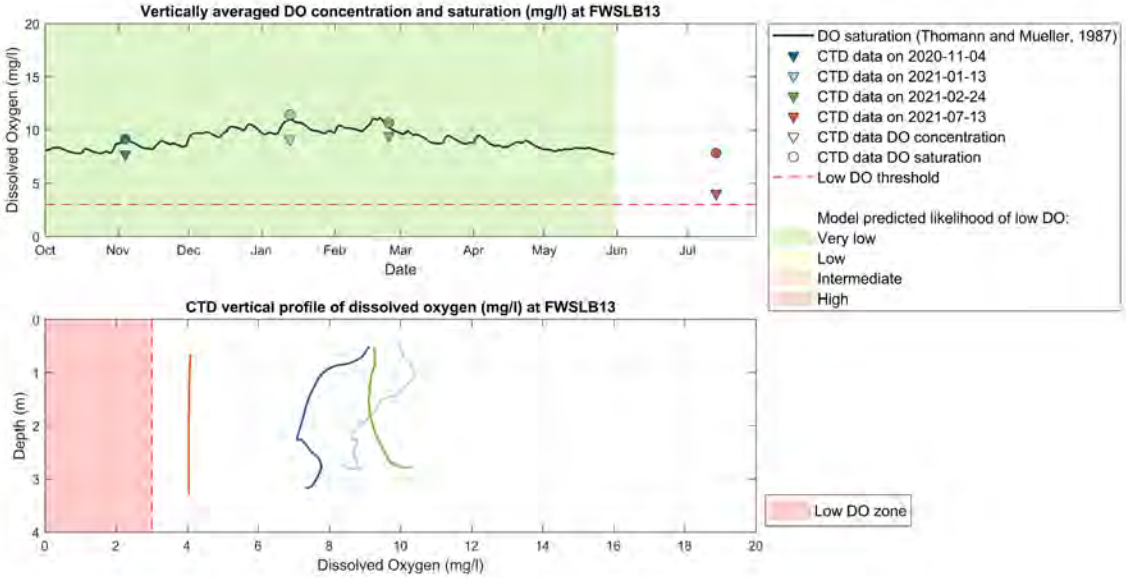

Figure F-18. DO proxy validation with CTD casts at FWSLB13. Top graph: DO saturation estimated with Eq.8 (blue line), depth averaged DO saturation (circles) and concentration (triangles) measured by the CTD casts at FWSLB13. Background color shows the likelihood of low DO predicted using the Hydrodynamic Model results and the rules in Table 8. Bottom graph: vertical DO concentration CTD profiles collected at FWSLB13. The colors of the CTD vertical profiles in the bottom graph match the color of the depth averaged CTD observation in the top graph. The zone of low DO is highlighted in red.

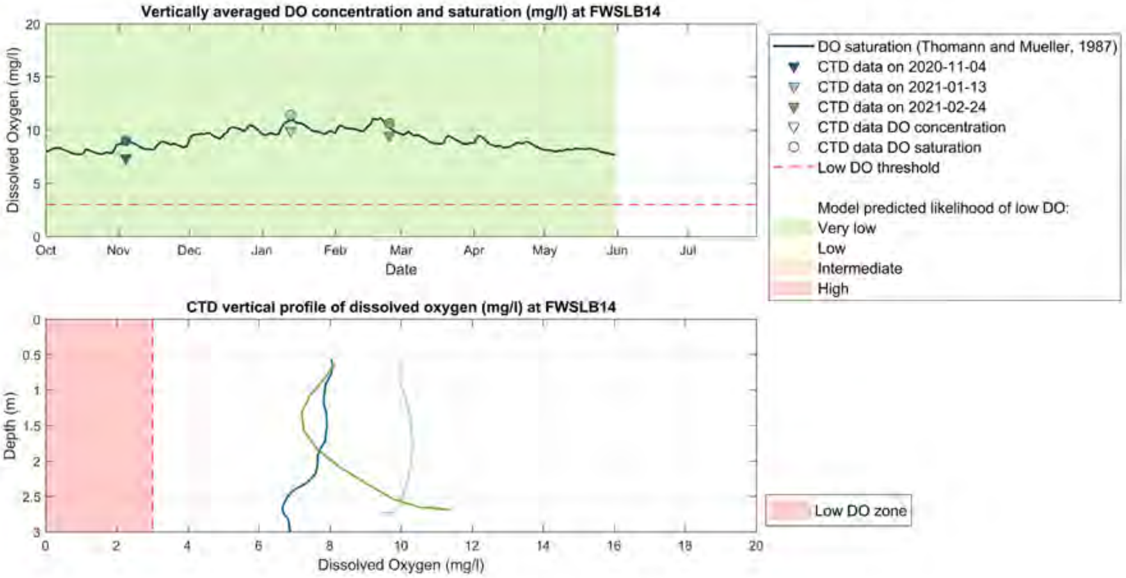

Figure F-19. DO proxy validation with CTD casts at FWSLB14. Top graph: DO saturation estimated with Eq.8 (blue line), depth averaged DO saturation (circles) and concentration (triangles) measured by the CTD casts at FWSLB14. Background color shows the likelihood of low DO predicted using the Hydrodynamic Model results and the rules in Table 8. Bottom graph: vertical DO concentration CTD profiles collected at FWSLB14. The colors of the CTD vertical profiles in the bottom graph match the color of the depth averaged CTD observation in the top graph. The zone of low DO is highlighted in red.

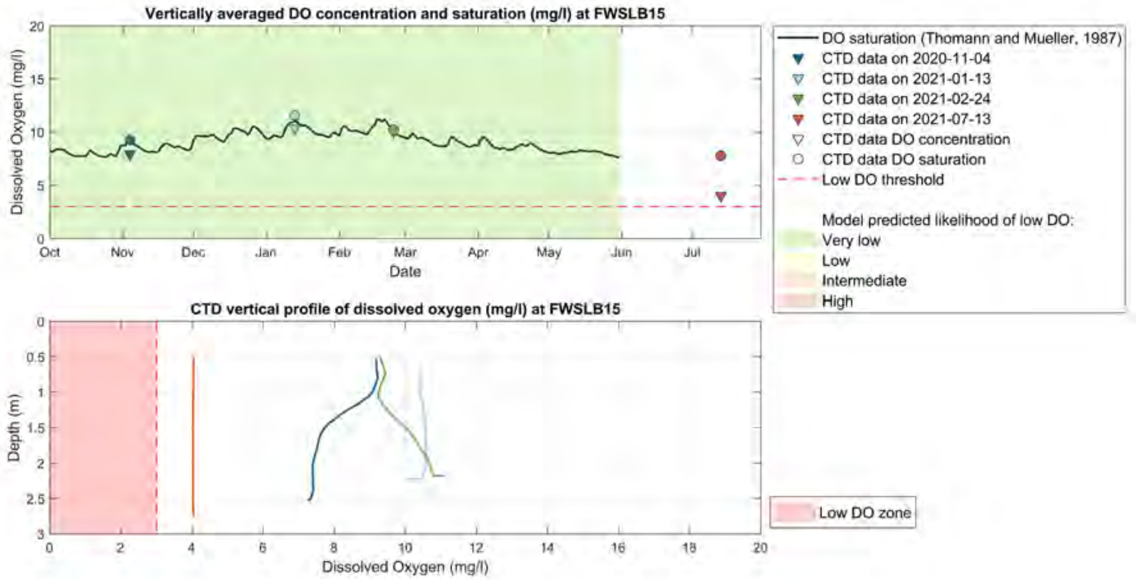

Figure F-20. DO proxy validation with CTD casts at FWSLB15. Top graph: DO saturation estimated with Eq.8 (blue line), depth averaged DO saturation (circles) and concentration (triangles) measured by the CTD casts at FWSLB15. Background color shows the likelihood of low DO predicted using the Hydrodynamic Model results and the rules in Table 8. Bottom graph: vertical DO concentration CTD profiles collected at FWSLB15. The colors of the CTD vertical profiles in the bottom graph match the color of the depth averaged CTD observation in the top graph. The zone of low DO is highlighted in red.

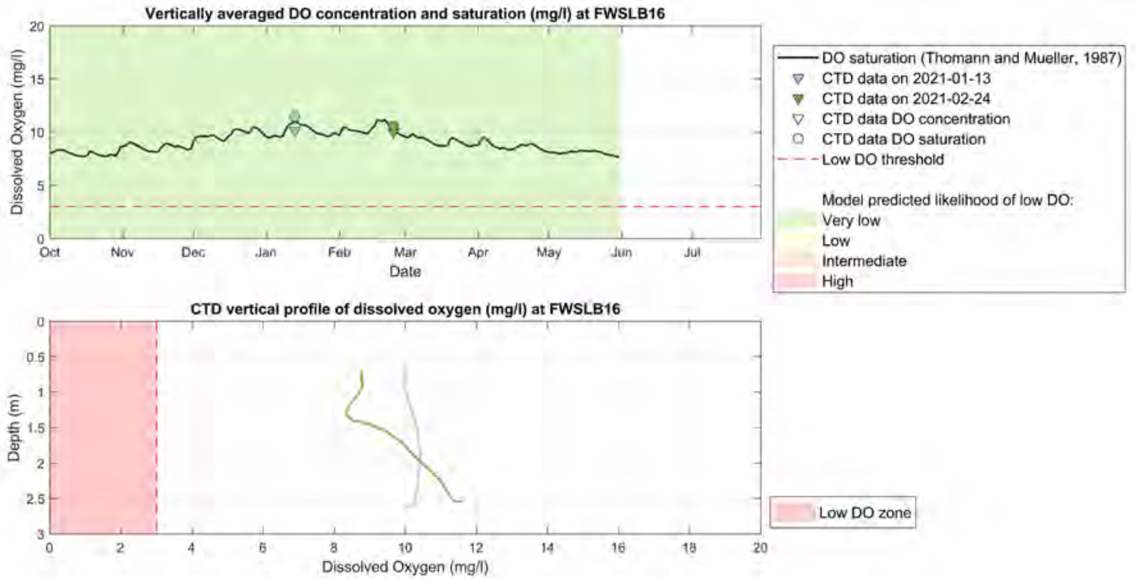

Figure F-21. DO proxy validation with CTD casts at FWSLB16. Top graph: DO saturation estimated with Eq.8 (blue line), depth averaged DO saturation (circles) and concentration (triangles) measured by the CTD casts at FWSLB16. Background color shows the likelihood of low DO predicted using the Hydrodynamic Model results and the rules in Table 8. Bottom graph: vertical DO concentration CTD profiles collected at FWSLB16. The colors of the CTD vertical profiles in the bottom graph match the color of the depth averaged CTD observation in the top graph. The zone of low DO is highlighted in red.

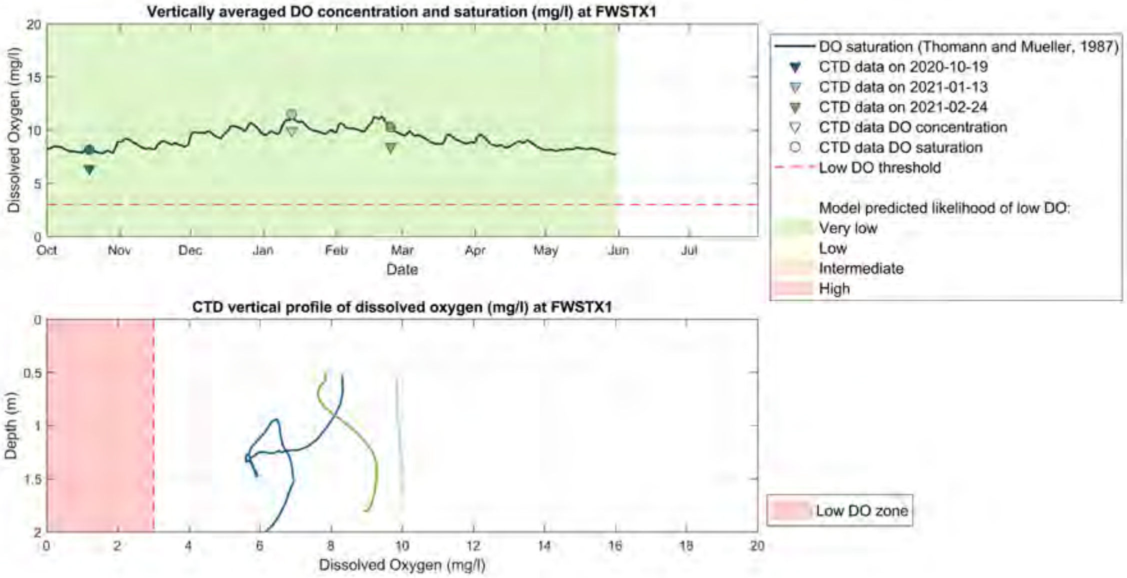

Figure F-22. DO proxy validation with CTD casts at FWSTX1. Top graph: DO saturation estimated with Eq.8 (blue line), depth averaged DO saturation (circles) and concentration (triangles) measured by the CTD casts at FWSTX1. Background color shows the likelihood of low DO predicted using the Hydrodynamic Model results and the rules in Table 8. Bottom graph: vertical DO concentration CTD profiles collected at FWSTX1. The colors of the CTD vertical profiles in the bottom graph match the color of the depth averaged CTD observation in the top graph. The zone of low DO is highlighted in red.

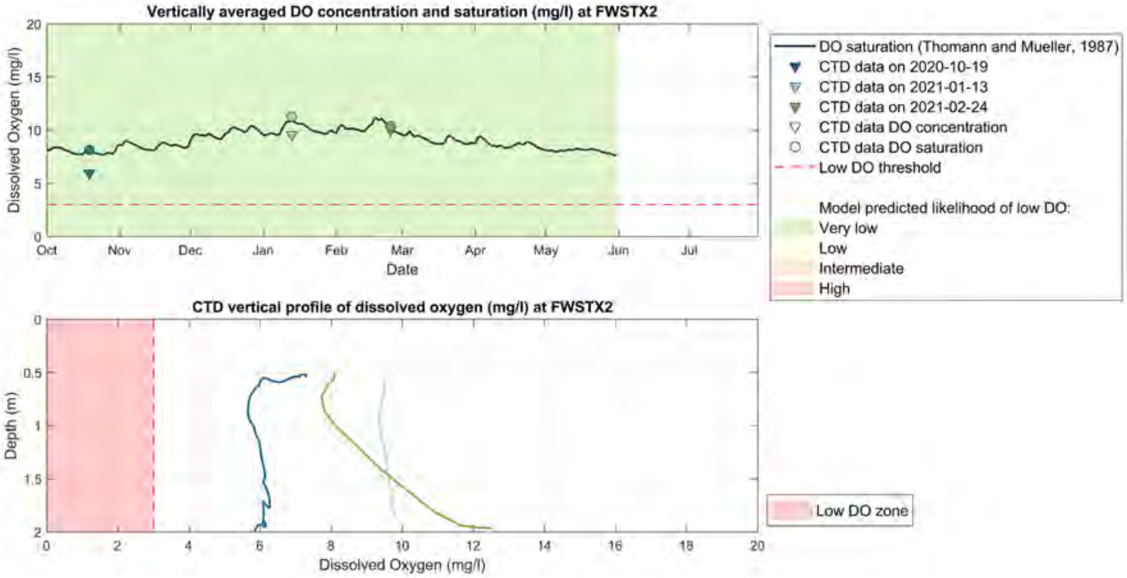

Figure F-23. DO proxy validation with CTD casts at FWSTX2. Top graph: DO saturation estimated with Eq.8 (blue line), depth averaged DO saturation (circles) and concentration (triangles) measured by the CTD casts at FWSTX2. Background color shows the likelihood of low DO predicted using the Hydrodynamic Model results and the rules in Table 8. Bottom graph: vertical DO concentration CTD profiles collected at FWSTX2. The colors of the CTD vertical profiles in the bottom graph match the color of the depth averaged CTD observation in the top graph. The zone of low DO is highlighted in red.

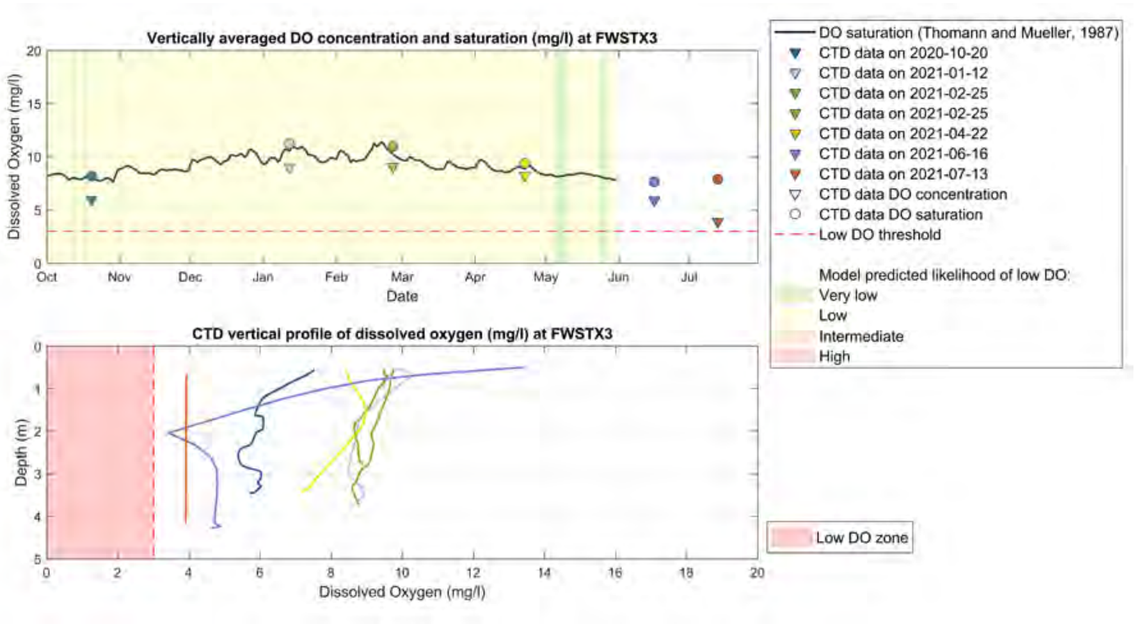

Figure F-24. DO proxy validation with CTD casts at FWSTX3. Top graph: DO saturation estimated with Eq.8 (blue line), depth averaged DO saturation (circles) and concentration (triangles) measured by the CTD casts at FWSTX3. Background color shows the likelihood of low DO predicted using the Hydrodynamic Model results and the rules in Table 8. Bottom graph: vertical DO concentration CTD profiles collected at FWSTX3. The colors of the CTD vertical profiles in the bottom graph match the color of the depth averaged CTD observation in the top graph. The zone of low DO is highlighted in red.

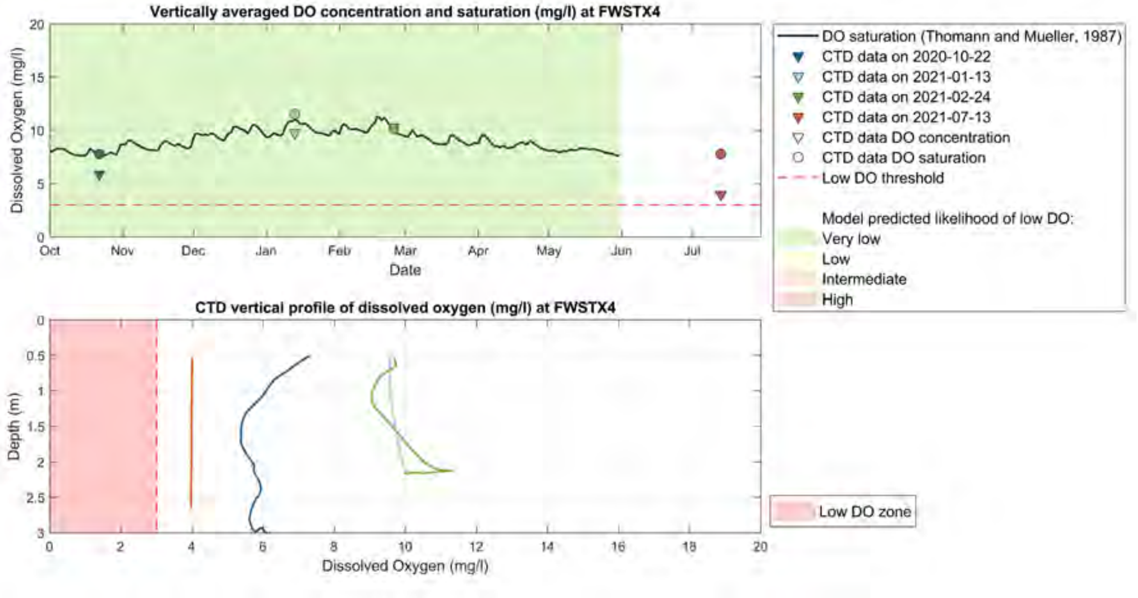

Figure F-25. DO proxy validation with CTD casts at FWSTX4. Top graph: DO saturation estimated with Eq.8 (blue line), depth averaged DO saturation (circles) and concentration (triangles) measured by the CTD casts at FWSTX4. Background color shows the likelihood of low DO predicted using the Hydrodynamic Model results and the rules in Table 8. Bottom graph: vertical DO concentration CTD profiles collected at FWSTX4. The colors of the CTD vertical profiles in the bottom graph match the color of the depth averaged CTD observation in the top graph. The zone of low DO is highlighted in red.

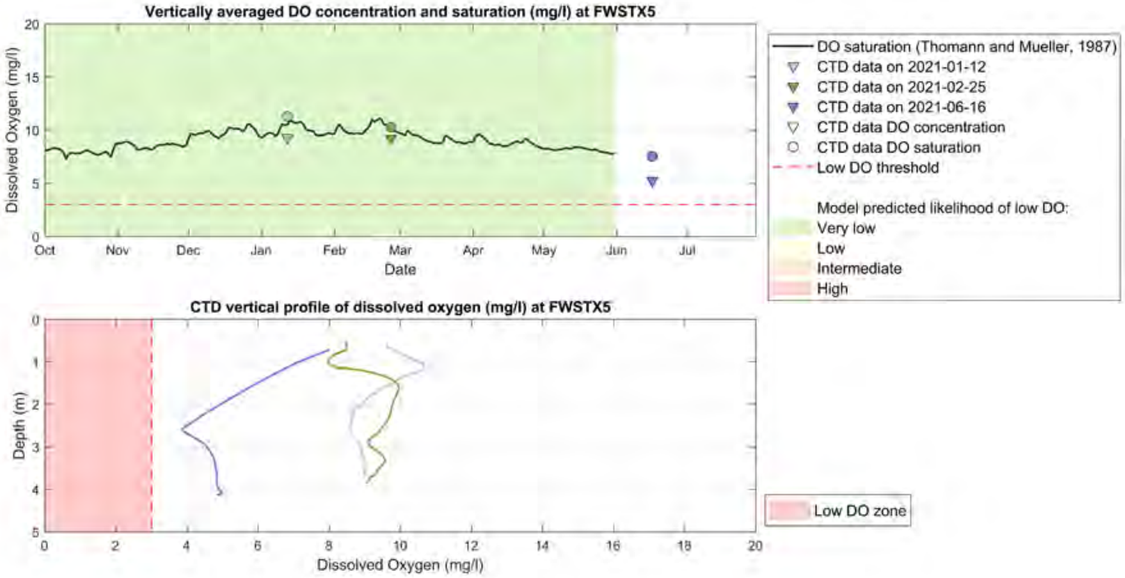

Figure F-26. DO proxy validation with CTD casts at FWSTX5. Top graph: DO saturation estimated with Eq.8 (blue line), depth averaged DO saturation (circles) and concentration (triangles) measured by the CTD casts at FWSTX5. Background color shows the likelihood of low DO predicted using the Hydrodynamic Model results and the rules in Table 8. Bottom graph: vertical DO concentration CTD profiles collected at FWSTX5. The colors of the CTD vertical profiles in the bottom graph match the color of the depth averaged CTD observation in the top graph. The zone of low DO is highlighted in red.

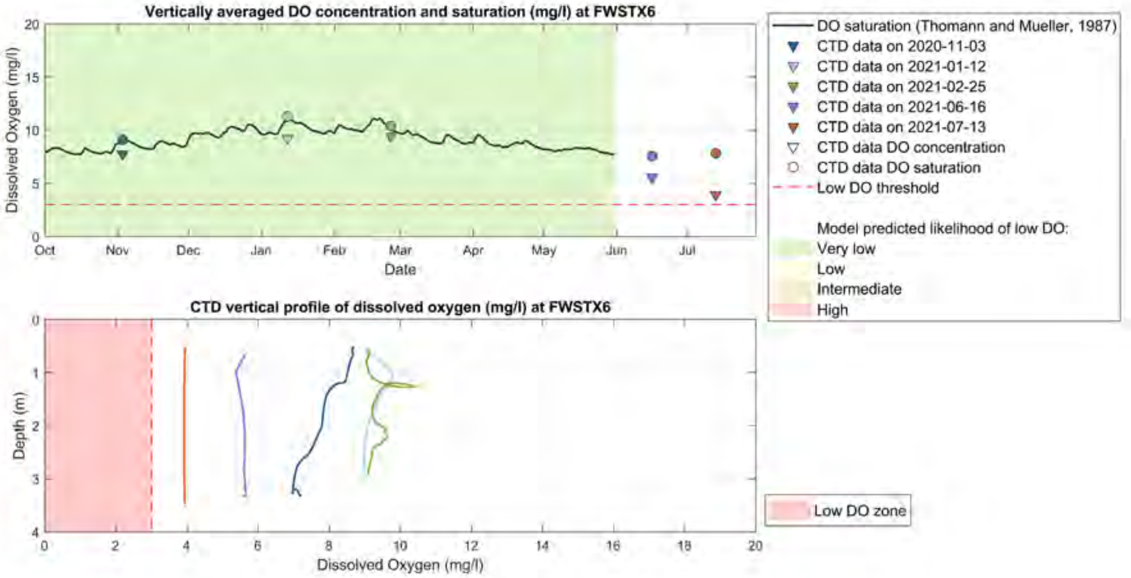

Figure F-27. DO proxy validation with CTD casts at FWSTX6. Top graph: DO saturation estimated with Eq.8 (blue line), depth averaged DO saturation (circles) and concentration (triangles) measured by the CTD casts at FWSTX6. Background color shows the likelihood of low DO predicted using the Hydrodynamic Model results and the rules in Table 8. Bottom graph: vertical DO concentration CTD profiles collected at FWSTX6. The colors of the CTD vertical profiles in the bottom graph match the color of the depth averaged CTD observation in the top graph. The zone of low DO is highlighted in red.

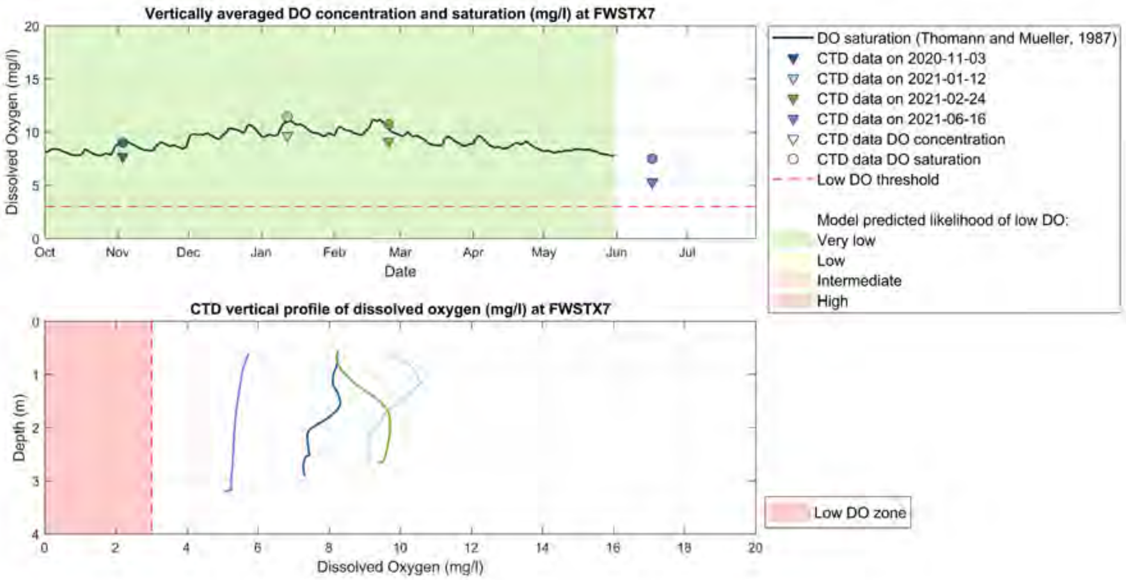

Figure F-28. DO proxy validation with CTD casts at FWSTX7. Top graph: DO saturation estimated with Eq.8 (blue line), depth averaged DO saturation (circles) and concentration (triangles) measured by the CTD casts at FWSTX7. Background color shows the likelihood of low DO predicted using the Hydrodynamic Model results and the rules in Table 8. Bottom graph: vertical DO concentration CTD profiles collected at FWSTX7. The colors of the CTD vertical profiles in the bottom graph match the color of the depth averaged CTD observation in the top graph. The zone of low DO is highlighted in red.

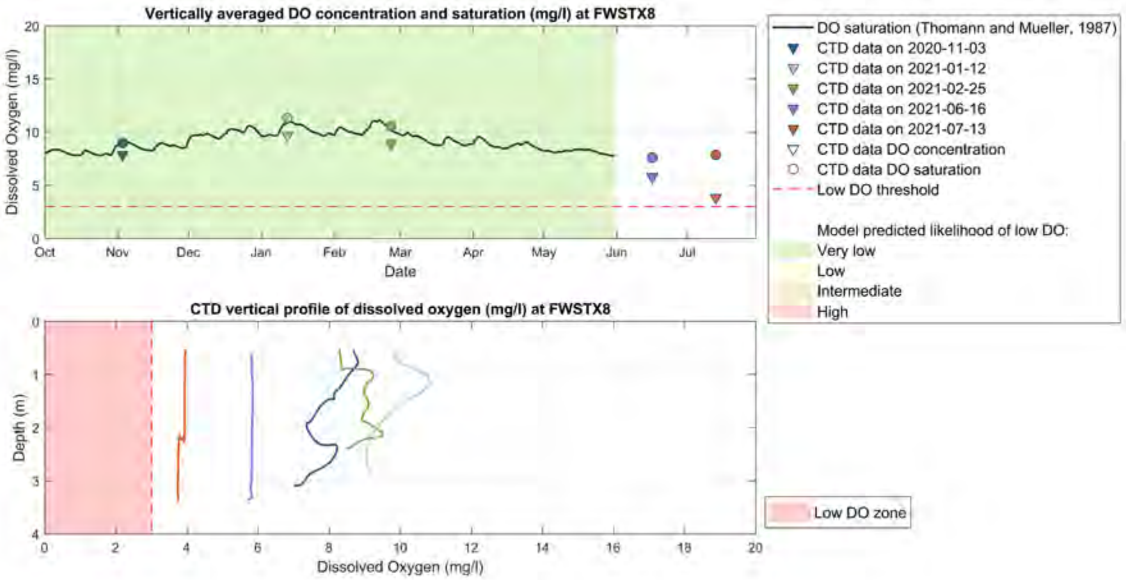

Figure F-29. DO proxy validation with CTD casts at FWSTX8. Top graph: DO saturation estimated with Eq.8 (blue line), depth averaged DO saturation (circles) and concentration (triangles) measured by the CTD casts at FWSTX8. Background color shows the likelihood of low DO predicted using the Hydrodynamic Model results and the rules in Table 8. Bottom graph: vertical DO concentration CTD profiles collected at FWSTX8. The colors of the CTD vertical profiles in the bottom graph match the color of the depth averaged CTD observation in the top graph. The zone of low DO is highlighted in red.

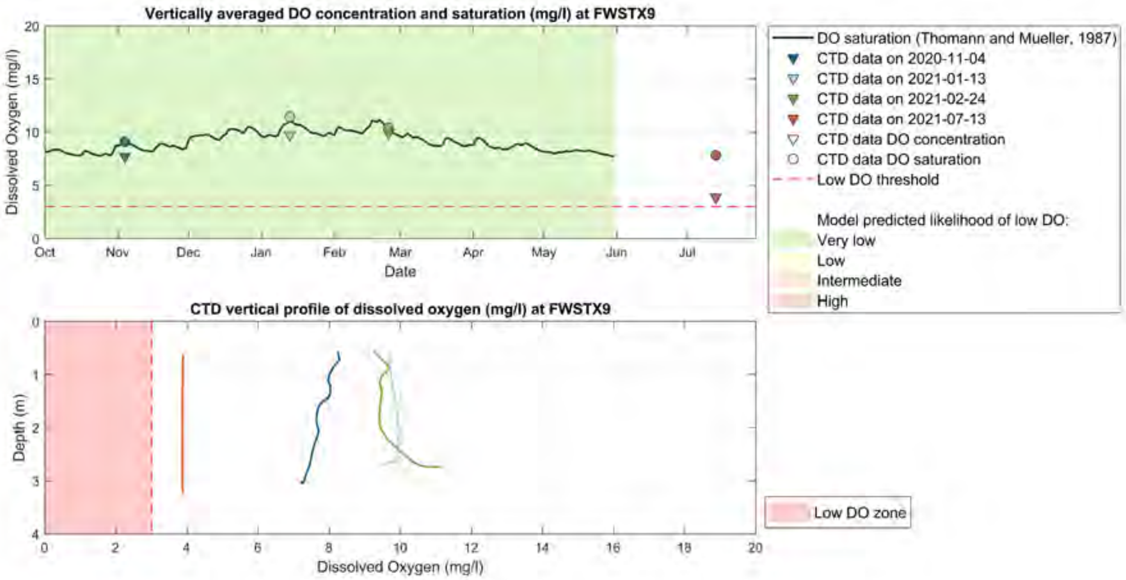

Figure F-30. DO proxy validation with CTD casts at FWSTX9. Top graph: DO saturation estimated with Eq.8 (blue line), depth averaged DO saturation (circles) and concentration (triangles) measured by the CTD casts at FWSTX9. Background color shows the likelihood of low DO predicted using the Hydrodynamic Model results and the rules in Table 8. Bottom graph: vertical DO concentration CTD profiles collected at FWSTX9. The colors of the CTD vertical profiles in the bottom graph match the color of the depth averaged CTD observation in the top graph. The zone of low DO is highlighted in red.

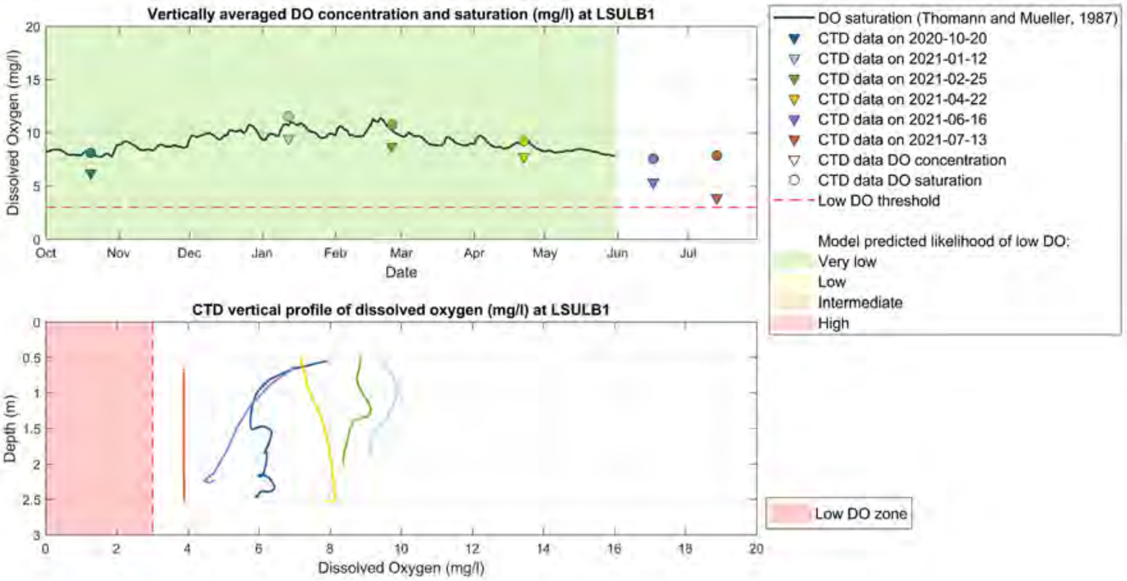

Figure F-31. DO proxy validation with CTD casts at LSULB1. Top graph: DO saturation estimated with Eq.8 (blue line), depth averaged DO saturation (circles) and concentration (triangles) measured by the CTD casts at LSULB1. Background color shows the likelihood of low DO predicted using the Hydrodynamic Model results and the rules in Table 8. Bottom graph: vertical DO concentration CTD profiles collected at LSULB1. The colors of the CTD vertical profiles in the bottom graph match the color of the depth averaged CTD observation in the top graph. The zone of low DO is highlighted in red.

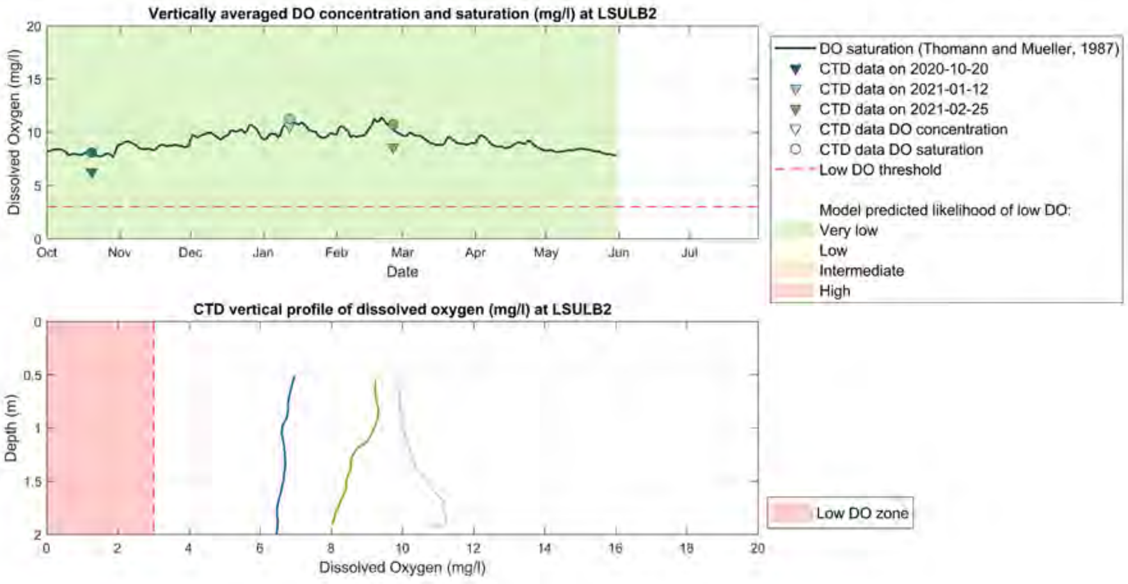

Figure F-32. DO proxy validation with CTD casts at LSULB2. Top graph: DO saturation estimated with Eq.8 (blue line), depth averaged DO saturation (circles) and concentration (triangles) measured by the CTD casts at LSULB2. Background color shows the likelihood of low DO predicted using the Hydrodynamic Model results and the rules in Table 8. Bottom graph: vertical DO concentration CTD profiles collected at LSULB2. The colors of the CTD vertical profiles in the bottom graph match the color of the depth averaged CTD observation in the top graph. The zone of low DO is highlighted in red.

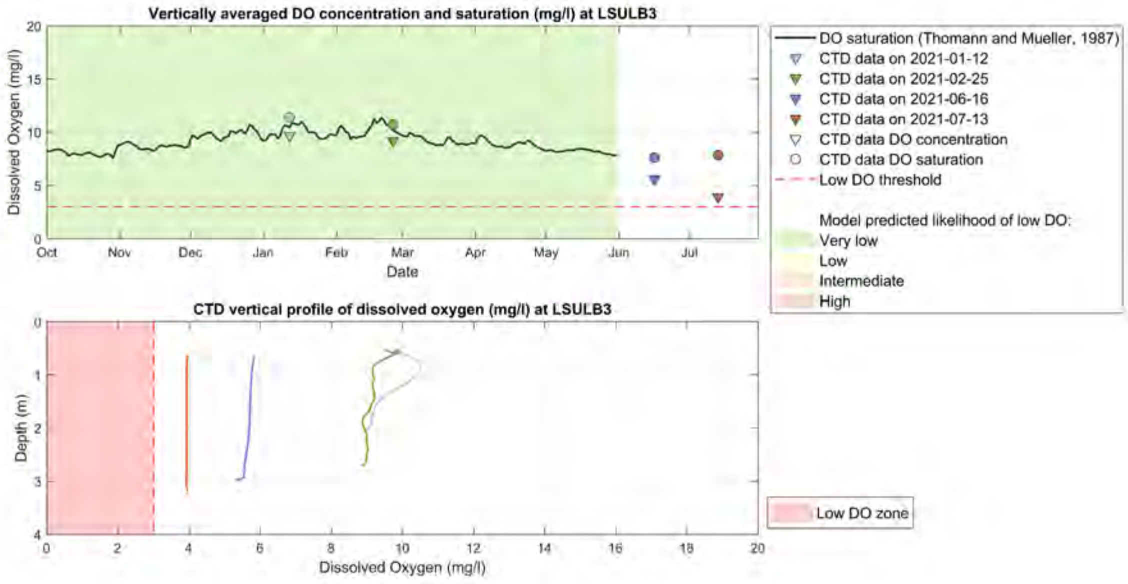

Figure F-33. DO proxy validation with CTD casts at LSULB3. Top graph: DO saturation estimated with Eq.8 (blue line), depth averaged DO saturation (circles) and concentration (triangles) measured by the CTD casts at LSULB3. Background color shows the likelihood of low DO predicted using the Hydrodynamic Model results and the rules in Table 8. Bottom graph: vertical DO concentration CTD profiles collected at LSULB3. The colors of the CTD vertical profiles in the bottom graph match the color of the depth averaged CTD observation in the top graph. The zone of low DO is highlighted in red.

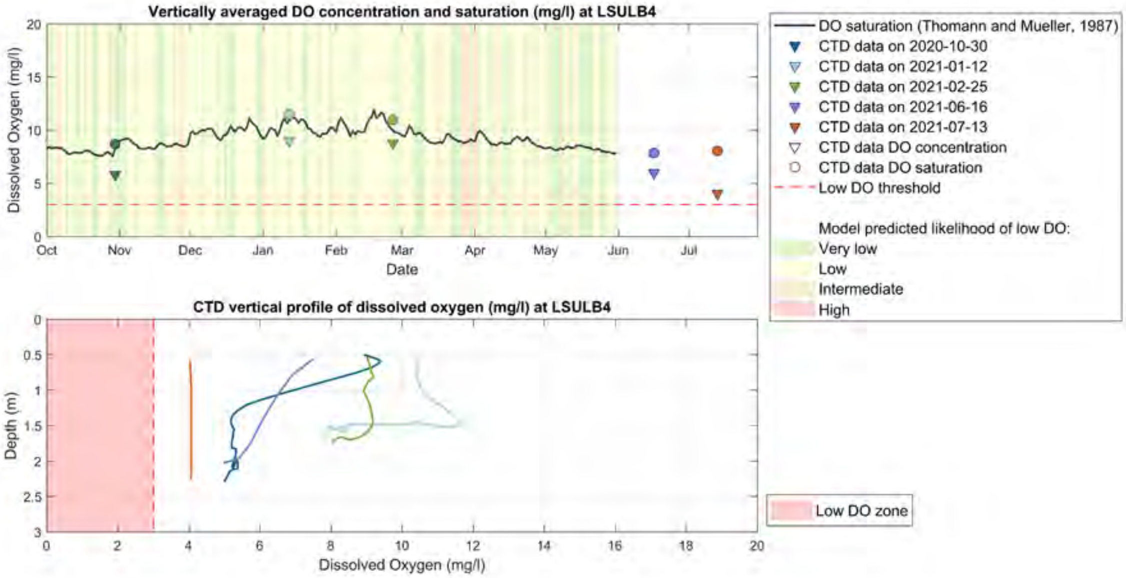

Figure F-34. DO proxy validation with CTD casts at LSULB4. Top graph: DO saturation estimated with Eq.8 (blue line), depth averaged DO saturation (circles) and concentration (triangles) measured by the CTD casts at LSULB4. Background color shows the likelihood of low DO predicted using the Hydrodynamic Model results and the rules in Table 8. Bottom graph: vertical DO concentration CTD profiles collected at LSULB4. The colors of the CTD vertical profiles in the bottom graph match the color of the depth averaged CTD observation in the top graph. The zone of low DO is highlighted in red.

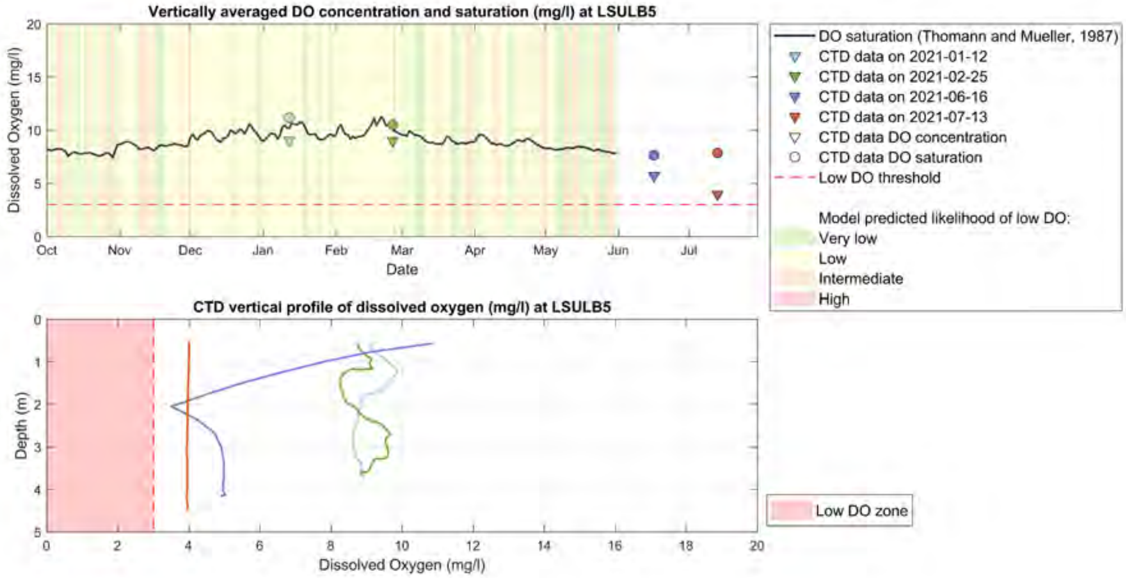

Figure F-35. DO proxy validation with CTD casts at LSULB5. Top graph: DO saturation estimated with Eq.8 (blue line), depth averaged DO saturation (circles) and concentration (triangles) measured by the CTD casts at LSULB5. Background color shows the likelihood of low DO predicted using the Hydrodynamic Model results and the rules in Table 8. Bottom graph: vertical DO concentration CTD profiles collected at LSULB5. The colors of the CTD vertical profiles in the bottom graph match the color of the depth averaged CTD observation in the top graph. The zone of low DO is highlighted in red.

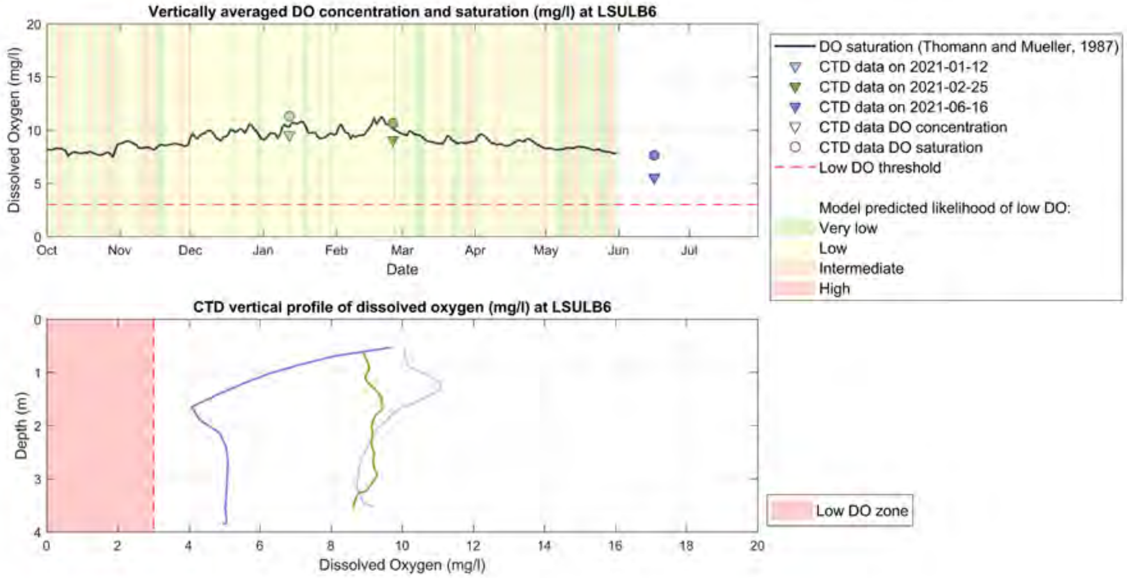

Figure F-36. DO proxy validation with CTD casts at LSULB6. Top graph: DO saturation estimated with Eq.8 (blue line), depth averaged DO saturation (circles) and concentration (triangles) measured by the CTD casts at LSULB6. Background color shows the likelihood of low DO predicted using the Hydrodynamic Model results and the rules in Table 8. Bottom graph: vertical DO concentration CTD profiles collected at LSULB6. The colors of the CTD vertical profiles in the bottom graph match the color of the depth averaged CTD observation in the top graph. The zone of low DO is highlighted in red.

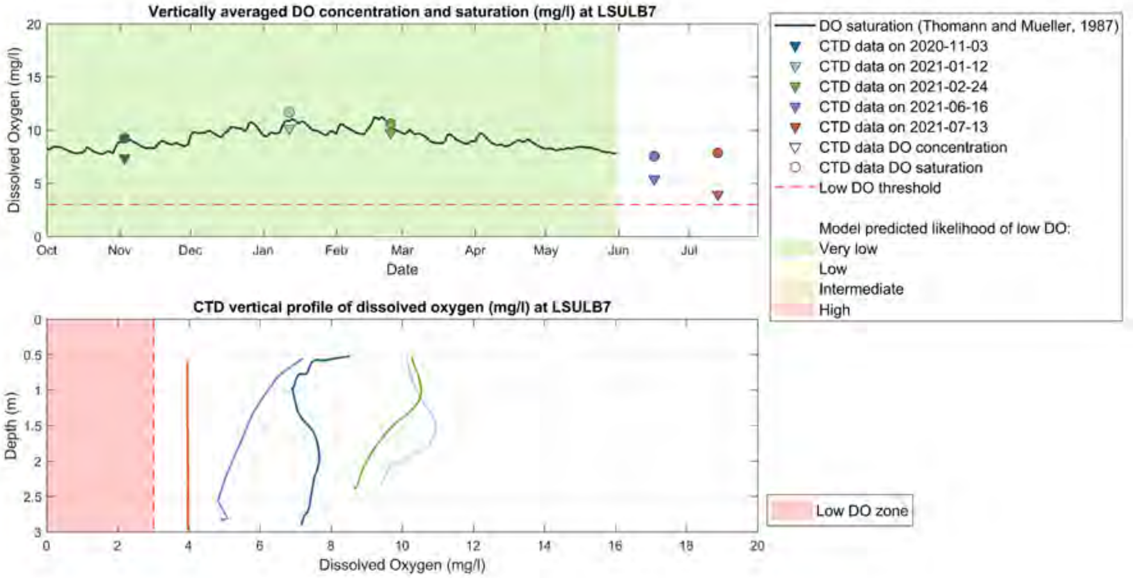

Figure F-37. DO proxy validation with CTD casts at LSULB7. Top graph: DO saturation estimated with Eq.8 (blue line), depth averaged DO saturation (circles) and concentration (triangles) measured by the CTD casts at LSULB7. Background color shows the likelihood of low DO predicted using the Hydrodynamic Model results and the rules in Table 8. Bottom graph: vertical DO concentration CTD profiles collected at LSULB7. The colors of the CTD vertical profiles in the bottom graph match the color of the depth averaged CTD observation in the top graph. The zone of low DO is highlighted in red.

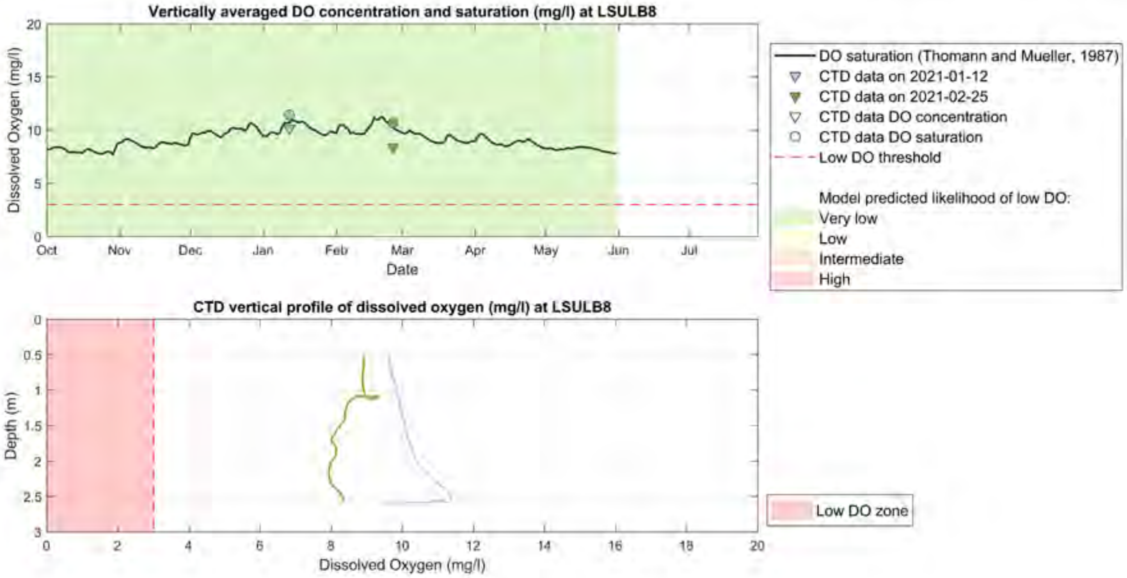

Figure F-38. DO proxy validation with CTD casts at LSULB8. Top graph: DO saturation estimated with Eq.8 (blue line), depth averaged DO saturation (circles) and concentration (triangles) measured by the CTD casts at LSULB8. Background color shows the likelihood of low DO predicted using the Hydrodynamic Model results and the rules in Table 8. Bottom graph: vertical DO concentration CTD profiles collected at LSULB8. The colors of the CTD vertical profiles in the bottom graph match the color of the depth averaged CTD observation in the top graph. The zone of low DO is highlighted in red.

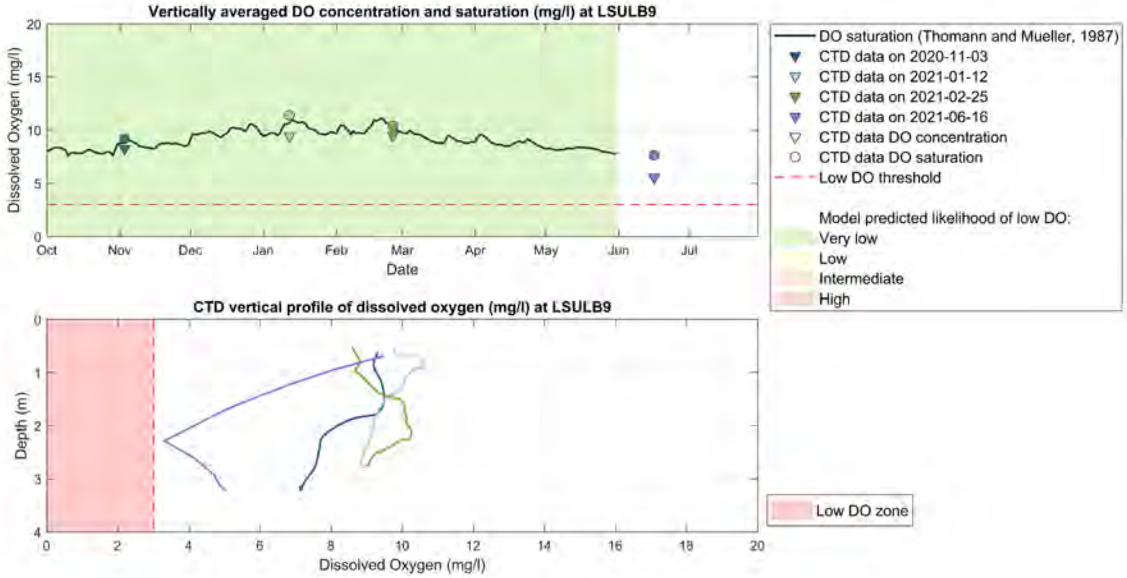

Figure F-39. DO proxy validation with CTD casts at LSULB9. Top graph: DO saturation estimated with Eq.8 (blue line), depth averaged DO saturation (circles) and concentration (triangles) measured by the CTD casts at LSULB9. Background color shows the likelihood of low DO predicted using the Hydrodynamic Model results and the rules in Table 8. Bottom graph: vertical DO concentration CTD profiles collected at LSULB9. The colors of the CTD vertical profiles in the bottom graph match the color of the depth averaged CTD observation in the top graph. The zone of low DO is highlighted in red.

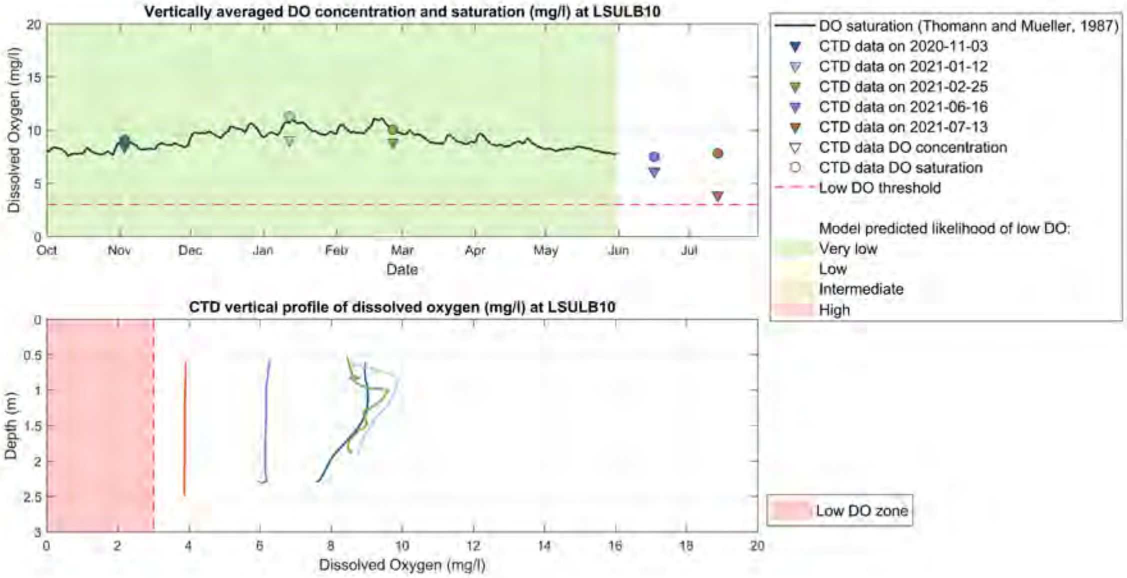

Figure F-40. DO proxy validation with CTD casts at LSULB10. Top graph: DO saturation estimated with Eq.8 (blue line), depth averaged DO saturation (circles) and concentration (triangles) measured by the CTD casts at LSULB10. Background color shows the likelihood of low DO predicted using the Hydrodynamic Model results and the rules in Table 8. Bottom graph: vertical DO concentration CTD profiles collected at LSULB10. The colors of the CTD vertical profiles in the bottom graph match the color of the depth averaged CTD observation in the top graph. The zone of low DO is highlighted in red.

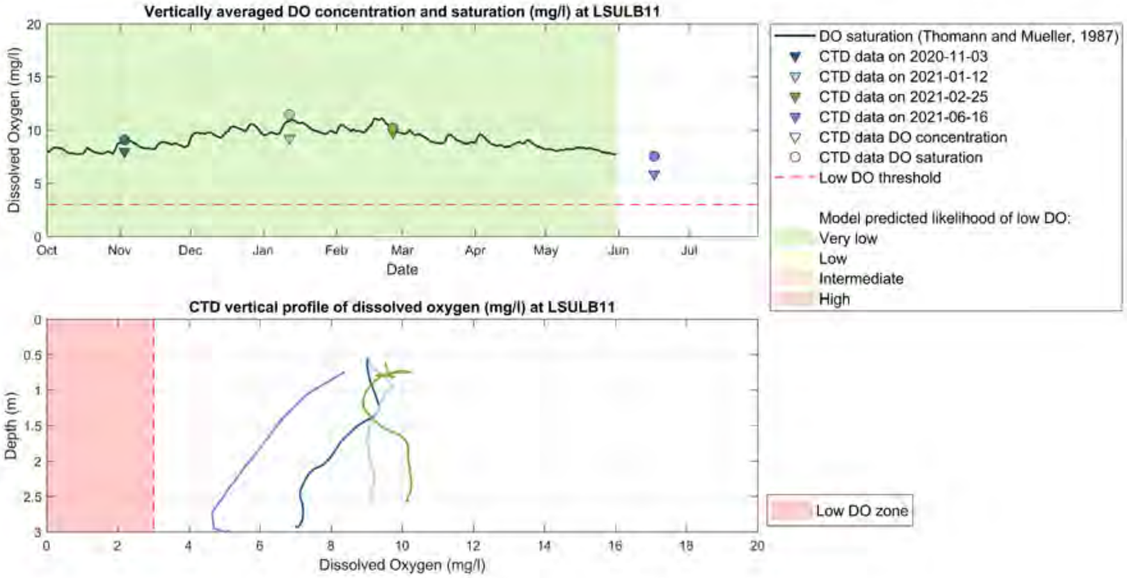

Figure F-41. DO proxy validation with CTD casts at LSULB11. Top graph: DO saturation estimated with Eq.8 (blue line), depth averaged DO saturation (circles) and concentration (triangles) measured by the CTD casts at LSULB11. Background color shows the likelihood of low DO predicted using the Hydrodynamic Model results and the rules in Table 8. Bottom graph: vertical DO concentration CTD profiles collected at LSULB11. The colors of the CTD vertical profiles in the bottom graph match the color of the depth averaged CTD observation in the top graph. The zone of low DO is highlighted in red.

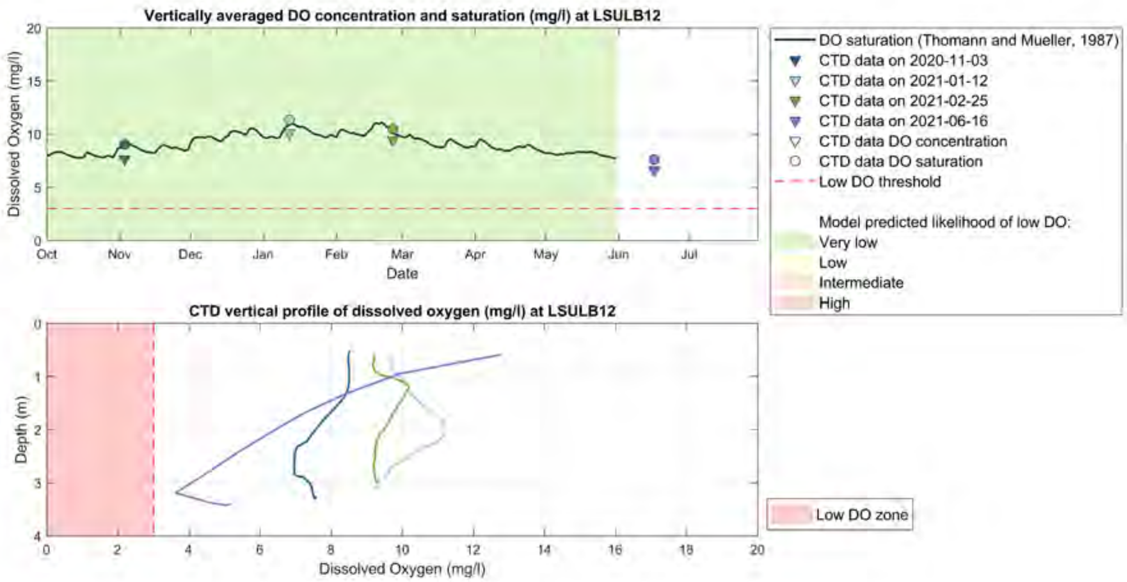

Figure F-42. DO proxy validation with CTD casts at LSULB12. Top graph: DO saturation estimated with Eq.8 (blue line), depth averaged DO saturation (circles) and concentration (triangles) measured by the CTD casts at LSULB12. Background color shows the likelihood of low DO predicted using the Hydrodynamic Model results and the rules in Table 8. Bottom graph: vertical DO concentration CTD profiles collected at LSULB12. The colors of the CTD vertical profiles in the bottom graph match the color of the depth averaged CTD observation in the top graph. The zone of low DO is highlighted in red.

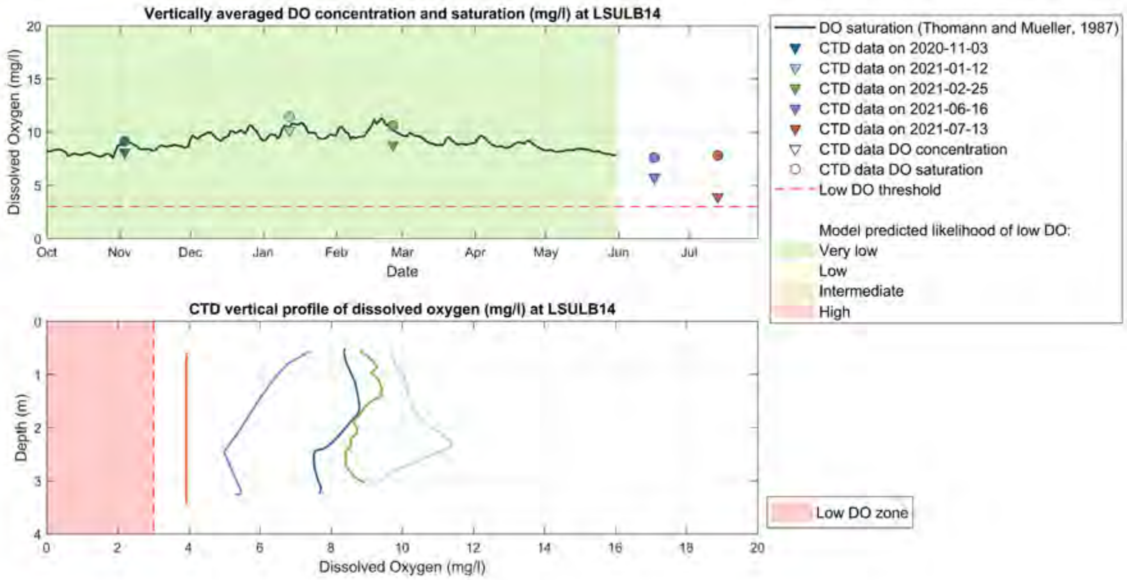

Figure F-43. DO proxy validation with CTD casts at LSULB14. Top graph: DO saturation estimated with Eq.8 (blue line), depth averaged DO saturation (circles) and concentration (triangles) measured by the CTD casts at LSULB14. Background color shows the likelihood of low DO predicted using the Hydrodynamic Model results and the rules in Table 8. Bottom graph: vertical DO concentration CTD profiles collected at LSULB14. The colors of the CTD vertical profiles in the bottom graph match the color of the depth averaged CTD observation in the top graph. The zone of low DO is highlighted in red.

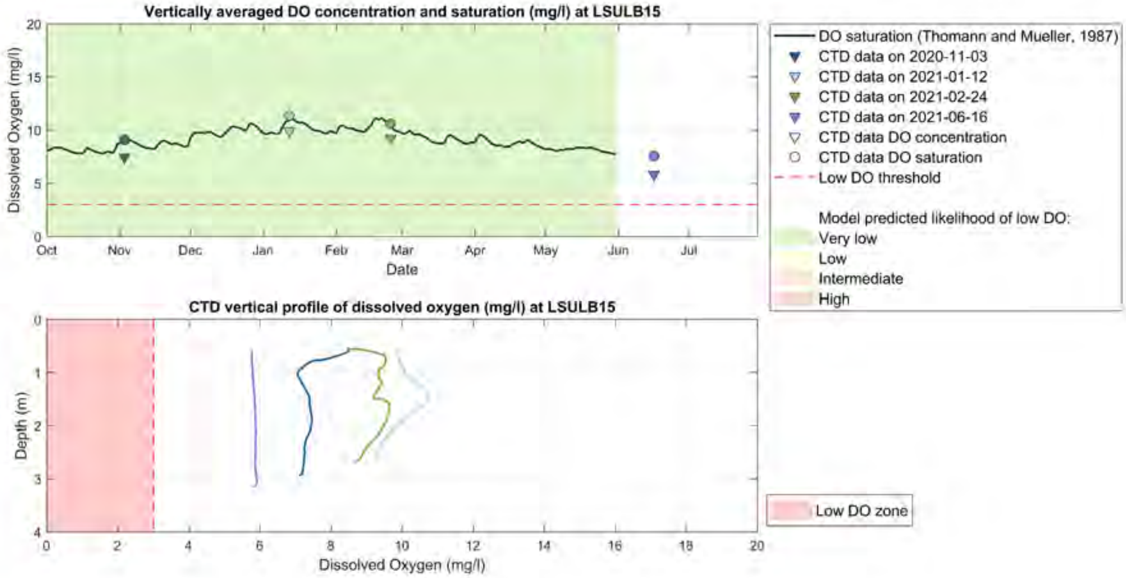

Figure F-44. DO proxy validation with CTD casts at LSULB15. Top graph: DO saturation estimated with Eq.8 (blue line), depth averaged DO saturation (circles) and concentration (triangles) measured by the CTD casts at LSULB15. Background color shows the likelihood of low DO predicted using the Hydrodynamic Model results and the rules in Table 8. Bottom graph: vertical DO concentration CTD profiles collected at LSULB15. The colors of the CTD vertical profiles in the bottom graph match the color of the depth averaged CTD observation in the top graph. The zone of low DO is highlighted in red.

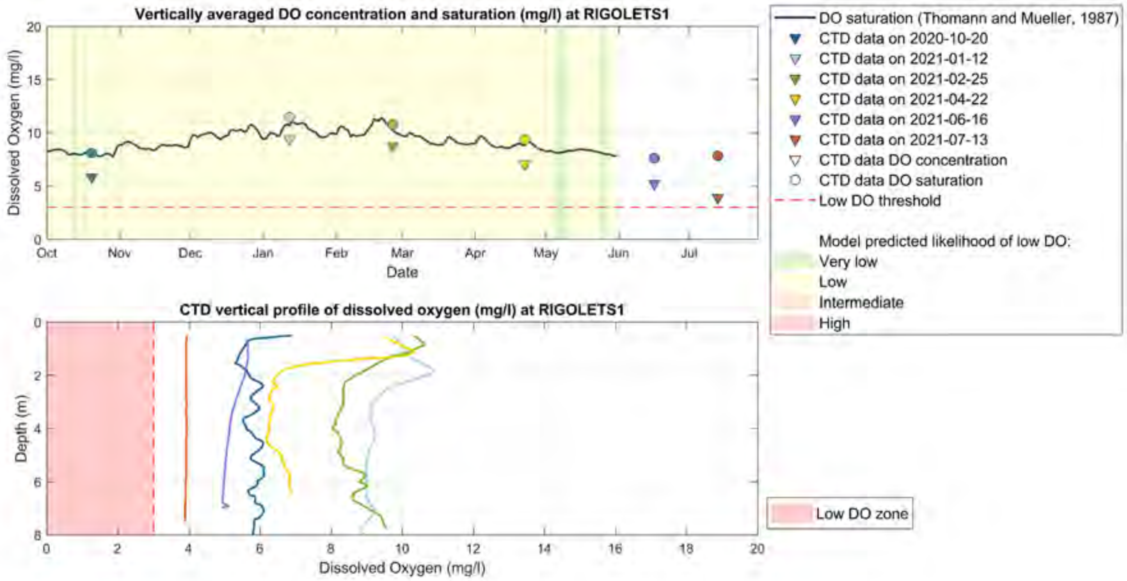

Figure F-45. DO proxy validation with CTD casts at RIGOLETS1. Top graph: DO saturation estimated with Eq.8 (blue line), depth averaged DO saturation (circles) and concentration (triangles) measured by the CTD casts at RIGOLETS1. Background color shows the likelihood of low DO predicted using the Hydrodynamic Model results and the rules in Table 8. Bottom graph: vertical DO concentration CTD profiles collected at RIGOLETS1. The colors of the CTD vertical profiles in the bottom graph match the color of the depth averaged CTD observation in the top graph. The zone of low DO is highlighted in red.

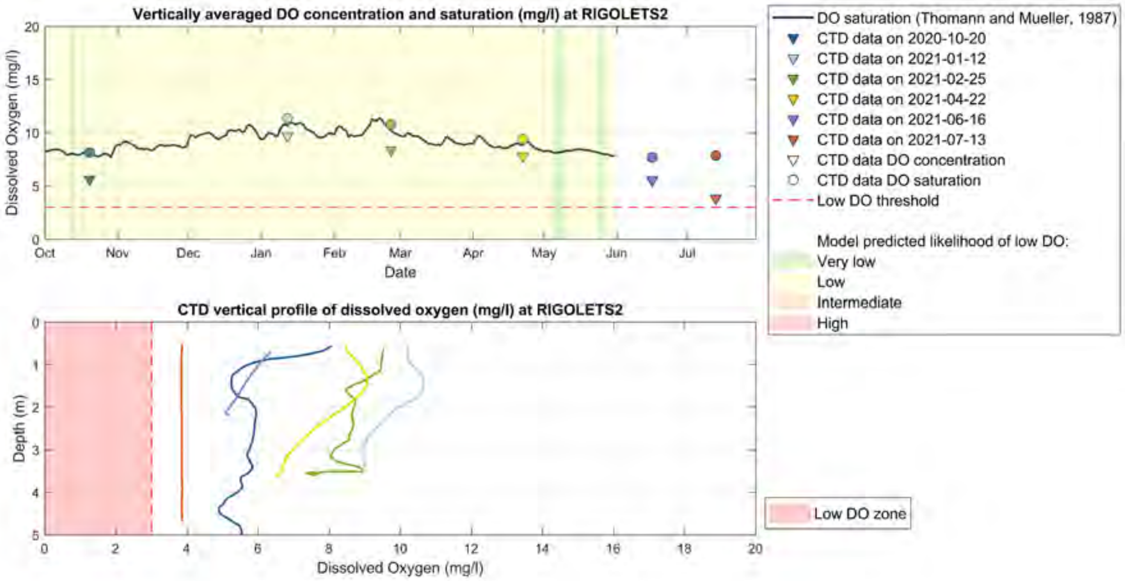

Figure F-46. DO proxy validation with CTD casts at RIGOLETS2. Top graph: DO saturation estimated with Eq.8 (blue line), depth averaged DO saturation (circles) and concentration (triangles) measured by the CTD casts at RIGOLETS2. Background color shows the likelihood of low DO predicted using the Hydrodynamic Model results and the rules in Table 8. Bottom graph: vertical DO concentration CTD profiles collected at RIGOLETS2. The colors of the CTD vertical profiles in the bottom graph match the color of the depth averaged CTD observation in the top graph. The zone of low DO is highlighted in red.

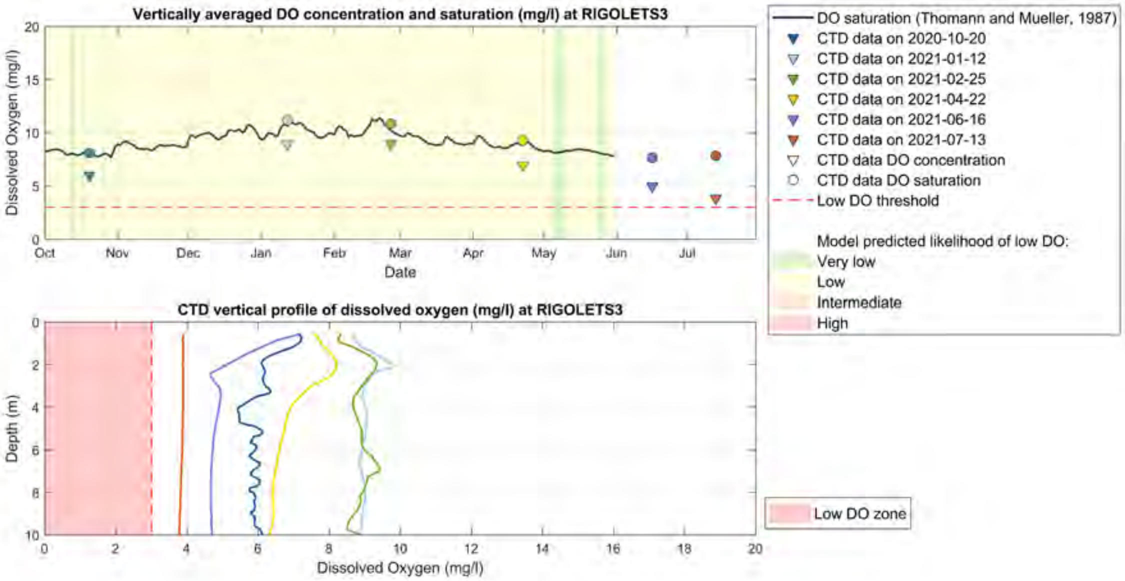

Figure F-47. DO proxy validation with CTD casts at RIGOLETS3. Top graph: DO saturation estimated with Eq.8 (blue line), depth averaged DO saturation (circles) and concentration (triangles) measured by the CTD casts at RIGOLETS3. Background color shows the likelihood of low DO predicted using the Hydrodynamic Model results and the rules in Table 8. Bottom graph: vertical DO concentration CTD profiles collected at RIGOLETS3. The colors of the CTD vertical profiles in the bottom graph match the color of the depth averaged CTD observation in the top graph. The zone of low DO is highlighted in red.

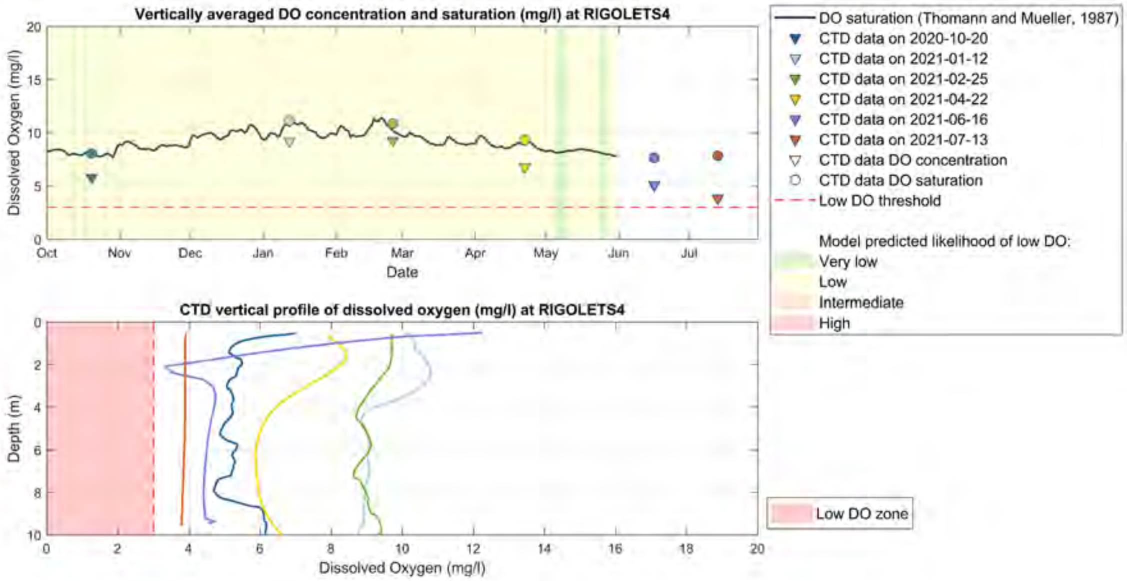

Figure F-48. DO proxy validation with CTD casts at RIGOLETS4. Top graph: DO saturation estimated with Eq.8 (blue line), depth averaged DO saturation (circles) and concentration (triangles) measured by the CTD casts at RIGOLETS4. Background color shows the likelihood of low DO predicted using the Hydrodynamic Model results and the rules in Table 8. Bottom graph: vertical DO concentration CTD profiles collected at RIGOLETS4. The colors of the CTD vertical profiles in the bottom graph match the color of the depth averaged CTD observation in the top graph. The zone of low DO is highlighted in red.

THE WATER INSTITUTE
OF THE GULF®

1110 RIVER ROAD S., SUITE 200
BATON ROUGE, LA 70802

(225) 448-2813
WWW.THEWATERINSTITUTE.ORG